Evolution of X-ray Properties of Galaxy Groups

by

AURELIA PASCUT

A thesis submitted to
The University of Birmingham
for the degree of
DOCTOR OF PHILOSOPHY

Department of Physics and Astronomy

University of Birmingham

March 2013

ABSTRACT

Studies of scaling relations in groups and clusters of galaxies have shown that the X-ray properties of groups deviate the most from the self-similar prediction. This is because groups are more affected by non-gravitational processes due to their shallower potential well, a behaviour which makes groups an ideal class of systems for the study of the impact of feedback. From the observational point of view, the study of the X-ray properties of groups, especially at high redshifts is hindered by their lower surface brightness compared to their more massive counterparts. We present the result from the Chandra Deep Group Survey, a survey dedicated to find high redshift groups in the deepest observations available in the Chandra archive. We found 26 groups and 36 clusters with available redshifts, with largest redshift being 1.3. We have used this sample to investigate the evolution of cool cores in these two classes of systems using cooling time divided by the age of the cluster as a parameter to describe the cooling state. We have found that groups and clusters have similar evolution in their cool core properties. Both classes of systems have a wide spread in the cool core parameter at low redshifts, which then narrows at high redshifts showing a lack of strong cool core systems.

ACKNOWLEDGMENTS

First and foremost, I would like to express my deepest gratitude to my supervisor, Prof. Trevor Ponman for his support and encouragement throughout my PhD and for being a role-model of a scientist, supervisor and person for me.

Special thanks goes to Prof. Steve Phillips from Bristol University for giving me the opportunity to work in his group, an experience which made me discover the beauty of astrophysics.

I would also like to thank to all people from the Extragalactic group especially to Alaistar Sanderson, Ewan O'Sullivan and Dr. Somak Raychaudhury for useful discussions and suggestions.

I am also very grateful for the good friends I made during my PhD . I also would like to thank Michael LoCicero for proof reading my thesis and David Stops for his technical support any time it was needed. Last but not least, I would like to thank my family and my husband for their support.

STATEMENT OF ORIGINALITY

This thesis describes the research work carried out at the University of Birmingham between October 2008 and March 2013.

Chapter 1 is an introductory chapter which gives an overview of the Λ-CDM cosmological model, formation and properties of groups and clusters of galaxies. Most of the images used in this chapter are part of literature results or manuals, and a reference or credit has been given.

Chapter 2 describes the Chandra Deep Group Survey (CDGS), which is a search for groups of galaxies in observations publicly available in the data archive of *Chandra* X-ray observatory. My contribution to the work has been to collect all data available in the archive, reduce and analyze it, and produce a final catalogue of X-ray selected groups and clusters. I have developed all software necessary for the above mentioned processes (with the exception of the extension test which has been developed by Dr. Nathan Slack at the University of Birmingham), using mainly tools from Chandra Interactive Analysis of Observations (CIAO) software. Data reduction and interpretation have been done with constructive input from my supervisor, Prof. Trevor Ponman and are also a result of useful discussions with group members, especially Dr. Somak Raychaudhury, Dr. Alaistar Sanderson and Dr. Ewan O'Sullivan.

Chapter 3 represent a study of the evolution of cool cores in groups and clusters using the sample constructed as described in Chapter 2. This Chapter has been written in form of a paper: The *Chandra* Deep Group Survey - cool core evolution in groups and clusters of galaxies, which has been published in the Monthly Notices of the Royal Astronomical Society (Pascut & Ponman 2015). My contribution to the paper, in addition to the data reduction and analyze, was to write the first draft under the guidance of my supervisor, who wrote the final form of the paper.

Chapter 4 presents a discussion of the work presented in this thesis, a short summary and suggestions of possible work which could follow from this thesis.

Contents

List of Figures

List of Tables

Chapter 1

Introduction

1.1 Standard ΛCDM cosmological model

The aim of any modern cosmological model is to give a mathematical description of the Universe, to explain its observed properties and make predictions about its evolution. Various models have been proposed over time, but the expanding knowledge about the Universe obtained through observations has allowed the ruling out of some of them. Since there is a mutual dependence between mathematical models and observations, new improved observations are able to put constraints on theoretical models. On the other hand, models give predictions which have to be tested by observations.

For example, one of the first models of modern cosmology was Einstein's model of the Universe. This model assumed that the Universe is static, has positive curvature (i.e. is finite and unbounded) and is filled with non-relativistic matter. This model of the Universe was ruled out after the assumption of a static Universe was proven wrong by early optical observations of galaxies. These observations showed that galaxies have an higher recessional velocity with increasing distance, a property which is expected if the Universe was expanding.

Currently, the most accepted model for the Universe is the ΛCDM model. According to this model, the Universe has the following characteristics:

- it is expanding, and the rate of expansion is given by the Hubble parameter
- it has an accelerated expansion
- the largest contribution to the total matter in the Universe is given by cold dark matter
- it has a flat geometry
- total energy density dominated by dark energy

ΛCDM model is the most accepted because it is able to explain best the observed properties of the Universe such as its accelerating expansion, the existence and characteristics of the radiation emitted immediately after the Big Bang, known as Cosmic Microwave Background (CMB), the large scale structure of galaxy clusters and the distribution of chemical elements. The following sections of this Chapter will give a brief description of the observational evidence which supports the ΛCDM model.

1.1.1 Expanding Universe; Distances in an expanding Universe

One important property of the Universe revealed by observations is its expansion. The fact that distances in the Universe increase with time was an early discovery based on observations of nearby galaxies. Hubble compared distances to nearby galaxies with their recessional velocities and found a linear dependence between them, with higher velocities for more distant galaxies. To describe mathematically the change in distances between astrophysical objects, a **scale factor** is used. For now on I will use the notation $a(t)$ for the scale factor at a moment t and adopt the usual convention $a(t_0)$ to represent the scale factor at the present time. The scale factor at a time t represents the ratio of the distance between two objects at that time to the distance between objects at a reference time t_0. Therefore, the scale factor at the present time, is by convention equal to 1 which leads to scale factors > 1 in the future, when the distances between objects increase, and < 1 in the past, when the Universe was smaller. One important consequence of the expansion is the change in the wavelength of radiation received from objects in the expanding Universe. The increase in distances leads to an increase in the wavelength of the radiation detected from an object compared to the wavelength of that radiation at the time it was emitted. The fractional change in the wavelength is characterized by the cosmological redshift, which is given by:

$$z = \frac{\lambda_{\rm obs} - \lambda_{\rm em}}{\lambda_{\rm em}} \tag{1.1}$$

where $\lambda_{\rm em}$ is the wavelength of radiation at the time it has been emitted and $\lambda_{\rm obs}$ is the wavelength at the time it has been observed. The relation between redshift and scale factor is then given by the ratio between scale factor at the present time and the scale factor at the time the light has been emitted ($t_{\rm em}$):

$$1 + z = \frac{a(t_0)}{a(t_{\rm em})} \tag{1.2}$$

There are different ways of defining distances in an expanding Universe, including the following: comoving distance, proper distance, luminosity distance and angular diameter distance.

Comoving distance (r) can be interpreted as a benchmark based on which distances in an expanding Universe can be measured. It is the actual physical distance between two objects measured at a particular reference time. If the Universe is expanding/contracting with a scale factor a, the comoving distance between these two objects will remain constant, although the actual physical distance between them is changing. Generally, the reference time adopted is the present time ($t_0 = 0$), at which the scale factor is 1 and is the only time when the comoving distance represent the actual distance between two objects.

Proper distance (d) represents the actual physical distance between two objects. It is the comoving distance (r) multiplied by the scale factor (a). Compared to comoving distance, which is constant with time, proper distance varies with it if the Universe is expanding/contracting.

Luminosity distance (d_L) is a simple approximation of the distance to one object for which its luminosity (L) is known. Since the observed flux of the source (f) is the luminosity per unit area of the sphere with radius d_L centred on the source, the relation between the distance to the object, its flux and luminosity is given by:

$$f = \frac{L}{4\pi d_\mathrm{L}^2} \tag{1.3}$$

For a flat and static Universe, luminosity distance equals proper and comoving distance. Nevertheless the Universe is expanding and as it expands, the observed flux is expected to decrease since the distance to the object increases. In addition to this, a decrease in the observed flux is seen because the energy of the photons passing through the unit surface area decreases by $(1+z)$ and their arrival time increases by $(1+z)$.

Therefore, the flux received at $z = 0$ is:

$$f = \frac{L}{4\pi a(t_0)^2 r^2 (1+z)^2} \tag{1.4}$$

Combining Equation 1.3 and Equation 1.4, luminosity distance is given by:

$$d_\mathrm{L} = (1+z)r, \tag{1.5}$$

where r is the previously defined comoving distance.

Angular diameter distance (d_A) is an estimate of the distance to extended objects for which the physical size of the object is known (D). If the source subtends an angle Θ on the sky, by using simple geometrical formula, we can obtain the distance to the source to be:

$$\Theta = \frac{D}{d_\mathrm{A}} = \frac{D}{ar} = \frac{D(1+z)}{a(t_0)r} \tag{1.6}$$

Therefore the angular diameter distance is:

$$d_{\mathrm{A}} = \frac{r}{(1+z)} \tag{1.7}$$

1.1.2 Evolution of the Hubble parameter

Information about the dynamics of the Universe can be obtained by studying the change of the scale factor as a function of time. The fractional rate of change of the scale factor is given by:

$$H(t) = \frac{\dot{a}(t)}{a(t)} \tag{1.8}$$

where $H(t)$ is called the Hubble parameter and $a(t)$ represents the scaling factor at a time t. The way in which Hubble parameter changes with time is given by the Friedmann equation:

$$H(t)^2 = \left(\frac{\dot{a}}{a}\right)^2 = \frac{8\pi G}{3}\rho + \frac{\Lambda}{3} - \frac{kc^2}{a^2} \tag{1.9}$$

where ρ is the mean matter density, which is a function of time, c is the speed of light, Λ is the cosmological constant and k is the curvature parameter, which gives indication about the geometrical properties of the Universe.

A special case of Friedmann equation is obtained for $k = 0$ (flat Universe) and $\Lambda = 0$ (matter dominated Universe). By rewriting Equation 1.9, the density of matter in this Universe is given by:

$$\rho_{\mathrm{crit}}(t) \equiv \rho(t) = \frac{3H(t)^2}{8\pi G} \tag{1.10}$$

This density, named critical density, represents the mean matter density required for a matter dominated Universe ($\Lambda = 0$) to have a spatially flat geometry ($k = 0$). Critical density is used as a reference value as function of which cosmological density parameters for various matter species and cosmological constant are defined: density parameter for matter ($\Omega_{\mathrm{m}}(t) = \rho_{\mathrm{m}}/\rho_{\mathrm{crit}}$; ρ_{m} is the density of matter; similarly, the density parameter for cold dark matter (Ω_{c}) and baryonic matter

(Ω_b) can be defined), density parameter for radiation ($\Omega_\mathrm{r}(t) = \rho_\mathrm{r}/\rho_\mathrm{crit}$; ρ_r is the density of radiation) and density parameter for the cosmological constant ($\Omega_\Lambda(t) = \rho_\Lambda/\rho_\mathrm{crit}$; ρ_Λ is the density associated with the cosmological constant). Using these parameters, Equation 1.9 can be written:

$$\Omega - 1 = \frac{kc^2}{a^2H^2} \tag{1.11}$$

where $\Omega = \Omega_\mathrm{m} + \Omega_\mathrm{r} + \Omega_\Lambda$ ($\Omega(t) = \rho/\rho_\mathrm{crit}$) is the total density. If the density parameter for curvature, Ω_K, is defined as $\frac{kc^2}{a^2H^2}$, then the Hubble parameter as a function of density parameters is given by:

$$H^2(z) = H_0^2[a(t)^{-4}\Omega_\mathrm{r} + a(t)^{-3}\Omega_\mathrm{m} + a(t)^{-2}(1 - \Omega_\mathrm{m} - \Omega_\Lambda) + \Omega_\Lambda] \tag{1.12}$$

From Equation 1.11 it is evident that the curvature of the Universe is determined by the evolution of total density. Best estimates for density parameters obtained from observations (Hinshaw et al. 2013) give us evidence that the Universe is flat ($\Omega = 1.0027^{+0.0038}_{-0.0039}$ and $\Omega_\mathrm{k} = -0.0027^{+0.0039}_{-0.0038}$), the energy density is dominated by the energy associated with the cosmological constant ($\Omega_\Lambda = 0.717 \pm 0.011$), while the matter density of the Universe represent only $\sim 30\%$ of the total matter ($\Omega_\mathrm{m} = 0.2855^{+0.0096}_{-0.0097}$) which is dominated by dark matter ($\Omega_\mathrm{c} = 0.2402^{+0.0088}_{-0.0087}$). The contribution from the baryonic matter to the total density is only $\sim 5\%$ ($\Omega_\mathrm{b} = 0.04628 \pm 0.00093$).

1.1.3 Dark matter

The concept of dark matter emerged as a results of studies of star dynamics and galaxy clusters mass measurement. It is used to describe a matter component of the Universe that can not be traced based on observations of electromagnetic radiations but rather through its gravitational effect on baryonic matter. Observational proof for the existence of dark matter came from the measurements of the mass of galaxy clusters, from its gravitational effect on photons (phenomenon known as gravitational lensing), or from its gravitational effect on gas and galaxies in clusters.

When observations of the circular motion of stars in spiral galaxies had been used to estimate the gravitational mass of these galaxies, it have been observed that the orbital circular velocity of stars is not decreasing at large radii, as expected if the total mass was given by that of stars and was concentrated at the centre, but it rather remains constant with radius. This was interpreted as evidence for existence of matter, in addition to that of stars within galaxies. Additional evidence for dark matter had been found when estimates of the total mass of clusters of galaxies inferred from the total amount of light received from stars and galaxies had been compared with mass estimates based on the galaxy dynamics and a significant difference had been found, with dark matter component being the dominant one.

Another indirect way to detect the presence of dark matter is through gravitational lensing, a phenomenon by which a massive object can change the light path from background objects and therefore create a distorted image of the background object. The amount of distortion makes it possible to map the mass of the object which behave like a lens. This method has been applied to observations of clusters to show that their total mass estimated from lensing exceeds the mass of the gas estimated from X-ray observations. Proof for the existence of dark matter has been found from multiwavelength studies of cluster 1E 0657-56, also known as the Bullet Cluster (Figure 1.1). In Figure 1.1, which represents an optical image of the cluster, dark matter distribution obtained from lensing and gas distribution inferred from X-ray observations, are overlaid in blue and pink colours. What is known as Bullet cluster is actually a system formed after the collision of two individual clusters. Combining the information obtained from lensing and X-ray, the behaviour of gas, dark matter and their interaction can be studied. The disturbed morphology seen in X-ray data suggests an interaction between the gas within the two clusters during the collision, while lensing ‘observation‘ of dark matter show its dissipationless nature.

Besides evidence for the existence of dark matter and information about its properties gained from observations like the ones mentioned above, constraints on the density of dark matter have been

Figure 1.1: Bullet Cluster (1E 0657-56). The background image represents the optical image of the cluster, while the blue and pink overlays represent X-ray emission from intracluster medium and the distribution of mass inferred from gravitational lensing mass maps. Credit: X-ray: NASA/CXC/CfA/ M.Markevitch et al.; Lensing Map: NASA/STScI; ESO WFI; Magellan/U.Arizona/ D.Clowe et al. Optical: NASA/STScI; Magellan/U.Arizona/D.Clowe et al.

obtained from observations of CMB. More recent estimates for the matter density parameter show evidence that this matter component dominates over the baryonic matter component, with about 85% of dark matter and 15% baryonic matter (Collaboration et al. 2013b; Hinshaw et al. 2013). Although knowledge about the density and properties of dark matter exists, the nature of dark matter is not a solved puzzle yet. Among the most important dark matter candidates are: i) Massive Compact Halo Objects (MACHOs); These are are astrophysical sources that do not emit any radiation or are too faint to be detected, such as black holes, brown dwarf, neutron stars and white dwarfs. If these sources are numerous then a significant fraction of the dark matter can be accounted by these MACHOs. The tool used to detect these objects is through gravitational microlensing (Paczynski 1986; Roulet & Mollerach 1997). When a MACHO passes close enough to the line of sight to a luminous background object (a star), there is a lensing effects (microlensing) as a result of which, the intensity of the background object is increased. A number of surveys have been designed to search for these microlensing effects from stars in the Large Magellanic Cloud, Small Magellanic Cloud or in the Galactic Bulge: EROS (Tisserand et al. 2007), OGLE (Wyrzykowski et al. 2009, 2010, 2011), MACHO (Alcock et al. 2000), etc. Results from these projects suggest that although MACHOs account for between 8% and 50% of Milky Way's dark matter halo, they are far less numerous to represent the only dark matter candidate.

ii) Weakly Interacting Massive Particles (WIMPs), which are considered to be elementary particles which interact only through gravitational and weak forces, neutrinos and axions. The search for these dark matter candidates is a challenging on-going work. Different experiments are built to directly detect WIMPS, based on their interaction with baryonic matter. The Large Underground Xenon experiment (LUX; Akerib et al. 2013), DarkSide-50 (Agnes et al. 2014), XENON (Aprile et al. 2005), Particle and Astrophysical Xenon Detector (PandaX; Cao et al. 2014), the Cryogenic Dark Matter Search (CDMS) and SuperCDMS (Akerib et al. 2004) experiments are some of them. Although the results obtained so far show no conclusive evidence for the existence of WIMPs

(Agnes et al. 2014, PandaX Collaboration et al. 2014), due to the fact that WIMP events are rare (and therefore it is more difficult to separate their signal from background events), the search for their existence is an on-going effort.

1.1.4 Dark energy

Observations of galaxies have led to the discovery of one important dynamical property of the Universe: its expansion (see Section 1.1.1). It is also observations, in particular those of Type Ia supernovae, which led to the discovery that the Universe has an accelerated expansion. The proof for an accelerated expansion of the Universe came independently from two different projects: Supernova Cosmology Project (Perlmutter et al. 1999) and High-Z Supernova Search (Riess et al. 1998). On one hand, high luminosity and almost similar brightness of Type Ia supernovae, makes them a very useful tool to measure the distance to their host galaxy, even for very distant supernovae, using the luminosity distance (see Section 1.1.1). On the other hand, the measurement of their redshift gives indication about how much the Universe has expanded since their light has been emitted. The study of the relation between these two gives information about the expansion of the Universe.

To explain the observed acceleration of the Universe the concept of dark energy has been introduced. The origin and nature of this energy component is currently unknown, and large surveys are dedicated to its study. Information about dark energy can be obtained by using different observational probes like: Type Ia supernovae, galaxy clusters, weak lensing and baryon acoustic oscillations. It has already been explained how measuring the luminosity and redshift of supernovae can give information about the expansion.

Clusters of galaxies and galaxy lensing observations represent very useful observational probes for dark energy (Alam et al. 2011). They can give information about the expansion of the universe by investigating how the number of clusters within a given volume changes as the volume is increased by the expansion. Moreover, the redshift distribution of clusters depends on the way in which the structure forms in the Universe, a process which is dictated by dark energy.

Baryon acoustic oscillations represent pressure waves created by oscillations of the photon-baryon fluid that existed before decoupling epoch in the early times of the Universe. These oscillations leave an imprint on the large-scale clustering of galaxies and can be used to measure distances and the acceleration of the expansion rate (Cole et al. 2005; Eisenstein et al. 2005; Blake et al. 2011; Kazin et al. 2014).

1.1.5 Geometry of the Universe

The best evidence for a flat geometry of the Universe comes from the study of CMB, and in particular of the temperature anisotropies observed in the CMB (Dodelson & Knox 2000; Jaffe et al. 2001; Netterfield et al. 2002). The amplitude of these fluctuations as a function of the angular scales at which these anisotropies are observed (i.e. angular power spectrum), represent a valuable tool which can be used to put constraints on cosmological parameters. A map of CMB anisotropies and the angular power spectrum obtained by *Planck* are showed in Figure 1.3. The angular scale corresponding to the position of the first peak is the one which depends on the spatial geometry of the Universe. Therefore, the good agreement between the observed power spectrum and the one predicted by a model with total matter density almost equal to unity provides evidence for a flat Universe ($\Omega_{\mathrm{K}} = -0.0014 \pm 0.017$; van Engelen et al. 2012).

1.2 Big Bang Nucleosynthesis

Another observational signature of the Universe which supports the ΛCDM model is the abundance of elements in the Universe. The Big Bang model predicts how the first elements in the Universe are created, a process called Big Bang Nucleosynthesis (BBN). This process takes place in the first 20 minutes after the Big Bang, when the temperature and density of the Universe is so high that nuclear reactions can occur.

The first nuclide to be created is deuterium (D), an isotope of hydrogen formed as a result of the collision between a proton and a neutron. The interaction of deuterium with a neutron/proton leads to the formation of tritium (T)/ ^{3}He. With the rapid expansion of the Universe, accompanied by a drop in temperature, the synthesis of elements stops and the Universe is filled only with light nuclides: D, ^{3}He, ^{4}He and ^{7}Li.

According to the BBN model, the abundances (relative to protons) of these nuclides are determined by only one free parameter: the ratio of baryons to photons (Steigman 2001). Since this ratio can be estimated independently from the observations of the anisotropies of the CMB, a good test for the Big Bang model is to compare the abundances predicted by the BBN with those estimated directly from observations.

Figure 1.2 shows the BBN predictions of how the abundance of each element depends on the baryonic matter density. Red circles mark the expected values for the abundances of each element for the matter density value estimated from the Wilkinson Microwave Anisotropy Probe (WMAP; red line). A set of abundances relative to hydrogen predicted from the BBN for D, ^{3}H and ^{7}Li is: $(2.68 \pm 0.15) \times 10^{-5}$, $(1.05 \pm 0.15) \times 10^{-5}$ and $(5.14 \pm 0.50) \times 10^{-10}$, while the mass fraction prediction for ^{4}He is 0.2476 ± 0.0004 (Coc & Vangioni 2010).

Because after BBN, stellar nucleosynthesis can change the primordial abundances of the nuclides (with the exception of D which is only destroyed after BBN), astrophysical sources used to estimate the primordial abundances are generally those which have not been enriched with stellar-produced nuclides during the evolution of the Universe.

Observations of clouds at high redshift on the line of sight of distant quasars have been used to estimate the abundance of deuterium. Some of the estimated abundances are: $2.42^{+0.35}_{-0.25} \times 10^{-5}$ (Kirkman et al. 2003), $3.31^{+0.49}_{-0.42} \times 10^{-5}$ (O'Meara et al. 2006), $2.75^{+0.27}_{-0.24} \times 10^{-5}$ (Pettini et al. 2008) and $2.82^{+0.20}_{-0.19} \times 10^{-5}$ (Fumagalli et al. 2011).

The abundance of ^{4}He is determined from extragalactic regions of ionized hydrogen (H II). Among mass fractions reported in the literature are: 0.2477 ± 0.0029 (Peimbert et al. 2007), 0.250 ± 0.004 (Fukugita & Kawasaki 2006) and 0.2565 ± 0.0010 (Izotov & Thuan 2010).

Since ^{3}He is both created and destroyed in stars and the evolution of its abundance is not well known, a secure estimation of its primordial abundance is difficult to obtain. For example, Bania et al. (2002) have estimated the abundance of ^{3}He from observations of an H II region within our Galaxy and inferred a value of $(1.1 \pm 0.2) \times 10^{-5}$.

^{7}Li is estimated from observations of metal-poor Galactic halo stars. These stars are showed to have a constant ^{7}Li abundance independent of their metallicity which suggests that lithium is in its primordial form, without being affected by Galactic nucleosynthesis (Spite & Spite 1982). Some literature estimates for lithium abundance are: $(1.23^{+0.34}_{-0.16}) \times 10^{-10}$ (Ryan et al. 2000), $1.1 - 1.5 \times 10^{-10}$ (Asplund et al. 2006) and $1.58 \pm 0.31 \times 10^{-10}$ (Sbordone et al. 2010).

A comparison between observed and predicted abundances for primordial nuclides shows a good agreement for all elements except for ^{7}Li. This good agreement represent a confirmation of the Big Bang model and the ΛCDM model. However, this is not a total agreement, since the observed abundance of ^{7}Li is a factor between 2 and 4 lower to the predicted value. This discrepancy, dubbed 'the lithium problem', is still an unresolved puzzle and the key to it is sought by improving the way

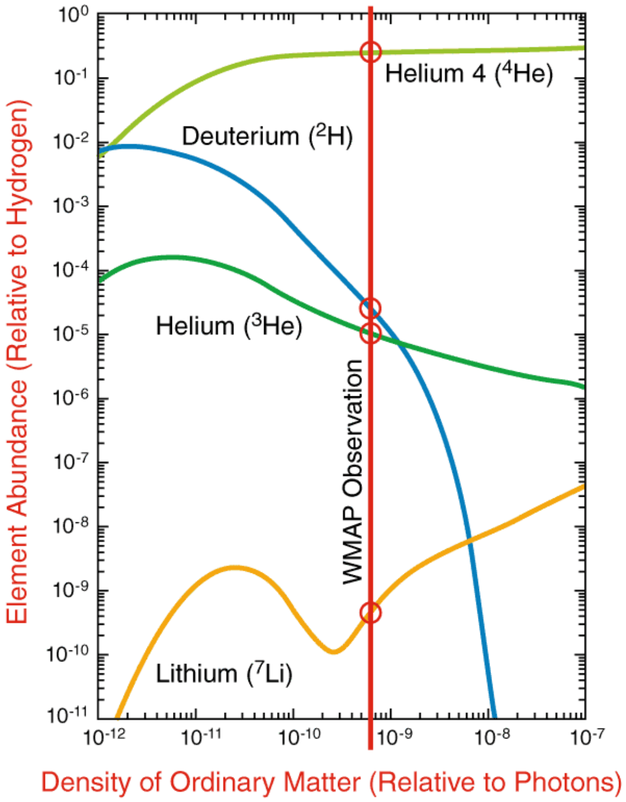

Figure 1.2: The predicted abundance of deuterium, helium and lithium as a function of matter density. The vertical red line marks the value of the matter density measured by WMAP. For this value of the density, the expected abundances of shown elements are marked with red circles. Figure credit: NASA / WMAP Science Team.

in which the primordial lithium abundance is measured or by investigating for possible errors in the BBN light element predictions (Fields 2011).

1.3 Formation of large-scale structure

The ΛCDM cosmology, as an extension of the Big Bang model, is based on the Cosmological Principle which assumes that the Universe is homogeneous and isotropic. Observations of the radiation emitted immediately after the Big Bang confirmed that indeed, on large scales, larger than the size of clusters of galaxies, the Universe is uniform. On the other hand, the presence of stars, galaxies and clusters structured into filaments and voids is a clear indication that on scales of the size of clusters, the Universe is non-uniform. This section will give a description of the current accepted model for the formation of the large scale structure which can be observed today.

The key observation than can be used to answer the question of how the large scale structure in the Universe has formed, is the Cosmic Microwave Background (CMB), which represents the flux received in the microwave energy regime from all over the sky.

The most accepted explanation for the origin CMB comes from the Big Bang Theory. According to this theory, the photons which can be detected as CMB represent radiation emitted shortly after the Big Bang. One of the observed properties of the CMB spectrum is its very good agreement with that of a black body spectrum, with a temperature of 2.7 K. For a source to produce a blackbody spectrum, it has to be non-reflecting, isothermal and opaque. According to the Big Bang Theory, these are the properties of the Universe immediately after the Big Bang, in a period known as the recombination epoch. At the time of recombination, the Universe was very hot and very dense, and filled with hot plasma of particles (protons, neutrons, electrons) and photons. It is the time at which ions and electrons combine and density of neutral baryonic matter starts to increase. The Universe is opaque and the energy distribution of photons follows a black body spectrum. At the same time, the Universe expands and the interaction between photons and electrons is less. The Universe enters into the epoch of photon decoupling, in which it became more transparent to photons. In the last phase, called the last scattering, the large expansion has created a transparent Universe in which CMB photons can travel without interacting with electrons. It is during recombination/decoupling when the CMB is created and its spectral properties are fixed.

Another property of the CMB is the almost uniform distribution of its temperature. All sky, high

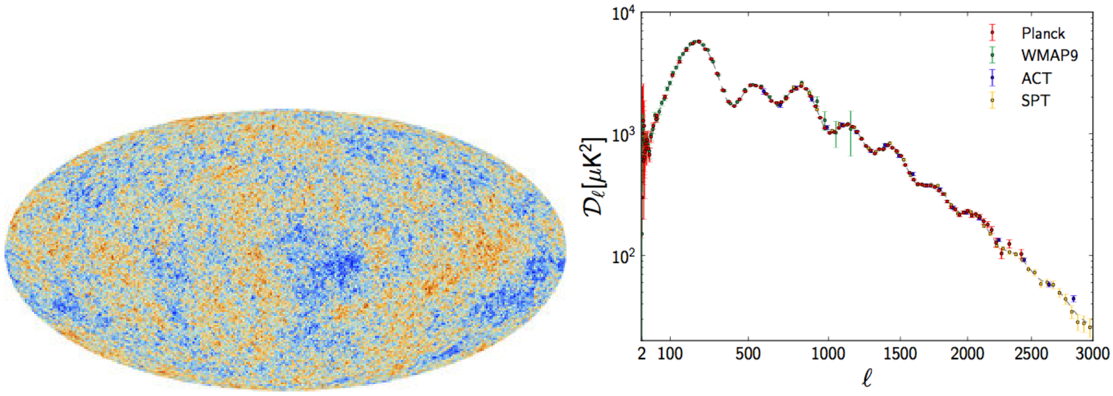

Figure 1.3: Left panel: Full sky Cosmic Microwave Background (CMB) measured by Planck satellite. Credit: ESA and the Planck Collaboration; NASA / WMAP Science Team. Right panel: Angular power spectrum measured from Planck, Wilkinson Microwave Anisotropy Probe (WMAP), the Atacama Cosmology Telescope (ACT) and the South Pole Telescope (SPT). Figure from: Collaboration et al. (2013a)

resolution observations of CMB has been performed with WMAP and more recently with *Planck* satellite. Based on these observations, small temperature fluctuations have been detected in the black body temperature fitted from the CMB spectrum extracted from regions with different scales. Figure 1.3 shows the anisotropy temperature map obtained by *Planck*.

These temperature fluctuations indicate the presence of small fluctuations in the density distribution of matter at the time when radiation from the CMB had been created. CMB, through its temperature fluctuations gives important information about the matter distribution and the formation of large-scale structures in the Universe.

Gravity plays a crucial role in determining the evolution of density fluctuations, through a mechanism known as **gravitational instability**. As the Universe expands, the mean density surrounding over-dense regions decreases. On the other hand, in the over-dense regions the gravitational fields is stronger than that in the surrounding regions and will resist Hubble expansion. The result of this will be that positive density fluctuations will grow over time. The opposite effect is seen for the underdense regions, for which the self-gravity is weaker than that which corresponds to Hubble expansion and therefore the amplitudes of these density fluctuations will increase as well in modulus.

The simplest model which describes the collapse of matter and formation of virialized objects is the **top hat model**. This model represents overdensites as spherical regions with a uniform mean density. As these overdensies grow, these regions will evolve independently of the background medium in which they reside. The perturbations will grow until they reach a maximum radius, called the turn around radius, at which point, the overdensity will not follow anymore the Hubble expansion. The overdensity will start collapsing and entering into a process called virialization, at the end of which a virialized object is formed. A gravitationally bound system of particles is said to be virialized if it obeys a simple relation between the total kinetic (K_{E}) and potential energy (P_{E}), given by the virial theorem:

$$K_{\mathrm{E}} - 2P_{\mathrm{E}} = 0 \tag{1.13}$$

The response of the mean density of the perturbation to these processes is to increase as the process of collapsing and virialization start. It is useful to compare these densities to the critical density at a corresponding time and get the density contrast ($\Delta = \rho/\rho_{\mathrm{crit}}$). For a matter dominated universe, the density contrast after virialization is: $\Delta_{\mathrm{v}} = \rho/\rho_{\mathrm{crit}} \approx 178$. For a ΛCDM cosmology, this density contrast can be approximated with:

$$\Delta_{\mathrm{v}} = 18\pi^2 + 82[\Omega_{\mathrm{m}}(z) - 1] - 39[\Omega_{\mathrm{m}}(z) - 1]^2 \tag{1.14}$$

(Bryan & Norman 1998), where Ω_{m} represents the ratio between total matter density of the Universe and critical density.

The density contrast (Δ_v) it is used to define the radius of virialized systems as the radius r_v within which the mean matter density is $\Delta_\mathrm{v}\rho_\mathrm{crit}$ (Eke et al. 1996).

1.3.1 Virial shocks in galaxy and cluster haloes

In the ΛCDM model, the formation of large scale structures takes place in an hierarchical fashion, with smaller objects being the first one to form and then grow into more massive objects like groups and clusters of galaxies. In the standard spherical collapse model (Gunn and Gott1972), the formation of large scale structures starts when a spherical symmetric overdensity decouples from the Hubble flow, slows down, turns around and collapses. From this point on, this collapsed object will start growing through accretion of smaller units by gravitational infall and mergers.

The simple model for gas accretion is the generalized spherical model for gas accretion (Knight & Ponman 1997; Tozzi & Norman 2001; Voit et al. 2003), in which a shell of gas which is accreted on the cluster experiences different processes. The shell of gas which decouples from the Hubble flow, starts falling back and suffers adiabatic compression during its infall. At some point during its supersonic flow towards the centre of the halo, the gas reaches the accretion radius, where it encounters nearly stationary gas that had already collapsed. The gas is shock heated to the virial temperature of the halo. Then, the gas is further compressed within the potential well of the cluster due to further growth of the halo.

A prediction of 3D cosmological N-body and hydrodynamical simulations is the existence of an expanding accretion shock, known as “virial shock”, generated at the interface between the inner hydrostatic gas and the external medium (e.g. Evrard 1990; Bryan & Norman 1998; Keshet et al. 2003). However, the assumption that matter is accreting on clusters in spherical shells with uniform density is not a valid one for a cold dark matter dominated Universe in which the accretion is lumpy and anisotropic. With gas falling into the cluster along filaments, the location and strength of the shock varies along different directions.

More complexity is added to this picture of gas accretion if the cooling time of the post-shocked gas is taken into account. If the cooling of the post-shocked gas is inefficient then the post-shocked gas will be able to support the shock against gravitational collapse at approximately virial radius. On the other hand, if cooling times are sufficiently short, the gas will collapse and will not be able to support the shock which will form at much smaller radii compared to virial radius (Birnboim & Dekel 2003). The 1-D hydrodynamic model of Birnboim & Dekel (2003) predicts a critical value of about 10^{11} $M_\odot$ for the mass of a dark matter halo above whcih the shock is supported at the virial radius.

Although from a theoretical point of view the presence of shocks at about virial radius is required, at least for massive systems, during the process of the formation of large scale structures, there is no significant observational confirmation for these shocks. The main reason for the lack of observational evidence is the difficulty to detect shocks close to virial radius, where cluster gas density is very low and therefore reliably detect any density discontinuities which are a characteristic of a shock. Compared to X-ray observations, in which the X-ray flux is proportional to the square of the density, in the case of SZ observations the flux is proportional to the gas density. Since the SZ surface brightness has a less rapid drop than X-ray surface brightness, SZ observations of clusters provide a better chance of detection of virial shocks. Although there are no SZ detections of virial shocks reported in the literature yet, high resolution telescopes like Atacama Large Millimeter Array (ALMA) are predicted to allow the detection of strong shocks around the virial radii of clusters (Kocsis et al. 2005).

1.3.2 Galaxy formation

In the hierarchical model of structure formation, galaxies represent the building blocks for the formation of larger scale structures like groups and clusters. According to an early model of galaxy formation, when galactic size dark matter haloes are collapsing, they accrete gas which is able to cool efficiently and condense at the centre of the halo and form a galactic disk (White & Rees 1978). Attempts to confirm this model with observations of galaxy properties have run into several problems, one of them being known as the “overcooling” problem. The overcooling problem is the discrepancy between the amount of gas which has cooled and condensed during the galaxy formation and the subsequent formation of galaxy groups and clusters in cosmological simulations compared to observations.

Cosmological N-body simulations can predict the number density of dark matter haloes within a given mass range (i.e. halo mass function) (Reed et al. 2007; Tinker et al. 2008). From the observational point of view, the property which is more easily measurable is the galaxy luminosity function (galaxy luminosity number density within a given luminosity interval), a function which is expected to have a similar shape to that of the halo mass function. However, observations show that the galaxy luminosity function is different to theoretical expectations at the low luminosity end, as well as the high luminosity end (see Figure 1.4 for a qualitative representation of the discrepancy between observations and theoretical expectations).

The faint-end slope of the observed luminosity function has been found to vary depending on the observed band and galaxy environment between ~ 0.9 and ~ 1.5 (Ryan et al. 2007), while simulations predict a steeper slope of ~ 2 (Finlator et al. 2006; Night et al. 2006; Jaacks et al. 2012). This discrepancy suggests that star formation must be inefficient in low mass systems. The most likely process thought to be responsible for the discrepancy between predicted and observed faint-end slope of luminosity function is the supernovae (SN) feedback. Supernovae explosions

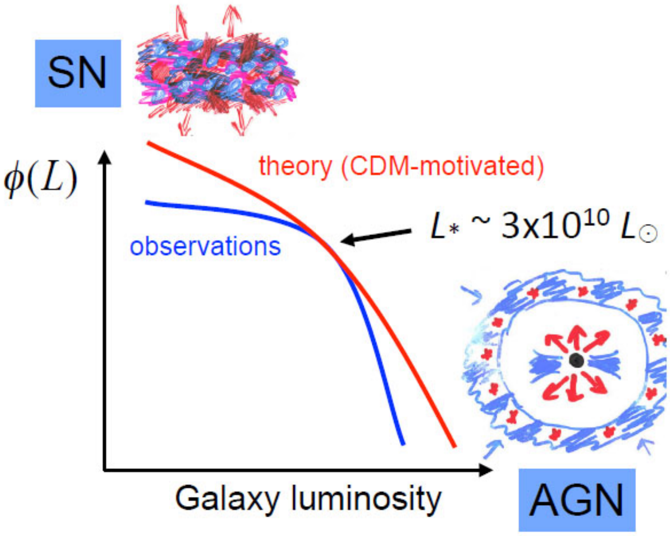

Figure 1.4: A schematic representation of the discrepancy between the expected (red line) and observed (blue line) galaxy luminosity function at low- and high-luminosity end. Figure from Silk & Mamon (2012).

are able to reduce the efficiency of star formation and therefore the galaxy luminosity by heating or ejecting the gas out of galaxies through galactic winds.

While including SN feedback in cosmological simulations is able to bring the predicted and observed faint-end luminosity functions into an agreement (Kauffmann et al. 1999; Efstathiou 2000), SN feedback however, is not able to match the luminosity functions at the bright end by suppressing the number of very luminous galaxies (Borgani2004). This is because SN feedback is more efficient in lower mass haloes, with a shallower potential well from which they can expel or heat the gas more efficiently (Benson et al. 2003). Therefore, a more efficient heating mechanism is required to solve the problem of overproduction of bright galaxies in cosmological simulations compared to observations. This mechanism is AGN feedback (see 1.6 for more details on AGN feedback).

One important observational evidence which suggests that AGNs must play an important role in the process of galaxy formation is the fact that all galaxies host a central supermassive black hole (SMBH) and there is a tight relation (known as Magorrian relation) between the mass of the SMBH and that of the bulge of a galaxy (Magorrian et al. 1998; Marconi & Hunt 2003; Häring & Rix 2004). This relation can be interpreted as evidence that black holes were responsible for determining the growth of galaxies or vice versa. Moreover, since more massive galaxies host larger black holes, the energy injection from an AGN is greatest in more massive systems, in contrast to the case of stellar feedback. Including AGN feedback in semi-analytical models of galaxy formations have demonstrated the necessity of this mechanism for reproducing the bright end of the galaxy luminosity function (Bower et al. 2006; Croton et al. 2006; De Lucia & Blaizot 2007; Somerville et al. 2008).

1.3.3 Dark matter density profile

The distribution of matter in collapsed and virialized systems is, as already showed, dominated by dark matter. A dark matter halo includes 80% dark matter and only 20% baryonic matter whose distribution inside the dark matter halo is dictated by the gravitational potential of the halo. But what is the distribution of dark matter? An answer to this question has been sought by various studies mostly from a theoretical point of view, with analytical models and N-body numerical simulations, but also from an observational point of view.

Simple analytical models and early lower resolution numerical simulations describe the shape of the density distribution of matter by a power law, with a function given by the **Singular Isothermal Sphere (SIS)**:

$$\rho(r) = \frac{1}{r^2}$$

Later on simulations, with improved resolution showed that the slope of the density profile changes with radius, with a steeper profile at larger radii. A function adopted by Dubinski & Carlberg 1991 to parametrize the different distribution of density in the inner and outer region of the halo is the **Hernquist profile** (Hernquist 1990) given by:

$$\rho(r) \propto \frac{1}{(r/r_\mathrm{s})(1+r/r_\mathrm{s})^3}$$

A similar form with that of the Hernquist profile although with a different outer logarithmic slope is the **The NFW profile** (Navarro et al. 1995), which is described by

$$\rho(r) = \frac{\rho_\mathrm{s}}{(r/r_\mathrm{s})(1+r/r_\mathrm{s})^2}$$

where ρ_s represent the amplitude of the density profile and r_s is a characteristic radius since it is the radius at which the slope of the density profiles changes. For $r << r_\mathrm{s}$, $\rho \sim r^{-1}$ while for $r >> r_\mathrm{s}$, the profile is steeper, with $\rho \sim r^{-3}$. This radius is used to define a concentration index as the ratio between r_{200} and $\mathrm{r_s}$ ($c = r_{200}/r_\mathrm{s}$), which gives information about mass concentration. If r_s is much smaller than r_{200} it means that the mass is more strongly concentrated towards the centre. The only difference between the NFW profile and Hernquist profile is the behaviour of density at very large radii, where the NFW profile is shallower than the Hernquist.

One important result obtained by Navarro et al. (1997) is that NFW is an universal profile which represent a good approximation to halos of different mass range at various radii.

Generalized NFW Density Profile (Zhao 1996) represent another parametrization for the halo density profile based on more recent N-body simulations. The form of density profiles is given by:

$$\rho(r) = \frac{\rho_s}{(r/r_\mathrm{s})^\alpha(1+r/r_\mathrm{s})^{3-\alpha}}$$

where α is called inner slope and is the central, negative, logarithmic density slope. From the equation it can be seen that this is a generalisation of the NFW profile, which can be obtained from $\alpha = 1$. α represent a parameter in the fitted model and determination of its value represent the aim of several number of works, from the theoretical point of view as well as observational. Typical values for alpha lie in the 1.1 ± 0.4 range (Moore et al. 1999; Ghigna et al. 2000; Diemand et al. 2005). The universal profile found by Navarro et al. (1997) has also been confirmed by the study of Moore et al. (1999). Like Moore et al. (1999), Jing & Suto (2000) find a steeper profile for the inner profile slope compared to the NFW. However, they do not find that DM density profiles are universal across a wide range of masses, but they show that profiles become less cuspy with increasing mass. Moreover, they even found a scatter for the same mass.

A common feature of all these profiles is an increasing density towards the centre, with an infinite density at $r = 0$. Some studies have showed that the Einasto profile provides a better description of CDM halos than the NFW or the gNFW (Navarro et al. 2004, 2010; Merritt et al. 2005, 2006-Empirical models for DM halos: I; Stadel et al. 2009; Reed et al. 2011). Dutton & Macciò (2014) showed that CDM halos are better described by Einasto profile. Compared to all above mentioned profiles, the Einasto profile has a finite central density. **Einasto profile** is given by:

$$\rho(r) = \rho_{\rm s} exp(-2/(\alpha)(r/r_{\rm s})^{\alpha} - 1)$$

α is called shape parameter.

Comparison with observations of the density distribution of DM is hindered by the presence of baryonic matter within DM halos. The gravitational potential created by baryonic matter has an influence on the DM density distribution, whose profile is different from that obtained from pure dark matter simulations. If all DM halos have an universal shape, then information about DM distribution can be obtain from observations of objects residing in small DM halos, like galaxies or observations from clusters of galaxies which inhabit the largest DM halos.

Based on X-ray observations of 34 dynamically relaxed clusters, Schmidt & Allen (2007) found a good agreement with NFW model (alpha consistent with unity 0.88 ± 0.29), while the isothermal sphere model can be ruled out in almost all cases.

1.4 X-ray properties of groups and clusters of galaxies

1.4.1 Scaling relations

Clusters of galaxies have been discovered in optical images as galaxy overdensities, hence their name. Dark matter has an important effect on the observed properties of X-ray groups and clusters since it determines the shape and depth of the potential well. Depending on the strength of the potential well, the gas is heated to high temperatures, and emits X-ray radiation through thermal bremstrahlung and line emission. Temperatures found for these systems are varying from about 0.7 keV to about 12 keV. On the other hand, the distribution of the potential well determines the distribution of gas density. Since X-ray emission is proportional to the square of its density, galaxy clusters are the most luminous extended objects in X-ray with luminosities ranging between $10^{43} - 10^{45}$ erg s^{-1} while groups' luminosity ranges between $10^{42} - 10^{43}$ erg s^{-1}. The fact that X-ray luminosity is scaling with the density of the gas, makes it a reliable estimate of the total gas mass.

Although X-ray emission is associated with a large majority of clusters and its presence suggest the existence of a virialized system, there are groups and clusters for which X-ray emission could not be detected. It is not clear if the lack of X-ray emission is due to an absence of gas within those clusters or the fact that gas is not heated to X-ray emitting temperatures. Figure 1.5 shows the X-ray (left panel) and optical image with X-ray contours overlaid (right panel) of a cluster. The regular X-ray emission suggests the existence of an evolved system, which has a strong potential and a high concentration of gas at their centre.

According to simple models of structure formation that involve only gravitational processes, clusters are the result of the gravitational collapse of overdense regions in the matter density distribution in the Universe. These models predict a universal density profile for dark matter halos

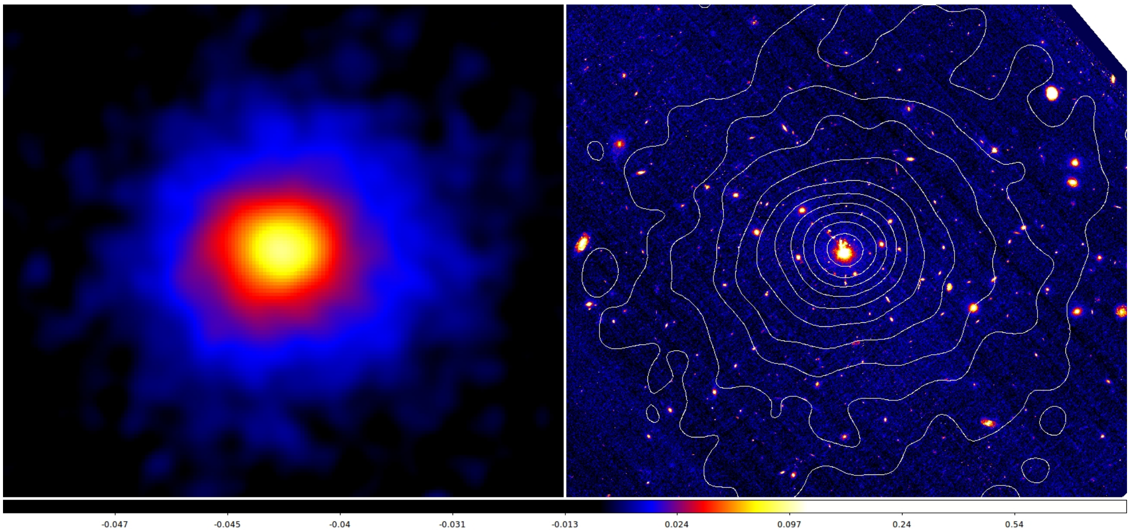

Figure 1.5: Left: *Chandra* X-ray image of the MACS J0913.7+4056 cluster of galaxies (observation ID: 10445, PI: Kenneth Cavagnolo). Right: Optical image of the same cluster, obtained with the *Hubble Space Telescope* (*HST*). The image shows an overdensity of galaxies with a dominant galaxy at the centre of the X-ray emission, which is marked by the white overlaid contours. (*HST* image PI: Harald Ebeling)

irrespective of their mass. Since gas in the ICM is tracing dark matter, the same universal density profile is expected for clusters and groups and therefore $\rho \propto \rho_{\rm g}$, where $\rho_{\rm g}$ is the gas density. As a result, the observed global properties of X-ray clusters, like temperature and luminosity are expected to scale with the system mass. Therefore, systems with masses spanning several orders of magnitudes should be self-similar and a set of scaling relations between X-ray global properties like mass, temperature and luminosity can be defined. These scaling relations are derived using the virial theorem, under the assumption that the emission from the gas within ICM is due to thermal bremsstrahlung. To derive these relations, one aspect which has to be considered is how the radius of the system is defined. If the size of the system is defined as the radius at which the system has an overdensity (Δ) above the critical density, then this radius is given by:

$$r \propto M^{1/3}\rho^{-1/3}$$

Since density can be written like: $\Delta\rho_{\rm crit}$, the set of scaling relations are given by:

$$r \propto M^{1/3}\Delta^{-1/3}H(z)^{-2/3}$$

$$\rho_g \propto \rho$$

$$M_{\rm g} \propto T^{3/2}\Delta^{-1/2}H^{-1}$$

$$L_{\rm X} \propto T^2\Delta^{1/2}H$$

$\rm R_v$ is the virial radius of the cluster, M its total mass and L and T its luminosity and temperature.

If σ is the line of sight velocity dispersion of the galaxies in the cluster, then $\sigma^2 \propto \frac{M}{R_{\rm v}}$ which based on the above equations leads to:

$$\sigma \propto \sqrt{T}$$

Two aspects related to self-similarity can be investigated by studying the scaling relations: strong and weak self-similarity. Strong self-similarity appears when systems at same redshift show similar properties across a wide range of masses. If this strong self-similarity between objects at a particular redshift is obeyed for all redshifts, then systems are in the weak self-similar regime. Validity of self-similar evolution has been tested with observations of clusters of galaxies (Vikhlinin et al. 2002; Ettori et al. 2004; Lumb et al. 2004; Branchesi et al. 2007; Pacaud et al. 2007; Reichert et al. 2011; Hilton et al. 2012; Maughan et al. 2012) as well as simulations (McCarthy et al. 2002; Muanwong et al. 2006; Kay et al. 2007).

Figure 1.6 shows the observed scaling between luminosity and temperature, as well as velocity dispersion and temperature for a sample of 60 groups from Osmond & Ponman (2004) to which they add for comparison a sample of low redshift clusters. In each plot, solid line represents the fit to the whole sample, the dashed line the fit to clusters and the dotted line the fit to groups only.

One of the best studied scaling relation is the L-T relation (Wu et al. 1999; Pratt et al. 2009; Mittal et al. 2011). Studies of the correlation between temperature and luminosity over a large temperature range showed that both groups and clusters (Markevitch 1998) depart from the self-similar predictions, with a larger deviations for groups than for clusters (see left panel in Figure 1.6). While slope in the L-T relation for clusters vary between $2.52 - 3.26$, for groups it has been found to have slopes as high as 5.57, which is much steeper than the self-similar expectations of a slope equal to 2.

One way to interpret the observed deviations in the L-T relation is that groups have a lower luminosity than expected for their temperature. In order to study possible sources responsible for the deviations of a system from the self-similar expectations, one can look at the structural distribution of several of its properties like gas density, temperature and gas entropy.

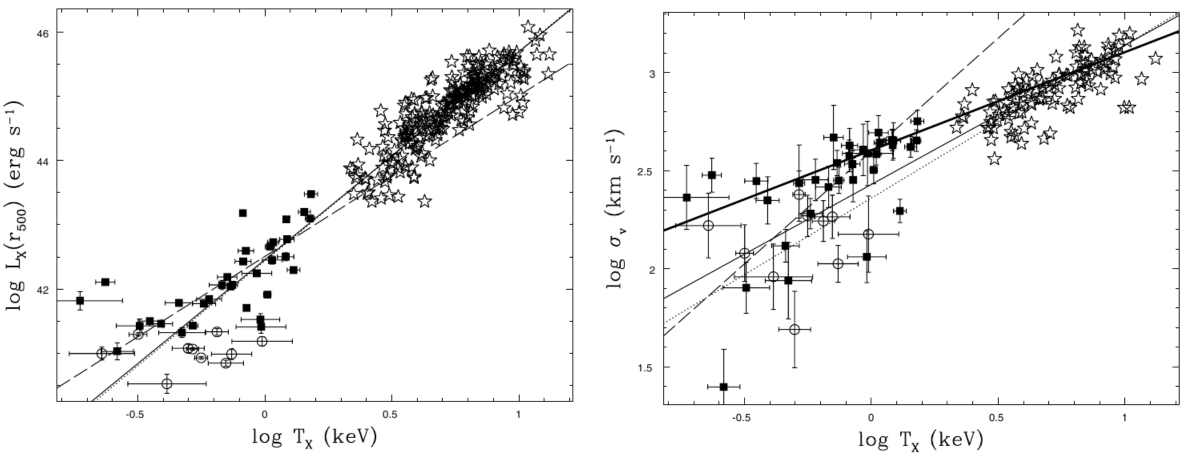

Figure 1.6: Left: L-T relation for a sample of groups and clusters (Osmond & Ponman 2004). In addition to their sample of groups (squares and circles), Osmond & Ponman (2004) use a sample of clusters from Horner (2001) (stars) to compare the properties of groups with those of more massive systems. The group sample is divided into two subsamples, depending on the detectable extent of group emission: groups with extent radius greater than 60 kpc (G-sample; filled squares) and groups with extent radius less than 60 kpc (H-sample; open circles). The dashed line represents a fit to the G-sample, the dotted line a fit to the clusters and the solid line a fit to the G-sample plus clusters (the H-sample is plotted but not used in the fitting). Right: The sigma-T relation for the same sample. The meaning of symbols and line styles is the same as in the left-hand side panel. In addition, the bold line marks the points of equality between galaxy and gas specific energies.

1.4.2 Gas density and surface brightness distribution

An universal profile for the distribution of gas in groups and clusters is a prediction of the self-similar model because gas traces dark matter and dark matter halos are self-similar. Figure 1.7 shows the density and surface brightness distribution for two samples of groups and clusters. The surface brightness profile reflects the shape of the gas distribution. This is because surface brightness represents the projection on the sky of gas emissivity and emissivity is linked to density squared through cooling function:

$$\varepsilon_\nu = n_{\mathrm{e}}^2 \Lambda_\nu$$

, where ε_ν is emissivity at a frequency ν, n_{e} is the gas density and Λ_ν is the cooling function for a particular frequency ν. Cooling function is dependent on the gas temperature (T_{g}) but also on its abundance (see also Equations 5.82 and 5.19 from Sarazin (1988)).

The left hand side image shows, in addition to the gas distribution, the distribution of the cluster total density. A self-similarity in the total density profile is observed for all systems in the sample. As regards the gas distribution, the self-similarity is observed only at large radii. At a radius of about $0.1\mathrm{R}_{500}$, there is a clear separation between groups and clusters, with groups having a shallower distribution than clusters. The same dependence of profile steepening with temperature can be observed in the right hand side panel. Therefore, groups and clusters seems to have a universal density profile beyond 0.2 of virial radius, while inside this radius, a large scatter in the density distribution can be observed. Same result has been obtained by Neumann & Arnaud (1999).

Croston et al. (2008) showed that at very small radii ($0.03\mathrm{R}_{500}$) the density profile of a sample of groups and clusters with temperatures greater than 2 keV show a large dispersion, with no correla-

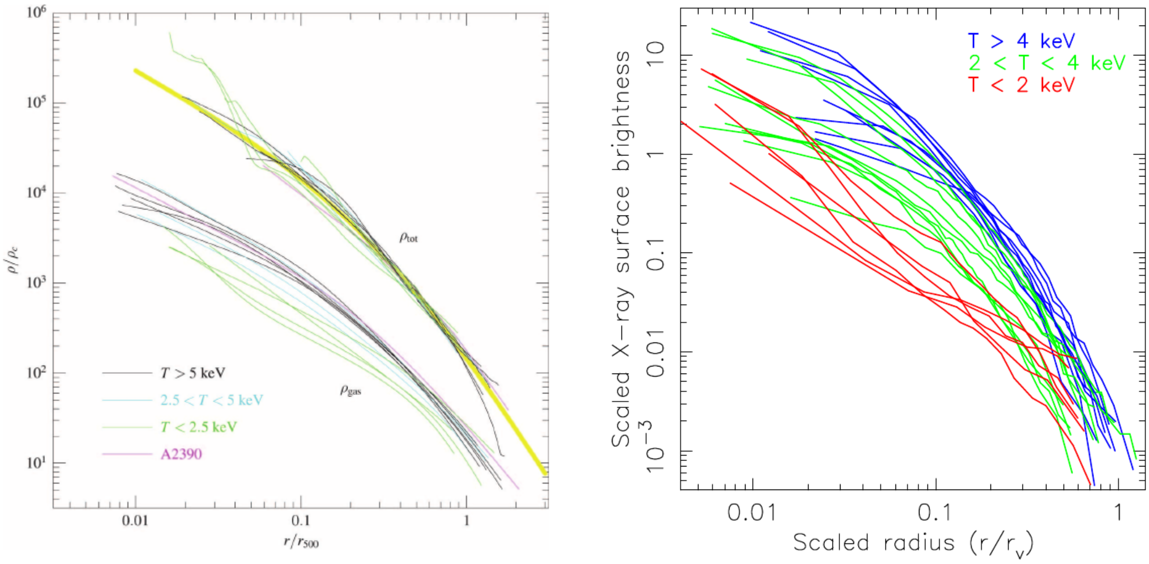

Figure 1.7: Left: Density profiles for a sample of groups and clusters from Vikhlinin et al. (2006). Right: Surface brightness profiles for a sample of groups and clusters from Ponman et al. (1999)

tion with temperature. At a larger radius ($0.3R_{500}$), there is a strong correlation with temperature of the slope of the density distribution. This correlation weakens at larger radii ($0.7R_{500}$), where both groups and clusters show a self-similar behaviour.

This steepening in the groups' density distribution at smaller radii compared to clusters determines a reduction in X-ray luminosity for groups and therefore can explain the larger deviations of groups from the self-similar expectations.

1.4.3 Temperature distribution

Like for the case of density distribution, self-similar models assume universal temperature profiles. Observations show that in general groups and clusters have a self-similar temperature profile outside $0.15R_{200}$ with a dispersion of the profiles in the central region. Figure 1.8 shows the radial

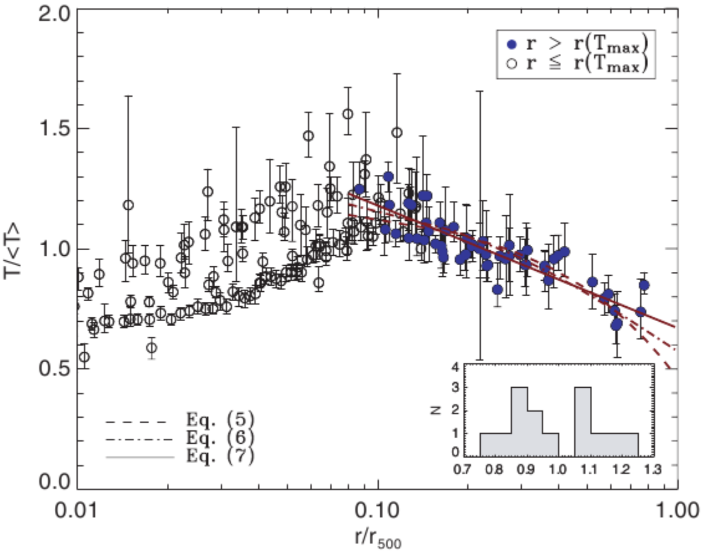

Figure 1.8: Temperature profiles for a sample of 15 nearby groups observed with *Chandra* (Rasmussen & Ponman 2007). Profiles are normalized to the mean temperature of each group ($\langle T \rangle$) and the group's R_{500}. An agreement between temperature profiles outside the position of the temperature peak can be seen in this figure. Blue filled circles mark the profile outside the temperature peak, while open circles mark the profile inside the core. Lines represent fits to the data outside the core, using various functional forms of $T/\langle T \rangle$ versus r. The dispersion in the central temperature profiles is showed by the inset histogram of $T/\langle T \rangle$, calculated at a radius of $\approx 0.03R_{500}$.

temperature distribution for a sample of groups studied by Rasmussen & Ponman (2007). The radius is scaled with R_{500} and temperature normalized to the mean temperature of the group. As seen in this Figure, their profiles show a peak at $0.1R_{500}$, beyond which temperature starts to decline and drop by a factor of 2 up to R_{500}. In the inner region, there is a large variation for the slope of the profiles and the temperature at the centre can drop up to half of the mean temperature of the cluster.

The same trend in temperature profiles is found by Sun et al. (2009) in a sample of groups, with a peak at the same fraction of R_{500} (0.1 R_{500}) and similarity outside this radius. When mean groups temperature profile is compared to that of clusters, the peak in the distribution is at smaller radii than in clusters, for which the peak appears at $0.15\mathrm{R}_{500}$ (Vikhlinin et al. 2005).

1.4.4 Entropy distribution

The study of entropy distributions gives valuable information about the sources responsible for self-similarity breaking. This is because entropy distribution, together with the shape of the dark matter potential well determines the observed distribution of density and temperature of the gas. Under the assumption of self-similarity for clusters, the gas entropy at a fixed fraction of virial radius would be directly proportional with temperature. Moreover, analytical modelling of shock heating in spherical collapse predict an increase in the entropy with radius in a form of a power law with a slope of 1.1 (Tozzi & Norman 2001). Entropy is defined as:

$$K = \frac{kT}{n_e^{2/3}}, \tag{1.15}$$

where kT is the gas temperature and n_e is the electron number density. This definition is widely adopted in X-ray studies of clusters, and the standard thermodynamic definition of entropy can be obtained from it by applying a logarithm and adding a constant (Voit 2005).

Figure 1.9 shows in the left panel the entropy distribution for a sample of groups and clusters studied by Cavagnolo et al. (2009). Each cluster is colour coded according to its temperature. The continuous line represents the expected power law with a slope of 1.1. It can be clearly seen that at large radii the entropy distributions have a similar power law, while a large variations in entropy shapes can be seen at smaller radii. Cavagnolo et al. (2009) fitted a power law plus a constant model to each profile and for radii larger than $0.1\mathrm{R}_{200}$ all profiles are well approximated by power laws with index values between 1.1 and 1.2. This shows that at large radii clusters and groups are self-similar. In their study they also investigated the correlation between entropy at $0.1\mathrm{R}_{500}$ and

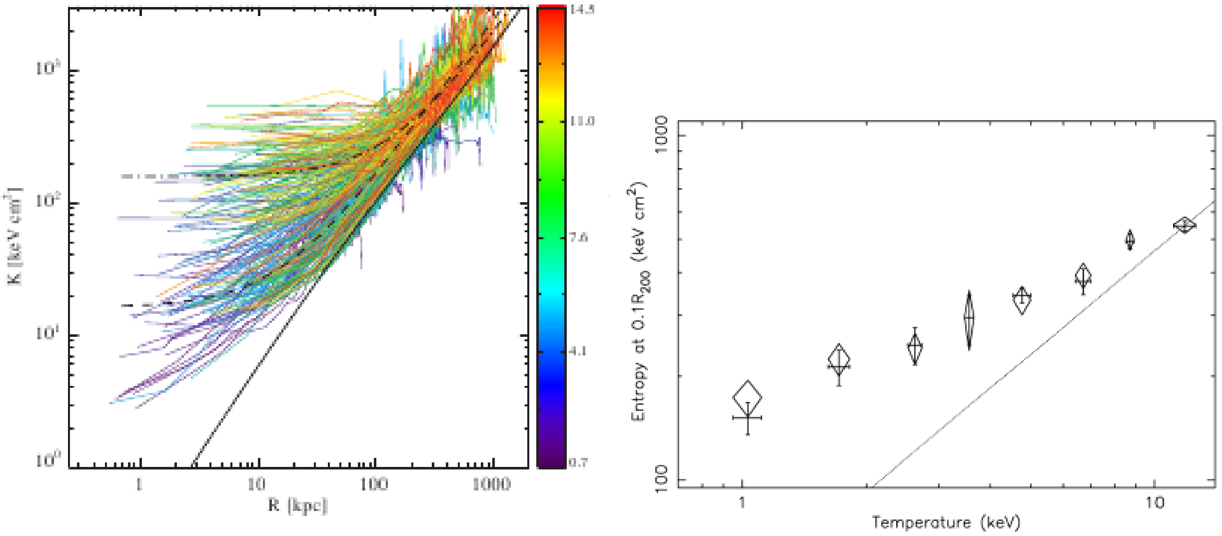

Figure 1.9: Left: Entropy profiles for a sample of groups and clusters from Cavagnolo et al. (2009). Right: Relation between entropy at $0.1R_{200}$ and temperature for a sample of groups and clusters. The solid line represents a power law with a slope equal to 1, which is the expected self-similar relation. Figure from Ponman et al. (2003)

the system's temperature and their result is presented in the right panel of Figure 1.9. It shows that groups have an excess entropy with respect to that expected from the self-similar model and the amount of this entropy excess is decreasing with temperature. This extra entropy which is higher in groups than clusters is responsible for the departures of groups from the scaling relations. Therefore groups are ideal systems to investigate the processes responsible for this observed deviation by studying their entropy distribution. Whichever mechanism is responsible for this, its effect will be on the central entropy.

1.5 Cool cores and non cool cores in groups and clusters

The hot ionized gas in clusters of galaxies, also known as intra-cluster medium (ICM), loses its thermal energy through X-ray radiation. The time scale on which an isothermal parcel of gas with uniform density can radiate away its thermal energy is inversely proportional to its density. As a result, cooling times at the centre of the clusters, where the density is high, are shorter than in the outer regions. Observations of low redshift clusters show that clusters with central cooling time shorter than their age are common in the local Universe, and they represent $\sim 50\% - 90\%$ of the population (Peres et al. 1998; Sanderson et al. 2006; Chen et al. 2007; Hudson et al. 2010; Santos et al. 2010). In the light of this, clusters have been divided into two classes: cool core (CC) systems, which have a short central cooling time, a cuspy central surface brightness and usually manifest a drop in their central temperature, and non cool core (NCC) clusters, with the opposite properties.

Evidence for the existence of two distinct cluster populations came from the observation of bimodality in the distribution of the cooling time (Cavagnolo et al. 2009) or the closely related gas entropy (Cavagnolo et al. 2009; Sanderson et al. 2009; Mahdavi et al. 2013) in the central regions of clusters. On the other hand, other studies have found no clear evidence for bimodality in cluster properties, and some authors, e.g. Santos et al. (2008), have split core properties into *three* classes, with an intermediate weak cool core (WCC) class between strong cool cores (SCC) and NCC clusters. Whether the observed distribution is representative for the cluster population depends on the sample used for the study. Biases in sample selection can affect the observed distribution and lead to misinterpretation of the results. For example, the study of Cavagnolo et al. (2009), which is based on an X-ray selected archival sample, might have a bias against WCC clusters if observations of strong CCs and/or disturbed clusters (i. e. generally NCCs) are preferred over the regular, WCC clusters.

Different models have been put forward to explain the observed distribution in core properties in terms of the dynamical and/or thermal history of clusters. In the model of Burns et al. (2008), cluster merging is the mechanism which creates NCC clusters by destroying the cooling core in CC clusters. The natural state of a cluster is the CC one since most clusters have central cooling times which are less than their age. This model agrees with the high fraction of CC at low redshift and the observed bimodality in the central cooling state. The simulations of Burns et al. (2008) predict no evolution in the CC fraction up to a redshift of 1. Moreover they show that the probability of mergers increases with the system mass and therefore CC are more common in low mass systems. It is not yet clear whether this prediction is borne out observationally due to the substantial variation in CC fraction found by different methods used for CC/NCC classification, and the lack of statistically selected samples of galaxy groups. However, there is observational evidence in favour of this merger-driven model from the fact that most cool core clusters have a regular surface brightness, whilst many NCC clusters are disturbed (O'Hara et al. 2006; Maughan et al. 2012). Also, Rossetti & Molendi (2010) showed that none of the clusters classified as cool cores in their sample have detected radio relics, which are a sign of mergers. On the other hand, some simulations (Poole et al. 2006) suggest that CCs cannot be destroyed by mergers. If the main effect of mergers is to redistribute the core gas, rather than to raise its entropy, then the core is reassembled quite rapidly, and even the most massive mergers would only temporarily disrupt it.

Another class of models assumes that the observed thermal state of the cluster core was established early, as a result of the entropy level established in the intergalactic gas before cluster formation (McCarthy et al. 2004). NCC clusters will then be those for which the entropy of the intergalactic gas has been raised to a sufficiently high value that the cluster has not had enough time to radiate away its thermal energy and develop a cool core. Conversely, CC clusters experienced a lower level of entropy injection.

Irrespective of the mechanism which generates the distribution of core properties, there is an observed tendency for cool core clusters to host a central active galactic nucleus (AGN)(Dong et al. 2010). Moreover, it has been shown that there is a correlation between the strength of the cool core and the radio power of the central AGN (Mittal et al. 2009). The coexistence of an AGN and CC plays an important role in the thermal evolution of ICM. AGN, through their feedback, are thought to represent the main heating source for the ICM, whilst the cool gas in the cluster core constitutes the reservoir for black hole accretion (Croston et al. 2005; Rafferty et al. 2006; McNamara & Nulsen 2007, 2012; Ma et al. 2013; Russell et al. 2013).

One way in which AGN interact with the ICM is through relatvistic plasma jets, which can push aside the ICM, creating lower density regions detectable in X-ray images of clusters as 'cavities' with reduced surface brightness. Cavities have been detecetd in clusters at low (Boehringer et al. 1993; Fabian et al. 2000; McNamara et al. 2000; Blanton et al. 2011; Gitti et al. 2011) and high redshift (Hlavacek-Larrondo et al. 2012), while evidence for cavities in groups is currently limited to low redshift systems (Morita et al. 2006; Gastaldello et al. 2009; Randall et al. 2009; Gitti et al. 2010; O'Sullivan et al. 2011a) due to to groups' lower surface brightness compared to clusters. Based on the volume and pressure of these cavities, the energy input from the AGN can be estimated. Studies of cavities in clusters have shown that AGN can typically provide the necessary power to balance the energy lost through cooling in clusters (Bîrzan et al. 2004; Rafferty et al. 2006), whilst in galaxy groups their impact is even more significant, and they may be able to provide more energy than is lost through cooling (O'Sullivan et al. 2011b).

These results demonstrate that the contribution of AGN to the thermal state of the ICM cannot be ignored, and McCarthy et al. (2008) introduced a model which combines pre-heating at high redshifts and AGN feedback to explain the existence of CC and NCC systems. More recently, Voit and collaborators (Voit 2011; Voit et al. 2014) have explored the relationship between cooling, thermal conduction, thermal instability and AGN feedback within cluster cores. They find that many properties of the gas in cluster cores can be explained in terms of the balance between these processes.

Studies of the evolution of cool cores face two major problems: the construction of an unbiased sample with the necessary statistics at high redshift to be able to draw any conclusion about any evolutionary trends, and the definition of a parameter that can separate a CC cluster from a NCC one for a variety of systems at different redshifts and for data with different quality.

One parameter frequently used to characterize the thermal state of a cluster core is the central cooling time (Edge et al. 1992; Peres et al. 1998; Bauer et al. 2005; Mittal et al. 2009), which is directly related to the physical definition of a cool core as one in which cooling is significant. Central entropy, which is closely related to cooling time, is another physical parameter used to characterize CCs (Cavagnolo et al. 2009). Other cool core estimators have been defined based on the observed X-ray properties associated with CC clusters, such as the central temperature drop (Maughan et al. 2012) and central surface brightness excess (Vikhlinin et al. 2007; Santos et al. 2008; Maughan et al. 2012).

How well do these various parameters perform in separating CC and NCC systems? Hudson et al. (2010) applied 16 cool core estimators to the HIFLUGCS (HIghest X-ray FLUx Galaxy Cluster Sample) sample of low redshift clusters and found that cooling time and entropy are the quantities which show the most pronounced bimodality in their distribution.

Studies of the evolution of cool cores, using X-ray selected samples, have shown that CC are common at low redshift (Peres et al. 1998). Bauer et al. (2005) showed that their fraction in X-ray luminous clusters does not change strongly up to a redshift of 0.4 when the central cooling time is used as a CC estimator. The investigation of how this fraction changes with redshift has been extended beyond redshift 0.5, mainly by studies which use CC estimators based on the surface brightness excess (Vikhlinin et al. 2007; Santos et al. 2008; Maughan et al. 2012). These studies found that the fraction of cool core clusters drops significantly, resulting in a lack of strong cool cores at high redshift. In contrast, the study of Alshino et al. (2010), which used a CC estimator based on central surface brightness excess to examine a sample of groups and clusters from the *XMM* -LSS survey, confirmed the lack of strong CCs in *clusters* at high redshift, but reported an *increase* in the strength of cool cores in cooler groups. Further evidence on the evolution of core properties comes from optical studies, since CC clusters have associated H_α (Bauer et al. 2005) and other optical line emission. Samuele et al. (2011) studied a sample of 77 clusters up to a redshift of 0.7 and found a lack of cool core clusters at redshifts greater than 0.5.

Recent results (Semler et al. 2012; McDonald et al. 2013) based on samples of clusters selected by the Sunyaev-Zeldovich (SZ) effect, with *Chandra* follow-up, demonstrate that CC clusters do exist at redshifts greater than 0.5. Moreover, McDonald et al. (2013) found that there is no evolution in central cooling time out to redshifts ~ 1. There are also studies on individual clusters, although not very numerous, which show that there are strong cool cores at high redshift. The WARPS cluster studied by Santos et al. (2012) is a CC cluster at redshift 1.03. Another interesting system is 3C188, studied by Siemiginowska et al. (2010), which is a strong CC system at z=1.03 with a powerful radio AGN at its centre. Signs of cooling at the centre of the cluster surrounding the $z = 1.04$ powerful quasar PKS1229-021 have also been reported by Russell et al. (2012). While most of these evolutionary studies have concentrated on rich clusters, and show a reduction in the incidence of strong CCs at high redshift, the one study (Alshino et al. 2010) which covers groups, finds a conflicting trend in less massive systems, whereby the CC strength tends to increase at high redshift.

1.6 Feedback

The observed departure from self-similarity in the L-T relation, together with the overcooling problem represent strong evidence that gravitation alone cannot be the mechanism responsible for the observed X-ray properties of systems spreading over a wide range of masses. Therefore, non-gravitational processes are needed in order to explain the variations in the global and structural X-ray properties and the deviations from expected scaling relations. Amongst mechanisms proposed for raising the entropy of the ICM to the observed levels are heating by AGN feedback or supernovae, cooling through X-ray emission and gas expulsion. This heating may occur at high redshifts (preheating), before the cluster has collapsed and formed, or after cluster formation. Observations show clear evidence for the presence of cooling and AGN feedback, in the form of large cool core clusters and large cavities in the cluster X-ray emission due to the interaction of AGN radio jets. Expulsion of low entropy gas from the system can also happen at high redshifts or after cluster formation. In order to separate the dominant source responsible for the heating, constrain the time when this source has the largest impact on the ICM and the mechanism by which it injects the energy, one can study the energy budget of the ICM. The excess heating required to reach the observed entropy floor for groups of 100 keV cm^2 is of about 1-3 keV per gas particle (Babul et al. 2002; Borgani et al. 2002; Brighenti & Mathews 2001).

Radiative **cooling** has been proposed as a mechanism for increasing the central entropy in groups and clusters (Voit & Ponman 2003; Bryan 2000) by removing the low entropy gas at the centre of these systems. Clusters cores have the highest gas density and therefore shorter cooling time when compared to the outer regions. If cooling time is shorter than Hubble time, the gas radiates away its thermal energy and drops out of the X-ray emitting phase. This gas lost from the ICM is replaced by the higher entropy gas from outer radii, and therefore raising the central entropy of the ICM. An increase in the central entropy to a level that marginally matches the observed entropy floor has been found in simulations that add cooling to gravitational only models (Xue & Wu 2003). Although cooling can increase the central entropy, it requires a too large amount of gas to cool in order to raise the entropy of poor systems to the level needed to obtain an agreement with the observed L-T relation. Therefore cooling alone is not able to solve the overcooling problem

(McCarthy et al. 2004; Xue & Wu 2003). Another problem with cooling is that the structural properties predicted by this model are not able to match the wide range of properties observed in groups and clusters. For example, temperature profiles from pure cooling models do not show the observed drop beyond $0.1R_{200}$ (see Section 1.4), but rather have a constant temperature (McCarthy et al. 2004). In the inner region, all profiles from this model show a steep drop towards the centre and they lack the large variations in the distribution of the slope of the central profiles seen in observed clusters. Therefore cooling only models cannot explain the existence of clusters with flat central temperature profiles corresponding to the observed non cool core clusters (Bower et al. 2001).

Another mechanism by which the entropy of groups and clusters is increased, is heating by AGN and/or supernovae. In the **preheating** model (McCarthy et al. 2004), the heating of the gas which will form the core of a cluster occurs at high redshifts, before cluster formation. During the subsequent growth of the system by gas accretion, the only process which can increase the entropy of the newly accreted gas is shock heating. Since the strength of shock heating increases with cluster mass, early in a clusters' history, the entropy excess of the accreted gas above the preheating level is small and increases progressively as cluster evolves. Therefore, the entropy profile of clusters predicted by the preheating model should have a large isentropic core and a power law behaviour outside the core region. The size of this isentropic core is expected to be larger for groups and decrease with system's mass. Also, groups are expected to have a higher entropy core because the same energy input will increase more the entropy of lower density gas than higher density one. This excess entropy of groups compared to clusters predicted by the model is consistent with observations and represents the cause of deviations from L-T relations. Depending on the level of the entropy injection and the redshift at which this entropy has been injected, preheating is able to offset cooling (Oh & Benson 2003) by increasing the central cooling time. Simulations which include preheating shows that an agreement with the observed L-T relation over a large temperature range can be obtained by tuning the level of the entropy injection (Babul et al. 2002). Although a good match with observed L-T relation can be obtained, the level of the entropy injection required to obtain this agreement is about 330 keV cm^2, which is higher than that observed at the centre of the groups which corresponds to 100-150 keV cm^2. Another disagreement between observations and the model is the presence of groups with no evidence for a large isentropic core as predicted by the model (Ponman et al. 2003; Pratt & Arnaud 2003).

On the other hand, the highest advantage of the preheating models is that the energy input required to increase the entropy of the gas by a given amount before cluster formation, when its density is lower, is less than the one required after cluster formation (McCarthy et al. 2008). Therefore, no matter which sources are responsible for preheating the gas, they are energetically more efficient at a redshift between 2 and 3, before cluster formation (Oh & Benson 2003; Ponman et al. 1999). For example, heating by supernovae, which has been showed to have little impact on the central entropy of groups at low redshifts, can bring the entropy level to the one observed in groups if the SN feedback happens at a redshift of 2 (Ponman et al. 1999).

SN feedback has been introduced as a possible mechanism for heating the gas through galactic winds resulted from supernovae explosions (Menci & Cavaliere 2000; Bower et al. 2001). The effect of SN feedback on the ICM is not only to increase its entropy through heating but also to raise its metallicity by introducing heavy elements produced by the stars. Therefore, observations of the clusters' metal content can be used to derive the total energy released by supernovae Rasmussen & Ponman (2009). Observational results, together with numerical and hydrodynamical simulations showed that the amount of heating introduced by SN feedback is almost negligible in clusters and is below the level of 1 keV per particle required to match the L-T relation for groups. Even if an efficiency of energy transfer from SN to the ICM of 100% is assumed, SN heating alone cannot account for the observed L-T relation or even prevent overcooling (Borgani et al. 2002; McCarthy et al. 2011).

AGN feedback is another mechanism responsible for increasing the central entropy of the ICM through heating or gas expulsion. As it has already been mentioned, this entropy increase can take place at high redshift or at lower redshifts, after cluster formation. Depending on the accretion rate of the central black hole, there are two models of AGN feedback: the quasar mode (Springel et al. 2005; Scannapieco & Oh 2004), which corresponds to high accretion rates and the radio mode (Croston et al. 2005), corresponding to lower accretion rates. AGN can heat the ICM through outflows.

Observational evidence for AGN heating in clusters through mechanical feedback from the radio jets generated by the AGN is represented by the large X-ray cavities that can be seen in the surface brightness of several clusters. These cavities can be used to estimate the energy introduced by the AGN based on the work required to inflate them and their internal energy. It has been showed based on observations that the amount of heating introduced by radio AGNs is sufficient to offset cooling over a wide range of mass scales (McNamara & Nulsen 2007; Wang et al. 2010; Rafferty et al. 2006). Moreover, several studies of the correlation between the cavity power and the energy loss due to radiative cooling for groups and clusters showed that while the energy from the AGNs is enough to balance cooling in massive clusters it exceeds that required for groups (O'Sullivan et al. 2011a). This suggests that AGN feedback is not only the necessary mechanism to avoid overcooling but it might provide the excess entropy in groups required to explain deviations from self-similarity. Evidence for temperature increase in groups by AGN feedback has been presented by Croston et al. (2005) who showed that radio-loud groups are hotter than radio quiet ones of similar X-ray luminosity. Regarding the energetics required to explain X-ray group properties, they showed that an average radio source would have the necessary energy input to offset cooling. A similar result has been found by Jetha et al. (2007) who showed that a less luminous AGN could provide sufficient energy to counteract radiative cooling and raise the entropy of the group.

In addition to the AGN feedback models, in which the entropy of the gas is raised by heating the

ICM gas, there are models in which AGNs can increase the entropy by ejecting the low entropy gas from collapsed groups (Bower et al. 2008) or from the high redshift progenitors of groups (McCarthy et al. 2011).

The conclusion that can be drawn from the literature results presented so far is that in order to be able to explain the observed entropy levels in groups as well as clusters and at the same time avoid overcooling, a non-gravitational mechanism more complex than simple radiative cooling or feedback from SN or AGNs is required in addition to the gravitational only process. Observations show that at various levels, each of these mechanisms are present during the evolution of groups and clusters. Therefore, a model which includes contribution from each of these processes is required to match observed properties of these systems. Two main questions that this model would have to address are: which of these non-gravitational processes is the dominant one? and when during the cluster formation is the dominant process acting?

Hydrodynamical simulations which include cooling and SN feedback can bring the L-T relation for groups into the right direction, but are not able to raise the central entropy to a high enough level to avoid overcooling (Borgani et al. 2002). The addition of AGN feedback has been showed to be able to match the L-T relation, avoid overcooling and predict temperature and entropy profiles similar to the observed ones.

Numerical simulations which include AGN and SN feedback are able to reproduce the observed entropy profile and the L-T relation but only for NCC. Only with the addition of radiative cooling entropy and temperature profiles similar to those observed for CC clusters can be predicted and overcooling avoided (Short et al. 2012).

Simulations which include cooling and some level of entropy injection, before or after the cluster formation can explain better the observed properties. Using a model which includes cooling and various levels of preheating, McCarthy et al. (2004) showed that depending on the level of preheating, a good agreement with the observed L-T relation can be obtained. Moreover, this model can predict structural properties similar to observations. Cool core clusters are those with a lower level of preheating which had enough time to radiate a significant fraction of their thermal energy, while non cool core clusters had a higher level of preheating. With this preheating model, depending on the amount of the entropy injection, systems with different central states ranging from strong cool cores to non cool cores can be obtained.

1.6.1 Methods for detecting groups and clusters of galaxies

Historically, the definition and name of clusters of galaxies is based on the optical observations that galaxies are not distributed uniformly on the sky but rather in clusters. They have been discovered in optical images as galaxy overdensities, hence their name. Together with their lower mass equivalent (i.e. groups), clusters were well known systems by the time X-ray emission from them was discovered. X-ray observations of clusters and groups revealed the presence of another baryonic component besides galaxies, which is represented by the hot gas surrounding these galaxies. This hot gas which represents the intracluster medium (ICM) dominates the total baryonic mass and constitute 15% of the total mass of the cluster, while galaxies represents only 5%. The dominant component, with a mass contribution of 80% is represented by dark matter. The detection of clusters takes great advantage of their multi-component structure. Depending on the wavelength at which they are observed, different source searching algorithm can be design to detect one of the components or signs of its presence by the impact on other components. For example, in optical surveys clusters are detected as overdensity of galaxies or by looking at the properties of galaxies. In X-rays, emission from the cluster can be detected from their ICM. The presence of clusters can be detected in microwave, where the presence of the hot ICM distorts the CMB radiation. In the following I am going to present several methods used to detect clusters in various wavelength.

- Optical/IR methods

  The search for **galaxy overdensity** is the first method used to detect clusters in optical observations. Various methods have been designed to look for enhancement of galaxy surface density. The counts in cell method (Couch et al. 1991; Lidman & Peterson 1996), friends-of-friends method (Huchra & Geller 1982; Geller & Huchra 1983) and percolation method (Davis et al. 1985; Efstathiou et al. 1988; Dalton et al. 1997; Ramella et al. 2002) are the most used techniques.

  Other optical methods for cluster search are those which are based on the observed properties of member galaxies in a cluster. For example, one of the widely used method, the red sequence method (Gladders & Yee 2000), is based on the observed property that compared to field galaxies, early-type galaxies in a cluster have a strict relation between their colour and magnitude. A significant number of clusters (429 cluster candidates) has been detected over an area of about 100 deg^2 using the red sequence method as part of the Red-sequence Cluster Survey (RCS1; Gladders et al. 2007). In addition to this, the RCS2 survey is an on-going survey using the same detection method as RCS1 over an area of about 10 times larger and predicts the detection of $\sim$ 30000 clusters (Gilbank et al. 2011).

- X-ray methods

  In addition to optical methods for cluster detection, X-ray astronomy offers an extensively used method for direct detection of these systems. In X-ray images, although cluster's individual galaxies can not be detected, its presence can be unambiguously inferred by the detection of X-ray emission from its ICM. In these images, clusters appear as spatially extended sources, a property which represents the basis of all X-ray source detection techniques. A more in depth look at various X-ray surveys and their results will be presented in section 1.7.

- Sunyaev-Zeldovich (SZ) effect method

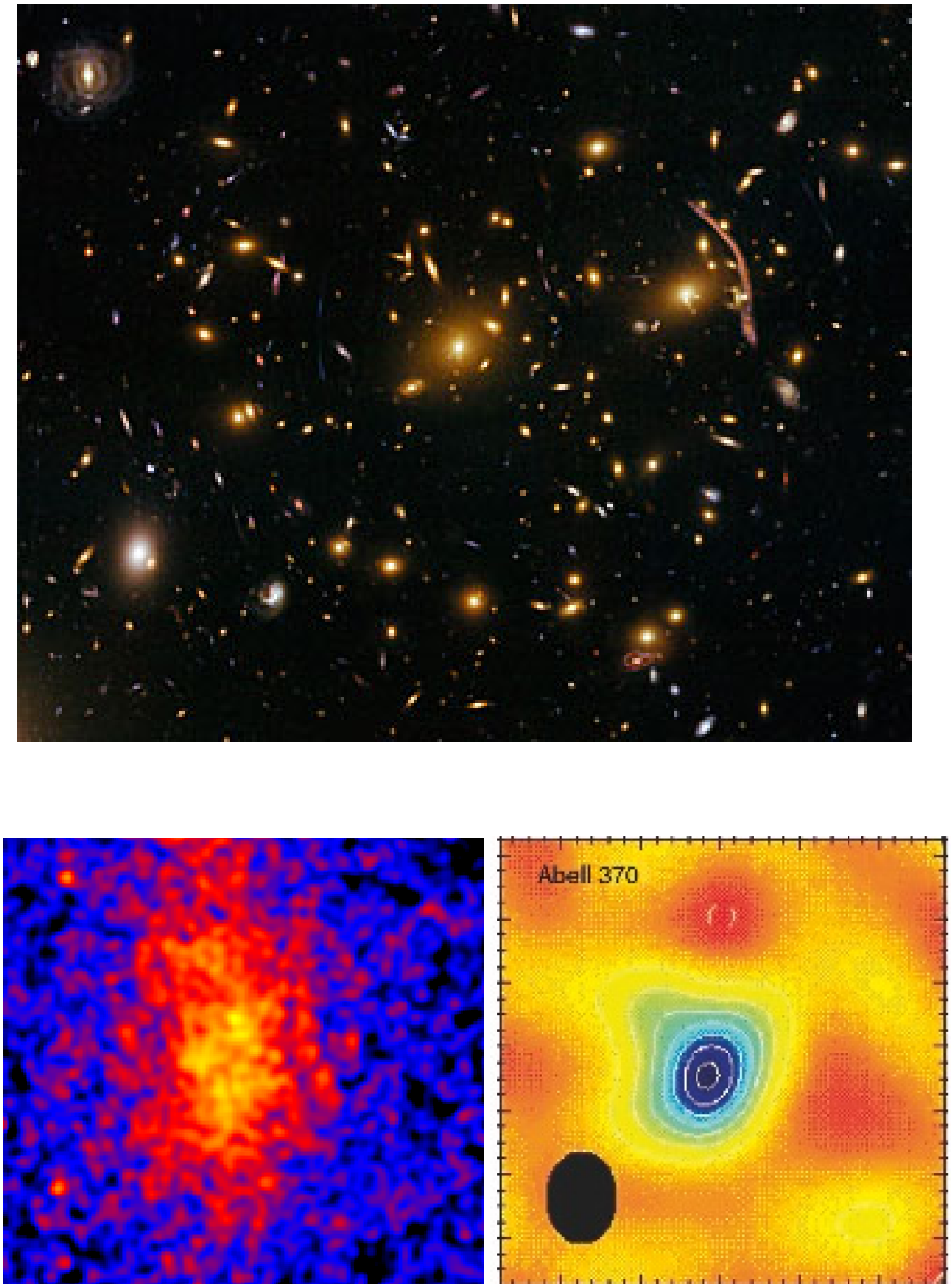

Figure 1.10: Multiwavelength observations of the Abell 370 cluster. In the top panel, which represent an optical image of the cluster, the cluster can be identified by the high concentration of galaxies. Figure credit: NASA, ESA, the Hubble SM4 ERO Team and ST-ECF; The bottom left panel represent X-ray emission from the gas between galaxies (*Chandra* image; observation ID: 515; PI: Gordon Garmire). Bottom right panel represent a SZ map of the cluster (Grego et al. 2001).

If optical and X-ray methods are methods for direct detection of clusters, SZ and gravitational lensing are indirect methods for cluster detection, based on the observed effect the cluster has on other astrophysical sources. In the case of SZ effect, the presence of a cluster can be inferred from the effect of its ICM on the CMB. The energy of photons from the ICM is changed when they interact with the ICM and the effect is an observed shift in the spectrum of the CMB. A large survey designed to search for clusters using the SZ method is has been performed with the South Pole Telescope (SPT). The SPT-SZ survey (Carlstrom et al. 2011; Reichardt et al. 2013; Bleem et al. 2015) covers a large area of 2500 deg^2 and contains a number of 677 cluster candidates. The Atacama Cosmology Telescope (ACT) is another major SZ survey which covers an area of 504 deg^2 and contains a number of 68 galaxy clusters Hasselfield et al. (2013). The largest catalogue of SZ selected clusters comes from the all-sky observations performed with *Planck* satellite. The catalogue contains about 1000 SZ sources out of which 861 are confirmed clusters Planck Collaboration et al. (2014).

- Gravitational lensing methods

  The presence of clusters of galaxies can also be inferred indirectly based on a phenomenon known as gravitational lensing. Gravitational lensing appears when the path of light from a distant object like a galaxy is deflected by encountered massive objects. As a result, multiple images of the object can be seen and the shape of the source is distorted and sometimes magnified. The amount of the distortion depends on the properties of the object which acts like a lens like its mass, its distance to the source and the distribution of mass. Clusters of galaxies, which are the most massive objects in the Universe, behave like lenses. Therefore, gravitational lensing can be used to detect them by mapping their density distribution which is dominated by dark matter. Various surveys have been dedicated to the search of clusters using gravitational lensing (Wittman et al. 2002, 2006; Shan et al. 2012). Compared to X-ray surveys, the search for clusters using gravitational lensing benefits from the very wide area coverage which can be achieved with very large, ground-based multi-colour optical surveys (e.g. Deep Lens Survey (Wittman et al. 2002); Subaru Weak Lensing Survey (Miyazaki et al. 2007)).

1.7 X-ray surveys of groups and clusters of galaxies

Clusters of galaxies represent the target population for a significant number of past (Voges 1993; Vikhlinin et al. 1998; Gioia et al. 1990a; Romer et al. 2000; Perlman et al. 2002; Pierre et al. 2004; Burenin et al. 2007; Horner et al. 2008), on-going (Pierre et al. 2011) and future (Merloni et al. 2012) X-ray surveys whose aim is to assemble large samples that can be used for cosmological and evolutionary studies. The search for clusters is motivated by the fact that these massive systems are tracing the dark matter potential and therefore the study of their surface number density and two point correlation function can put independent constraints on the cosmological parameters. Moreover, this search is eased by the fact that clusters are amongst the most luminous X-ray sources on the sky and therefore they could be detected up to high redshifts. The evolution of clusters' luminosity over cosmic times is another issue addressed with large and deep samples obtained from X-ray surveys. Also, determination of reliable scaling relations that can relate clusters observed X-ray properties with their mass, require a large sample of clusters.

Compared to clusters, groups of galaxies represented a less studied class of systems. This is because their lower gas density and therefore luminosity makes groups detection more difficult even at intermediate redshifts. The existence of *Chandra* and the *X-ray Multi-Mirror* (*XMM*) allowed a better study of these poor systems due to their higher resolution and sensitivity compared to older missions like the *Röentgen SATellite* (*ROSAT*) . Since the launch of *Chandra* and *XMM*, much higher importance has been given to selecting samples of groups. This is also partly because these low mass systems are the ideal place to study the effects of non-gravitational feedback which has a higher impact on systems with shallower potential well.

Ideally, for all studies involving groups and clusters would be the construction of a uniform sample from a deep survey covering a large area. This would provide a large sample, covering a wide range in redshifts, that can be used for evolutionary studies of X-ray properties. The assemble of such a sample would require the use of a telescope with a high resolution, sensitivity and large field of view.

Since there are no current missions satisfying all three characteristics at once, the design of each survey is optimised depending on the science questions it addresses and the capabilities of the telescope used for cluster detection. Cosmological studies and studies of large scale structures require a volume limited sample, while for evolutionary studies of X-ray properties a large and deep sample is crucial. Therefore different type of survey exists which vary according to their survey strategy: surveys which cover large contiguous areas with almost uniform exposure and deep, pencil beam surveys. In addition to these, an important class of surveys is represented by serendipitous surveys, which use archival data. Archival surveys, although they are heterogeneous, can cover large areas if the survey includes a significant fraction of the observations available in a telescope's archive and therefore can lead to the ensemble of large samples of clusters. Table 1.1 and Figure 1.11 shows a comparison between some of the most important surveys conducted with *Einstein Observatory*, *ROSAT*, *XMM* and *Chandra*. In the Figure, depending on the telescope used for the survey, the symbols are plotted in green (*ROSAT*), blue (*XMM*) and purple (*Chandra*). In addition, open symbols containing a filled circle represent contiguous surveys.

We can see in the Figure and Table that in general *ROSAT* surveys cover the largest areas, but they have the lowest sensitivity compared to *XMM* and *Chandra* surveys. This can be explained by the fact that *ROSAT* has a larger fields of view compared to *XMM* and *Chandra*, but has a much lower effective area. One *XMM* survey, which is comparable to *ROSAT* surveys in respect to the area covered, but with a much higher sensitivity, is XCS (Romer et al. 2001; Sahlén et al. 2009; Lloyd-Davies et al. 2011; Mehrtens et al. 2012). This archival survey provides the largest number of optically confirmed clusters compared to other *Chandra* and *XMM* surveys. *Chandra*, which has the smallest fields of view is used for very deep surveys, which cover a very limited area, but reaches the lowest flux limits compared to all other surveys. Since *Chandra* has the best spatial resolution compared to all above mentioned telescopes, it is mostly used for surveys in which the target population is represented by point-like sources such as Active Galactic Nuclei (AGNs). The aim of these surveys is to detect these systems up to highest redshifts possible.

In the following we give a short description of few of the most important X-ray surveys existing in the literature.

- **Extended Medium-Sensitivity Survey (EMSS)** (Gioia et al. 1990a,b) is a serendipitous search for clusters of galaxies over a 778 deg^2 area. From a catalogue of 835 sources, 91% are classified based on optical information. The catalogue suffers from a significant contamination by AGNs (52%), while the contamination from other sources is: 29% from stars, 2% from individual galaxies and 4% from BL Lac objects.

- ***ROSAT* All Sky Survey (RASS)** (Voges et al. 1999) is the only full sky X-ray survey performed at exposures which vary between 0.4 and 40 ks. A catalogue of all bright X-ray sources detected in RASS, the *ROSAT* All-Sky Survey Bright Source catalogue (RASS-BSC), was presented in Voges et al. (1999) and consists of X-ray sources detected above a flux limit of 5×10^{-13}erg s^{-1} cm^{-2}. From the very large number of bright sources detected (18811) only 1.2% had been classified as extended.

- ***ROSAT* -ESO Flux Limited X-ray Galaxy Cluster Survey** (REFLEX I; Böhringer et al. (2001)) and REFLEX II; Böhringer et al. (2014b)) is a search for clusters over $\sim$ 35% of the sky area which had been covered by *ROSAT* as part of the RASS. The sample con-

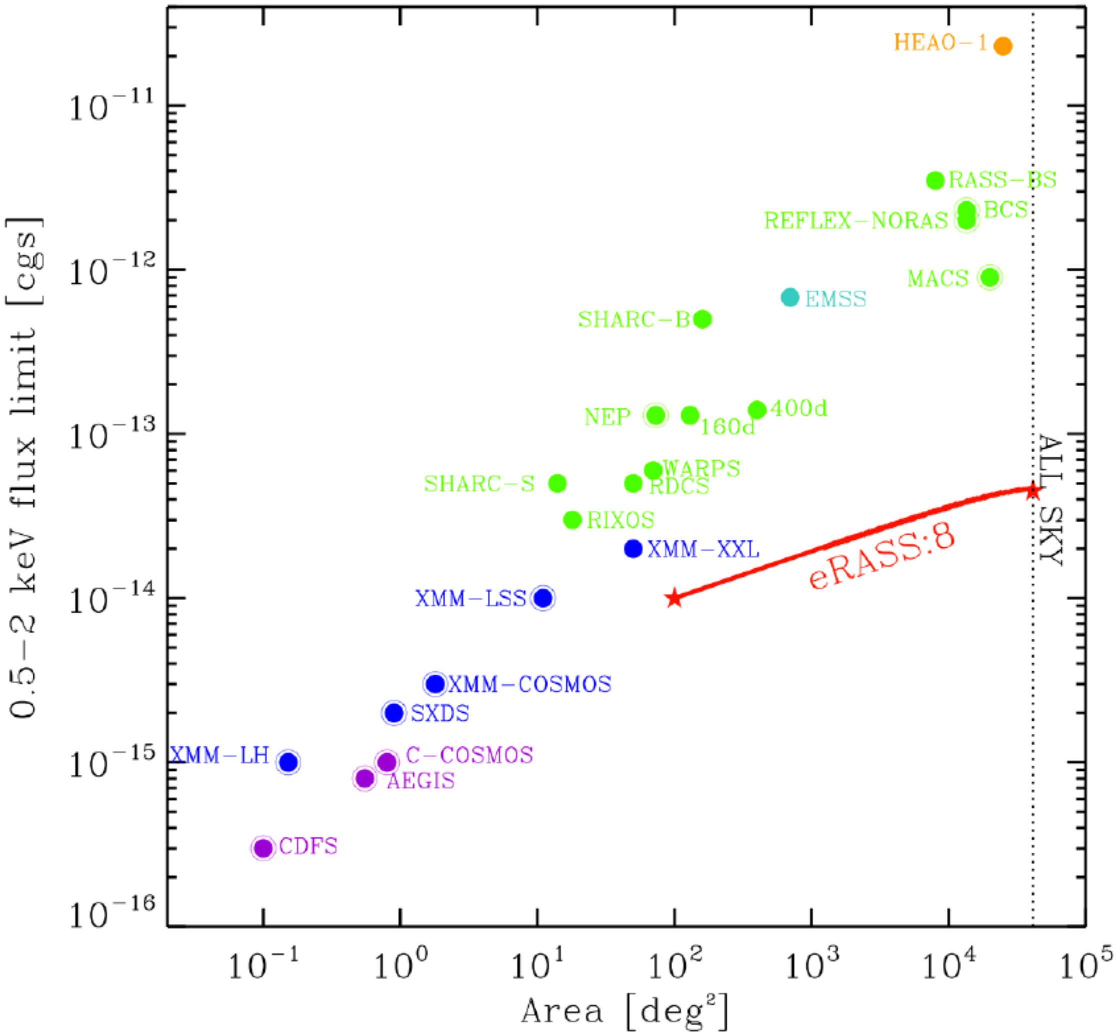

Figure 1.11: Different X-ray surveys performed with *ROSAT* (red), *XMM* (green) and *Chandra* (blue). Filled circle symbols represents serendipitous surveys, while filled plus empty symbols represent contiguous surveys. Figure adapted from Merloni et al. (2012)

structed from the survey is a flux limited sample aimed for cosmological studies. The first REFLEX catalogue of clusters (Böhringer et al. 2001) comprises 452 clusters with a flux limit of 3×10^{-12}erg s^{-1} cm^{-2}. This flux limit of the survey has been increased by REFLEX II survey, which covers the same area, but with deeper exposure. For the new flux limit of 1.8×10^{-12}erg s^{-1} cm^{-2}, 915 (861 with more than 20 counts) clusters has been selected out of 4460 extragalactic sources detected. The sample of confirmed clusters from REFLEX II is a low redshift sample, with a median redshift of 0.102 and a maximum redshift of 0.5.

- **Rosat Deep Cluster Survey (RDCS)** (Rosati et al. 2000, 1995) is a serendipitous *ROSAT* survey over an area of 50 deg^2. The catalogue is constructed based on a wavelet-based detection technique and it contains 160 cluster candidates, detected above a flux limit of $\sim 10^{-14}$erg s^{-1} cm^{-2}. A significant fraction of these (115) are optically confirmed clusters whose redshift distribution peaks at a redshift of 0.1 and has a maximum value of 1.2.
- **Wide Angle *ROSAT* Pointed Survey (WARPS)** (Scharf et al. 1997; Perlman et al. 2002) is a *ROSAT* serendipitous survey to detect all significant X-ray sources using a Voronoi tessellation and percolation technique. It covers an area of 70.9 deg^2 and the catalogue contains 159 clusters above a flux of 6.5×10^{-14}erg s^{-1} cm^{-2}. The survey has been constructed in two stages: WARPS I (Perlman et al. 2002), which covers an area of 14.1 deg^2, and WARPS II (Horner et al. 2008) which covers 56.7 deg^2 and is an extension of WARPS I obtained by the addition of 215 *ROSAT* observations. WARPS-I detects 39 cluster candidates out of which 34 are confirmed clusters with redshifts between 0.06 and 0.75, while WARPS II catalogue contains 125 clusters detected in the redshift range of 0.029 and 0.92 with median if 0.29.
- **160 Square Degree (160d)** (Vikhlinin et al. 1998) is a flux-limited survey aimed at detecting clusters serendipitously in the *ROSAT* archival data. An area of 158 deg^2 had been searched

for X-ray sources with an wavelet-based algorithm. From all detected sources, cluster candidates are selected based on a maximum-likelihood fitting of beta models. In this method, a beta model and then a delta function is fitted to the data. Depending on the quality of each fit, a source is classified as extended or point-like. Only sources detected at high significance and with a significant extend are catalogued as potential clusters. This strict selection criteria assures a low contamination by point sources, and as a result, 91% (203 out of 223) of their extended sources are confirmed clusters. Their redshift distribution spreads from 0.015 to 0.73.

- **400 Square Degree Survey (400d)** (Burenin et al. 2007) is an extension of the 160d. It detects 287 clusters candidates over an area of 397 deg^2, with a minimum flux of 1.4×10^{-13}erg s^{-1} cm^{-2}. Out of these, 93% (266) are optically confirmed clusters, groups or individual galaxies. The median redshift of their detected sources is 0.2
- **The *XMM* -Newton Distant Cluster Project (XDCP)** (Fassbender et al. 2011) is a search for serendipitous high redshift clusters in *XMM* archival data. Is a non-contiguous survey covering an area of 76.1 deg^2 with a minimum exposure time of 10 ks. The aim of the survey is to detect high redshift clusters of galaxies, beyond redshift 0.8, which can be used to study the evolution of these massive systems. Their scientific objective is to investigate the evolution of scaling relations, of X-ray gas properties and that of the luminosity function. They have divided their survey area in three different parts or levels used to construct samples with different statistical properties. The first level is the full survey, from which they detected 990 cluster candidates. The high redshift sample of optically confirmed clusters obtained from the whole survey contains 22 systems with redshift greater than 0.9. Maximum sensitivity obtained with this data is $\sim 10^{-15}$erg s^{-1} cm^{-2}.

  The second level, which occupies 49.4 deg^2 includes only the inner $12'$ of the detector and allowed them to detect 752 cluster candidates. The last level covers the best 17.7 deg^2 of the data and allowed the detection of 310 cluster candidates. The data constructed from this subset has a well defined selection function, which is a requirement for cosmological applications.

- ***XMM* Cluster Survey (XCS)** (Romer et al. 2001; Sahlén et al. 2009; Lloyd-Davies et al. 2011; Mehrtens et al. 2012) is the largest serendipitous survey based on *XMM* archival observations. The aim of the survey is to measure cosmological parameters and trace the evolution of scaling relations. It covers an area of 410 deg^2. The search for clusters has been done with a wavelet-based algorithm and lead to the detection of 3675 cluster candidates with more than 50 counts. The result of optical follow-up (Mehrtens et al. 2012) is the catalogue of 503 optically confirmed, serendipitous groups and clusters. This is one of the larges X-ray selected sample compared to other X-ray surveys. The sample redshift distribution ranges from 0.06 to 1.46, with a peak at redshift of about 0.3. The sample is dominated by systems in the groups temperature regime of about 2 keV.
- ***XMM* Large Scale Structure Survey (*XMM* -LSS)** (Pierre et al. 2004; Pacaud et al. 2006; Pierre et al. 2007; Pacaud et al. 2007; Pierre et al. 2011; Chiappetti et al. 2013) is a 11.1 deg^2, medium depth, wide-area survey performed by *XMM* . It has an almost uniform exposure of 10 ks. The sample constructed from the survey has been divided into two classes based on the likelihood of source detection and that of source extension. The C1 class, with strict criteria for extension and detection, is uncontaminated by misclassified point sources, while C2 class (the rest), with more relaxed criteria, displays a contamination of 30-50 %. From 5 deg^2, Pacaud et al. (2007) found 28 C1 clusters with fluxes between 1 and 50 $\times 10^{-14}$erg s^{-1} cm^{-2}. Most of their systems have temperatures of about 1.5 keV and are at a redshift of 0.3 (as it can be seen from Figure 3 in Pacaud et al. 2007). The whole 11 deg^2 survey contains 50 C1 and 60 C2, with 44 C1 and 27 C2 confirmed from optical spectroscopy (Willis et al. 2013).

- **XXL** (Pierre et al. 2011), represent an extension of the of the MM-LSS survey to an area of 50 deg^2. It is planned to be the largest wide angle *XMM* survey. It is a medium deep survey, with almost uniform 10 ks exposure and with a plan to increase the exposure to 40 ks.

- ***Chandra* COSMOS Survey (C-COSMOS)** (Puccetti et al. 2009; Elvis et al. 2009) is a *Chandra* contiguous X-ray coverage of the central 0.9 deg^2 of the 2 deg^2 area covered by the multi-wavelength Cosmic Evolution Survey. This survey is dedicated to the study of the evolution of galaxies, AGNs and dark matter. It has been designed to optimize between a large area and a deep exposures, and as a result of this, is the largest contiguous survey with deep exposures covered by *Chandra*. A slightly larger area of this field has been covered by *XMM*, but at lower exposure. A search for clusters of galaxies has been performed in the *XMM* COSMOS field by Finoguenov et al. (2007), who found 72 clusters with fluxes as low as 3×10^{-15}erg s^{-1} cm^{-2}. The *Chandra* COSMOS field had been received more interest for the study of the point-like classes of sources, in special the AGN population (Elvis et al. 2012).

- ***Chandra* Deep Field North (CDF-N)** (Brandt et al. 2002) is the first deep, pencil beam survey performed with *Chandra* . It covers a very small area of only 0.11 deg^2, but has an almost uniform exposure of 1 Ms. This deep exposure allows detection of sources with fluxes as low as 3×10^{-15}erg s^{-1} cm^{-2}. Bauer et al. (2002) detects 6 galaxy clusters with redshifts between 0.2 and 1, using a Voronoi Tesselation detection algorithm.

- ***Chandra* Deep Field South (CDF-S)** (Giacconi et al. 2002) and Extended *Chandra* Deep Field South (E-CDFS) (Lehmer et al. 2005; Castellano et al. 2011) The first CDFS (Giacconi et al. 2002) is similar as area and depth to CDFN, being an overlap of single ACIS-I observations with similar pointing adding up to a total depth of 1 Ms. The depth of the survey has been increased with the addition of another Ms. A further increase in exposure up to 4 Ms and also area up to 0.3 deg^2 makes E-CDFS the deepest survey performed by *Chandra* . 19 extended sources had been identified in 1 MS of CDFS with fluxes as low as 9.5×10^{-17}erg s^{-1} cm^{-2}, with the addition of 3 more sources from the E-CDFS.

- ***Chandra* survey of Extended Groth Strip (AEGIS-X)** (Laird et al. 2009). It is a contiguous, deep survey of the region known as the Extended Groth Strip performed with *Chandra* over an area of 0.67 deg^2. The aim of the project is to bring complementary information for the multi-wavelength study of galaxy and large-scale structure formation. The limiting flux for point source detection is 5.3×10^{-7}erg s^{-1} cm^{-2}. Although the targeted population for this survey are AGNs, the area has been also searched for groups and clusters of galaxies (Jeltema et al. 2009; Erfanianfar et al. 2013). Using combined *Chandra* and *XMM* observations of this field for detection, Erfanianfar et al. (2013) found 52 clusters with redshift between 0.07-1.54, with a peak at about 0.7. The flux for observed sources ranges from 6×10^{-16}erg s^{-1} cm^{-2} to 4×10^{-14}erg s^{-1} cm^{-2} (note that the flux from *XMM* observations contributes to this estimated flux).

- ***Chandra* Multiwavelength Project (ChaMP)** (Kim et al. 2004; Barkhouse et al. 2006) is a serendipitous survey for X-ray sources in *Chandra* archival data. It uses ACIS-I and ACIS-S observations available in the archive to search for sources using a wavelet detection method. All observations available in the archive are used, except those in the galactic plane, those contaminated by the target of the observation or if the observation is part of the survey (e.g. CDFS, CDFN,ELAIS). Barkhouse et al. (2006) searched for serendipitous extended sources all 13 deg^2 covered by ChaMP and detected 55 extended sources out of which 31 are optically confirmed clusters. The flux limit reached by their survey is $\sim 10^{-14}$erg s^{-1} cm^{-2}. The peak in their redshift distribution is at 0.41, with highest redshift of 0.8. Their systems are in the cluster regime, with typical luminosity of 5×10^{43}erg s^{-1}. The ranges of exposures corresponding to observations within which the extended sources have been detected, is from about 4 ks to 120 ks. Most of their sources ($\sim 85\%$) are detected in observations with exposures < 50 ks.

- **Boschin (2002)** performs a serendipitous search for clusters in *Chandra* archival observations with a minimum exposure of 10 ks. The total area covered is of 5.55 deg^2 with a depth which varies from 11 to 168 ks. The source detection method is based on the Voronoi Tessellation and percolation method and the extent of the source is determined based on the comparison between the size of the source calculated from the source searching algorithm and the size of the Point Spread Function (PSF), which is assumed to have a Gaussian distribution. 51 sources are detected as extended out of which 15 are single galaxies. The final catalogue contain 36 cluster candidates. Since they do not have any redshift information about their sources, their catalogue dos not give any information about the redshift or temperature range of their sample.

Table 1.1: X-ray surveys

Survey name	**Telescope**	**Type**	**Area** (deg^2)	**Flux limit** (erg s^{-1} cm^{-2})	**No. sources**	**Clusters**
EMSS	Einstein	Archival	778	5.1×10^{-14}	835	98
RASS	*ROSAT*	Contiguous	All sky	5×10^{-13}	225	
RDCS	*ROSAT*	Archival	50	3.4×10^{-12}	160	115
WARPS	*ROSAT*	Archival	70.9	6.5×10^{-14}		159
160d	*ROSAT*	Archival	158	1.6×10^{-14}	223	203
400d	*ROSAT*	Archival	397	1.4×10^{-14}	287	266
REFLEX	*ROSAT*	Contiguous	13924	1.8×10^{-12}		915
XDCP	*XMM*	Archival	76.1	$\sim 10^{-14}$		22
XCS	*XMM*	Archival	410	5×10^{-14}	3675	503
XMM -LSS	*XMM*	Contiguous	11	$\sim 10^{-14}$	110	71
XXL	*XMM*	Contiguous	50			
SXDF	*XMM*	Contiguous	1.3	2×10^{-15}	92	57
CDF-N	*Chandra*	Contiguous	0.11	3×10^{-16}		6
CDF-S	*Chandra*	Contiguous	0.109	5.5×10^{-16}	18	—
E-CDFS	*Chandra*	Contiguous	0.3			
AEGIS-X	*Chandra*	Contiguous	0.67	5.3×10^{-17}	56	52

C-COSMOS	*Chandra*	Contiguous	0.5			
ChaMP	*Chandra*	Archival	13		55	31
Boschin	*Chandra*	Archival	5.5		36	—

1.8 Thesis overview

Groups and clusters of galaxies represent important astrophysical sources because their study can help answer a number of scientific questions about the origin and evolution of the Universe, but also about the origin and properties of other astrophysical sources which leave an imprint on their observed properties. Clusters, as most massive objects in the Universe, represent ideal objects that can be used to test cosmological models by studying, for example, their distribution or the evolution of their number density.

Groups of galaxies on the other hand, have a shallower potential well compared to clusters, a key property which makes groups the ideal sources for the study of baryonic physics and in special the non-gravitational processes like cooling, AGN and supernovae feedback.

Given the importance of groups and clusters, many surveys dedicated to the detection of these sources have been carried out in multiple wavebands such as optical, infrared, X-ray and microwave. The detection and ensemble of large samples of groups and clusters using X-ray methods represent a past, current and on-going effort. New instruments with large collecting area and/or high spatial resolution such as *XMM-Newton* and *Chandra* are able to construct samples of groups and clusters at high redshifts which are ideal for detailed as well as evolutionary studies of these systems.

The work presented in this thesis is dedicated to the search of high redshift groups and the study of the evolution with redshift of their intragroup medium. A survey, named the *Chandra* Deep Group Survey, has been dedicated to the search for high redshift groups. These objects are searched in all observations available in the *Chandra* data archive. The detection of groups at high redshift requires deep observations, since groups are low surface brightness systems compared to clusters. In addition, a detailed study of groups at high redshift requires high spatial resolution, a condition which can be meet by using *Chandra* telescope for the survey, a telescope that offers highest angular resolution achievable at the moment.

Groups are detected as X-ray sources in the images using a Voronoi Tesselation and Percolation detection method and are discriminated against other X-ray detected sources using their property to have spatially extended emission. However, since groups are not the only extended sources, a confirmation of these objects is done only by verifying the presence of galaxies overdensity using optical observations. For all detected groups with available redshifts, X-ray properties like temperature, the surface brightness distribution of their intragroup medium, the entropy at the centre of the cluster as well as the time within which the gas ought to cool due to radiation are estimated for each system.

A scientific question addressed using a subsample of groups and clusters detected from *Chandra* Deep Group Survey is how the thermal state of the gas at the centre of groups and clusters evolve with redshift and if this evolution is different in groups compared to clusters.

Chapter 2 of this thesis describes the *Chandra* deep group survey project. The beginning of the Chapter presents the motivation behind the CDGS and the strategy adopted to select observations from the *Chandra* data archive which will be further used to search for groups. The whole process of group detection and confirmation is presented in detail and a catalogue of group candidates is included. However, to confirm the nature of these group candidates, spectroscopic information of galaxy members is required. An description of how this information is obtained from literature and how a series of X-ray properties such as temperature and R_{500} are estimated is given. Finally, the CDGS catalogue of confirmed clusters and a discussion of the statistical properties of the survey in comparison with other surveys of groups and clusters available in the literature is presented.

Chapter 3 represents a study of the evolution of cooling state of the central gas in groups and clusters using a subsample of 62 systems from CDGS with temperature between 1 and 12 keV and redshifts that span the range between 0.07 and 1.3. Six different parameters used to estimate the cool core strength are presented: central gas entropy, central gas cooling time, cooling time as a fraction of the age of the Universe and three estimators based on the cuspiness of the X-ray surface brightness profile. One important result obtained is that the observed evolutionary trend is dependent on the parameter used to characterize the cooling state of the system. However, irrespective of the CC estimator, the evolution of CCs in groups and clusters show similar trends. Whether any of the evolutionary trend seen in this study is a characteristic of the population of groups and clusters or a result of potential biases due to the way in which the sample has been selected is also investigated in this Chapter.

A brief discussion of the work described in this thesis as well as suggestions for future work are presented in Chapter 4.

Chapter 2

Chandra Deep Group Survey

CDGS is an X-ray survey dedicated to finding high redshift groups of galaxies in *Chandra* archival observations in order to study the evolution of their X-ray properties and the correlations between the X-ray and other wavelength properties. The main scientific questions we are trying to address are the following: how are groups evolving with redshift and are these low mass systems evolving differently from clusters? To find the answer to these questions we are going to investigate the evolution of the thermal state, of dynamical properties and the impact of AGN on the evolution of both groups and clusters. Detection of groups is more challenging compared to clusters, especially at high redshifts due to their lower surface brightness and smaller angular size.

The observing strategies adopted for our survey are determined by the type of objects we are studying and the scientific question we are addressing. Therefore, to be able to detect high redshift groups of galaxies we require deep observations. Moreover, because evolutionary studies require a large sample (in order to provide the necessary statistics at high redshifts), we are interested for our survey to cover a sky area as large as possible. On top of this, resolution is another important aspect which must be considered because it allows resolving core regions up to high redshifts and also resolve and remove contaminated point sources. To maximize all these requirements we have chosen to use *Chandra* telescope for our survey. The telescope offers the highest resolution possible at the cost of lower effective area and field of view which means less sensitivity and less sky covered area. The one way in which we can increase our sample is by using an area as large as possible which can be obtained by using all available deep observations from the archive. This Chapter contains a description of the CDGS, the sample selection strategy and the methodology used to derive the X-ray and optical properties for each system in the sample.

2.1 Survey strategy

The approach used to design an X-ray survey is motivated by the scientific questions which are addressed with the sample constructed from the survey. Several aspects have to be taken into consideration when planning a survey: What is the best telescope that can be used to construct the sample?; What is the sensitivity of the survey?; How large has to be the sample?; How deep are the observations used? All of these have an impact on the statistical properties of selected sample and have to be taken into account when interpreting the results obtained by using the sample. The scientific question we wish to address with our sample is the evolution of gas properties within groups and clusters. In the following three subchapters we will discuss few aspects related to the strategy adopted for our survey. We will motivate the use of *Chandra* telescope for our source detection, the threshold of 100 detected source counts adopted as the lower limit for a source to be included in our sample and the amount of sky area used to search for groups of galaxies.

2.1.1 *Chandra* X-ray observatory

The ideal telescope to use for X-ray groups and clusters surveys would be characterized by a large collecting area, high spatial resolution and a large field of view. A large collecting area means more photons can be detected, which leads to the discovery of faint or/and high redshift sources. The resolution is crucial for deciding if a detected source is a potential cluster, deblending sources, being able to study the core properties or eliminate point sources. Finally, a large field of view makes possible the construction of a large sample. Table 2.1 shows a comparison between the properties of *Chandra* and two other X-ray telescopes used for clusters surveys: *XMM* and *ROSAT*. The Table shows that all three telescopes complement each other regarding their survey capabilities. When comparing *Chandra* and *XMM*, *Chandra* offers a high spatial resolution and a lower collecting area while *XMM* has a significantly larger collecting area, but a poorer resolution. The strength of *ROSAT* is a very large field of view, at the cost of much less effective area and poorer spatial resolution.

Table 2.1: Main characteristics of *Chandra*, *XMM* and *ROSAT* telescope.

Telescope	**Mirror PSF FWHM** (arcsec)	**Effective Area** (cm^2) at 1keV	Energy (keV)	Field of view / Instrument (deg^2)
Chandra	0.2	800	0.1-12	0.08 / ACIS-I
				0.12 / ACIS-S
XMM	6	4650	0.15-15	0.23 / MOS1
				0.23 / MOS2
				0.20 / PN
ROSAT	3.5	400	0.1-2.4	3.14 / PSPC

Since spatial resolution is a crucial property required for our survey, we select *Chandra* as our detection instrument. *Chandra* is an X-ray imaging spectrometer that records both spatial and spectral information for all photons received in the 0.1-12 keV energy band. *Chandra* observatory allows taking observations with high spectral and spatial resolution using different types of detectors situated at the focal plane. It has two ACIS (Advanced CCD Imaging Spectrometer) detectors that can be used for imaging and spectroscopy: ACIS-I and ACIS-S. ACIS-I is a 2x2 array of CCDs with a field of view of 17x17 arcminutes, while ACIS-S is a 6x1 array of CCDs with a field of view of 8x50 arcminutes. Both types of detectors offer almost similar capabilities, with the exception of two chips on ACIS-S which are back-illuminated (BI) chips. These BI chips have a higher spectral resolution and larger effective area than front illuminated (FI) ones. During an observation, only 6 chips can be operating simultaneously, including any combination of ACIS-I and ACIS-S chips. A common configuration used for surveys includes all 4 ACIS-I chips because they have a lower level of degradation in the PSF size (due to the shorter distance from the aim-point to the edge of the field) compared to the ACIS-S only configuration. We have chosen only observations taken with ACIS-I detector for our survey because the geometrical arrangement of its four CCDs allows a larger covering area if multiple observations with similar pointings are merged together.

Chandra's collecting area depends on the effective area, while its resolution depends on the mirror's PSF. The effective area of the telescope is the geometric area of the mirror multiplied by its reflectivity, vignetting and quantum efficiency (QE). Vignetting represents a gradual decrease in the number of photons detected from the on-axis position towards the outer regions of the field of view. Since reflectivity, vignetting and QE depend on photon energy as well as grazing angle, *Chandra*'s effective area varies with X-ray energy and the source location in the field of view. For example, for on-axis position, the effective area is: 110, 600 and 40 cm^2 corresponding to energies of 0.5, 1.5 and 8.0 keV respectively. For a single energy ($\sim$ 1.5 keV), effective area can vary as much as 20% from the centre to the edge of the field. The variation of effective area with off-axis angle, as well as energy, will cause different sensitivities for sources having different energies and positions in the field of view. Figure 2.1 shows a comparison of the effective area for *Chandra* (for both ACIS-I and ACIS-S detectors) and *XMM*. It can be seen that compared to ACIS-I, *XMM* has

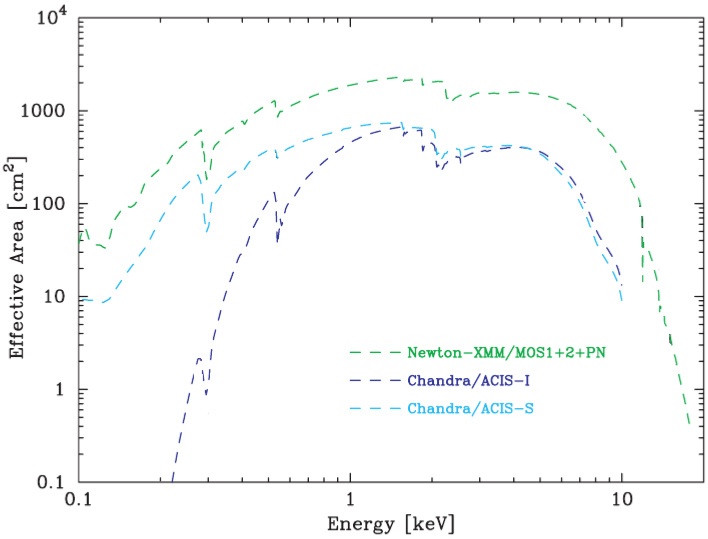

Figure 2.1: Comparison between *Chandra* and XMM effective area. Image adapted from Serlemitsos et al. (2007)

an effective area which is more than double at almost all energies. The implications of this difference is that *XMM* has a higher sensitivity and therefore allows the detection of fainter sources, like groups, up to higher redshifts.

For an ideal telescope, with a perfect mirror, the observed flux distribution of a point like object can be well approximated with a delta function. The telescope's PSF describes the changes in the size and shape of the surface brightness distribution of a point source due to broadening effects introduced by the imperfections in the telscope's mirror. The shape and size of *Chandra* PSF varies significantly with source location in the field of view, as well as with spectral energy distribution of the source. Figure 2.2 shows simulated images of PSFs for the same source detected at different off-axis angles. The left panel corresponds to a source with a constant spectral distribution with energy of 1.49 keV and the right panel to a source with energy of 6.4 keV. One noticeable thing in both panels is the large increase in the PSF size with increasing off-axis angle. In addition to the size variations of the PSF, significant changes in its shape can also be observed. While an on-axis

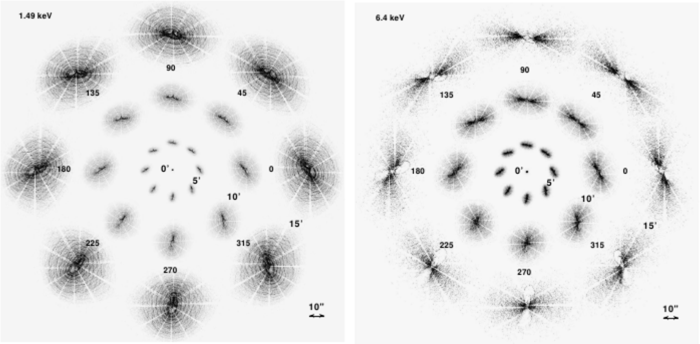

Figure 2.2: Simulated images for PSFs at different off-axis angles and two different energies. Figure taken from The *Chandra* Proposers' Observatory Guide

PSF has a radially symmetric distribution, imperfections in the mirror generate deviations from this symmetry for off-axis sources and introduce several features in the shape of the PSF, which are complicating the modelling of its shape.

If we approximate the size of the PSF with the radius of the circle enclosing 90% of its flux (90% encircled energy (EE) radius), then direct comparison between PSFs at various off-axis angles can be made. The relationship between the 50% and 90% EE radius and source off-axis angle for two different energies is plotted in the left panel of Figure 2.3. The Figure quantifies the idea already seen in Figure 2.2: for a monochromatic source with energy of 1.49 KeV, the size of the PSF (90% EE radius) increases gradually up to an off-axis angle of about $5'$ beyond which it has a very steep increase. If at $5'$ it increases by a factor of 4, at $10'$ the PSF is 13 times the size of the on-axis PSF while at very large off-axis angles of $15'$ (not visible in the plot) it is 27 times. In the right panel of Figure 2.3, the 50% and 90% EE radius as a function of energy is showed for *XMM* PSFs observed at five different off-axis angles. If we compare *Chandra*'s 90% EE radius for a 1.5 keV source with *XMM*'s, one can immediately see that *Chandra*'s PSF is at least four times smaller than *XMM*'s up to off-axis angles of $10'$. This demonstrates *Chandra*'s advantage compared to *XMM* with respect to spatial resolution.

The degradation in PSF properties with off-axis angle has a very important impact on the observed spatial distribution of astrophysical sources. Their observed size and shape will be the convolution of their intrinsic distribution with the PSF. To account for this change, images of the PSF can be simulated and used during the source modelling. Simulations can be created using the *Chandra* SAOsac raytrace code (ChaRT) or Model of AXAF Response to X-rays (MARX) software which are software that trace and project on the detector the incoming photons from a simulated source through the *Chandra* X-ray optics using detailed models for the telescope's mirrors and detectors.

2.1.2 Source selection

The method adopted for selecting sources which are used to construct the final source catalogue of a survey has a large impact on the sample properties. There are several constraints that can be imposed when selecting a sample: adopting a threshold for the minimum flux required for a source, imposing a maximum/minimum redshift for detected sources, adopting a minimum number of counts or any combination of these.

For CDGS, since we are interested in studying the evolution of X-ray properties of groups, we require a minimum number of detected source counts which will allow us to obtain an reliable estimate of these properties. Therefore, one question which we have to address is: **What is the minimum number of counts** for a source to be include in our sample? In addition to this, since we want to detect sources up to high redshifts, another question is: **What is the minimum exposure time** needed to detect a minimum number of source counts equal to our threshold from a high redshift source?

The number of counts threshold is selected such as to be able to perform a spectral and spatial

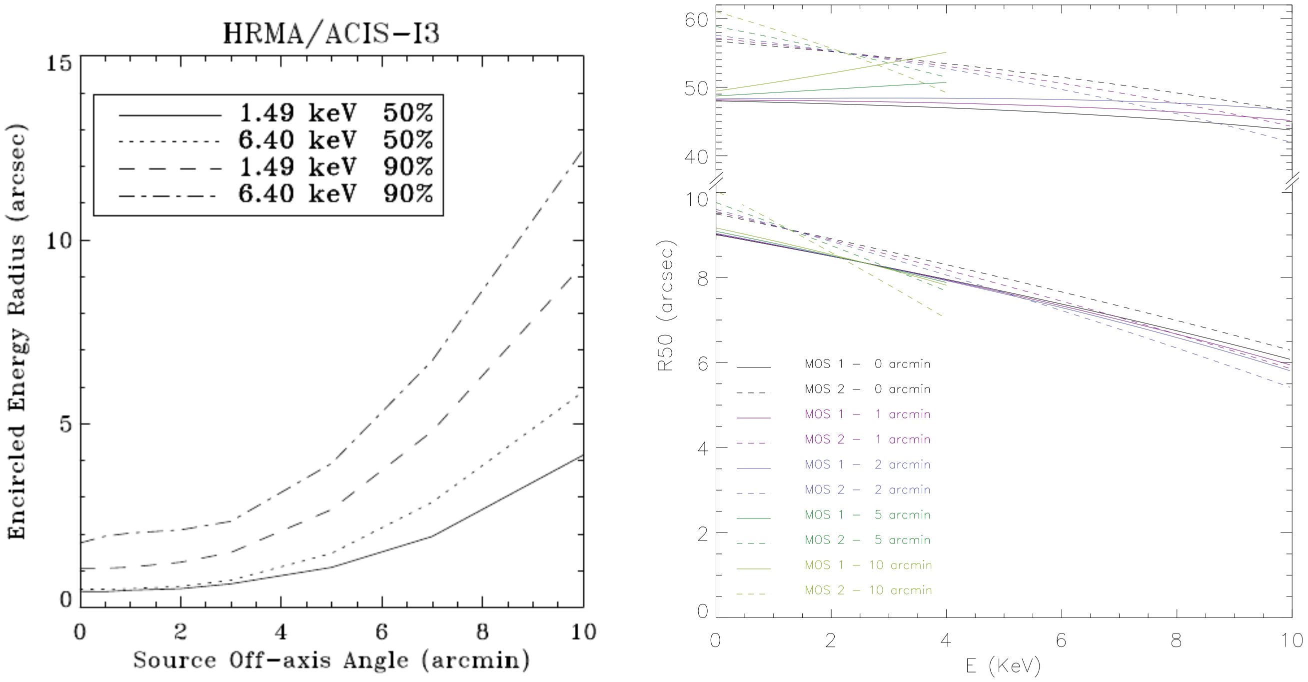

Figure 2.3: Left: *Chandra* HRMA/ACIS encircled energy fraction radius as a function of off-axis angle. Encircled energy (EE) radius of the PSF is the radius of the circle enclosing a particular fraction of the PSF's flux. Figure taken from The *Chandra* Proposers' Observatory Guide (POG). Right: *XMM* 50% (bottom set of curves) and 90% (top set of curves) EE fraction radius as a function of energy and off-axis angle for two *XMM* detectors: MOS1 and MOS2. Figure adapted from *XMM* technical notes: Ghizzardi, S., 'In-flight calibration of the on-axis and near off-axis PSF for MOS1 and MOS2 cameras', EPIS-MCT-TN-011.

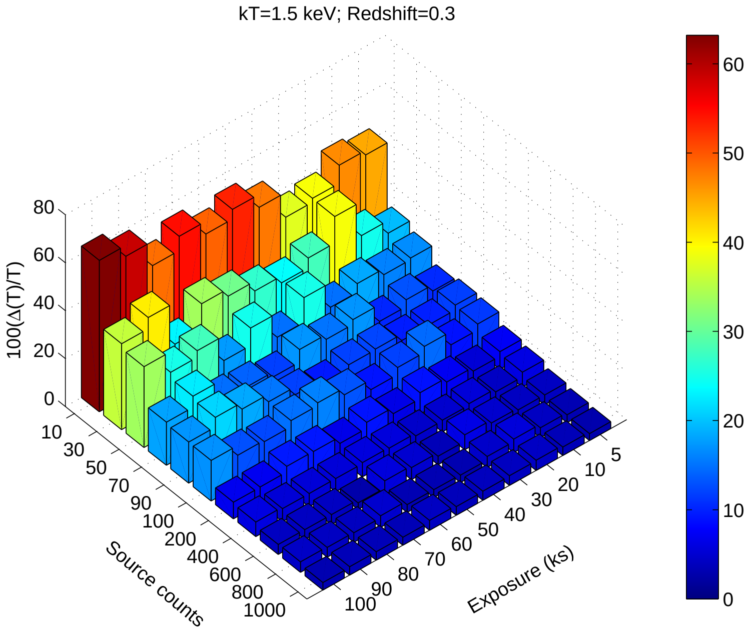

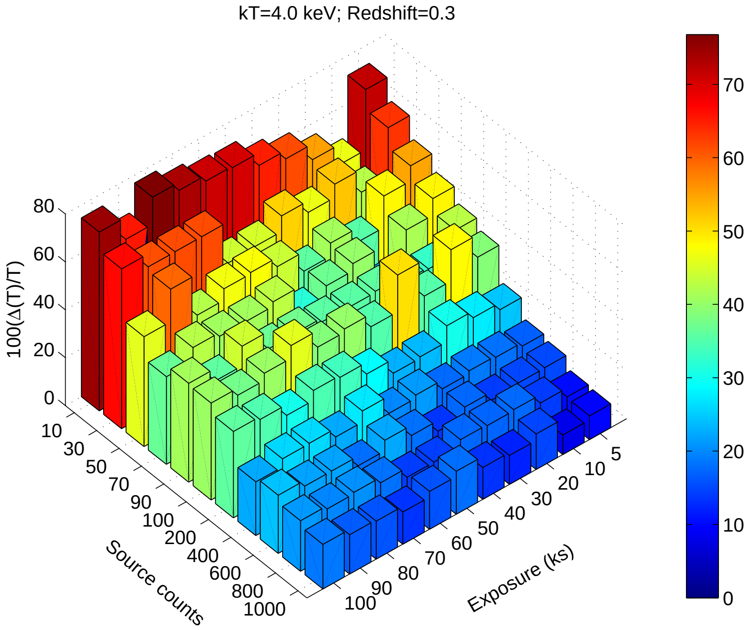

Figure 2.4: Fractional error obtained for a kT=1.5 group (top) and a kT=4.0 keV cluster (bottom), both at redshift 0.3, obtained from simulations of 10 spectra for each pair of exposure and source counts within the range plotted. Both, the hight and colour of the bin have the same value given by Equation 2.1.

analysis of each detected system. Spectral analysis involves extracting spectra for each source and fitting a thermal plasma model in order to estimate the gas temperature. These temperatures will be further used to estimate other properties derived based on the temperature such as R_{500}, cooling time and entropy. Spatial analysis involves fitting beta models to surface brightness profiles to obtain information about the source flux distribution.

To investigate the minimum number of source counts needed to be able to perform a spectral and spatial analysis, we have simulated source spectra for two classes of sources: groups (kT = 1.5 keV) and clusters (kT = 4.0 keV), both at a redshift of 0.3 and with an abundance of 0.3 $Z_{\odot}$. For each class, 1210 source spectra are simulated for various exposure times and number of source counts using *fake_pha* function in SHERPA. For each exposure time and each number of counts, 10 spectra are simulated. The background is simulated separately using a background model with multiple components as described in Chapter 2.6 and then the simulated source and background spectra are added to form a single source plus background spectrum. The parameters used for the background model during simulations are obtained by fitting this model to an observed background spectrum. All parameters are fixed to the values obtained from the fit, with the exception of the amplitude, which is changed depending on the exposure time used for the simulation.

Figure 2.4 shows the results obtained by applying our spectral analysis (see also Chapter 2.6.2) to all simulated spectra. For each fit, the redshift and abundance is frozen to the value used to simulate spectra: 0.3 in both cases. The hight and colour of each bin, given by H, is calculated using:

$$H = 100\frac{|\frac{1}{n}\sum_{i=1}^{n} T_{f,i} - T_s|}{T_s} \tag{2.1}$$

where n is the number of simulations for a particular exposure and number of counts (10 in our case), $T_{f,i}$ represents the temperature obtained from the thermal fit to simulates spectra and T_s represents the input temperature used to simulate spectra. We can see that adopting a count limit of 100 counts allow us to get reliable estimates for groups temperature, to within 20%. For clusters, this lower limit gives less reliable estimates of temperatures, with errors below 50%.

So far we have decided on a limit of 100 counts required for a source to be part of our sample. The next step is to decide which is the minimum exposure needed in order to be able to detect 100 counts for a high redshift group. Figure 2.5 shows the minimum exposure time needed to detect 100 counts from a source at a particular redshift and with different luminosities: 10^{42}erg s^{-1} (red), 5×10^{42}erg s^{-1} (orange), 10^{43}erg s^{-1} (green), 5×10^{43}erg s^{-1} (blue) and 10^{44}erg s^{-1} (black). These luminosities correspond to temperatures of 0.7, 1.1, 1.5, 2.7 and respectively 3.6 keV if an observed luminosity-temperature relation for low redshift groups and clusters with a slope of 2.52 and intercept of 0.10 is used (Eckmiller et al. (2011), their Table 4).

Figure 2.5 shows that for a typical group of 1.5 keV and luminosity of 10^{43}erg s^{-1}, the range of exposures needed to be able to detect at least 100 counts increases steeply from 30 ks at redshift 0.3 to 500 ks for a redshift of 1. The exposure needed for clusters, on the other hand, has a much less steeper increase, with exposures within 10 and 40 ks. On the basis of this Figure, we choose 70 ks as our minimum threshold, an exposure for which we can detected groups up to redshifts of 0.5.

We remind the reader that CDGS is a survey based on the observations available in the *Chandra* data archive. This means that the same position on the sky might be observed several time and be at different off-axis angle in each observation, depending on the observing preferences of the Principal Investigator of that particular observation. To increase the number of counts which can be detected for a source, we combine all these overlapping observations and perform our source detection and further data analysis on these merged images. For the rest of this Chapter, when we refer to a field, we mean the sky area covered by overlapped observations, while an observation represent the image obtained from a single pointing. In Figure 2.8 we show two examples of fields

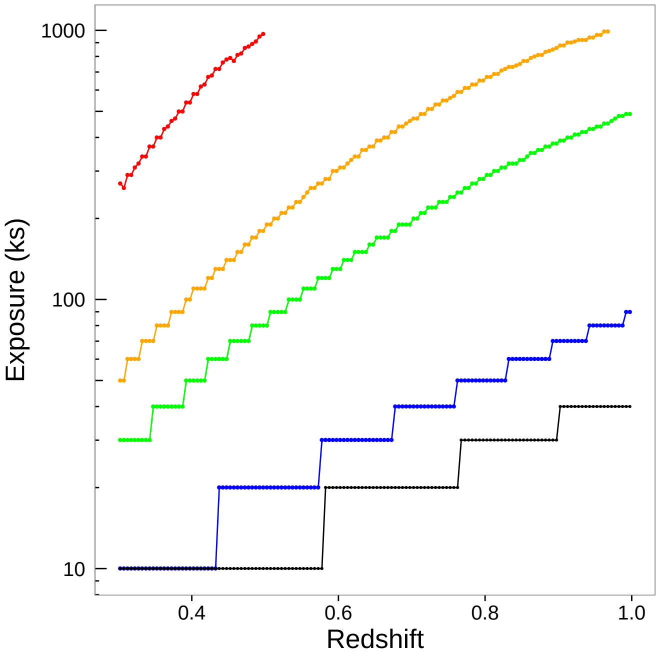

Figure 2.5: Curves of minimum exposure needed to detect 100 counts from a source with a given luminosity as a function of redshift. Different curves correspond to different source luminosities: 10^{42}erg s^{-1} (red), 5×10^{42}erg s^{-1} (orange), 10^{43}erg s^{-1} (green), 5×10^{43}erg s^{-1} (blue) and 10^{44} erg s^{-1} (black)

with different degree of overlapping between individual observations. The value of each pixel in the image represent the total exposure time at that particular point obtained from the sum of exposure times in each individual observation. The left panel, which represents the *Chandra* Deep Field North (CDFN), is an example of a field with a high degree of overlapping between individual pointings, while the right panel, which corresponds to the COSMOS field, is an example of a field with a much lesser degree of overlap. This Figure also show that the actual exposure time across the field can vary significantly and therefore our threshold of 70 ks is not a simple cut which can be applied to each point in the field. One of the options would be to require a minimum exposure of 70 ks for at least a very small fraction of the total field of view. If we use this method, some fields with moderate exposure would be excluded if none of the points in the field reach this threshold. Although our interest is the detection of high redshift groups of galaxies, we do not dedicate the survey exclusively to these types of sources. Therefore we want to search for extended sources in moderately deep fields, which are selected by requiring a minimum exposure of 70 ks for the total exposure of the field. Left panel of Figure 2.21, which we show at the end of this Chapter in the Survey statistics chapter (Chapter 2.8), shows a histogram for the exposure time of all individual observations which are used for our survey, while the left hand side panel shows the distribution of exposure times for the merged image. We can see in the left panel that the peak in the exposure of individual observations is at about 30 ks, with a second, although much lower peak at 70 ks. When we look at the right hand side plot we can see that the large majority of fields have a total exposure of about 100 ks. Also, there are 4 fields with very high exposures which corresponds to the CDFN, CDFS, COSMOS and AEGIS which are individual surveys, with CDFS and CDFN being a pencil beam survey with 20 respective 63 individual observations and COSMOS and AEGIS covering the largest area from all of our fields.

Figure 2.6 shows the area covered by our survey at each exposure. From this Figure we can see that most of our area covers exposures below 150 ks. If we combine this with the information from

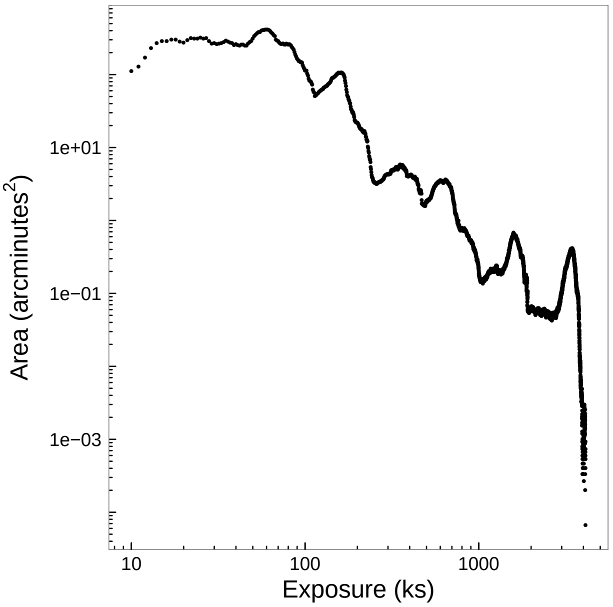

Figure 2.6: The area covered by CDGS as a function exposure time.

Figure 2.5 we can estimate that the majority of groups detected will be at redshifts below 0.5, but we expect to discover also high redshift groups with redshifts up to 1.

2.1.3 Survey area

If the aim of the survey is the ensemble of a sizable sample, then the selection of an area as large as possible to use for source searching represents a priority.

Since we are interested in detecting a large number of groups, we construct our survey area starting from all observations available in *Chandra* archive to which we impose a few constraints to optimize the number of detected systems. A more detailed discussion of the procedure used to select observations from the archive and construct the fields used to search for extended sources is presented in Chapter 2.2, in which we derive a total area for our survey of 9.7 deg^2.

Although this total area gives an idea about the size of the survey, a more important area is the one covered by a survey for which the exposure is high enough to detect sources above a particular flux. This area, although in most cases stated as a function of flux, depends also on other factors which influence source detection, like the source size, its position in the field of view, the background or other contaminating sources. A proper estimation of the probability to detect a source with a particular flux (survey selection function) has to take into account all the above mentioned factors which has an impact on source detection. This can be done with extensive image simulations of sources with different properties on which the survey detection algorithm is run.

Given the effective area as a function of flux, the number of clusters expected to be detected from a survey can be estimated a priori. This number depends on two factors: the real number density of clusters as a function of luminosity and redshift and the number of clusters which can be detected in the survey . Therefore, what is needed to calculate the predicted number of clusters is: a way to approximate the number density of clusters as a function redshift and of luminosity or mass (it can be the observed luminosity function or simulations), knowledge about the expected luminosity range which should be observable with the instrument used for detection and survey strategy (selection function).

Number of clusters per unit comoving volume and per unit luminosity interval ($dn(L_x,z)$) can be obtained from luminosity function:

$$\Phi(L_x,z) = \frac{dn(L_x,z)}{dL_x dV} \tag{2.2}$$

This luminosity function can be constructed from observations and the function usually adopted to parametrize it is the Schechter (Schechter 1976) function, given by:

$$\Phi\left(L_x,z\right)dL_x = \Phi^{\star}\left(-\frac{L_x}{L_x^{\star}}\right)^{-\alpha} exp\left(-\frac{L_x}{L_x^{\star}}\right)\left(\frac{dL_x}{L_x^{\star}}\right) \tag{2.3}$$

An example of a luminosity function for the nearby Universe, together with a Schecter function fit is showed in Figure 2.7. This function has been obtained by Böhringer et al. (2014b) using 910 galaxy groups and clusters with luminosities in the $0.03 - 10 \times 10^{44}$ erg s^{-1} interval from *ROSAT* All Sky Survey. The Figure shows the fit to the luminosity function created for clusters in two redshift intervals: 0.0-0.1 and 0.0-0.3. Luminosity functions for clusters of galaxies constructed based on observations has been obtained from Einstein Medium Sensitivity Survey (EMSS; Gioia et al. 1990a), *ROSAT* surveys (Ebeling et al. 1998, 2000; De Grandi et al. 1999; Böhringer et al. 2002; Koens et al. 2013; Böhringer et al. 2014a), *XMM* surveys or *Chandra* surveys.

One important scientific question is if the luminosity function evolves with redshift. The *ROSAT* all-sky survey allowed the construction of large flux-limited sample which are used to construct the low-redshift luminosity function. These functions are usually used as a baseline for determining and quantifying the evolution of X-ray luminosity function obtained from deeper surveys. There is no clear consensus if the cluster luminosity function evolves or not. Some studies predict positive evolution in luminosity function (Edge et al. 1990), others predict no evolution (Ellis & Jones 2002; Jones et al. 2002), while others predict a negative evolution (Edge et al. 1990; Gioia et al. 1990a; Mullis et al. 2004; Koens et al. 2013).

We have calculated the predicted number of clusters for our survey by integrating Equation 2.2 over the luminosity and redshift range covered by our survey using the following equation:

$$N = \int_{L_{X,min}}^{L_{X,max}} \int_{z_{min}}^{z_{max}} \Phi(L_X, z)\Omega(f_X)\frac{dV(z)}{dz}dzdL_X \tag{2.4}$$

In this equation $\Omega(f_X)$ is the survey area as a function of the flux limit imposed by the survey and $dV(z)/dz$ is the comoving volume corresponding to a unit solid angle at a redshift z.

As already mentioned, to estimate area for which the survey is sensitive to, require good knowledge about the selection function. Since we have not modelled our selection function, the number obtained from Equation 2.4 is only an approximation to the more precise number of expected systems determined with a proper selection function. The survey area as a function of exposure for

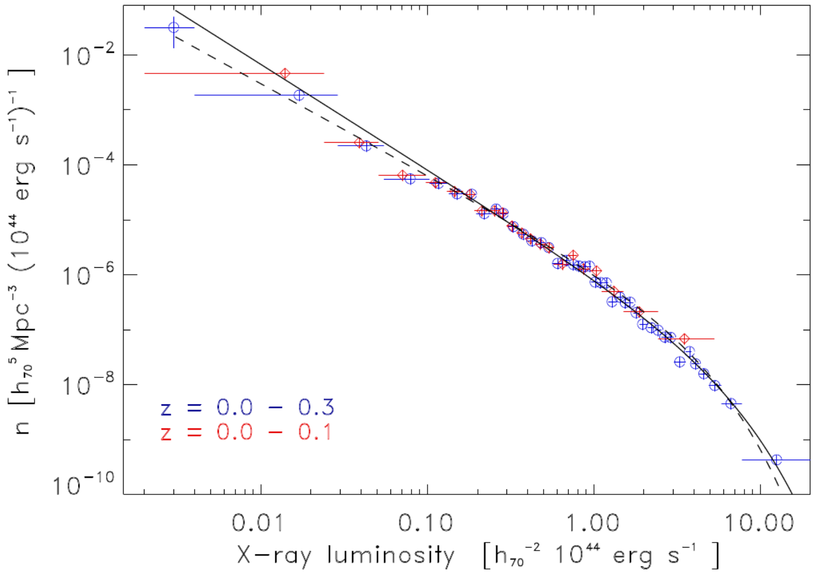

Figure 2.7: The X-ray luminosity function for a sample of 910 galaxy clusters from *ROSAT*-ESO Flux-Limited X-ray (REFLEX II). The luminosity function is plotted for two redshift intervals: low redshift (below 0.1) and intermediate redshift (below 0.3). Points represent the luminosity function obtained from the data and continuous line represents the best fit Schechter function for these two samples. (Figure from Böhringer et al. 2014b)

our survey is given in Figure 2.6. To obtain the survey area for each redshift and luminosity bin, we integrated the function from this Figure as explained in the following. For each redshift and luminosity bin, we have calculated the corresponding flux using the luminosity distance relation. For the flux obtained, we then calculate the number of counts which would be detected for each exposure between the $10-400$ ks exposure range covered by our survey. The conversion between flux and count rate is done using the *modelflux* tool from CIAO assuming an absorbed thermal plasma model (APEC) for our source. The temperature of the model is the temperature which would correspond to a luminosity dL_x in the L-T relation of clusters of galaxies obtained by Eckert et al. (2011). The abundance is fixed at 0.3 $z_\odot$. If the number of expected counts is above our threshold of 100 counts, then the area corresponding to that exposure time is added to the total survey area for that luminosity and redshift bin. The area calculated in this way represent an approximation of the actual effective area covered by the surveys and it is expected to be an overestimate of the real survey area because we assume 100% detection rate for sources with at least 100 counts. The degree of the overestimation depends on the efficiency of our detection method and can be calculated only with good knowledge about the selection function.

The comoving volume covered by a solid angle ($d\Omega$) at a particular redshift, ($dV(z)/dz$) is given by:

$$\frac{dV(z)}{dz} = \frac{c}{H_0}\frac{(1+z)^2 D_A^2}{E(z)} d\Omega \tag{2.5}$$

where c is the speed of light, H_0 is the Hubble constant, D_A is the angular diameter distance.

Solving equation 2.4 we expect to detect 149 systems from our survey with redshifts between 0.1 and 1.0 and luminosities in the 0.01-0.5 times10^{44} erg s^{-1} cm^{-2}. This number represent only an approximation to the number of sources expected from our survey since we simplified the calculation by introducing several assumptions like: no evolution of the luminosity function, the ability to detect all sources with at least 100 counts irrespective of their flux distribution or other factors which might affect source detection, no evolution in L-T relation.

2.2 Fields selection

To construct our X-ray selected sample, we have searched for extended sources in all observations available in the *Chandra* data archive as of September 2009, which match all three criteria that we introduce to optimize our survey efficiency. The flowchart in Figure 2.9 shows the steps followed in order to obtain the final list of fields (a field is obtained by merging individual observations with similar pointings) used in our survey to search for groups and clusters of galaxies. Our filtering criteria are:

- select only high galactic latitude pointings ($|b| > 20°$) in order to avoid observations affected by high absorption from gas in the galactic plane
- select only ACIS-I observations; As mentioned in Chapter 2.1.1, ACIS-I detector is preferred over ACIS-S for surveys due to its geometrical configuration which allows the covering of a more contiguous area for the case of multiple observations with similar pointings.
- select only those fields for which the total exposure time of merged fields is greater than 70 ks (as explained in Chapter 2.1.2). The aim of this filter was to increase our survey sensitivity by selecting only those fields with a long exposure time thus allowing us to detect high redshift groups of galaxies. This lower limit exposure will allow us to detect a minimum of 100 counts from a 1.5 keV group at redshift 0.3 and with a lower flux limit of 10^{-14} erg cm^{-2} s^{-1}.

Finally, we have excluded from our list also those fields for which the target is a low redshift group or cluster which occupies most of the field of view and therefore reduces the chances of detecting any serendipitous sources. Our final list, which contains 66 fields, is presented in Table 2.2. The

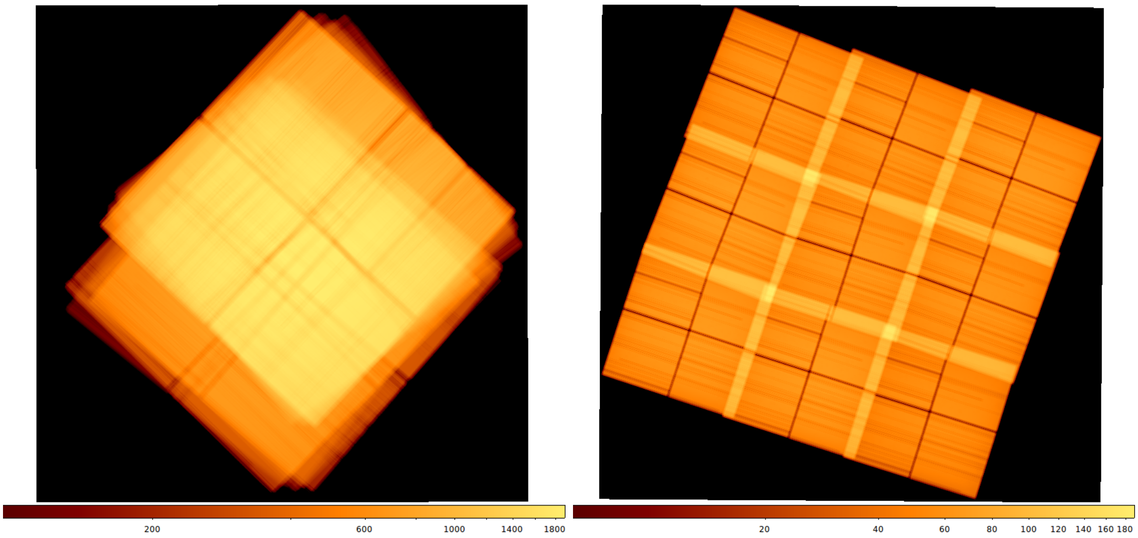

Figure 2.8: Example of different geometries for fields included in our sample. The colorbar shows the total exposure time corresponding to each point in the field. Left: *Chandra* Deep Field North, a field with a high degree of overlapp between individual observations. Right: COSMOS field, which has an almost uniform exposure, with a almost no overlapp for several individual pointings.

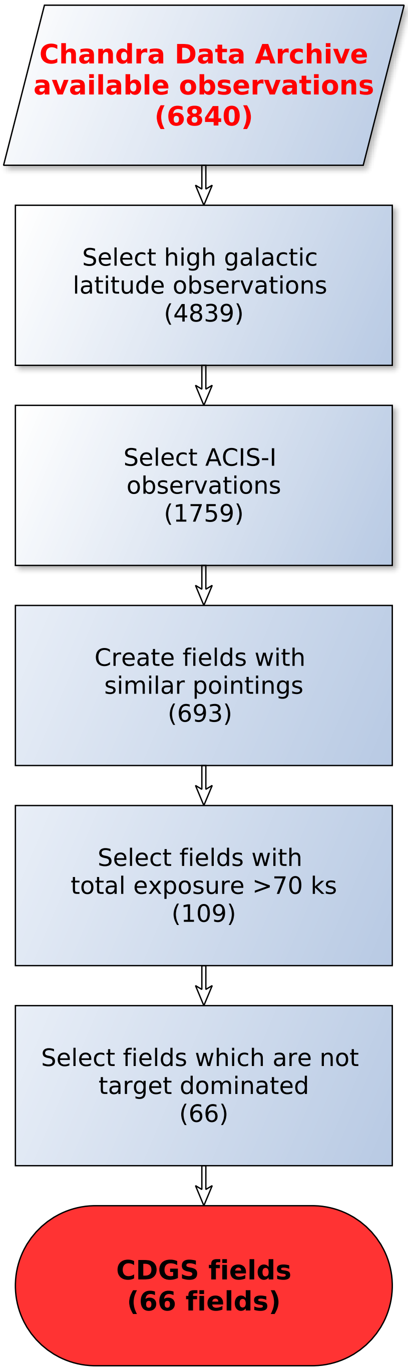

Figure 2.9: Flowchart describing the filtering used to obtain the list of fields used in the CDGS to search for groups and clusters of galaxies.

name assigned to each field in the Table is the name of the target in the observation with longest exposure time from all observations merged to create the respective field. The name of the target in the longest exposure time observation is the name chosen by the Principal Investigator of that observation and in most cases is the the name of the target source. Figure 2.10 shows the position of our fields, in galactic coordinates. The size of the circle is proportional to the field size, while the colour is proportional to the total exposure time (after filtering for flares; see **Data Reduction**), where grey represents the lowest exposure (70 ks) and red the highest (5 Ms). Marked on the plot are several of the main *Chandra* continuous surveys which includes: Extended *Chandra* Deep Field South (CDFS)- which is the deepest survey of about 5 Ms covering a small area of only 0.3 deg^2, COSMOS- which is the field with the largest area from our survey of 1 deg^2 and with a an exposure of about 1.5 Ms and AEGIS- which is a 0.3x2 degree strip with uniform exposure adding up to 3 Ms. The total area covered by our survey is 9.7 deg^2.

Table 2.2: List of fields from CDGS survey. The columns in the table represent: Index number, the name of the field (this represents the name given by the PI of the observation), the Right Ascension and the Declination (for J2000) for the centre of the field, total exposure of the field, clean exposure after applying background filtering (see Section 2.3.1), the field area, the type of the field and the observation ID in the *Chandra* archive for all individual observations merged to create the field. The type of the observation can be : ‘s‘ for fields which are surveys and ‘t‘ for fields which have as target an astrophysical object.

No	Field name	Ra (deg)	Dec (deg)	Exposure (ks)	Exposure clean (ks)	Area (arcmin^2)	Type	Obs ID
1	CDFS	52.9581	-27.9540	4938	4807	1139	s	441 582 1431 1672 2239 2312 2313 2405 2406 2409 5015 5016 5017 5018 5019 5020 5021 5022 6164 8591 8592 8593 8594 8595 8596 8597 9575 9578 9593 9596 9718 12043 12044 12045 12046 12047 12048 12049 12050 12051 12052 12053 12054 12055 12123 12128 12129 12135 12137 12138 12213 12218 12219 12220 12222 12223 12227 12230 12231 12232 12233 12234
2	AEGIS	214.5505	52.6161	3340	3340	2412	s	5841 5842 6210 6211 7180 5843 5844 6212 6213 9873 9875 9876 5845 5846 6214 6215 9450 9451 9452 9453 9721 9722 9723 9724 9725 9726 9793 9794 9795 9796 9797 9842 9843 9844 9863 9866 9870 5847 5848 6216 6217 9454 9455 9456 9457 9727 9729 9730 9731 9733 9878 9879 9880 9881 5849 5850 6218 6219 9458 9459 9460 9461 9734 9735 9736 9739 9740 10769 10847 10848 10849 10876 10877 10896 10923 5852 6220 6391 7169 7188 7236 7237 7238 7239 5851 7181 5853 5854 6222 6223 6366 7187 3305 4357 4365
3	CDFN	189.1537	62.2449	1990	1962	449	s	580 957 966 967 1671 2232 2233 2234 2344 2386 2421 2423 3293 3294 3388 3389 3390 3391 3408 3409
4	COSMOS	150.2127	2.3346	1744	1698	3401	s	7995 7996 7997 7998 7999 8000 8001 8002 8003 8004 8005 8006 8007 8008 8009 8010 8011 8012 8013 8014 8015 8016 8017 8018 8019 8020 8021 8022 8023 8024 8025 8026 8027 8122 8123 8124 8478 8482 8483 8493 8494 8496 8497 8503 8549 8550 8552 8553 8555
5	Swire Lockman	161.9817	59.0990	620	598	2279	s	5030 5031 5023 5024 5025 5026 5027 5028 5029
6	Abell520	73.5209	2.9359	535	528	576	t	4215 528 7703 9424 9425 9426 9430
7	MS0735.6+7421	115.5665	74.2155	483	477	345	t	10468 10469 10470 10471 10822 10918 10922
8	SSA22	334.4033	0.2592	397	392	331	s	8034 8035 8036 9717
9	LH-NW-4	158.5025	57.7702	393	376	1417	s	3347 3348 1698 3347 3348 1697 1698 1699 3343 3345 3346 3347 3348 3344

10	HS1700+643	255.4422	64.2012	245	239	381	t	547 8032 8033 9756 9757 9758 9759 9760 9767
11	Abell1650	194.6902	-1.7284	205	203	471	t	822 5823 6356 6357 6358 7242 7691
12	A1689	197.8869	-1.2892	120	197	485	t	1663 5004 540 6930 7289 7701
13	Abell1835	210.2498	2.8421	196	194	462	t	6880 6881 7370
14	RDCS1252-29	193.2830	-29.4815	192	185	292	t	4198 4403
15	CL0848.6+4453	132.2289	44.9098	189	185	294	t	1708 927
16	LYNDS1551	67.8870	18.1346	178	176	315	t	1866 5381
17	Lala Cetus Field	31.1837	-5.0882	177	175	292	s	4129 4402
18	MACSJ1621.3+3810	245.3879	38.1739	166	145	481	t	10785 3254 3594 6109 6172 7720 9379
19	RXJ0910+5422	137.6668	54.3326	173	163	302	t	2227 2452
20	ELAIS_S1	8.4367	-43.3584	161	161	1277	s	7016 7017 7017 7018 7019 7020 7328
21	MACS0025.4-1222	6.4133	-12.4055	160	158	492	t	10413 10786 10797 3251 5010
22	Abell1995	222.9249	58.1431	156	154	387	t	7021 7022 7023 7713
23	RCS2318+0034	349.6379	0.6055	152	150	291	t	11718
24	A1413	178.9491	23.4294	138	136	645	t	1661 5002 5003 537 7696
25	XMM13HR	203.5800	37.8243	120	118	758	s	2235 2236 2237 2238
26	A2125	235.2063	66.2223	119	117	621	t	2207 6891 7708
27	NGC6861	301.8459	-48.3843	118	116	412	t	3190 11752
28	MS1137.5+6625	175.2081	66.1184	119	116	291	t	536
29	MACS1311.0-0311	197.7375	-3.1972	116	114	441	t	3258 6110 7721 9381
30	NGC752	29.4096	37.7735	134	114	291	t	3752
31	MACSJ1931.8-2634	292.9628	-26.6033	114	113	318	t	3282 9382
32	RXJ1317.4+2911	199.3020	29.1717	112	110	291	t	2228
33	MS1455.0+2232	224.2629	22.2749	110	109	488	t	4192 543 7709
34	H230230	345.6977	8.7532	109	105	291	t	918
35	A907	149.5719	-11.0963	107	102	349	t	3185 3205 535
36	Willman	162.3267	51.0544	102	101	291	t	10534
37	CNOC2150-05	327.6824	-5.7496	101	101	291	s	6791
38	CLJ1113.1-2615	168.2264	-26.2614	105	101	291	t	915
39	A2744	3.4894	-30.3613	102	100	457	t	7712 7915 8477 8557
40	NGC1232	47.4506	-20.5860	101	100	292	t	10720 10798
41	IRAC	264.9963	68.9890	101	99	344	s	7359 8471 9595
42	XMM1HR	26.3071	-4.4884	117	98	479	s	3307 4275 3306 4276
43	CNOC1447+09	221.7937	9.3546	98	97	291	s	6792
44	SC1604+4323	241.0820	43.1707	97	96	529	s	4192 543 7709
45	NGC6868	302.4954	-48.4093	97	96	386	t	3191 11753

46	MS2053.7-0449	314.0777	-4.5765	90	89	488	t	1667 551
47	MACS0744.9+3927	116.2160	39.4850	91	88	398	t	3197 3585 6111
48	CLJ1415.1+3612	213.8132	36.1768	90	88	291	t	4163
49	3C295	212.8278	52.2028	92	88	291	t	2254
50	RXJ0439.0+0715	69.8929	7.3691	88	84	655	t	1449 1506 3583 3905 3906
51	DaddiField1	222.3545	8.9614	89	84	515	s	5032 5033 5034
52	SPT-CL2341-5119	355.3303	-51.2736	81	80	296	t	11799 9345
53	MACSJ0717.5+3745	109.4345	37.7640	80	78	435	t	1655 4200
54	V1221+4918	185.3797	49.2527	80	78	291	t	1662
55	cl0405-4100	61.2795	-41.0083	78	77	475	t	5756 7191
56	MACSJ0329.6-0211	52.4440	-2.2148	77	76	375	t	3257 3582 6108 7719
57	IRAS09104+4109	138.4201	40.9761	77	76	291	t	10445
58	A3112_off	49.4082	-44.4068	85	75	316	t	6972 7323 7324
59	Elais_N2	249.1968	41.0265	74	73	291	s	887
61	MACS0159	29.9718	-8.8557	74	72	405	t	3265 6106 9376
60	ELAIS_N1	242.5850	54.5567	73	73	291	s	888
62	47TUC	5.9769	-72.0730	74	71	293	t	78 953 954 955 956
63	NGC3521	166.4554	-0.0271	72	71	291	t	9552
64	WHDF	5.6388	0.3438	72	71	291	s	2252
65	V1121+2327	170.2032	23.4029	72	69	291	t	1660
66	SC1120-1202	170.0389	-12.0373	70	66	291	s	3235

2.3 Data analysis to create extended source list

2.3.1 Data Reduction

Each individual observation has been reprocessed starting from level=1 eventfile in order to correct it for charge transfer inefficiency (CTI), time-depended gain adjustment and create a new bad pixel file. The aim of reprocessing is to apply these corrections using the latest calibration files available in the *Chandra* Calibration Database (CALDB; version 5.5).Data reduction and all subsequent data analysis have been performed using *Chandra* analysis software (CIAO; version 4.4)

CTI represents a loss in the transfer efficiency of the charge produced by X-ray photons during its shift in the CCD towards readout nodes. The effect of CTI will be a loss in energy resolution and a shift in the apparent gain. The time-dependent gain adjustment has to be applied in order to account for the change with time in "effective gains" of the detectors.

All corrected observations have been filtered using three types of filters: one for the properties and quality of each event in the evtfile and two for the X-ray background events generated by interaction of cosmic charged particles with the detector. Each event recorded in the evtfile has an assigned number (grade) depending on the amplitude of the 8 pixels (for FAINT telemetry mode) or 24 pixels (for VFaint telemetry mode) surrounding the pixel corresponding to that specific event. Based on the number and position of pixels with an amplitude above the event split threshold, a grade is assigned to each event. For example a single event pixel will have a grade of 0, a grade of 2 will represent a vertical split up or down, and a grade of 4 will represent an horizontal split to the right and left. The use of grades is helpful because it can separate between X-ray events and those due to charged particles whose charge split pattern is different from that of X-ray photons. Besides grades assignment, each event has a status column which consists of 32 bits, each bit having a value of 0 or 1 depending on the quality and origin of the event (e.g. event in a bad pixel, cosmic

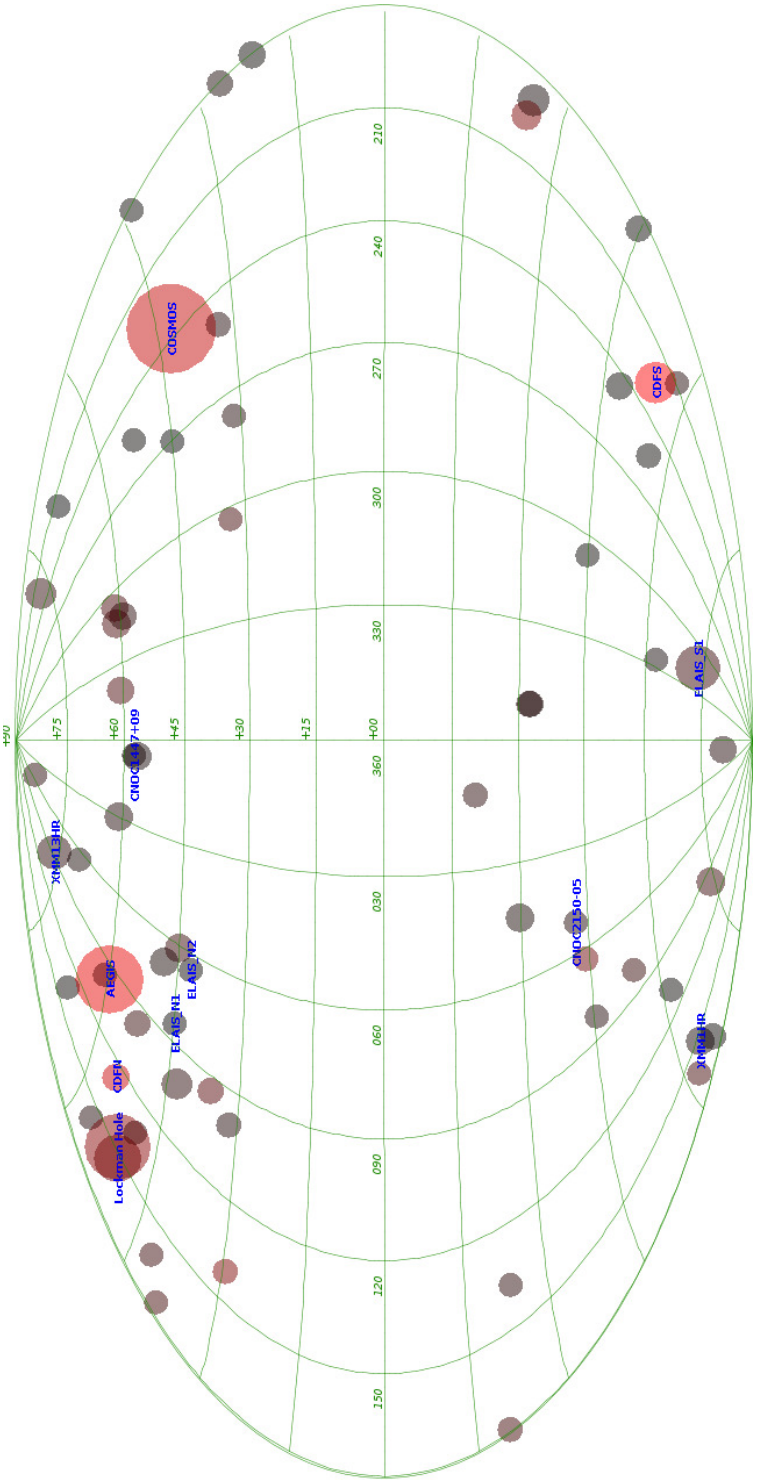

Figure 2.10: Fields used in CDGS to search for extended sources. Galactic coordinates projection is used and the size of the symbol is proportional to the total exposure time of the field. Few of the most important *Chandra* surveys are labelled.

ray event, afterglow event, etc.). We have filtered our eventfiles for bad grades (we used ASCA grades 0,2,4,6) and for ‘clean‘ status column, choosing only events with all bits in the STATUS column equal to 0.

The first background filter applied is the lightcurve cleaning whose aim is to filter periods of time with enhanced count rate above the mean value, also known as flares. Flares has been observed to be present in several if not most observations (De Luca & Molendi 2004). They are highly variable in time and intensity (Kuntz & Snowden 2008) and we can take advantage of their variability to filter them out. A lightcurve is extracted from all observations excluding sources and periods of time with count-rates 20% higher than the median count rate are excluded. The efficiency with which the flares are filtered out depends on the bin size and energy chosen to create the lightcurve. Although this method filters out most of the flares, there may be some log period of time flares with low amplitude or high amplitude very short flares which can not be detected and filtered. Therefore some observations may still be affected by flares even after filtering. Following Markevitch et al. (2003) we have used an energy band of 0.3-12 keV and 2.5-7.0 keV for ACIS-I respectively ACIS-S chips and time bins of 259.28 and 1037.12 seconds.

The second background filtering is not applied to all observations but only to those taken in the VFaint mode. The VFaint mode setup allow for identification of events coming from high energetic particles by analysing the 5x5 pixel island centred on the pixel corresponding to that particular event. In this way events coming from high energy particles can be removed from the eventfile and the amplitude of the uniform X-ray particle background reduced.

Following data reduction and evtfile filtering, individual observations with similar pointings has been merged in order to create a single merged eventfile used for data analysis. Since groups of galaxies radiate most of their energy in the soft part of the spectrum, their detection is more efficient in the soft band images. Therefore the image used for source searching and spatial analysis has been filter for the 0.5-2.0 keV energy band, while the one used for spectral analysis covers a wider energy range of 0.5-7.0 keV.

2.3.2 PSF modelling

Very good knowledge about the size and shape of the PSF is a key element for our survey (see 2.1.1 for a definition of PSF and few properties of *Chandra*'s PSF in comparison with *XMM*'s PSF). Firstly, PSF is crucial for deciding if a source is spatially extended or it can be classified as point-like. A source which appears point-like in X-ray images (e.g. stars, AGNs) will have a surface brightness distribution coincident with the telescope's PSF. On the other hand, extended sources like clusters will show a surface brightness excess when compared with the distribution of the PSF. Secondly, during the surface brightness fitting, any model used to describe the source spatial distribution has to take into account the observed blurring of the source introduced by imperfections in the telescope's mirror. A model of the PSF is used in the fit in order to allow for this blurring and determine proper parameter estimates.

Several methods are available to model the PSF. ChaRT, the *Chandra* Ray Tracer, is the *Chandra* PSF simulator which can be used to create images of the PSF. ChaRT is considered the best method to create a PSF at any off-axis angle and for any energy or spectrum because it uses same detailed models for mirror's physical and reflecting properties like those used for calibration. Unfortunately this method is not optimal for our survey because it uses a web-page interface to simulate one PSF at a time. We require a method which can be applied in automatically fashion on a large number of sources at different off-axis angles. Another way to create a PSF based on simulations is to to use MARX, which can simulate images of the PSF. Comparing to ChaRT, MARX uses simpler models for the telescope's mirror and therefore the PSFs created with MARX lack the details of ChaRT PSFs. In addition to methods based on simulations, one could create a PSF by using observed astrophysical sources which are known to be point like-sources such as stars, AGNs or quasars. This method, although good requires good knowledge about the physical properties of the source.

We have generated PSFs for each detected source using MARX simulator. The parameters needed for the simulation are: source type, source position on the sky and source energy, which can be an input source spectrum or a flat spectrum with energies between two limits given by the user. We have chosen to create the PSFs as sources with a flat spectral distribution, with an energy of 1keV. In cases where a source is detected in multiple observations and at different off-axis angles, an image of the PSF is simulated for each observation. These individual PSFs are then merged to create the PSF corresponding to the detected source. In the merging process, each individual PSF is weighted by the exposure time of the observation which the PSF has been created.

As we have already mentioned, a proper modelling of the PSF is crucial to distinguish between extended and point-like sources. Therefore, we would like to test if our modelled PSF created with MARX is a good approximation of the telescope's PSF. Images of known astrophysical point-like sources such as AGNs and stars represent the best approximation of *Chandra*'s PSF, under the assumption that the intrinsic properties of these source are well known. We have used a sample of AGNs detected in the COSMOS field from the catalogue published in Merloni et al. (2010), to compare their surface brightness distribution with that of PSFs simulated with MARX and ChaRT. Their catalogue contains a list of 89 AGNs which are all classified as broad-line AGNs based on the inspection of their optical spectra. COSMOS is a well studied field using multi-wavelength observations. COSMOS field has also been observed by *Chandra*, with ACIS-I. *Chandra* COSMOS field is an overlap of 49 individual observations which cover an area of about 1 deg^2 with an uniform exposure of about 50 ks. Since each AGN from the catalog is present in more than one individual observation, the same source will be detected at various off-axis angles. For each AGN and for each observation in which it has been detected, we have extracted an image centred on the source. This wil represent our observed PSF whose surface brightness distribution will be used to compare the distributions of PSFs simulated with ChaRT and MARX. Then we simulate a PSF using MARX and ChaRT for the corresponding off-axis angle and an energy of 1 keV. To improve the statistics, the images for PSFs with similar off-axis angle have been merged and surface brightness profiles has been extracted from each merged images. This assumes that all AGNs have similar properties, and therefore their surface brightness distribution will have the same shape when observed at a particular off-axis angle. Same procedure has been applied for simulated PSFs.

Figure 2.11 shows a qualitative comparison between PSFs obtained by all three above mentioned methods. PSFs obtained from simulations are plotted in green (MARX) and red (ChaRT), while the profile of observed AGN is plotted with black circles. Each panel shows the distributtion of all three types of PSFs for sources with off-axis angle in the interval mentioned in the top right corner. The dotted line marks radius at which the integrated number of counts represents 95% of the total counts in the PSF. This Figure shows that, in general, there is a good agreement between all three methods between the 95% EE radius at all off-axis angles. A perfect match between ChaRT and MARX PSFs is seen at all off-axis angles, with the exception of a small difference at off-axis angles smaller than 2 arcminutes, with MARX PSF being a little bit narrower than ChaRT PSF. If we look in more detail at the match between data and simulated PSFs, we can see that simulated PSFs matches the data well for sources at off-axis angles up to 8 arcminutes, beyond which there is less agreement.

The conclusion which can be drawn from this plot, although it is made only on a qualitative comparison, is that the PSF used for our survey, which we model using MARX, is a good representation of a point-like source for sources detected at small off-axis angles, up to about 8 arcminutes. Idealy, in the process of selecting potential clusters as extended sources when compared to the surface brightness distribution of the PSF, one would like to exclude sources detected at large off-axis angle. For our survey, this would have a double negative impact: firs we lose from survey area, leading to a lower number of detected sources and in the second place we can lose flux from our detected sources. This is because our fields on which we perform source searching are created by merging several individual images with similar but different pointing and therefore the same source can be detected at different off-axis angles in each individual observation.

2.3.3 Source detection

From the point of view of source searching algorithms, a source is defined as a flux enhancement above the background level. In X-ray astronomy, source detection is hindered by the low count statistics especially for the fainter extended sources for which separating the source flux from the background becomes more challenging. Different algorithms used for source detection are based on various assumptions about the background and source distribution. Most of them assume that the background flux is uniformly distributed while some of them make assumption about the intrinsic shape of the source which is often approximated to a Gaussian distribution.

In reality sources are not perfect Gaussians nor the background is constant and these deviations from the ideal case make impossible the existence of a perfect source searching algorithm. Therefore the performance of a detection method is affected by different factors like: the intrinsic properties of the source, the proximity to other sources, the uniformity of the background and in addition to this is the performance of the telescope used to observe them.

Clusters have different intrinsic properties which make their flux distribution depart from a perfect Gaussian: disturbed morphology due to mergers, cool cores, with peaked surface brightness and point sources embedded in their intracluster medium.

Although the uniformity of the background is a general valid assumption, variations in the level of the background might be present in an observation due to variations in the Galactic absorption or different particle background levels. This can lead to an overestimation of the background level

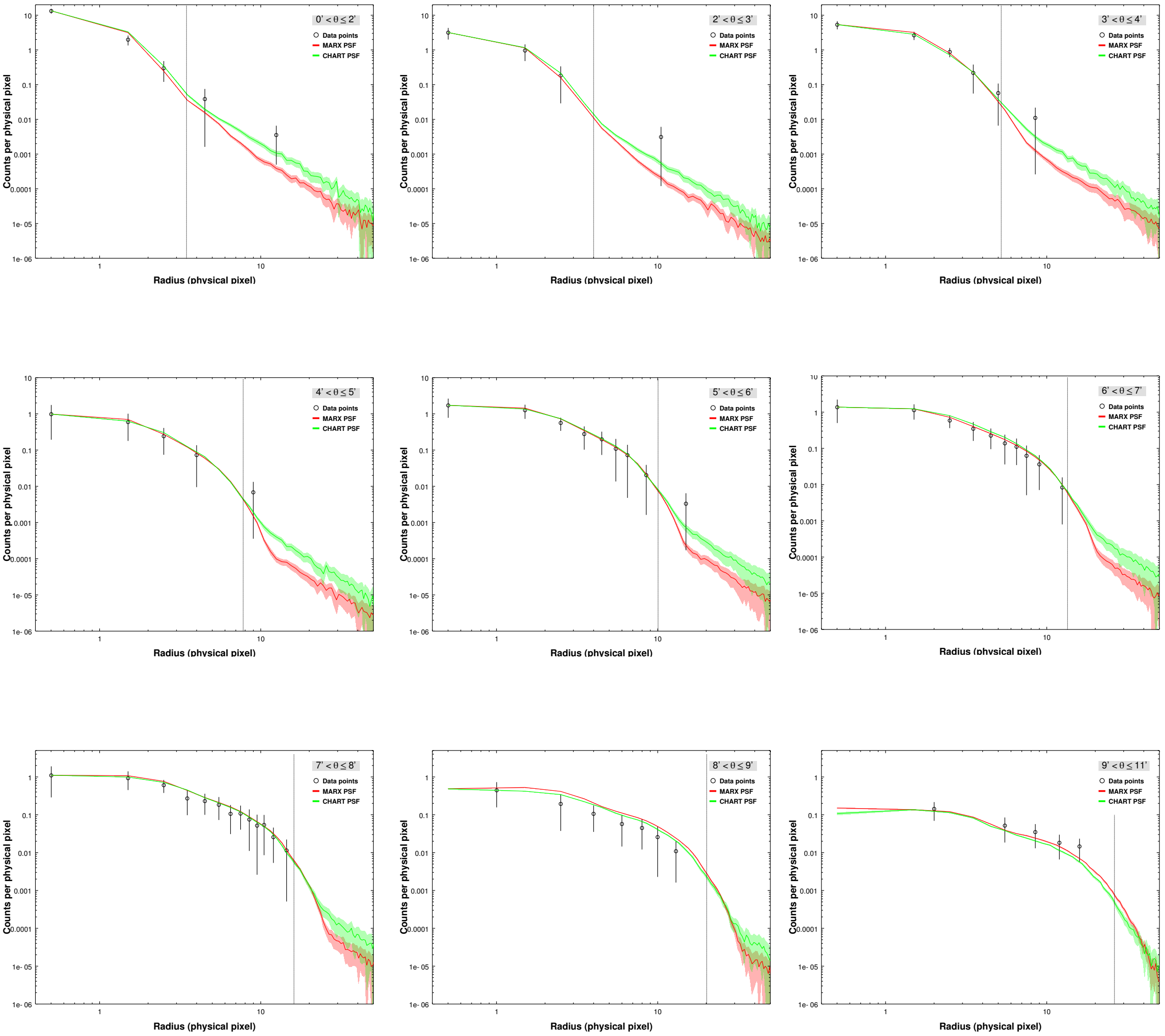

Figure 2.11: A qualitative comparison between different approximations to *Chandra* PSF obtained by simulations (ChaRT, MARX) or by using observed data of AGNs, which are approximations of point-like sources. PSFs corresponding to various off-axis angles have been created and the mean surface brightness profiles of the PSFs from increasing off-axis angle intervals is plotted in each bin. The off-axis angle interval, in arcminutes is showed in the top right legend panel. The vertical dotted line marks the radius at which the integrated number of counts represents 90% of the total counts in the PSF. Error bars on data points represent 1σ errors using Gehrels approximation (Gehrels 1986) for Poisson distribution. Shaded regions for MARX and ChaRT shows regions corresponding to 1σ errors.

and faint sources might not be detected. On the other hand an underestimate of the level of the background might lead to the detection of two closely spaced sources as a single one.

In X-ray astronomy, two source detection techniques are commonly used: one based on the wavelet decomposition algorithm (Freeman et al. 2002) and the other one the Voronoi tesselation and percolation algorithm (Ebeling & Wiedenmann 1993). Both algorithms are implemented in CIAO as the wavdetect and vtpdetect tools.

The **wavdetect** tool firstly transforms the original image by repeatedly convolving it with a Mexican Hat function with different scale sizes in order to identify source pixels. Then the significance of each potential source is calculated and the final catalogue list created. The effect of image smoothing with the wavelet function is to emphasize structures with Gaussian distribution and sizes similar to that of the wavelet kernel. Therefore running wavedtect with a small-scale kernels will lead to detection of point-like sources, while extended sources are detected by large scale kernels. The number and size of the kernels is chosen by the user. The background at each step is estimated iteratively from the whole image after eliminating the most significant sources detected at that particular scale until convergence is reached.

Wavdetect depends on PSF, exposure map, size and number of scales, significance threshold.

The **vtpdetect** tool exploits the property of the X-ray background to be Poisson distributed and identifies sources as significant deviations from the background cumulative flux distribution function.

To estimate the background, a Voronoi tesselation, which is a uniquely defined set of convex cells containing only one point is computed for the original photons. Because each cell in the tesselation is associated with one incoming photon, a flux estimation can be made by considering the inverse area distribution. The background is estimated by comparing this distribution to that of a random Poisson distribution expected for a real background.

A flux threshold for the global background is determined and using this value, a source list is created by the percolation algorithm. This algorithm, also named friends-of-friends starts at one position, and all pixels above the flux limit situated within a maximum distance from that position are considered part of one source. The process is repeated and at the next step the last added structures are the new starting point.

In the rest of this subchapter we give a comparison between the behaviour of wavdtect and vtpdetect on some particular test cases chosen to highlight advatanges and disatvanteges of each method. We test the performance of these two tools in fields dominated by points sources with a sparse spatial distribution, on fields which contain closely spaced point sources, extended sources or extended sources contaminated by other point sources. Based on these tests, we choose the detection tool for our survey and describe the source searching procedure adopted for CDGS.

Some of the important input parameters for vtpdetect (wavdetect) are: scale (scales) and limit (sigthresh). The scale (default value=1) parameter represent the the threshold used to separate between background flux and source flux. In wavdetect the default has two scales of 2 and 4 , which represent the size of the wavelet used to convolve the image. Limit and sigthresh have the same default value for both tools (default=10^{-6})

For each test we perform, the results obtained by running each detection tool with the default parameters are presented first. Both tools accept an exposure map as an input to allow for variations in exposure. We use a merged image of the field and exposure map. The result of the detection tool is a list of regions, represented by ellipses with sizes proportional to the standard deviation of the source distribution and the factor used to scale their sizes is given by the user.

- **Detection of point sources in uniform, uncrowded fields;** This represents the simplest case for any detection tool since field is not affected by variations in the background or the presence of other sources and the distribution of the source flux can be well approximated with a

Gaussian. We have tested the performance of both tools for the default input parameters. The results of this test is showed in Figure 2.12, in which sources detected by vtpdetect are encircle with red ellipses, while sources detected by wavdetect are marked with green ellipses. For a better illustration, we show an increased size for the ellipses which encircle the source region and which represent the output of the source detection tool. The Figure shows that for bright, isolated sources, both methods give very similar results. There are although some differences between these two methods. It can be seen that in some cases, two closely spaced sources are detected as a single source with vtpdetect, while wavdetect ‘sees‘ them correctly as two independent sources. This is because both methods are sensitive to the scale size used for detection, a feature which will be proved later in this section. Another thing to notice is that vtpdetect finds more sources at large off-axis angle, while the number of sources detected with wavdetect is larger at small off-axis angle. The lower number of sources detected by vtpdetect compared to wavdetect is due to a low threshold adopted for the minimum number of source counts required for a detected source to be considered a real detection. The default value is 10. We have tested the detection method with a lower threshold (5 counts) and found a better agreement with the number of low off-axis angle sources detected by wavdetect. The fact that wavdetect misses large off-axis angles is due to the scale sizes used for detection.

- **Source deblending**

  The ability to correctly identify two closely spaced sources as distinct sources (e.g. deblending) is an important feature of any source searching algorithm. This is because the flux distribution of each source departs significantly from Gaussianity in the presence of other close-by source. We have tested how well both algorithms are able to detect each source from a pair of close-by sources. Figure 2.13 shows the results of source searching on a part of a field which contains three close-by sources. Green ellipses in the top rows of panels

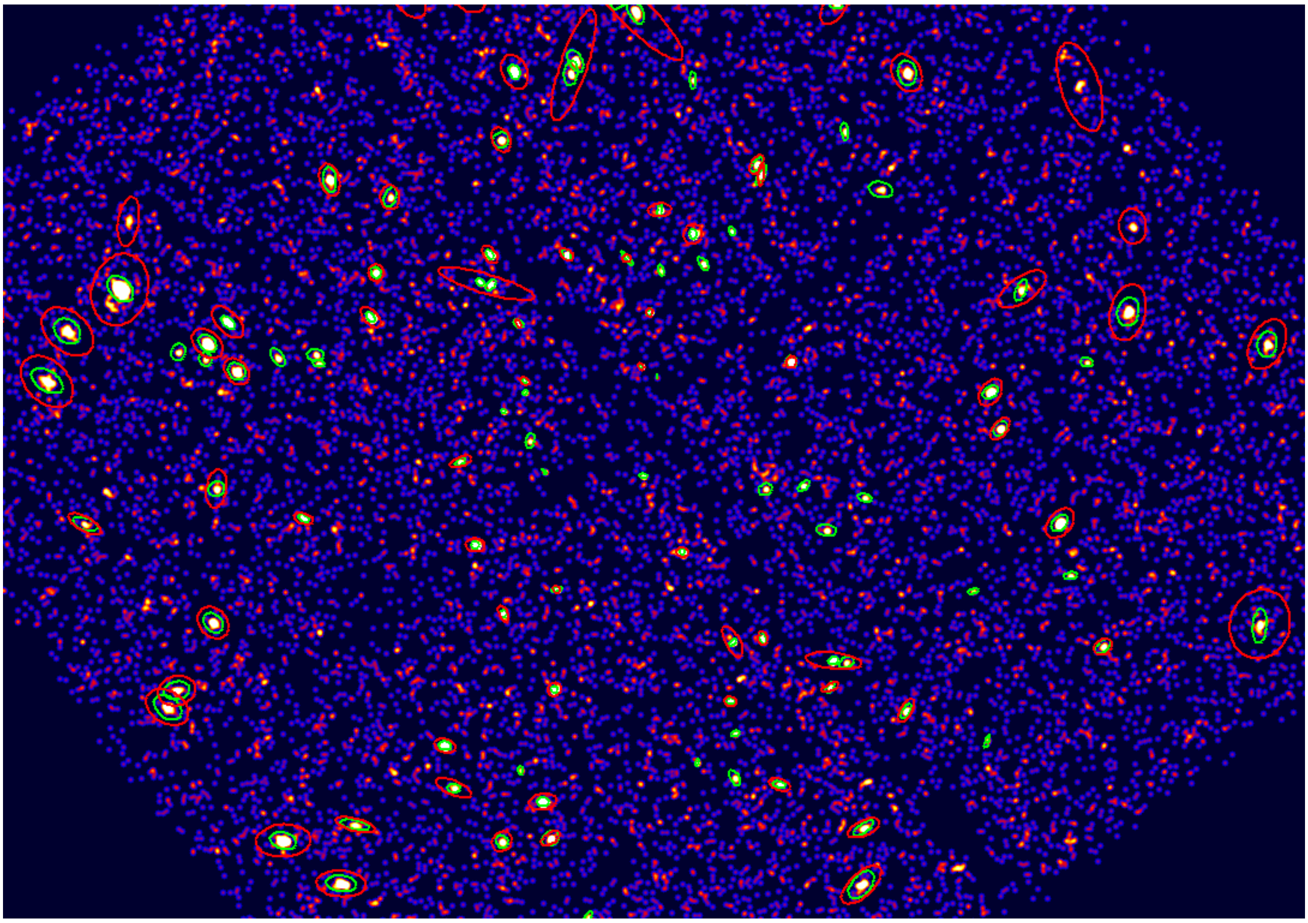

Figure 2.12: The result of source detection in the NGC752 field. Green ellipses shows the sources detected by wavdetect while red ellipses shows the result obtained from vtpdetect. In both cases, the size of the ellipse which should correspond to 3 sigma detection has been increased for display purposes.

shows the results obtain by using vtpdetect with default values for all parameters with the exception of scales. The results obtained from different scales are presented in each panel. Top left panel corresponds to a vtpdetect run with scale=1, middle one for a scale of 2.5 and right one for a scale of 9. It can be seen that for the default scale of 1, vtpdetect is not able to detect any of these three sources as an individual source. Once the scale is increased to a value of 2.5, one of the sources is detected as an individual source, while the other two are still detected as a one large sources. Only at a very large scale of 9, all three point sources are detected as three separated sources.

The bottom row of panels shows the results for wavdetect. Wavdetect has been run on three sets of scales: 2.0 4.0 in the left panel, 0.5 1.4 2.2 4.5 8 16 32 64 in the middle panel and 32 64 in the right hand side panel. In contrast to the results from vtpdetect, the image shows that wavdetect works better for the default case which includes only small scales and with the increase of the scale sizes, the tool tends to blend sources. The conclusion we can draw from this test is that for default parameters wavdetect is able to deblend closely-spaced point sources, while vtpdetect detects them as a single source. However, if proper scales are chosen, both methods give the same result. Therefore the way scales are chosen has an impact on the way point sources are detected: larger scales for vtpdetect will lead to deblending sources while larger scales for wavdetect will tend to blend sources.

- **Extended sources** We have seen that scale size chosen for detection tool has an impact in the way point sources are detected. We want to test how the scale size affects the detection of extended sources. Figure 2.14 shows the results obtained by running the two detection tools on a field which contains an extended source. Top row of panels shows the results obtained by vtpdetct and the bottom panels are those obtained by wavdetect. Vtpdetect has been run for three scales: 0.8, 1.0 and 2.5. Wavedtect has been run for the same scales as for the Deblending case. The behavior observed for the deblending test, is seen for extended

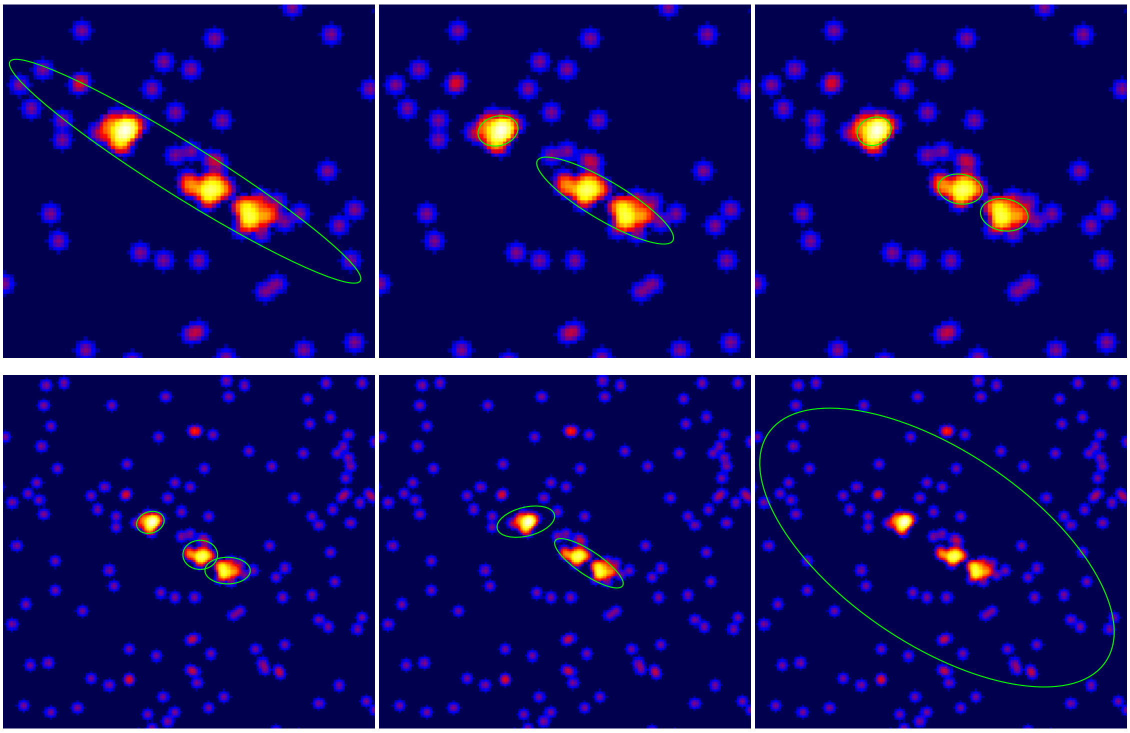

Figure 2.13: Example of the results obtained from vtpdetect (top row) and wavdetect (bottom row) for a field with closely-spaced point sources. Different scales have been used for each tool: 1, 2.5 and 9 (in the top left, middle and right panels) and 2.0 4.0 (bottom left), 0.5 1.4 2.2 4.5 8 16 32 64 (bottom middle) and 32 64 (bottom right).

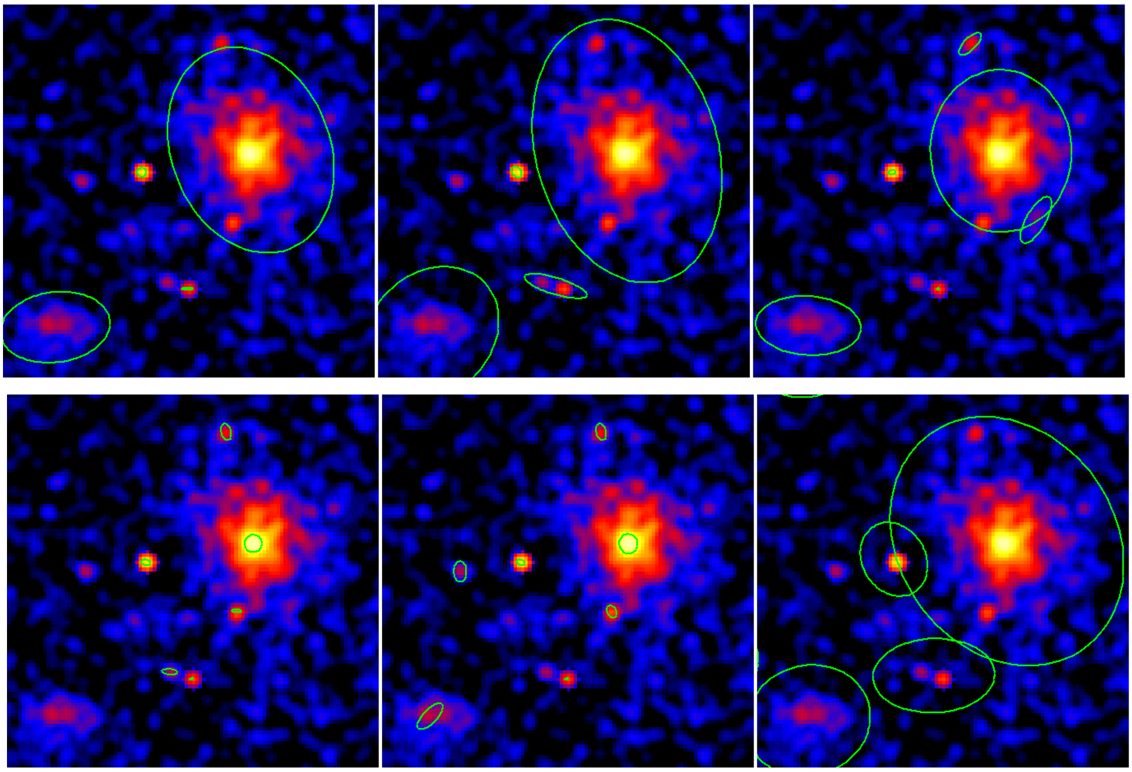

Figure 2.14: Example of the results obtained from vtpdetect (top row) and wavdetect (bottom row) for a field with extended source. Different scales have been used for each tool: 0.8, 1 and 2.5 (in the top left, middle and right panels) and 2.0 4.0 (bottom left), 0.5 1.4 2.2 4.5 8 16 32 64 (bottom middle) and 32 64 (bottom right).

sources as well: vtpdetect tends to deblend sources with increasing scale and become more sensitive to point-like sources, while wavdetect tends to blend sources with increasing scales and become more sensitive to extended sources. We can see that for wavdetect, small scales is not able to detect the extended source from the low left corner, which is picked up only when large scales are used.

- **Extended sources contaminated by point-like sources** The last test we make is the one in which an extended source is contaminated by the presence of a point-like source. This is presented in Figure 2.15. Scales used for vtpdetect are: 0.8, 1.0, 2.5 and 10. We can see

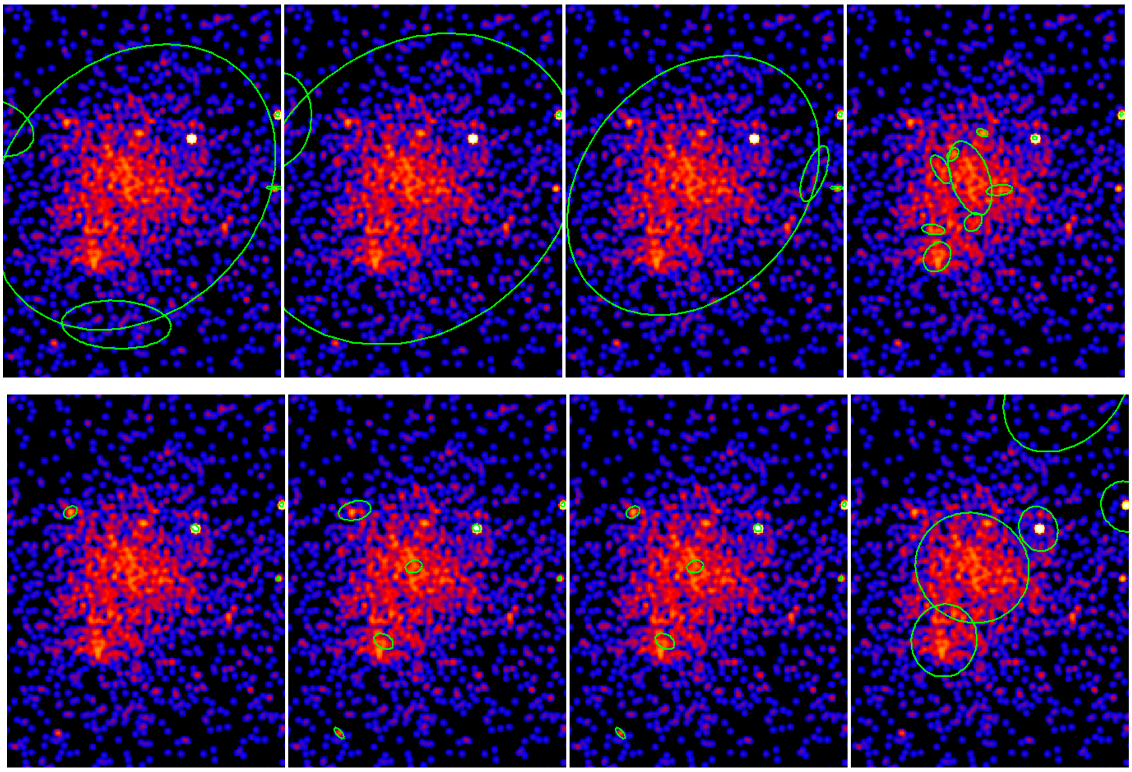

Figure 2.15: Example of the results obtained from vtpdetect (top row) and wavdetect (bottom row) for a field with an extended source contaminated by point sources. Different scales have been used for each tool: 0.8, 1.0, 2.5 and 10 for top row and 2 4, 0.5 1.4 2.2 4.5 8 16 32 64, 8 16 32 64 and 32 64 for bottom row.

that at smaller scales vtpdetect detects the cluster, but the contaminating point source is undetected unless a very large scale is used. In this case though, the cluster is not detected anymore. Wavdetect finds only point like sources at small scales and only at large scales it detects the cluster as well as the contaminating point source. Scaled used are, from left panel to righ one: 2.0 4.0, 0.5 1.4 2.2 4.5 8 16 32 64, 8 16 32 64 and 32 64.

- **Conclusions** We have seen from the tests we have described above that both wavdetect and vtpdetect are sensitive to the size of the scales used for detection. Since we have showed that none of them behave perfectly for all cases, the conclusion we draw is that the detection tool we adopt for our survey needs to be run on the same field several times, with a different scale each time. We have adopted vtpdetect as source detection tool for our survey since we have showed that this is more sensitive to extended sources. A more detailed description of how source searching is applied to create the source catalogue will be explained later in this chapter. Compared to wavdetect, vtpdetect is more sensitive to low surface brightness sources and irregular morphologies because it does not make any assumption about the size and shape of the source. For each individual field we have applied our source searching algorithm on the merged image filtered for the soft band (0.5-2.0 keV). Since our aim is to study X-ray properties of groups, we impose a low threshold limit of 100 counts for our source candidates. This lower limit will allow extraction of surface brightness profiles and temperature spectra.

Source detection algorithm used for CDGS As it has been showed in previous paragraph, each source searching algorithm has its own advantages and disadvantages and neither wavdetect nor vtpdetect can give satisfactory results for a single set of input parameters applied to a large variety of fields. Therefore one solution would be to combine the source catalogues obtained from different runs of the same algorithm with various input parameters. We have chosen vtpdetect as a detection method. We have performed three runs of vtpdetect on soft images of each field, each run with different input parameters. In the first run we have used a scale of 0.8 and a significance of 10^{-9}. This scale is optimum for the detection of extended sources. For the second run we used a scale of 2.5 and a significance of 10^{-7}. The scale used is ideal for the detection of point sources. The increased significance chosen compared to the first run is to avoid spurious point sources. The last run uses a scale of 5 and a significance of 10^{-7}. This very high scale is used to detect point sources which are embedded in diffuse extended emission. These would represent the highest peaks in the flux distribution. While this run picks these kind of sources, it misses some obvious point sources which are detected in the second run.

For each source detected by running vtpdetect with a scale of 0.8 each of the following three situations is tested. If the source region does not include another region or is part of a larger source, then the detected source region is added to the final source catalogue. This is the simplest case of an isolated source with a regular or close to regular shape and no other embedded sources. In the second case, if the detected region includes the region of another source, then the region is included in the final catalogue. This might be an extended source which includes substructure or other point sources. Lastly, if the source is included in another detected source, then we have to investigate if this is a spurious detection or it is an embedded point source. Therefore we checked if a match between this source and a source detected by vtpdetect at scales of 2.5 or 50 can be found. If a match exists, then the source is considered contaminating point source and is added to the final catalogue. Otherwise, the source is not included in the final source catalogue and we reject it as being a spurious detection.

2.3.4 Source extension

If groups and clusters are observed in X-ray, the emission from hot gas within groups/clusters of galaxies is detected as a spatially extended source when compared to the telescope's PSF, which is a good representation of a point-like source. This is the key property used by X-ray surveys to detect groups/clusters. Different algorithms used in the literature to classify X-ray sources as extended has been presented in the Introduction Chapter.

The algorithm adopted for our extension test has been presented in Slack & Ponman (2014) and uses a Bayesian approach to decide which of the following two models represents a better approximation to the observed surface brightness profile: a single beta model (see 2.6.3) which is often used to model the X-ray emission of clusters of galaxies or a very steep beta model which is considered a good representation of a point source. The source extension test based on this algorithm uses an image of the source and the PSF, a list of sources which are tested for extension, an exposure map and optionally a background map.

Firstly, the point source model is fitted to the data. The point source is approximated by a very steep beta profile, with a small core radius of 0.1 pixels and a steep slope of 1.4. Only the model normalization and the position of the centre of the source is allowed to fit. The position of the X-ray centre is allowed to vary up to 3 pixels in each dimension. After the point source model has been fit, the beta model is fitted to the data, by letting core radius and beta free. All the fitting procedure is done using Cash statistic (Cash 1979).

The key part of the extension test is to answer the question: which of the two models represents a better approximation of the data?

In order to do this, a Bayesian analysis has been performed to compare the two models. For any two models, the Bayes factor allows easy comparison between them. The Bayes factor (B_x) is given by:

$$B_x = \frac{P(d|m_\beta)}{P(d|m_{PSF)}}$$

where $P(d|m_\beta)$ is the marginal likelihood of the m_β model (in our case the beta model for source), and $P(d|m_{PSF})$ is the marginal likelihood of the PSF model (Slack & Ponman 2014). A Cash statistics is calculated for different set of values for the fitted parameters corresponding to the point source and extended source model, keeping only the position of the source frozen at the best fitted value. For these sets of parameters, a marginal likelihood is calculated for each model and integrated over the likelihoods in the parameter space. The extent statistics is given by the ratio between the extend marginal likelihood and the point marginal likelihood. Similarly, an existence statistics is obtained by dividing the source marginal likelihood by the background marginal likelihood.

Slack & Ponman (2014) has used simulations to choose a threshold value for the B_x parameter. They have simulated 180 sets of images containing only clusters and the same number containing only point sources. Four different exposure times have been used for the simulations: 10, 20, 50 and 100 ks. The results of their simulations are summarized in Figure 2.16 which shows the cumulative distribution of detected clusters (blue lines) and point sources (red lines) as a function of the extent statistics ($\log(\mathrm{B_x})$). On the figure, dark shading represents regions with an extent statistics less than unity, while the light shading covers the region below the adopted threshold for the statistics. It can be seen that the cumulative fraction of systems below a particular threshold decreases steeply for simulated point sources, while the cluster drop is not as steep. Therefore, a threshold of $\log(\mathrm{B_x})$=2, for a 10 ks observation will lead to a 98.5% point source rejection rate and a 76% cluster acceptance rate. Another thing to note is that for the adopted threshold, the fraction of point sources classified as extended increases with exposure time, from 1.5% at 10 ks to about 5% at 100 ks. On the other hand, for clusters, the fraction of clusters classified as point sources decreases from 24% to about 14%. Similarly, for the existence statistics, a threshold ($\mathrm{B_S} = 4$) is chosen.

The ability to distinguish between point sources and extended ones is crucial for any cluster surveys. The extension test depends not only on the exposure time of the observation but also on the other factors like: signal to noise ratio, the morphology of the cluster, how PSF is modelled.

We had applied the extension test on all detected sources using an extent threshold of 2. Images of the PSF corresponding to the position of each detected source has been created using MARX simulations (see 2.3.2). We did not use a background map during the beta model fitting, but we have chosen to treat the background uniform and we approximated it's amplitude as the mean number of counts from the observed image after removing all detected sources.

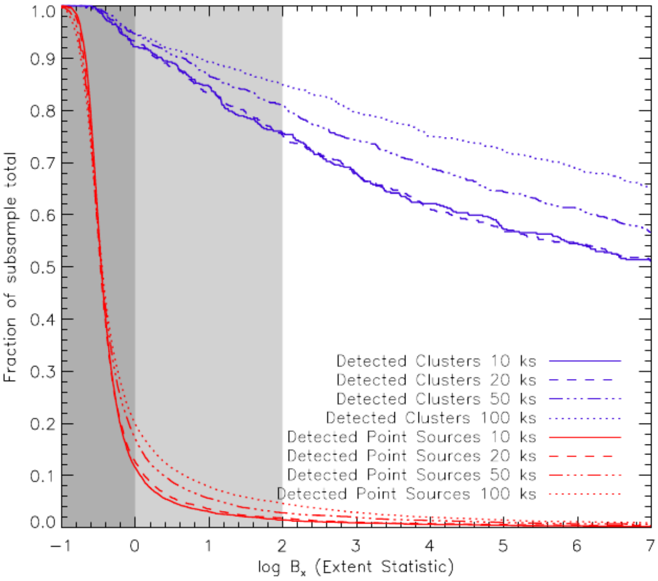

Figure 2.16: Cumulative fraction of sources above a given value of extension statistics. Blue and red lines represents the simulated clusters and point sources, respectively. Different line styles corresponds to different exposure times of the simulations. Dark shading covers the region below an extension statistics of unity, while light shading covers the region below the chosen B_x threshold. Figure from: Slack & Ponman (2014)

2.4 Catalogue of extended sources

A list of all sources detected with at least 100 source counts and characterized as extended by our extension test is given in Table 2.3. A source is extended if extension statistic calculated as described in Section 2.3.3 is greater than 2. The Table lists the source ID, the sky coordinates of the source the detection and extent statistic, source type, which can be a target or serendipitous and the field in which the source was detected.

From Tabel 2.3 we can see that the majority of sources are serendipitous and the largest contribution to the number of serendipitous sources comes from deep fields like COSMOS, CDFS, CDFN or AEGIS. Out of 162 extended sources, only 28 represent the target of the observation.

Table 2.3: List of all 162 CDGS cluster candidates. These are detected sources with at least 100 counts and with an extension statistic greater than 2. Columns in table represent: (1) source ID; (2),(3) Source Right Ascension and Declination (J2000); (4) Number of net source counts in the 0.5-2.0 keV band; (5),(6) Detection and statistics calculated as explained in Section 2.3.3; (7) Source type, which can be the target of the observation (t) or serendipitous (s)

CDGS ID	Ra (deg)	Dec (deg)	Counts	Detection	Extension	Type	Field
CDGSJ0024.7-7159	6.19965	-71.98887	826	208.6	92.7	s	47TUC
CDGSJ0024.8-1228	6.20723	-12.47657	230	119.1	19.8	s	MACS0025.4-1222
CDGSJ0025.5-1222	6.38849	-12.37811	11722	1000.0	1000.0	t	MACS0025.4-1222
CDGSJ0144.8-0432	26.20925	-4.54645	430	110.5	198.7	s	XMM1HR
CDGSJ0157.4+3756	29.35337	37.93898	198	70.0	56.8	s	NGC752
CDGSJ0159.8-0849	29.956828	-8.8329253	20837	1000.0	1000.0	t	MACS0159
CDGSJ0159.8-0855	29.96613	-8.91857	485	177.9	174.4	s	MACS0159
CDGSJ0200.2-0840	30.05335	-8.68106	3316	1000.0	11.1	s	MACS0159
CDGSJ0204.8-0456	31.2114	-4.93858	396	1000.0	9.1	s	Lala_Cetus_Field
CDGSJ0205.1-0501	31.28274	-5.0324	233	1000.0	3.2	s	Lala_Cetus_Field
CDGSJ0310.2-2036	47.55024	-20.60981	1514	1000.0	1000.0	s	NGC1232
CDGSJ033.7-4317	8.4437979	-43.291263	873	1000.0	1000.0	s	ELAIS_S1
CDGSJ034.4-4319	8.6207667	-43.319042	1866	1000.0	1000.0	s	ELAIS_S1

CDGSJ0331.3-2744	52.83176	-27.7433	108	68.5	7.5	s	CDFS
CDGSJ0331.4-2752	52.85365	-27.86896	218	188.7	6.3	s	CDFS
CDGSJ0331.7-2748	52.94894	-27.80804	399	193.7	10.5	s	CDFS
CDGSJ0331.8-2746	52.95598	-27.77632	541	1000.0	2.9	s	CDFS
CDGSJ0331.8-2749	52.96053	-27.826	687	79.4	51.9	s	CDFS
CDGSJ0332.0-2741	53.00613	-27.69422	858	1000.0	9.2	s	CDFS
CDGSJ0332.0-2746	53.0059	-27.77983	604	1000.0	9.3	s	CDFS
CDGSJ0332.0-2754	53.02453	-27.9137	288	119.5	58.6	s	CDFS
CDGSJ0332.1-2732	53.0255	-27.54391	193	226.9	12.0	s	CDFS
CDGSJ0332.1-2742	53.03338	-27.71107	1136	244.3	250.2	s	CDFS
CDGSJ0332.3-2739	53.09517	-27.66026	230	104.6	2.2	s	CDFS
CDGSJ0332.3-2747	53.07526	-27.78865	118	72.8	18.3	s	CDFS
CDGSJ0332.3-2754	53.08068	-27.90161	850	136.3	58.4	s	CDFS
CDGSJ0332.3-2758	53.09403	-27.96782	120	56.4	6.9	s	CDFS
CDGSJ0332.4-2744	53.12493	-27.73466	342	270.8	29.4	s	CDFS
CDGSJ0332.5-2739	53.14319	-27.65354	796	1000.0	47.5	s	CDFS
CDGSJ0332.7-2738	53.17741	-27.63782	322	274.3	26.9	s	CDFS
CDGSJ0332.7-2740	53.18967	-27.68237	398	64.5	29.5	s	CDFS
CDGSJ0332.7-2742	53.19489	-27.70344	562	1000.0	96.3	s	CDFS
CDGSJ0332.7-2757	53.17506	-27.95067	1403	1000.0	5.3	s	CDFS
CDGSJ0332.9-2748	53.23467	-27.80931	162	54.8	14.0	s	CDFS
CDGSJ0333.1-2748	53.29248	-27.81176	1403	1000.0	2.8	s	CDFS
CDGSJ0333.3-2747	53.33663	-27.79851	150	185.0	126.4	s	CDFS
CDGSJ0405.4-4100	61.35219	-41.00505	1461	1000.0	1000.0	t	cl0405-4100
CDGSJ0405.5-4058	61.39266	-40.98251	149	77.9	61.9	s	cl0405-4100
CDGSJ0431.4+1816	67.85462	18.27123	22548	1000.0	24.1	s	LYNDS1551
CDGSJ0431.5+1808	67.89202	18.13451	108	210.6	9.7	s	LYNDS1551
CDGSJ0431.6+1813	67.91698	18.23241	4063	1000.0	10.2	s	LYNDS1551
CDGSJ0453.6+0252	73.40989	2.87452	344	111.1	36.5	s	Abell520
CDGSJ0454.3+0249	73.58752	2.81753	2053	1000.0	2.0	s	Abell520
CDGSJ0716.7+3739	109.18376	37.66584	241	21.5	20.2	s	MACSJ0717.5+3745
CDGSJ0717.5+3745	109.3804	37.75535	20841	1000.0	1000.0	t	MACSJ0717.5+3745
CDGSJ0717.8+3742	109.47256	37.7026	282	119.9	91.8	s	MACSJ0717.5+3745
CDGSJ0848.6+4453	132.15218	44.89668	145	35.2	34.2	t	CL0848.6+4453
CDGSJ0848.7+4456	132.19945	44.93707	1014	1000.0	1000.0	t	CL0848.6+4453
CDGSJ0848.9+4451	132.24341	44.86507	327	133.8	143.9	t	CL0848.6+4453
CDGSJ0909.9+5429	137.483	54.48799	62672	1000.0	74.6	s	RXJ0910+5422
CDGSJ0910.1+5418	137.53642	54.31626	106	149.8	112.8	s	RXJ0910+5422

CDGSJ0910.7+5422	137.68701	54.36833	314	123.0	114.2	t	RXJ0910+5422
CDGSJ0913.7+4056	138.43929	40.94134	13215	1000.0	1000.0	t	IRAS09104+4109
CDGSJ0958.9+0214	149.74396	2.24975	956	1000.0	45.4	s	COSMOS
CDGSJ0959.3+0240	149.83858	2.67495	272	1000.0	2.4	s	COSMOS
CDGSJ0959.4+0146	149.85589	1.77027	942	139.2	236.6	s	COSMOS
CDGSJ0959.6+0219	149.91985	2.32746	784	1000.0	1000.0	s	COSMOS
CDGSJ0959.6+0231	149.92041	2.52074	1244	1000.0	2.4	s	COSMOS
CDGSJ1000.4+0158	150.10537	1.98105	3966	1000.0	2.1	s	COSMOS
CDGSJ1000.4+0231	150.10274	2.53004	549	186.2	116.8	s	COSMOS
CDGSJ1000.5+0147	150.132	1.79925	325	1000.0	5.4	s	COSMOS
CDGSJ1000.7+0139	150.19699	1.66044	2267	1000.0	1000.0	s	COSMOS
CDGSJ1000.7+0145	150.17922	1.76643	372	98.2	103.4	s	COSMOS
CDGSJ1000.7+0149	150.19989	1.82663	476	1000.0	9.2	s	COSMOS
CDGSJ1000.8+0205	150.20802	2.08335	1248	1000.0	5.5	s	COSMOS
CDGSJ1000.8+0217	150.20636	2.28552	321	1000.0	8.1	s	COSMOS
CDGSJ1001.6+0225	150.42374	2.42925	1510	1000.0	1000.0	s	COSMOS
CDGSJ1002.0+0213	150.50514	2.22578	621	186.2	116.8	s	COSMOS
CDGSJ1033.7+5749	158.43773	57.81968	460	1000.0	151.4	s	LH-NW-4
CDGSJ1034.1+5803	158.54239	58.06318	312	1000.0	10.2	s	LH-NW-4
CDGSJ1034.9+5730	158.74939	57.50902	471	1000.0	117.4	s	LH-NW-4
CDGSJ1035.2+5750	158.80566	57.83778	204	142.7	114.1	s	LH-NW-4
CDGSJ1035.3+5750	158.84952	57.84729	156	77.4	62.5	s	LH-NW-4
CDGSJ1035.5+5735	158.88389	57.59573	244	77.9	34.9	s	LH-NW-4
CDGSJ1047.6+5907	161.92058	59.117604	765	261.6	266.5	s	SWIRE_LOCKMAN
CDGSJ1113.0-2615	168.2725	-26.26068	1104	1000.0	1000.0	t	CLJ1113.1-2615
CDGSJ1119.9-1202	169.98152	-12.04225	659	1000.0	1000.0	t	SC1120-1202
CDGSJ1120.1-1205	170.02963	-12.08989	354	131.7	152.5	t	SC1120-1202
CDGSJ1120.1-1208	170.03964	-12.1449	481	1000.0	1000.0	t	SC1120-1202
CDGSJ1120.2-1158	170.05626	-11.98025	104	17.5	6.9	t	SC1120-1202
CDGSJ1120.5+2335	170.13941	23.5994	322	158.7	108.9	t	V1121+2327
CDGSJ1120.9+2326	170.23747	23.44226	1953	1000.0	1000.0	t	V1121+2327
CDGSJ1140.3+6608	175.09318	66.13776	3759	1000.0	1000.0	t	MS1137.5+6625
CDGSJ1154.7+2329	178.69521	23.48769	283	1000.0	4.4	s	A1413
CDGSJ1155.0+2331	178.76732	23.52158	345	1000.0	3.9	s	A1413
CDGSJ1155.5+2327	178.89963	23.45635	2161	1000.0	2.2	s	A1413
CDGSJ1221.4+4918	185.35494	49.30916	2998	1000.0	1000.0	t	V1221+4918
CDGSJ1235.6+6216	188.91027	62.27879	14145	1000.0	18.8	s	CDFN
CDGSJ1235.8+6215	188.95056	62.25378	128	51.4	32.3	s	CDFN

CDGSJ1235.9+6216	188.98423	62.27152	184	160.5	7.7	s	CDFN
CDGSJ1236.0+6220	189.02106	62.33708	186	1000.0	33.3	s	CDFN
CDGSJ1236.3+6215	189.07996	62.26444	227	31.5	28.7	s	CDFN
CDGSJ1236.5+6220	189.13708	62.34096	434	1000.0	8.4	s	CDFN
CDGSJ1236.8+6228	189.21812	62.46867	2144	1000.0	14.4	s	CDFN
CDGSJ1237.1+6208	189.28992	62.14424	107	59.2	9.6	s	CDFN
CDGSJ1237.9+6214	189.49188	62.24876	184	66.5	14.0	s	CDFN
CDGSJ1237.9+6215	189.48197	62.25312	264	127.0	97.3	s	CDFN
CDGSJ1238.1+6212	189.52748	62.21192	146	86.4	48.4	s	CDFN
CDGSJ1252.5-2925	193.14291	-29.41758	608	206.4	88.0	s	RDCS1252-29
CDGSJ1252.9-2927	193.22845	-29.45474	855	1000.0	1000.0	t	RDCS1252-29
CDGSJ1310.1-0309	197.54987	-3.1615	307	144.2	113.1	s	MACS1311.0-0311
CDGSJ1311.0-0310	197.75775	-3.177625	10775	1000.0	1000.0	t	MACS1311.0-0311
CDGSJ1317.3+2911	199.33881	29.18864	332	148.9	169.6	t	RXJ1317.4+2911
CDGSJ1400.7+0249	210.17986	2.81856	148	146.6	37.2	s	Abell1835
CDGSJ1401.2+0245	210.31714	2.75371	102	254.5	2.6	s	Abell1835
CDGSJ1411.3+5212	212.83748	52.20433	134	44.5	44.8	s	3C295
CDGSJ1411.6+5218	212.90229	52.31348	8938	1000.0	1000.0	t	3C295
CDGSJ1415.1+3612	213.79599	36.20134	1256	1000.0	1000.0	t	CLJ1415.1+3612
CDGSJ1415.3+3610	213.83316	36.17355	120	62.5	68.9	s	CLJ1415.1+3612
CDGSJ1415.3+5220	213.83484	52.34605	275	167.1	46.2	s	EGS6
CDGSJ1416.2+5206	214.06948	52.10036	309	1000.0	273.3	s	EGS7
CDGSJ1416.4+5227	214.11797	52.45215	150	77.8	40.5	s	EGS6
CDGSJ1417.3+5218	214.34016	52.30846	181	196.2	7.3	s	EGS6
CDGSJ1417.3+5235	214.33613	52.59477	133	39.2	16.6	s	EGS5
CDGSJ1417.5+5232	214.37745	52.54124	293	1000.0	84.1	s	EGS5
CDGSJ1417.5+5238	214.38581	52.63849	536	1000.0	8.6	s	EGS5
CDGSJ1417.8+5234	214.47327	52.58095	189	43.8	29.8	s	EGS5
CDGSJ1417.8+5241	214.45009	52.69536	616	1000.0	1000.0	s	EGS5
CDGSJ1417.9+5245	214.49884	52.76665	235	151.7	8.4	s	EGS4
CDGSJ1418.2+5245	214.55343	52.75969	313	295.9	3.2	s	EGS4
CDGSJ1419.1+5259	214.78213	52.99729	51	20.0	4.7	s	EGS3
CDGSJ1420.0+5306	215.00476	53.11234	238	53.8	25.4	s	EGS3
CDGSJ1420.5+5250	215.13649	52.83646	116	104.6	19.3	s	EGS3
CDGSJ1420.5+5308	215.13708	53.13881	517	122.7	60.3	s	EGS3
CDGSJ1446.6+0920	221.67197	9.33669	2674	1000.0	1000.0	s	CNOC1447+09
CDGSJ1448.8+0854	222.2233	8.90051	191	74.0	101.0	s	DaddiField1
CDGSJ1450.1+0904	222.53779	9.07669	107	50.5	38.9	s	DaddiField1

CDGSJ1450.4+5813	222.6051	58.2219	303	125.3	140.6	s	Abell1995
CDGSJ1452.9+5802	223.24437	58.04983	9947	1000.0	1000.0	t	Abell1995
CDGSJ1452.9+5810	223.23601	58.18024	274	63.9	62.0	s	Abell1995
CDGSJ1453.0+5803	223.2742	58.05255	145	1000.0	2.0	s	Abell1995
CDGSJ1539.8+6606	234.95263	66.10981	257	116.5	102.8	s	A2125
CDGSJ1539.8+6610	234.95884	66.17221	472	124.0	179.4	s	A2125
CDGSJ1540.2+6610	235.07043	66.177681	273	59.7	48.1	s	A2125
CDGSJ1541.1+6616	235.29018	66.268994	6800	1000.0	1000.0	t	A2125
CDGSJ1541.2+6626	235.30433	66.44255	1178	1000.0	1000.0	s	A2125
CDGSJ1636.5+4056	249.12693	40.94775	148	1000.0	15.7	t	Elais_N2
CDGSJ1636.6+4107	249.15659	41.13025	192	98.1	103.8	s	Elais_N2
CDGSJ1700.6+6412	255.1747	64.215616	14501	1000.0	1000.0	s	HS1700+643
CDGSJ1701.0+6412	255.25264	64.20253	1238	1000.0	2.0	s	HS1700+643
CDGSJ1701.3+6414	255.34696	64.234245	11003	1000.0	1000.0	t	HS1700+643
CDGSJ1702.1+6412	255.5373	64.20566	138	135.7	12.8	s	HS1700+643
CDGSJ1930.9-2632	292.7431	-26.54558	268	227.5	57.1	s	MACSJ1931.8-2634
CDGSJ1931.0-2638	292.75906	-26.64017	136	251.6	34.7	s	MACSJ1931.8-2634
CDGSJ1931.8-2634	292.95665	-26.57598	40747	1000.0	1000.0	t	MACSJ1931.8-2634
CDGSJ2009.2-4826	302.303	-48.4454	4850	1000.0	2.0	s	NGC6868
CDGSJ2055.8-0452	313.969	-4.86725	2512	1000.0	50.1	s	MS2053.7-0449
CDGSJ2056.2-0441	314.07103	-4.69887	143	164.1	58.7	s	MS2053.7-0449
CDGSJ2056.3-0437	314.08778	-4.63001	1803	1000.0	1000.0	t	MS2053.7-0449
CDGSJ2150.3-0551	327.59381	-5.85243	4646	1000.0	4.4	s	CNOC2150-05
CDGSJ2150.6-0541	327.67156	-5.68453	603	195.4	186.8	s	CNOC2150-05
CDGSJ2150.6-0548	327.67231	-5.81633	442	1000.0	3.0	s	CNOC2150-05
CDGSJ2150.8-0553	327.72381	-5.88827	1355	1000.0	2.7	s	CNOC2150-05
CDGSJ2217.7+0017	334.43468	0.29045	377	52.1	26.9	s	SSA22
CDGSJ2217.8+0011	334.46383	0.19622	457	1000.0	6.2	s	SSA22
CDGSJ2302.7+0843	345.69947	8.73157	1366	1000.0	1000.0	t	H230230
CDGSJ2302.8+0841	345.71766	8.6923	465	1000.0	1000.0	s	H230230
CDGSJ2318.5+0034	349.62842	0.56756	1709	1000.0	1000.0	t	RCS2318+0034
CDGSJ2341.1-5119	355.29826	-51.32847	1887	1000.0	1000.0	t	SPT-CL2341-5119
CDGSJ329.6-211	52.421933	-2.1952703	13900	1000.0	1000.0	t	MACSJ0329.6-0211

2.5 Optical properties

2.5.1 Redshift

CDGS is an X-ray survey for which a spectroscopic follow-up is not available yet. Optical information for our extended sources is crucial for determining the nature of the source. Therefore, in the absence of a optical follow-up, the only available source for redshifts is the literature. We have performed a literature search to obtain spectroscopic or photometric redshifts for systems in our sample. A fraction of 38% of sample is represented by systems which were previously identified as groups or clusters and have an available spectroscopic or photometric redshift. In the Table 3.1, which represents the list of optically confirmed clusters, we give the redshift found for each systems together with its reference. In addition to this we give the number of member galaxies used to estimate the redshift if this is available in the cited result.

2.6 X-ray properties of selected sample

For each cluster candidate in our sample with available redshift, we derived a set of X-ray properties used to characterize the thermal state (temperature), spatial distribution (surface brightness profiles, R_{500}) and dynamical state (centroid shift) of its intracluster medium. We use these properties to investigate the evolution of groups and compare evolutionary trends between systems within different mass ranges. Knowledge of the state of the intracluster gas is complemented by information obtained from other wavelengths imaging, especially optical. Optical redshifts are crucial to confirm the existance of a cluster while optical imaging gives information about system members and their interaction with the surrounding intracluster medium.

We have performed spectral and spatial analysis for all systems in our sample in order to characterize their thermal and spatial properties. Using estimated temperatures we have calculated a characteristic radius for each system (R_{500}). A list of all derived properties is presented in Chapter 2.8. In the process of estimating all X-ray properties, the CIAO (version 4.4) and CALDB (version 5.5) have been used. In addition, all model fitting has been done using SHERPA, which is the CIAO modelling and fitting application.

2.6.1 $\mathbf{R_{500}}$

R_{500}, the radius enclosing a mean density of 500 times the critical density at the system's redshift, is estimated iteratively using the observed relation between radius and temperature derived by Sun et al. (2009) for a sample of 57 low redshift groups and clusters of galaxies:

$$hE(z)R_{500} = 0.602\left(\frac{T_{500}}{3\mathrm{keV}}\right)^{0.53} , \tag{2.6}$$

where the evolution factor is

$$E(z) = \sqrt{\Omega_M(1+z)^3 + \Omega_\Lambda} , \tag{2.7}$$

with $h = 0.7$ for our cosmology, z is the system redshift, and T_{500} the gas temperature within R_{500}. Sun et al. (2009) evaluate T_{500} by creating a three-dimensional temperature profile and integrating it between $0.15R_{500}$ and R_{500}. They exclude the inner region of the system in order to remove the contribution of a CC or a central AGN which would bias the mean temperature towards lower or higher (respectively) values. In our case we lack the data quality required to create a temperature profile, so our T_{500} is derived by fitting a spectrum extracted from within a circle of radius R_{500}, and is therefore the projected mean temperature within R_{500}, including the central region. The only case in which we exclude a central region is when we find evidence for the existence of an X-ray AGN, which can be detected as a point like source in the hard band (2.0-7.0 keV) image of the system. In that situation, we remove data within a circle enclosing 95% of the counts from a point spread function at the position of the AGN. Since we include the central region in our spectrum, the contribution from a CC, if it is present, will bias our temperature downwards. However, the magnitude of this bias has been shown to be at the 4-5% level for both groups and clusters (Osmond & Ponman 2004; Pratt et al. 2009), which is much smaller that our statistical errors of $\sim$20%.

Evaluation of R_{500} involves an iterative procedure. A first estimate of T_{500} is derived by fitting a spectrum extracted from a region equivalent to the source detection region. This temperature is used to calculate R_{500} which provides the extraction radius for a new spectrum, from which we derive a new temperature. The process is then repeated until convergence.

2.6.2 X-ray estimated gas temperatures

To obtain the mean temperature of the gas within R_{500} for each system in the sample, we have fitted the X-ray spectrum extracted within a circular region with radius equal to R_{500} centred on the source position with a model formed of two main components: one component to account for the source contribution to the whole spectrum and the other one for the background contribution. We decide on modelling the background emission instead of subtracting it because it allows us to use Cash statistics (Cash 1979) in our fitting process, which has been shown to be a less biased statistics than χ^2 Humphrey et al. (2009). Cash statistics can be applied only to Poisson distributed data, condition which is not satisfied in the case of background subtracted data due to the possible negative value for the number of counts obtained as a result of background subtraction.

The background X-ray emission and its origin has been the object of several studies using *ROSAT*, *XMM-Newton* and *Chandra* observatory. It has been showed that the background emission is not due to a single source but it represents the added contribution of several components: an extragalactic, galactic, particle and instrumental component.

The extragalactic background is highly isotropic on large angular scale (Markevitch et al. 2003). As its name suggests, its origin is the integrated emission from unresolved extragalactic X-ray sources, with main contribution thought to be from absorbed and unabsorbed AGNs (Gilli et al. 2007). The shape and normalization of the extragalactic background has been found to be very stable and it can be modelled by a power law with a spectral index of 1.41 (De Luca & Molendi 2004), 1.46 (Chen et al. 1997) and 1.5 (Hickox & Markevitch 2006).

In contrast to the extragalactic background which is uniform, the galactic background presents spectral and spatial variations. It's dominating flux is in the soft part of the spectrum, at energies of about 1 keV and its origin and best model to characterize it is still a subject of research. Three sources that contribute to the galactic background emission are: the X-ray emission from the hot gas within the Galactic Halo (Snowden et al. 1998; Henley et al. 2010), Galactic disk (Snowden et al. 2008) and Local Hot Bubble (LHB; Snowden et al. (1998)), which is a region of hot plasma surrounding the Sun. This background varies from field to field due to large scale spatial structure and varying amounts of absorption and Lumb et al. (2002) showed that a variation in its intensity of up to 35% can be expected. Each of these these three thermal components are usually modelled by thermal plasma models with zero redshift and cosmic abundances (Henley et al. 2010; Lumb et al. 2002). Only the LHB component is unabsorbed, while the other two are affected by galactic absorption.

In addition to the background due to cosmic sources (extragalactic and galactic), there is the background X-ray emission produced by highly charged particles which interact with the telescope and its components. This background is due to the interaction of the particles directly with the CCDs (particle background) or with various components of the satellite (fluorescent X-ray background). The particle background includes a time variable component due to low energy particles (soft protons) and a quiescent component due to high energy particles.

The particle background due to soft protons is temporally and spatially variable with short increases in flux intensities by up to 40% with respect to the average value (Markevitch 2002). This property can be used to remove their contribution by looking for short variations in flux intensity during a particular observation and eliminate these periods of time. This method, called flare cleaning has been described in the Data Reduction chapter. As mentioned there, because some flares may have very low amplitude or the variability of the flare to be longer than the time of the observation, not all flares are always completely filtered from the background and a level of contamination might exist. The contribution of residual flares can be modelled using a power law which is not convolved through telescope's response because energetic particles interacts directly with the telescope's CCD and they are not reflected by its mirrors Markevitch et al. (2003).

The quiescent background has been showed to have a temporal and spectral stability. Is the dominant component of the total background above 2 keV (Kuntz & Snowden 2008; Snowden et al. 2008) and can be 25 times larger than the extragalactic background. It is modelled with a broken power law which is not convolved through instrumental response.

Spectral signature of the flaring background is line emission from fluorescent X-ray photons generated by the interaction of charged particles with the telescope's components. It can be modelled by several Gaussians, with very small width position known from calibrations tests.

Because of the contribution from all background components that have been previously discussed, the overall model we have used to account for the background flux in our extracted spectrum is a very complex one. A proper modelling of the background is crucial especially for sources with a low number of counts, like groups, for which its contribution is dominant compared to the source flux contribution. In our background model we have included several components for the:

extragalactic, Galactic, particle and instrumental background.

For the extragalactic component we use a power law model with the value of the power law index fixed at 1.4. Galactic emission is modelled by two thermal plasma models one for the Local Hot Bubble and an absorbed one for the Galactic halo. The redshift and abundances have been frozen to 0 and solar, respectively. The background due to high energy quiescent particles is modelled by a broken power law which is not convolved with the detector response. For fluorescent background we use 4 Gaussians to model the strongest instrumental lines: Al-Kα (1.49 keV), Si-Kα (1.74 keV), Au-Mα (2.11 keV) and Mn-Kα (5.89 keV). We do not include any component for the soft proton background because we have removed the contribution of soft particle background during flare cleaning and we assume that there is no flare left in our observation.

The left panel in Figure 2.17 shows an example of a background spectrum extracted from the whole chip excluding sources for one of our fields and the result obtained by fitting our background model to this spectrum. Data points are showed in black while the fitted model is showed in red. The right panel shows the individual components of the background model, each of them plotted in different colour: red for the quiescent particle background, yellow for instrumental lines, green for the extragalactic component, blue for the LHB and magenta for the Galactic Halo. When looking at all individual components, it can be seen that particle background is the dominant one over almost the entire spectral range.

We model the contribution from the source with a an absorbed thermal plasma model (APEC), in which the redshift and the abundance are fixed at the known literature value and 0.3 (Mushotzky & Loewenstein 1997) respectively. Also we fix the absorbing column at the Galactic value (Dickey & Lockman 1990).

In our fitting procedure, we first extract a background spectrum in the 0.5-7.0 keV band from the whole chip, excluding any detected sources and a background plus source spectrum from a

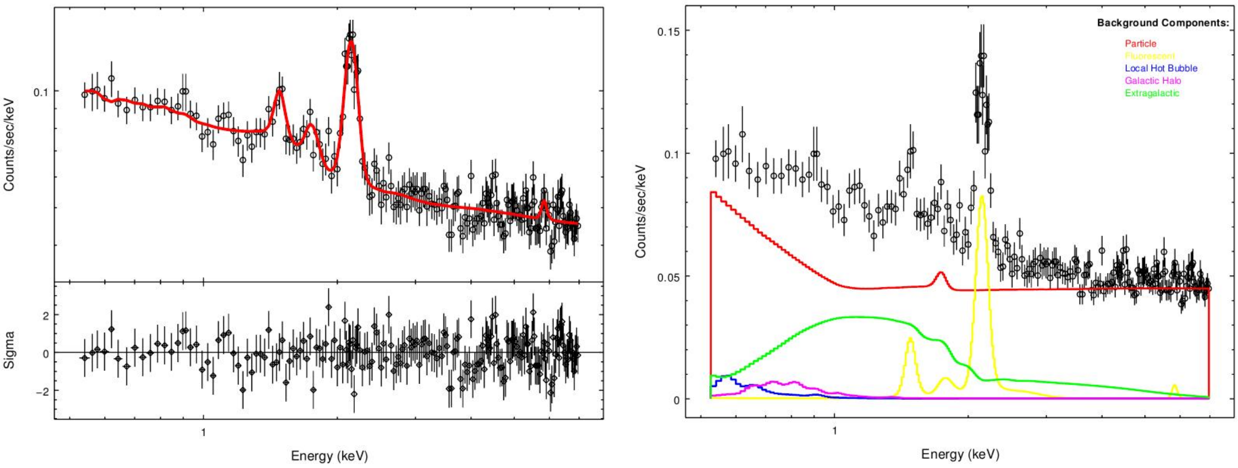

Figure 2.17: Left panel: Background spectrum (black points in upper panel) extracted from the entire field of view (excluding sources) of an observation in which a cluster has been detected. The red curve represents the complex background model used to fit the data and the lower panel shows the residuals (data - model) obtained as a result of the fitting. Right panel: Black points represent the same spectrum as in the left hand side panel, but now the individual components of the complex background model are showed with different colours.

circular region with radius equal to R_{500} centred on the position of the cluster. For cases in which multiple observations of the same system exists, we extract corresponding spectra for background and source plus background from each individual images, as previously described. All spectra are then merged to create the spectra used for our model fitting. Corresponding weighted merged response files are also created.

When fitting the source plus background model, the only components we allow to fit are: the thermal plasma normalization and temperature for the source model. For the background model, all components are kept frozen at the value obtained from the background fit with the exception of the Gaussian lines whose normalizations are let free to allow for any chip to chip variation in their intensity. We also add and let free to fit a scale constant for the background normalization which allow for variations of the particle background across the chip. Although the particle background is fairly constant, variations in its intensity has been observed at 10% level.

Figure 2.18 shows the results obtained by fitting a source plus background model to the spectra extracted for one source from our sample. In the upper left panel black points represent the spectrum which we fit with a complex model (red curve) represented by the addition of an absorbed thermal plasma component, to model cluster emission, and a background model. Black points in the lower panel show the residuals obtained after fitting the model to the data. The right hand side panel of the Figure contains the same information as left hand side one, with the addition of the green and blue curves which represent the extragalactic background and respectively the sum of the rest of all background components discussed in this subchapter and represented in the right hand side panel of Figure 2.17. As it can be seen from right hand side panel of Figure 2.18, for this particular source, there is little emission from the source above the background level. This accentuates the importance of a proper background modeling especially for sources with a low number of counts. Given the high number of counts in the background, which varies between $\sim 10^4$ and $\sim 2 \times 10^5$ counts, with a mean of $\sim 6 \times 10^4$ counts, we can get a good approximation of the background as a

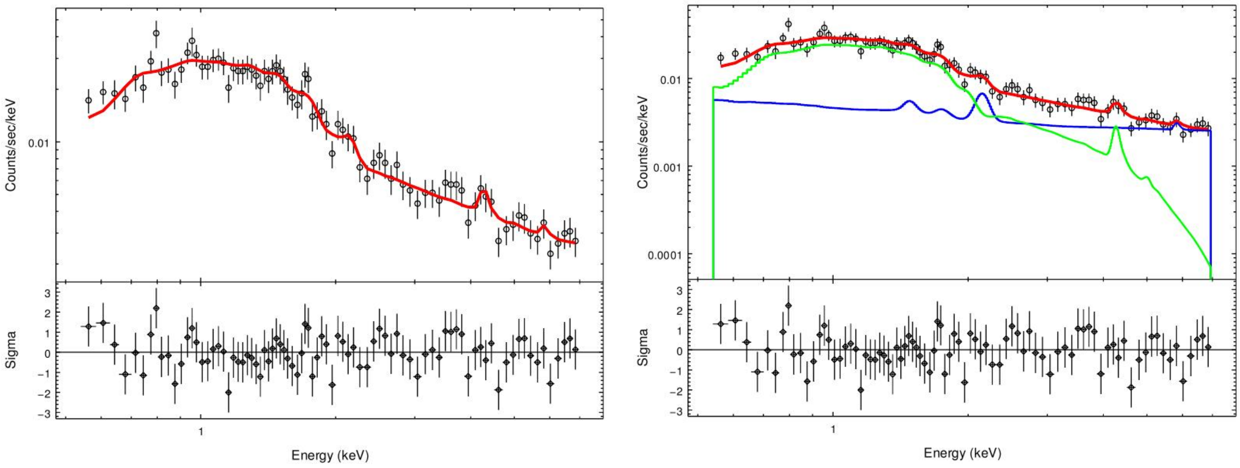

Figure 2.18: Left panel: Spectrum extracted for a system included in the CDGS sample (black points in upper panel), the model used to fit the data to get an estimate of the source's temperature (red curve) and the residuals obtained as a result of the model fit to the data (black points in the lower panel) The model is obtained by addition of an absorbed thermal plasma model to approximate the source emission and a complex background model formed of multiple components (see also right panel of Figure 2.17). Right panel: Black symbols and red curve have the same meaning as in the left panel. The green curve represents the extragalactic background component, while the green curve represent the sum of all other components used to model the background emission.

result of our background model fitting (see also 2.17).

2.6.3 Surface brightness profiles

Surface brightness profiles has been extracted for each system from the exposure corrected image of the source which has a bin size of one pixel (0.49 arcseconds). Each point in the distribution of surface brightness as a function of radius is calculated from an annulus centred on the X-ray peak emission and with the difference between the outer and inner radius equal to one pixel. The maximum outer radius equals to 2.5R_{500}, where R_{500} has been calculated as described in Section 2.6.1.

The surface brightness distribution has been approximated with a two dimensional beta function (Cavaliere & Fusco-Femiano 1976), which has the form:

$$S(r) = S_0(1 + (r/r_c)^2)^{-3\beta+0.5} + C \tag{2.8}$$

where S_0, r_c and C are the central surface brightness, core radius and the background constant, respectively.

The model is convolved with the exposure map, to allow for variations in exposure and effective area, and with the source PSF and fit to the data using the Cash statistics. We get first an estimate of the background by calculating the mean number of counts in the image, within an annulus with inner radius of 2R_{500} and 2.5R_{500}. The value obtained, normalized by the area of the annulus, is used as an initial guess for the value of C in the beta fit model. The final value for the background level is obtained by fitting a model represented by a constant to the image within a region between 2R_{500} and 2.5R_{500}. This constant is allowed to vary within 10% of our initial guess for the background. This represents the final value of C in the beta model, which will be frozen during the rest of the fit which will be done for the entire 0-2.5R_{500} region. We start by fitting the amplitude of the model, while the background is frozen, the slope is frozen at the value of 0.6, a typical value for the slope of low redshift clusters and the core radius is frozen at a value of 0.105R_{500}, which represent the typical core radius for low redshift clusters of galaxies (Helsdon & Ponman 2000). In the following steps the value of β and core radius are let to adujst, one at the time, while at the end the background level is let to adjust, while keeping the normalization, slope and core radius fixed.

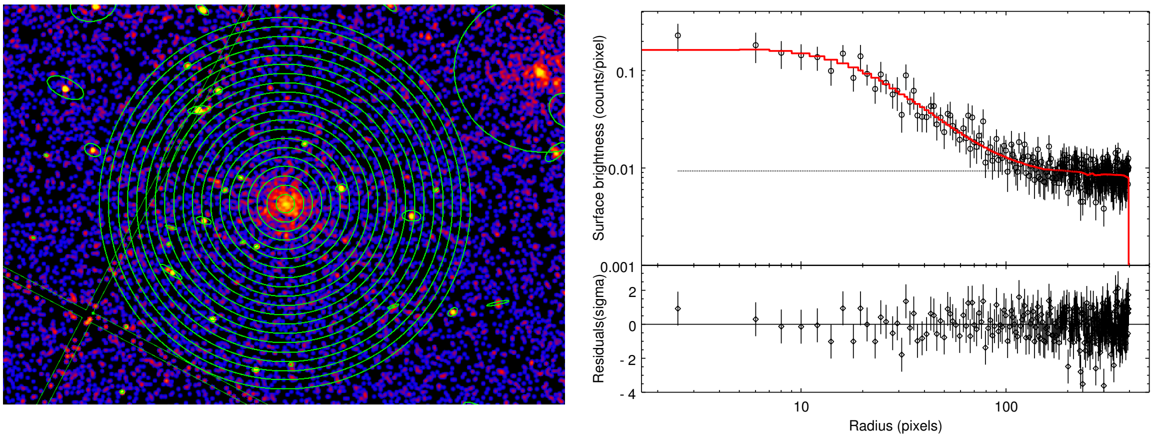

Figure 2.19: An example of the surface brightness profile extraction method and beta model fit obtained for one system from our sample. Left: X-ray exposure corrected image of the cluster. The total number of counts, including background counts, extracted from each annulus represent a data point in the radial surface brightness profile. The difference between the inner and outer radius of each annulus is one pixel, but we choose to display a lower number of annuli for better visualization. Contaminated sources, which are marked with green ellipses, are excluded when creating the profile. Regions corresponding to gaps between chips, marked by green lines, are also excluded. Right: extracted surface brightness profile (black points) and the beta model fit to the data (red line). Residuals of the beta model fit are showed in the bottom panel. The dotted black horizontal line marks the background level.

2.6.4 β_{spec}

It represents the ratio of the specific energy of galaxies to the specific energy of the gas (Mulchaey 2000):

$$\beta_{spec} = \frac{\sigma^2}{k_B T/(\mu m_p)}$$

where σ is the galaxy velocity dispersion, k$_B$ is the Boltzman constant, T is the gas temperature, μ is the mean molecular weight of the gas and m$_p$ is the proton mass. If clusters are isothermal and in hydrostatic equilibrium, then a value of 1 is expected for the β_{spec} parameter. Moreover, the value of this parameter should be equal with the surface brightness profile slope derived by fitting a beta model to the observed gas distribution.

2.6.5 X-ray peak position

The position of the peak in the X-ray surface brightness distribution is determined in an iterative mode from the exposure corrected image corresponding to each system. In the first step, we have smoothed the image with a gaussian with sigma of 15 pixels and determined the peak position. In the following steps, we start each time from the original image and smooth it with sigma with sizes decreasing from 15 to 7, 5, 3, 2 and 1 pixels. At each step, the peak value is calculated in the proximity of the peak position found in the previous step. This method has been found to be less sensitive to random noise, and for cases in which the system has a flat surface brightness distribution, with no obvious peak, the position of the peak coincides or is very close to that of the centroid.

2.6.6 Centroid variance

One parameter often used in the literature to characterize the dynamical state of a clusters and the presence of substructure is the centroid variance. It quantifies how much the centroid of the surface brightness within different annuli centred on the X-ray peak is moving compared to the peak position. We have calculated the centroid variance following the method described by Poole et al. (2006). Therefore, we have calculated the centroid positions for a series of concentric annuli centred on the X-ray peak and with increasing size radii with a step equal to $0.01\mathrm{R}_{500}$. For a range of centroid offsets from the peak coordinates O_i, the mean offset O is calculated. Then, the centroid variance, w, is then given by:

$$w = \sqrt{\frac{\sum_i (O - O_i)^2}{N-1}}$$

For each system, the centroid variance is scaled with the system's R_{500}.

2.6.7 Centroid shift

Centroid shift is also used as a parameter that can describe the dynamical state of a system. It is defined as the offset between the position of the X-ray centroid and that of the X-ray peak. The position of the centroid is determined iteratively. We start by calculating the position of the centroid in a circle with the size of the radius of 200 kpc and centred on the X-ray peak position. Then, at each step, the centre of the circle within which the new centroid is calculate is represented by the centroid position calculated at the previous step. Also, the distance between the new centroid position and the one obtained at the previous step is calculated. This procedure is repeated until the calculated distance between offsets is less than 4 pixels.

2.6.8 Error estimation

All uncertainties stated in Table 3.2 represent 68% confidence interval. This subsection gives a short description on how the errors for each parameter has been estimated.

Errors on properties obtained directly from fits to the spectra or surface brightness profiles are estimated during the Sherpa fit using the confidence function. The confidence method estimates errors by allowing the parameter for which the error is calculated to vary along a grid of values and calculates the fit statistic for each new fitted value. During each new fit, all the other thawed model parameters are allowed to change their value to a new best fit value. The confidence limits for the fitted parameter, in the case of Cash and chi-squared distribution, is defined as the value of the parameter for which the difference between the fit statistics on one of the points on the grid and the best fit statistics equals the quare of the standard deviation wanted for the confidence interval: $\sigma^2 = Stat - Stat_{min}$. For example, for a 1.6 standard deviation, a change in fit statistics of 2.56 is required. For a log-likelihood statistics, $\sigma^2 \sim 2(Stat - Stat_{min})$

Errors on quantities obtained based on complex formule like cooling time and entropy are estimated using the Monte Carlo method to propagate the errors. If one assumes that the quantity for which the uncertainty is measured ($Y = f(X)$) depends on N parameters: $X = (x_1, x_2, ..., x_N)$, each of them with a different distribution function (g), then to calculate the uncertainty in Y, the distribution function of Y has to be obtained. Based on this distribution, uncertainty intervals can be defined. The idea of Monte Carlo method is illustrated in Figure 2.20. This Figure shows that, given the distribution of input parameters, $g(x_1), g(x_2), g(x_3)$, by caluculating the model for various sets of parameters sampled from these distributions, a distrubution function for Y can be obtained. The steps followed to get error estimates are:

- Select N number of Monte Carlo simulations (usually N=1000)

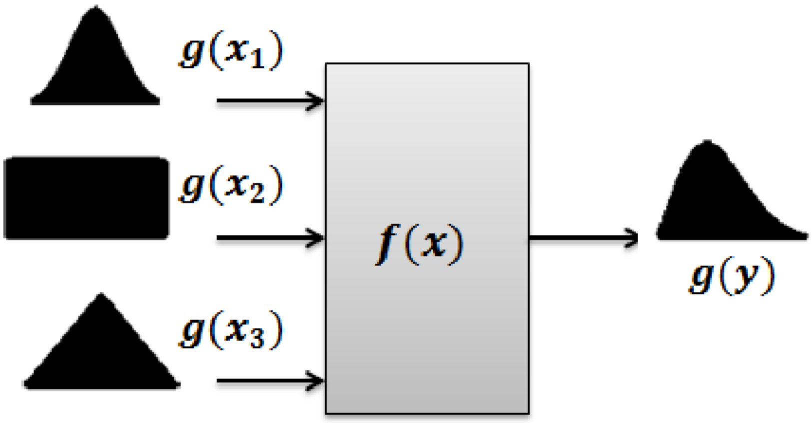

Figure 2.20: Illustration of the Monte Carlo method used to propagate the errors.

- Generate N samples corresponding to each input quantity (which is a parameter obtained from the spectral or surface brightess model), assuming that the distribution of each quantity is Gaussian with mean equal to the best fitted value and standard deviation equal to the uncertainty interval obtained for the respective parameter from the fit
- Evaluate the model for each generated sample
- Estimate the incertitude for our complex parameter as the standard deviation of the generated distribution

2.7 Catalogue of confirmed clusters

The full catalogue of confirmed clusters together with their optical and estimated X-ray properties is presented in Chapter 3, in Table 3.1 and Table 3.2.

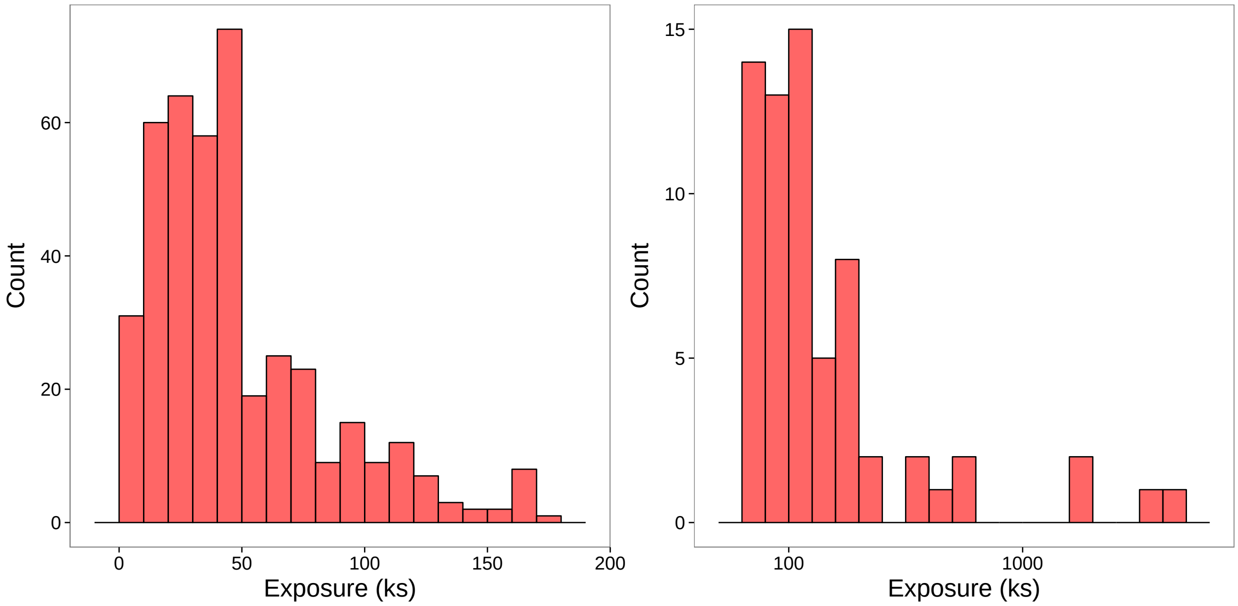

Figure 2.21: Left: Distribution of exposure time for all 426 individual observations used by CDGS. Right: Distribution of total exposure time for all fields (merged individual observations with similar pointings) used by CDGS to search for extended sources. All exposure times corresponds to periods of time left after background flare filtering.

2.8 Survey statistics

CDGS is a search for high redshift serendipitous groups of galaxies in *Chandra* archival data. We have searched for extended sources over an area of 9.6 deg^2 obtained from 66 fields, each with a total exposure time greater than 70 ks that. Figure 2.10 shows the distribution on the sky, in galactic coordinates, of the fields used in our survey. In Table 2.2 are listed for each field used in the survey, the position on the sky of the field, the total exposure time after filtering for particle background (see Section 2.3.1) and the area covered.

Figure 2.21 shows the distribution of exposure time of all 426 individual observations (left panel) and for total exposure of fields obtained by merging individual observations with similar pointings (right panel). The shape of these distributions is the result of one of our constraints applied for the selection of fields, according to which only fields with a total exposure time of more than 70 ks are included in our survey. From the left hand panel we can see that even if the lower limit for the merged field is 70 ks, most individual observations have an exposure time below 50 ks. The largest exposure time reached during a single pointing is 170 ks. It is clear from this that the merging of individual observations with similar pontings is necessary to reach a very deep exposure needed to detect high redshift groups (see also Figure 2.5). In the right hand side panel we can see that although the distribution of total exposure time of individual fields extends up to 4 Ms, most fields have an exposure time close to our adopted limit. The mean and median exposures are of 309 ks and 105 ks. The four outliers with very large exposure times represent four different X-ray surveys in their self: C-OSMOS, CDF-N (Brandt et al. 2002), E-CDFS (Castellano et al. 2011) and AEGIS-X (Laird et al. 2009).

To detect a significant number of high redshift sources, a deep wide area is desirable for our survey. Figure 2.22 represents a plot of the cumulative area of our survey as a function of exposure time. This shows that half of our area has exposures below 70 ks and a very limited amount of area of approximatively 10 % is covered with an exposure of more than 200 ks. This distribution gives us an indication about the fraction of high redshift systems in our sample detected in deep exposures, which is expected to be much lower compared to the large majority that will come from the larger and shallower area of the survey.

We have searched all fields included in our survey for extended sources with at least 100 counts, a lower count limit required in order to be able to perform spectral and spatial analysis of each detected source. Using the vtpdetect tool from CIAO and an extension test that quantifies the source surface brightness excess compared to that of a point source represented by the PSF, we found a number of 162 cluster candidates. A catalogue of extended sources detected in the survey

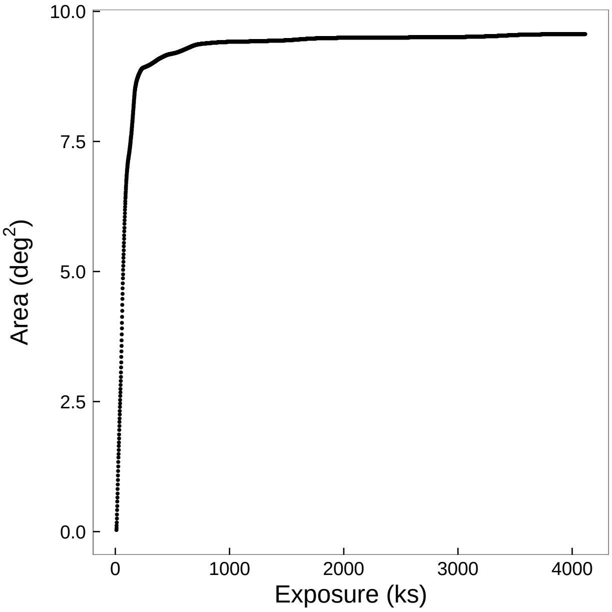

Figure 2.22: Cumulative area covered by CDGS as a function of exposure time for all 66 fields used in the survey.

has been presented in Table 2.3. We note that the target of the observation is included in our sample if this is a group or cluster with a redshift greater than 0.3. Fields in which the target is a low redshift cluster or group are excluded because of the large contamination from the target which occupies a large region of the field and therefore does not allow us to detect serendipitous sources. The cases in which we search for extended sources in fields with a low redshift group/cluster as a target are those for which the overlap between observations that are part of the field is not very large and therefore there is an area uncontaminated by the target which can be searched for serendipitous sources.

Since we search for extended sources in the fields composed of overlapping observations, any detected source might have different positions in the field of view, depending on the number of individual observations in which the source is detected and the geometry of the field. Figure 2.23 shows the distribution of the off-axis angles for all extended sources found in our survey. For each

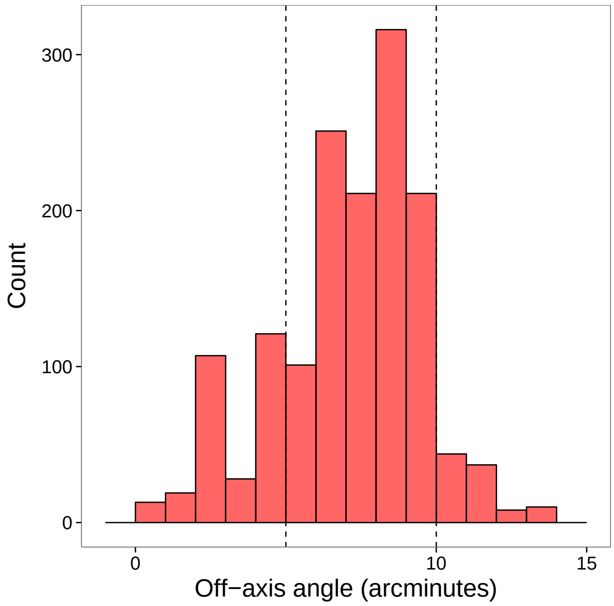

Figure 2.23: Distribution of off-axis angles for all extended sources (listed in Table 2.3) detected in CDGS. For each source detected in a field which has two or more overlapping observations there is an off-axis angle corresponding to each individual observation in which the source is detected. Therefore, for these cases more than one off-axis angle for each source is considered when plotting the histogram.

source, the off-axis angle is determined for each observation in which it is detected. Therefore, for the same source, multiple off-axis angles will be taken into account when constructing the histogram. The two vertical dashed lines delimits the histogram in three parts: on-axis sources (off-axis angles lower than 5 arcminutes), intermediate off-axis (off-axis angles between 5 and 10 arcminutes) and large off-axis sources (off-axis angles larger than 10 arcminutes). We can see that the large majority of sources are at intermediate of-axis angles, position on the chip where the size of the PSF, calculated as 90% enclosed energy fraction, is about 2 arcseconds. This PSF radius is significantly smaller than the radius at large off-axis angles, which is about 5 times larger (see also Figure 2.11).

Visual inspection of X-ray images, the distribution of the surface brightness profile compared with the distribution of the PSF and where it was possible, an inspection of a matching optical image has been done to confirm the existence of extended emission which can be associated to an optical galaxy overdensity. In addition, literature information has been used, where possible, to confirm the nature of a CDGS system. To confirm that an almost point-like source is an AGN using literature catalogues of known AGNs, we have matched the position of our source against those form AGN catalogues using a match radius of 10 arcseconds. Only in cases where there is a single match found within this radius and there is no other contaminating source in the X-ray image, the system is classified as an AGN. The same method has been applied to groups and clusters, but with a larger radius of 2 arcminutes. If we assume that a low redshif cluster has a R_{500} radius of 500 kpc, the maching radius chosen is $0.5R_{500}$, which is about 2 arcminutes. Of course that for high redshift systems this radius will correspond to a larger fraction of R_{500} than 0.5. If more than one match is found for a source, the best match is chosen as the source's optical counterpart and its redshift will be assigned to the CDGS source. We mention that the matching with literature cluster catalogues is done only for those catalogues which contain a redshift already compiled from redshifts of individual cluster members. Since the redshift used for systems from CDGS sample has been compiled by different authors, we present in Table 3.1 besides the redshift, the study from which the redshift has been taken and the number of galaxies used by the authors to estimate the redshift. For some systems, if the authors have assigned a name to the cluster, this name is included in the Table.

Out of 166 candidates, 15 were found to be spurious detections (e.g. double sources, bright stars), 45 were bright AGNs or quasars and 5 sources showed signs of extension but their flux were dominated by a bright AGN. Therefore our list of potential clusters had been reduced to 101. We note that our sample of confirmed systems contains serendipitous sources as well as the target of the observation, if this is a group or cluster with a redshift greater than 0.3.

To confirm the presence of a cluster or group, a literature search for redshifts has been performed. As a result of our literature search, 62 systems are confirmed groups or clusters with an available spectroscopic redshift (including photometric or spectroscopic). An X-ray spatial and spectral analysis has been done for each source in our sample of confirmed clusters. For each source, surface brightness profiles had been fitted with single beta models, while the temperature of the system had been estimated from their spectra by fitting thermal plasma models. The redshift and temperature distribution for the 62 confirmed groups or clusters with available redshifts is presented in Figure 2.24 in the left respectively right panels. The red histogram in each panel represent the entire sample of 62 systems, while the purple histogram is a subset of it, which contains only serendipitous sources.

The redshift distribution shows the wide range in redshifts covered by our survey, with the highest redshift being 1.27 and the mean redshift of 0.53 and a peak at 0.25. One thing that can be noticed is the lack of very low redshift systems which is due to the way in which we had selected our sample by excluding observations in which the target is a low redshift cluster that occupies a significant fraction of the field of view. Comparing the distribution of serendipitous sources with that of the total sample, it is evident from the histogram that most serendipitous sources had been detected at low redshifts of about 0.2. A second, although much smaller peak in the distribution is seen at redshift of about 0.7. The effect of this smaller peak on the distribution of serendipitous sources is to shift its mean towards a higher value of 0.47.

Temperature estimates has been obtained for each system with redshifts available in the literature and are listed in Table3.2. The large majority of systems in our sample are formed of clusters of galaxies with a a mean in the temperature distribution of 4 keV. On the other hand, if we look only at the distribution of serendipitous sources, we can see that most of them are groups, with a mean temperature of 2.6 keV. This histogram, together with the one in the left hand side panel, clearly show that target systems included in our sample is represented by a class of massive clusters

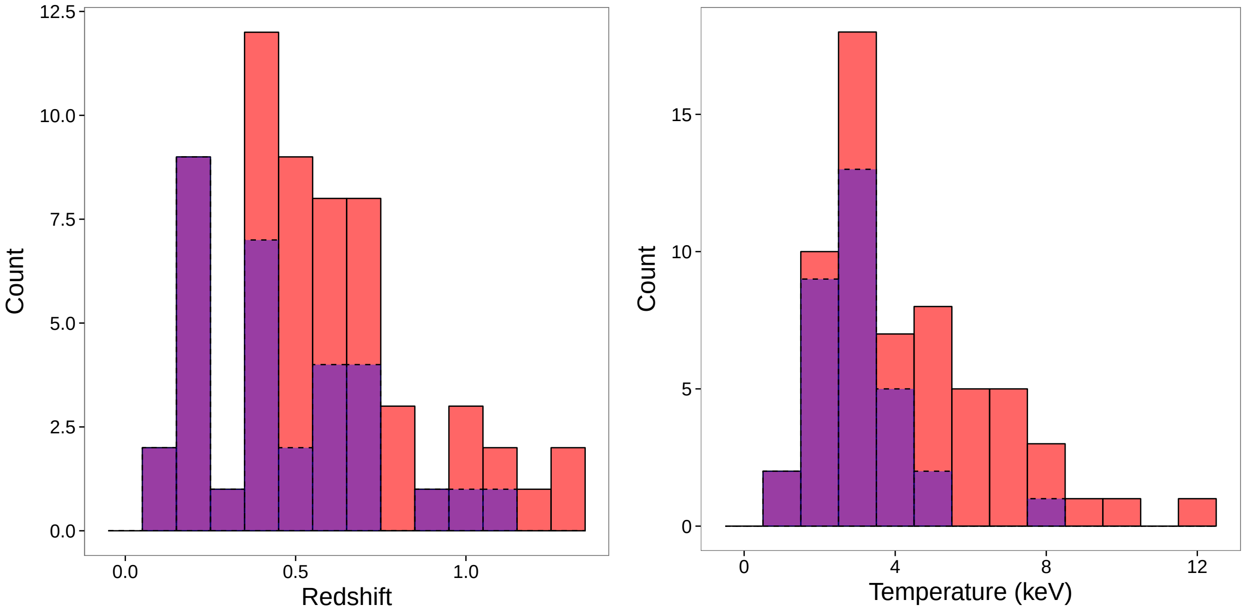

Figure 2.24: Redshift (left hand side panel) and temperature (right hand side panel) histograms for the sample of optically confirmed systems. Red histogram in both cases corresponds to all systems with redshifts (spectroscopic plus photometric). The distribution of redshifts and temperatures for the subsample of serendipitous sources is plotted in purple.

at intermediate (z=0.5) to high redshifts. The redshift distribution of temperatures derived for all systems with a spectroscopic and photometric redshift is showed in Figure 3.6 presented in Chapter 3. This shows that most of the groups detected in our survey are at low redshifts, below 0.5.

2.9 Discussion and conclusions

In this main thesis chapter we have described the survey we have conducted to search for groups of galaxies up to high redshifts, using deepest observations from *Chandra* archive. We have presented our survey strategy which takes into account the area covered, the minimum number of counts required for a source to be selected in our sample and the depth of the survey. We have constructed our search area based on 426 individual observations from the archive, which has been merged into 66 fields with a minimum total exposure time of 70 ks. We have chosen a threshold of 100 counts for a source which has been classified as extended to be part of our final catalogue. All these requirements has been imposed to construct a sample suitable for our scientific investigations.

With a total area of 9.6 deg^2, CDGS is one of the largest archival survey performed with *Chandra*(see also Figure 1.11 and Table 1.1 from Section 1.7 in the Introduction chapter in which we have presented some of the main surveys performed with *Chandra*, *XMM* and *ROSAT*). Two other surveys based on archival data has been reported in the literature: ChaMP Barkhouse et al. (2006) and the one in Boschin (2002). Whith respect to the total area covered, CDGS is intermediate between these two surveys: ChaMP covers an area of 13 deg^2 and the one of Boschin 5.5 deg^2. A more indepth comparison with these two surveys will be presented later in this section. Compared to *Chandra* contiguous surveys, which are very deep but also very narrow surveys with an area below 1 deg^2 , CDGS is significantly larger. This is an obvious consequence of the fact that all these deep surveys, like CDF-N, CDF-S, AEGIS-X, C-COSMOS are included in the data archive and therefore represent a part of our survey.

In comparison with *XMM* or *ROSAT* serendipitous surveys, CDGS is significantly smaller. For example, XCS - an *XMM* serendipitous survey, which uses all *XMM* archive to search for clusters, covers an area about 40 times larger. A similar area to that of the XCS is covered by 400d survey, which is the largest *ROSAT* archival survey. One factor which contributes to this difference between *Chandra* and *ROSAT* or *XMM* archival surveys is the much larger field of view of *ROSAT* and *XMM* compared to that of *Chandra* (see also Table 2.1).

In addition to a large area, a deep exposure is required for our survey to detect systems at high redshifts. From the point of view of depth, CDGS is a heterogeneous survey with a very wide range in exposures from 10 ks to 4 Ms (see Figure 2.6). Although this range is very wide, most of the area is covered with low to medium exposures, with 90% covered by exposures below 200 ks. For these exposures, we have showed in Figure 2.5 that we are sensitive to groups of galaxies up to a redshift of 0.6.

We have used a detection algorithm based on a Voronoi tesselation algorithm to search for clusters. Each detected system with at least 100 counts is tested for extension compared to the *Chandra* PSF and our list of extended sources contains 162 systems. Out of these, 45 are AGNs, 15 are spurious (e.g. bright stars or double sources) and 5 are extended sources dominated by a central AGN. Without an spectroscopic follow-up, which is not available for CDGS yet, we rely only on spectroscopic and photometric redshifts available from literature. The effect of this is that the subsample of spectroscopically confirmed clusters represent a small fraction of the entire sample of potential clusters.

Our catalogue of confirmed clusters contains 62 systems and represent only about 64% from our reduced list of extended sources of 97 systems. This suggest the importance for an optical follow-up to confirm the rest of extended sources.

For all confirmed members, we have performed a spectral and spatial analysis. Our systems are mainly clusters with temperatures of about 4 keV and redshifts of 0.6. We have mentioned that our sample includes serendipitous sources as well as targets of the observations. This will introduce a bias in our sample, because we are adding systems chosen to be observed because of their peculiar properties. The effect of this bias on the sample would be hard to be quantified since it depends on the scientific interest for which the target has been observed by the principal investigator of an observation. If we consider only serendipitous sources, the mean redshift is 0.47 and median 0.44. The mean and median temperature is 2.5. We have found that 42% of the entire sample with available redshifts is represented by groups, while the number of serendipitous groups is 22 with a mean and median redshift of 0.4 for all groups and 0.3 for serendipitous. A very small number (5) of high redshift (z>0.5) serendipitous groups has been detected.

If we compare our sample with the predictions calculated in Section 2.1 we found a much lower number of systems compared to our predictions. For example, we predicted a number of 149 groups at redshifts > 0.1 and we found only 26 out of which 22 are serendipitous. One causes which might be responsible for this discrepancy (we stress again that we rely only on redshifts available from literature), the number of systems is much underestimated compared to the one calculated for the entire area surveyed. From the multiple causes which might contribute to the observed discrepancy we mention a few. One of it is the fact that the number of predicted systems is overestimated. This is because we have assumed for our calculation that we have an 100% detection rate. We know that the detection of a source is affected by factors like source size, background and position on the chip. This might be also a case for a reduction in number of sources detected. To estimate the number of sources missed, a proper knowledge of the selection function of the survey is needed. Other thing might be the fact that we have assumed a luminosity function which does not evolve with redshift. We can not estimate how an evolving function would bias the number of predicted systems would be, until there is a consensus about the evolution of luminosity function.

We also compare our results with those of Barkhouse et al. (2006) and Boschin (2002), which are *Chandra* archival surveys, similar to CDGS. A better comparison can be done with the catalogue from Barkhouse et al. (2006) since this contains information about the source redshifts from their spectroscopic follow-up, while the sample from Boschin (2002) does not have any optical information. The total number of confirmed clusters in CDGS (62) is double than the number of optically confirmed clusters from Barkhouse et al. (2006) (31), although the area covered by CDGS is 25% smaller. This difference in the number of sources can have two causes. One of them is the wide range in exposures used for our survey which allows the detection of more sources. The second reason is the fact that our sample includes the target of the observation, while their sample is a serendipitous one. Moreover, they chose not include in the survey observations which are part of *Chandra* surveys like CDFS, CDFN, COSMOS, AEGIS, which represent the deepest fields from our sample. If we compare the number of serendipitous confirmed clusters from CDGS (22) is lower than theirs. With respect to the redshift distribution, a comparison between left panel of Figure 2.24 and Figure 8 from Barkhouse et al. (2006) shows that our distribution peaks at low redshifts, of about 0.3 for serendipitous and also entire sample, while their distribution is almost flat up to a redshift of 0.5 and then declines. Their highest redshift is 0.8, while while we reach a redshift of 1.0 for our serendipitous sources.

The comparison with the survey from Boschin (2002) can be done only for the number of extended sources, since their survey does not have an optical follow-up and their catalogue does not contain any information about the redshift of the sources. With a number of 162 extended serendipitous sources, the CDGS catalogue contains 4.5 times more extended sources than the one of Boschin (2002). This might be the combined effect of a larger area and deeper exposures for CDGS.

Compared to *XMM* archival surveys like XCS, CDGS is a significantly smaller survey with respect to the covered area and the number of cluster candidates. The XCS survey covers an area about 40 times larger than that of CDGS, and the number of potential clusters is 3675, out of which 503 are optically confirmed clusters. One explanation for the large difference between the number of systems in the CDGS compared to that from XCS is the difference between the telescope's field of view and effective area (see Table 2.1). Although *XMM* surveys have the advantage of detecting a larger number of sources, *Chandra* offers the advantage of high angular resolution, which is critical for studies of high redshift systems.

The redshift distribution of systems from our survey (see Figure 2.24) is similar to that of systems from XCS (see Figure 1 from Viana et al. 2013), with a peak at low redshifts of about 0.3 and a low number of systems above redshift 0.8. Temperature distribution, although is almost similar for CDGS and XCS, peaks at higher temperatures in CDGS (3 keV) compared to XCS (2 keV). Therefore, CDGS detects more low massive clusters, while groups are the dominant type of source in XCS.

Chapter 3

Cool core evolution of groups and clusters of galaxies

One scientific question addressed with a subsample of groups and clusters detected as part of the CDGS and presented in previous Chapter is how thermal properties of the gas at the centre of groups and clusters are evolving with redshift.

It is known that in the absence of heating, the gas at the centre of groups and clusters ought to cool due to loss of energy through radiation. If the time in which the gas would lose all its energy is less than Hubble time, then a central cool core characterized by a central drop in temperature and high central gas density will form.

The general picture formed based on observations is that CCs in clusters are common at low redshifts, while at high redshifts there is a dearth of clusters with very low central entropy. It is not well known what causes this type of evolution in the CC abundance and various models have been adopted to explain this evolutionary behaviour (see also Chapter 1.5 for a more detailed discussion on CCs in groups and clusters). While one model (Burns et al. 2008) assumes that the abundance of CCs is regulated by cluster mergers which are able to destroy CCs, the other (McCarthy et al. 2004) assumes that the entropy of the ICM is fixed before cluster formation by non-gravitational processes hence the fraction of CCs in the Universe is established at an early time. Therefore, the study of the evolution of CCs represent an important tool which can be used to distinguish between these two models.

The study of CCs is also important because it can help solving the puzzle of when and how non-gravitational processes like AGN feedback are affecting the thermal properties of the gas within groups and clusters. The interplay between a CC and an AGN is suggested by observations which show that a large number of CCs host an AGN and moreover, stronger CCs host stronger AGNs.

Some of the questions we are trying to address in this Chapter are: How is the evolution of CCs in groups and clusters? Is this evolution different for more massive systems compared to groups? What is the impact of AGNs in this evolutionary trend?

3.1 Sample Selection and Data reduction

Our study is based on a *Chandra* archival sample of 62 systems with temperatures between ~ 1 and ~ 12 keV and redshifts that span the range between 0.07 and 1.3, with means in temperature and redshift of 4.0 keV and 0.55 respectively. The sky coordinates of the systems in our sample together with the X-ray properties derived from our analysis are listed in Table 3.1 and Table 3.2.

Since our sample is represented by those systems from CGS for which a literature redshift is available, the strategy adopted for our sample selection is identical to that adopted for the CDGS. We have described in more detailed the CDGS selection strategy in Chapter 2.1. Here we remind the reader our twofold motivation: firstly, the necessity of a large sample, with enough statistics to allow the study of cool core evolutionary trends in groups and clusters, and secondly, the requirement for data of sufficient quality to permit spectral and spatial analysis for all systems in the sample.

The use of *Chandra* data is crucial for our study because of the high resolution required to resolve the cores in our systems out to high redshifts, in order to apply different cool core estimators and also to resolve and exclude contaminating point sources. *Chandra*'s advantage over all other X-ray telescopes is its high angular resolution of $\sim$0.5 arcsecond (FWHM), which corresponds to 4 kpc at a redshift of 1.

The observations used by CDGS to search for extended sources, have been selected from the Chandra archive using the following criteria:

- Only ACIS-I observations are used. To construct a sample as large as possible we made use of all ACIS-I observations available in the archive as of September 2009 (when the analysis commenced) which meet certain criteria.
- Only high galactic latitude ($|b| > 20^\circ$) pointings were included, to avoid heavy galactic absorption.
- Observations for which the target is a low redshift extended system that occupies most of the field of view were excluded. A consequence of this requirement is that our sample lacks very low redshift systems. This can be seen in Table 3.1 – with the exception of one system, all sources lie at redshifts greater than 0.1.

All individual observations from the archive with the above mentioned properties have been grouped into fields (i.e. a single observation, or a group of observations with similar pointings). In order to provide data of adequate quality for our analysis out to high redshift, we considered only fields with a total exposure time of at least 70 ks, though individual areas within a field can have shorter exposures than this. These selection criteria result in a total of 66 fields, covering an area of $\sim$ 10 degree^2.

Chapter 2.3.1 gives a detailed description of the data reduction of raw data extracted from *Chandra* archive. We searched all fields for sources using a source searching algorithm based on the Voronoi tessellation algorithm implemented in CIAO. All detected sources were tested for extension using a Bayesian extension test developed by Slack & Ponman (2014) which checks for a significant difference in fit statistic between a point source model and a beta model blurred with the point spread function. Our final candidate list includes only extended sources with at least 100 counts in the soft band (0.5-2.0 keV). This threshold is motivated by the fact that our subsequent analysis requires enough counts to construct a useful spectrum and surface brightness profile. This restriction also has the advantage of greatly simplifying selection biases, as we will see in Chapter 3.5.1. The flux corresponding to the 100 count limit varies with the exposure time of the source. Assuming a spectrum corresponding to a thermal plasma with a temperature of 3 keV and abundance 0.3 solar, at redshift 0.5, the 0.5-2.0 keV flux limit is approximately $8 \times 10^{-15} t_{100}^{-1}$ erg cm^{-2} s^{-1}, where t_{100} is the exposure time in units of 100 ksec, which varies from 0.1 to 40 for our sources.

A number of sources which, although extended, were found to be dominated by a bright central point source (presumably an AGN) were excluded, as described in Chapter 3.3.1, and four apparently bona-fide extended sources were also dropped from our list because no redshift was available for them. Our total X-ray selected sample of 62 groups and clusters is listed in Table 3.1. 33 are serendipitous detections, whilst the remaining 29 were the main target of the *Chandra* observation in which they were detected. The redshift value quoted in the Table for each system is derived from the literature. Note that some of these redshifts are photometric. The position given for each system corresponds to the R.A. and Declination (J2000) of the X-ray peak.

Table 3.1: Catalogue of groups and clusters used. Columns represent: source ID (increasing with redshift), Right Ascension (R.A.), Declination (Dec.), redshift, reference for redshift and the number of galaxies used to derive the cited redshift (when available), a source flag, alternative names given in the literature for the system and any other notes. R.A and Dec are given for J2000 and represent the position of the X-ray peak. All redshifts are spectroscopic except those marked with an asterisk which are photometric. For each source, the Flag column contains a 't' if the source is the target of the observation, an 'a' if is contaminated by a central AGN and a 'c' if the beta model fit to the surface brightness profile has been adjusted (see 3.3.1).

ID	R.A.	Dec.	z	Ngal	Flag	Literature names
	(deg)	(deg)				
CDGS1	214.4486	+52.6954	0.066	23[1]	–a–	EGSXG J1417.7+5241
CDGS2	149.8517	+01.7736	0.12*	—[2]	——	
CDGS3	150.4316	+02.4281	0.12*	—[2]	——	
CDGS4	26.2022	-04.5494	0.17*	—[3]	——	
CDGS5	215.003	+53.1122	0.200	19[1]	——	EGSXG J1420.0+5306
CDGS6	221.6679	+09.3385	0.204*	—[6]	——	
CDGS7	212.907	+52.3147	0.21*	—[4]	——	
CDGS8	150.1967	+01.6537	0.220	14[2]	——	
CDGS9	8.4430	-43.2917	0.223	1[5]	——	XMMES1_145
CDGS10	255.1737	+64.2167	0.225	1[7]	—c	RXJ1700.7+6413;Abell2246;
CDGS11	214.3371	+52.5964	0.236	9[1]	——	EGSXG J1417.3+5235
CDGS12	210.31717	+02.7534	0.245	—[8]	——	
CDGS13	235.3019	+66.4410	0.245	—[9]	——	
CDGS14	222.6074	+58.2201	0.28*	—[10]	——	
CDGS15	150.1798	+01.7689	0.346	14[2]	——	
CDGS16	170.0304	-12.0864	0.352	13[11]	t —	
CDGS17	292.9568	-26.5761	0.352	35[12]	tac	MACSJ1931.8-2634
CDGS18	161.9225	+59.1156	0.36*	—[10]	——	
CDGS19	170.0416	-12.1476	0.369	22[11]	t —	
CDGS20	8.6137	-43.3168	0.3925	1[5]	——	XMMES1_224
CDGS21	29.9557	-08.8331	0.406	31[12]	tac	MACS0159
CDGS22	29.9637	-08.9219	0.407*	—[13]	——	
CDGS23	249.1566	+41.1337	0.423	3[14]	——	
CDGS24	327.672	-05.6853	0.439	30[15]	——	

CDGS25	138.4395	+40.9412	0.442	1[16]	ta –	MACSJ0913.7+4056; CL09104+4109
CDGS26	52.4231	-02.1960	0.450	—[17]	t –c	MACSJ0329.6-0211
CDGS27	255.3481	+64.2366	0.453	—[18]	t –c	RXJ1701.3+6414
CDGS28	212.8357	+52.2027	0.460	21[19]	tac	Cl 1409+524
CDGS29	245.3532	+38.1691	0.461	—[20]	tac	MACSJ1621.3+3810
CDGS30	169.9805	-12.0402	0.479	17[21]	t —	
CDGS31	197.7571	-03.1768	0.494	—[22]	t —	MACS1311.0-0311
CDGS32	158.8557	+57.8484	0.5*	—[23]	—–	
CDGS33	158.8076	+57.8387	0.5*	—[23]	—–	
CDGS34	109.3822	+37.7581	0.546	142[24]	t –c	MACSJ0717.5+3745
CDGS35	170.2387	+23.4462	0.562	—[25]	t —	RXJ1120.9+2326; V1121+2327
CDGS36	132.1985	+44.9380	0.570	11[26]	t —	RX J0848+4456; CL0848.6+4453
CDGS37	6.3736	-12.3761	0.586	108[27]	t —	MACS0025.4-1222
CDGS38	314.0887	-04.6307	0.587	149[28]	t –c	MS2053.7-0449
CDGS39	314.0721	-04.6988	0.600	—[29]	—–	
CDGS40	222.5374	+09.0802	0.644	9[30]	—–	
CDGS41	52.9582	-27.8274	0.679	2[31]	—–	
CDGS42	214.4736	52.5795	0.683	11[1]	–a –	EGSXG J1417.9+5235
CDGS43	61.352	-41.0057	0.686	—[32]	t —	
CDGS44	185.3565	+49.3092	0.700	—[25]	t —	RXJ1221.4+4918; V1221+4918
CDGS45	345.6999	+08.7307	0.722	1[33]	t —	WARPJ2302.8+0843; CLJ2302.8+0844
CDGS46	168.2731	-26.2612	0.725	2[33]	t —	WARPS1113.0-2615 CLJ1113.1-2615
CDGS47	149.9211	+02.5229	0.730	12[2]	—–	
CDGS48	53.0401	-27.7099	0.734	4[31]	—–	
CDGS49	215.1388	+53.1392	0.734	17[1]	—–	EGSXG J1420.5+5308
CDGS50	349.6286	+00.5661	0.756	8[34]	t —	RCS2318+0034
CDGS51	175.0927	+66.1374	0.784	22[35]	t —	MS1137.5+6625
CDGS52	199.3407	+29.1889	0.805	6[36]	t —	RDCS 1317+2911
CDGS53	214.0694	+52.0995	0.832	1[1]	—–	EGSXG J1416.2+5205
CDGS54	150.504	+02.2246	0.9*	—[2]	—–	
CDGS55	53.0803	-27.9017	0.964	2[31]	—c	
CDGS56	355.3011	-51.3285	1.00	15[37]	t —	SPT-CLJ2341-5119
CDGS57	213.7967	+36.2008	1.026	25[38]	t –c	WARPS J1415.1+3612
CDGS58	137.6857	+54.3697	1.101	20[39]	t —	
CDGS59	137.5357	+54.3163	1.103	17[40]	—–	RXJ 0910+5419
CDGS60	193.2273	-29.4546	1.237	36[41]	t —	RDCS1252-29
CDGS61	132.2435	+44.8664	1.261	6[42]	t —	RXJ0848.9+4452; RDCS0848.9+4452
CDGS62	132.1507	+44.8975	1.273	8[43]	t —	RXJ0848.6+4453; RDCS0848.6+4453; CLG J0848+4453

Redshift References: 1:Finoguenov et al. 2007; 2:Knobel et al. 2012; 3:Mehrtens et al. 2012; 4:Wen & Han 2011; 5:Feruglio et al. 2008; 6:Hsieh et al. 2005; 7:Struble & Rood 1987; 8:Bonamente et al. 2012; 9:Romer et al. 2000; 10:Wen et al. 2012; 11:Tran et al. 2009; 12:Ebeling et al. 2010; 13:Hao et al. 2010; 14:Manners et al. 2003; 15:Finoguenov et al. 2009; 16:Kleinmann et al. 1988; 17:Kotov & Vikhlinin 2006; 18:Vikhlinin et al. 1998; 19:Dressler & Gunn 1992; 20:Allen et al. 2008; 21:Gonzalez et al. 2005; 22:Schmidt & Allen 2007; 23:Yang et al. 2004; 24:Ebeling et al. 2007; 25:Mullis et al. 2003; 26:Holden et al. 2001; 27:Bradač et al. 2008; 28:Tran et al. 2005; 29:Barkhouse et al. 2006; 30:Finoguenov et al. 2009; 31:Szokoly et al. 2004; 32:Burenin et al. 2007; 33:Perlman et al. 2002; 34:Stern et al. 2010; 35:Donahue et al. 1999; 36:Holden et al. 2002; 37:Song et al. 2012; 38:Huang et al. 2009; 39:Tanaka et al. 2008; 40:Rumbaugh et al. 2013; 41:Rosati et al. 2004; 42:Rosati et al. 1999; 43:Stanford et al. 1997

3.2 Data Analysis

Our aim is to study the evolution of CCs in groups and clusters of galaxies and compare evolutionary trends between these two classes of objects. Therefore an X-ray spectral and spatial analysis has been performed on each system in our sample in order to characterize the gas properties and derive parameters which can be used as CC estimators. We use mean gas temperature estimated from our spectral fits to distinguish between groups and clusters by applying a temperature cut of 3 keV. There is, of course, a degree of arbitrariness in this choice, and previous studies have adopted temperature thresholds between groups and clusters ranging from 1 keV to 3 keV (Sun et al. 2009; Finoguenov et al. 2001; Gastaldello et al. 2007).

3.3 X-ray derived parameters

The methods used to study the gas surface brightness distribution as well as some X-ray derived parameters such as R_{500} and gas temperature within R_{500} have been presented in Chapter 2. While these X-ray derived parameters are global parameters, in this chapter we present some X-ray derived parameters which are used to characterize the thermal state of the central gas: central cooling time and central entropy.

3.3.1 Surface brightness profiles

The single beta model used to characterize the spatial distribution of X-ray emission has been presented in detail in Chapter 2.6.3. In this Chapter we will present the analysis of surface brightness adopted for CC systems whose surface brightness distribution show deviations from the single beta model. While the single beta model can describe well the surface brightness distribution of NCC clusters (Mohr et al. 1999; Henning et al. 2009), it represents a poor approximation for CCs because of their central surface brightness excess above the model (Neumann & Arnaud 1999; Vikhlinin et al. 2006). Figure 3.1 shows an example of the surface brightness distribution (black points) for a CC cluster and the single beta model fit to the data.

Chen et al. (2007) showed that a significant improvement in the fit of CC clusters can be obtained by adding a second component to the model to account for the central excess emission. The quality of our data do not permit a more complex model to be fitted, and in practice our main aim will be to use the fitted profile to estimate the gas density in the core of each system (at r=$0.01R_{500}$) using geometrical deprojection, which has a relatively straightforward analytical form for the case of a single beta model (see Chapter 3.3.2 and Appendix B for details of the geometrical deprojection and the choice of r=$0.01R_{500}$). Because we need to obtain the density at a particular radius, our primary requirement is a good match of the model to the data around that radius. We checked the adequacy of our fit for each system and found that for most cases it matches the data well into $0.01R_{500}$. In a few cases with strongly peaked profiles, the default fit underestimates the data at small radii. For these cases, we first fit the central region using a beta-model with a small core

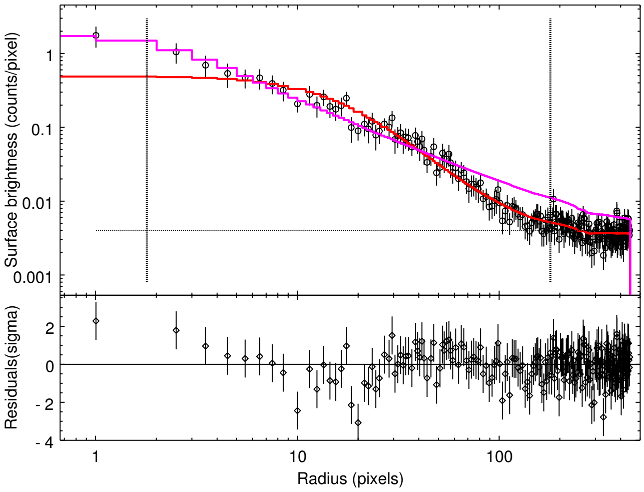

Figure 3.1: Surface brightness distribution (black points in upper panel) of gas within a CC cluster. Lower panel represents the residuals obtained by fitting a single beta model (red curve) to the data. As it can be seen, the model underestimates the data at small radii. The magenta curve represents the adjusted model (see text) used to match the the data at $0.01R_{500}$, which is the radius at which the gas cooling time and entropy is calculated. Vertical dotted lines mark the position of $0.01R_{500}$ and that of R_{500}.

radius, and then fix the amplitude whilst relaxing other parameters, to achieve the best fit possible at larger radii, subject to providing a good match near the centre. Figure 3.1 shows in red the single beta fit while the magenta line represents the adjusted fit. Systems for which such adjustment was needed are flagged with a ‘c’ in column 6 of Table 3.1.

It is well-established that the central galaxies in many low redshift groups and clusters display nuclear activity. Such AGN can be bright X-ray point sources, which may contaminate the cluster X-ray flux. We checked for the existence of a central AGN in three different ways: by looking for the presence of a central point source at the position of the cluster candidate in the hard band image, by comparing the surface brightness profile of the source with the point spread function, and by comparing the fit statistics of a thermal plasma plus power law model fit (to model the cluster emission plus the AGN) with a thermal plasma only model applied to the source spectrum. Cluster candidates in which we found evidence of AGN contamination were divided into three classes: (1) Sources with clear spatial extension in which the central AGN does not dominate the total flux – in this case the source was retained in the cluster list and the central AGN excised during data analysis. (2) Sources with clear extension but with a dominant central AGN. (3) Sources with only marginal extension, but with clear evidence for the presence of an AGN. In cases (2) and (3) the source was excluded from our catalogue. An example of each case is presented in Figure 3.2.

3.3.2 Cooling Time

The mechanism by which gas in clusters of galaxies cools is radiation of its thermal energy through X-ray emission. One simple parameter which can characterize the thermal state of the gas is the cooling time, which is defined as the characteristic timescale on which the gas radiates away its thermal energy. The cooling time at a radius r is

$$t_{cool}(r) = \frac{3}{2}\frac{\mu_e n_e V kT}{\mu L_x} , \tag{3.1}$$

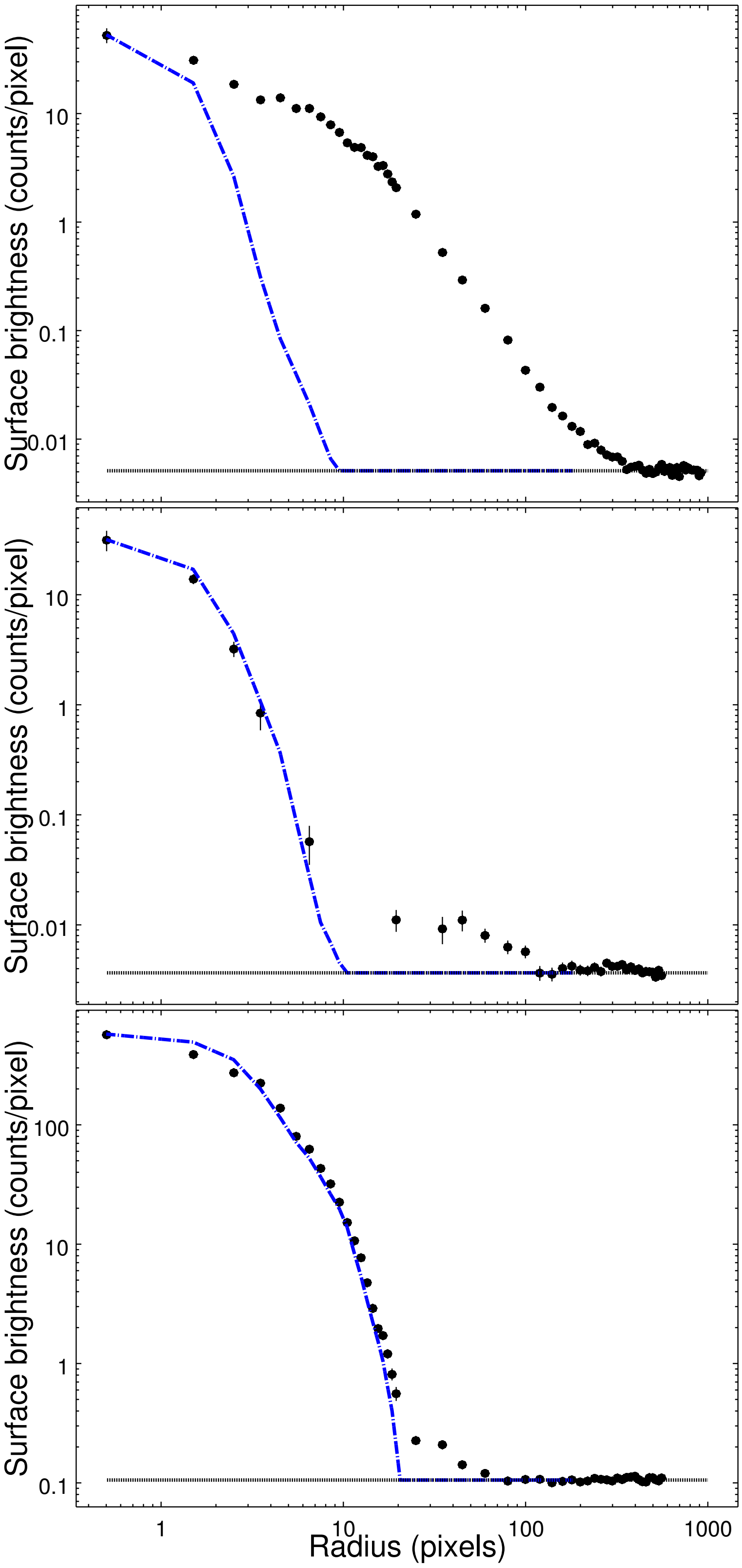

Figure 3.2: Three cases of AGN contamination. Top panel: the central AGN is strong but the cluster's flux dominates; source is kept in the sample. Middle panel: AGN dominates over the clusters' flux; the source is excluded from our sample. Bottom panel: The AGN is dominant and there is some evidence for the presence of extended emission; source is excluded from the sample.

where kT and n_{e} are the gas temperature and electron number density in a spherical shell of volume V at radius r, and L_{x} is the luminosity radiated by the shell. The mean mass per electron (μ_{e}) and mean mass per particle (μ) have values of 1.15 and 0.597, respectively, corresponding to a fully ionized thermal plasma with metallicity 0.3 $Z_{\odot}$ (Sutherland & Dopita 1993).

The gas density at radius r is derived from the normalization of the thermal plasma fit to the source spectrum and derived counts emissivity using the following equation:

$$n_e(r) = \sqrt{\frac{(n_e/n_H)\,N_{\mathrm{spec}}\,4\pi[D_a(1+z)]^2}{V\,10^{-14}}\,\frac{\varepsilon(r)}{C}}\ , \tag{3.2}$$

where D_a is the angular diameter distance , $\varepsilon(r)$ is the counts emissivity integrated over the volume of the shell (i.e. the total count/s from the shell) and C is the total number of counts from the source within R_{500}. N_{spec} is the normalization of the thermal plasma model fitted to the spectrum extracted within R_{500}, with all point sources excluded, which for the APEC model is related to the emission measure by

$$N_{\mathrm{spec}} = \frac{10^{-14}}{4\pi[D_a(1+z)]^2}\int n_e n_H dV\ . \tag{3.3}$$

The analytical expression for the counts emissivity profile

$$\varepsilon(r) = \varepsilon_0(1+(r/r_c)^2)^{-\eta}\ , \tag{3.4}$$

can be obtained from the surface brightness profile of the form given in Equation 2.8 by geometrical deprojection, assuming a spherically symmetric distribution. Since surface brightness represents the projection on the sky of emissivity, the surface brightness profile can be written as a integral along the line of sight of emissivity:

$$S(b) = 2\int_0^\infty \varepsilon(r)dl \ , \tag{3.5}$$

where $r^2 = b^2 + l^2$ and l is the direction along the line of sight. Solving the integral using the substitution $\tan^2\alpha = z^2/(r_c^2 + \omega^2)$, we can obtain the slope and the normalization of the emissivity profile as a function of the beta-model parameters. Hence $\eta = 3\beta$ and $\varepsilon_0 = S_0/(2r_c \int_0^{\pi/2} \cos\alpha^{2(\eta-1)} d\alpha)$.

The temperature of the gas is required to derive gas density from the emissivity, and hence to calculate entropy and cooling time. We use the global temperature, as our data quality does not allow us to construct temperature profiles. For CC systems, the temperature drops in the core, by a factor of up to 2 or 3 from its peak value (or a smaller factor compared to the *mean* global temperature). As a result, we will somewhat overestimate the central cooling time in CC systems, by a factor of approximately $\sqrt{2}$.

Clearly, the cooling time rises progressively with radius, as the density drops, so we need to pick a scale radius at which to extract the cooling time which will characterise the cluster core. We would like this radius to be as small as possible, subject to it being resolved in our observations. However, we do want the derived gas properties to represent the group/cluster core. Sun et al. (2007) has pointed out that some galaxy groups contain dense gas within the central galaxy, which he refers to as a 'compact corona'. These small gas halos are distinct from classic cool cores and are more closely associated with the central galaxy itself. These compact coronae have sizes typically between 1-4 kpc (Vikhlinin et al. 2001; Sun et al. 2007), though they can be as large as 10 kpc. On the basis of these considerations, we pick our scale radius for calculation of the cooling time to be $0.01R_{500}$, which is deep inside the CC region even for low mass systems but generally outside the inner 4 kpc. Our surface brightness profiles have a radial resolution of $0.49''$, which is similar to the FWHM of the *Chandra* on-axis PSF. This corresponds to a physical scale of 4 kpc at z=1, and is smaller than $0.01R_{500}$ for all our systems apart from CDGS62 at z=1.27, for which $0.01\mathrm{R}_{500}$ lies just inside the innermost bin. Although our cooling time is derived from the analytical emissivity profile fitted (allowing for PSF blurring) to the radial surface brightness profile, the value for CDGS62 should be regarded as slightly less robust than the others, since it involves a small extrapolation inwards from the innermost data bin.

3.3.3 Entropy

Another parameter which can be used to characterize the thermal state of the gas is its entropy, which was defined in Equation 1.15 . To characterise the cluster core properties, we evaluate the entropy at a scale radius of $0.01R_{500}$.

Table 3.2: X-ray derived properties. Columns represent: 1) Source ID, which is the same as in Table 3.1; 2) Number of soft source counts (0.5-2.0 keV); 3) R_{500}estimated iteratively as explained in 2.6.1; 4) Gas temperature estimated from a thermal plasma model fit to a spectrum extracted within R_{500}; 5) Cooling time; 6) Cooling time normalized by the age of the cluster which is the age of the Universe at the cluster's redshift; 7) Entropy; 8)-10) Three cuspiness cool core indicators (see 3.4.2). All errors are 1σ errors. Errors for cooling time and entropy are calculated using Monte Carlo simulations (see 2.6.8), while errors in cuspiness cool core indicators are estimated based on error propagation. Unconstrained errors are marked with asterisks.

ID	Counts	R_{500}	kT (keV)	t_{cool} (Gyr)	t_{cool}/t_{Uni}	K (keV cm^2)	Csb	Fratio	Fc
CDGS1	2522	0.470	$0.98^{+0.18}_{-0.06}$	1.12 ± 0.57	0.09 ± 0.04	22.95 ± 7.31	0.393 ± 0.606	0.402 ± 0.374	3.87 ± 0.26
CDGS2	1008	0.519	$1.30^{+0.21}_{-0.06}$	3.27 ± 6.12	0.27 ± 0.50	46.94 ± 42.62	0.139 ± 0.143	0.278 ± 0.208	1.62 ± 0.20
CDGS3	1982	0.557	$2.08^{+1.83}_{-0.52}$	16.81 ± 22.72	1.36 ± 1.85	156.47 ± 184.10	0.055 ± 0.008	0.173 ± 0.017	0.52 ± 0.08
CDGS4	357	0.562	$1.54^{+0.46}_{-0.30}$	1.57 ± 1.08	0.13 ± 0.09	29.48 ± 13.96	0.100 ± 0.024	0.152 ± 0.032	2.27 ± 0.64
CDGS5	1047	0.492	$1.25^{+0.11}_{-0.14}$	1.96 ± 0.91	0.17 ± 0.08	32.95 ± 9.24	0.153 ± 0.079	0.140 ± 0.105	1.79 ± 0.41
CDGS6	2132	0.864	$3.42^{+0.80}_{-0.45}$	22.19 ± 14.99	1.95 ± 1.32	244.52 ± 123.01	0.057 ± 0.008	0.195 ± 0.017	1.20 ± 0.19
CDGS7	173	0.437	$1.01^{+0.19}_{-0.11}$	4.26 ± 6.54	0.38 ± 0.58	55.70 ± 45.33	0.173 ± 0.055	0.360 ± 0.114	1.44 ± 0.50
CDGS8	2413	0.708	$2.54^{+0.50}_{-0.49}$	8.27 ± 1.99	0.74 ± 0.18	107.51 ± 28.49	0.048 ± 0.005	0.225 ± 0.013	0.61 ± 0.06

CDGS9	910	0.778	$2.93^{+1.19}_{-0.62}$	1.47 ± 1.25	0.13 ± 0.11	36.71 ± 24.66	0.157 ± 0.020	0.302 ± 0.031	1.88 ± 0.25
CDGS10	17428	0.833	$3.42^{+0.20}_{-0.22}$	1.67 ± 1.26	0.15 ± 0.11	43.69 ± 18.27	0.200 ± 0.004	0.509 ± 0.009	1.49 ± 0.04
CDGS11	324	0.630	$1.83^{+1.00}_{-0.36}$	3.80 ± 16.67	0.34 ± 1.51	56.18 ± 95.19	0.215 ± 0.297	0.343 ± 0.107	0.90 ± 0.21
CDGS12	1528	0.660	$2.11^{+0.45}_{-0.27}$	1.27 ± 0.62	0.12 ± 0.06	28.07 ± 9.81	0.137 ± 0.015	0.207 ± 0.018	2.39 ± 0.32
CDGS13	1254	0.819	$3.37^{+0.95}_{-0.57}$	9.96 ± 4.13	0.91 ± 0.38	142.31 ± 64.28	0.043 ± 0.008	0.167 ± 0.014	0.86 ± 0.10
CDGS14	440	0.727	$2.77^{+2.64}_{-0.86}$	1.27 ± 2.21	0.12 ± 0.21	32.36 ± 46.18	0.186 ± 0.028	0.357 ± 0.054	1.85 ± 0.27
CDGS15	499	0.557	$1.76^{+0.55}_{-0.20}$	0.71 ± 0.32	0.07 ± 0.03	17.79 ± 6.89	0.173 ± 0.029	0.250 ± 0.034	2.23 ± 0.42
CDGS16	368	0.720	$2.99^{+1.22}_{-0.86}$	10.07 ± 12.81	1.01 ± 1.29	133.72 ± 118.12	0.088 ± 0.021	0.295 ± 0.062	1.09 ± 0.36
CDGS17	48672	1.107	$6.57^{+0.35}_{-0.22}$	0.54 ± 0.06	0.05 ± 0.01	30.08 ± 2.79	0.216 ± 0.003	0.635 ± 0.005	2.17 ± 0.03
CDGS18	733	0.662	$2.53^{+0.42}_{-0.29}$	5.25 ± 3.00	0.53 ± 0.30	79.10 ± 31.32	0.085 ± 0.013	0.263 ± 0.027	0.86 ± 0.16
CDGS19	516	0.735	$3.10^{+1.30}_{-0.73}$	14.42 ± 9.86	1.47 ± 1.01	173.22 ± 101.88	0.055 ± 0.014	0.208 ± 0.034	0.77 ± 0.23
CDGS20	1345	0.803	$3.52^{+0.76}_{-0.57}$	6.23 ± 4.24	0.65 ± 0.44	106.58 ± 53.60	0.085 ± 0.010	0.234 ± 0.017	1.29 ± 0.19
CDGS21	22738	1.221	$8.38^{+0.87}_{-0.41}$	0.66 ± 0.05	0.07 ± 0.01	39.75 ± 4.10	0.224 ± 0.004	0.566 ± 0.006	1.94 ± 0.04
CDGS22	639	0.668	$2.73^{+0.68}_{-0.51}$	11.38 ± 5.50	1.20 ± 0.58	137.77 ± 54.19	0.050 ± 0.011	0.149 ± 0.021	0.86 ± 0.25
CDGS23	203	0.558	$1.92^{+1.41}_{-0.32}$	7.71 ± 9.43	0.83 ± 1.01	90.18 ± 88.01	0.084 ± 0.027	0.325 ± 0.073	0.96 ± 0.38
CDGS24	675	0.553	$1.94^{+0.28}_{-0.22}$	5.26 ± 3.66	0.57 ± 0.40	70.11 ± 33.75	0.081 ± 0.014	0.190 ± 0.023	1.25 ± 0.32
CDGS25	14141	0.956	$5.59^{+0.25}_{-0.21}$	0.39 ± 0.03	0.042 ± 0.003	22.06 ± 1.38	0.364 ± 0.006	0.715 ± 0.010	1.57 ± 0.03
CDGS26	14546	0.956	$5.59^{+0.48}_{-0.36}$	0.49 ± 0.03	0.053 ± 0.003	25.68 ± 2.22	0.272 ± 0.005	0.565 ± 0.008	1.94 ± 0.05
CDGS27	10852	0.865	$4.59^{+0.43}_{-0.42}$	0.76 ± 0.27	0.08 ± 0.03	30.68 ± 7.47	0.163 ± 0.005	0.324 ± 0.007	2.04 ± 0.09
CDGS28	9837	0.897	$4.89^{+0.48}_{-0.25}$	0.34 ± 0.03	0.038 ± 0.003	18.59 ± 1.91	0.330 ± 0.007	0.654 ± 0.011	1.91 ± 0.06
CDGS29	17937	1.090	$7.10^{+0.58}_{-0.53}$	0.93 ± 0.08	0.10 ± 0.01	45.50 ± 4.23	0.242 ± 0.005	0.554 ± 0.007	2.10 ± 0.05
CDGS30	654	0.660	$2.66^{+0.45}_{-0.35}$	2.84 ± 1.65	0.32 ± 0.19	54.02 ± 22.41	0.109 ± 0.016	0.311 ± 0.030	1.21 ± 0.26
CDGS31	11194	1.013	$6.44^{+0.39}_{-0.55}$	1.59 ± 0.17	0.18 ± 0.02	61.31 ± 6.64	0.170 ± 0.005	0.619 ± 0.010	1.27 ± 0.04
CDGS32	205	0.476	$1.57^{+0.24}_{-0.20}$	2.48 ± 2.80	0.28 ± 0.32	40.00 ± 25.63	0.095 ± 0.027	0.259 ± 0.054	1.00 ± 0.26
CDGS33	428	0.664	$3.01^{+0.93}_{-0.94}$	12.20 ± 7.38	1.40 ± 0.84	152.60 ± 74.42	0.078 ± 0.019	0.208 ± 0.034	0.99 ± 0.32
CDGS34	20101	1.392	$12.36^{+0.73}_{-0.63}$	7.60 ± 0.40	0.90 ± 0.05	248.07 ± 15.62	0.032 ± 0.002	0.229 ± 0.004	0.70 ± 0.03
CDGS35	1745	0.763	$4.18^{+0.39}_{-0.37}$	12.29 ± 1.06	1.48 ± 0.13	185.34 ± 19.19	0.029 ± 0.005	0.128 ± 0.010	0.51 ± 0.11
CDGS36	1142	0.625	$2.87^{+0.41}_{-0.58}$	5.05 ± 1.65	0.61 ± 0.20	82.47 ± 23.62	0.097 ± 0.011	0.282 ± 0.021	1.01 ± 0.17
CDGS37	11370	1.077	$7.96^{+0.35}_{-0.36}$	9.76 ± 0.32	1.20 ± 0.04	233.19 ± 10.84	0.032 ± 0.002	0.248 ± 0.006	0.59 ± 0.04
CDGS38	1850	0.821	$4.83^{+0.85}_{-0.95}$	1.18 ± 0.55	0.14 ± 0.07	42.45 ± 14.67	0.104 ± 0.009	0.339 ± 0.018	1.17 ± 0.14
CDGS39	193	0.751	$3.58^{+9.00}_{-1.53}$	0.63 ± 1.18	0.08 ± 0.15	23.35 ± 54.95	0.328 ± 0.059	0.713 ± 0.167	1.17 ± 0.19
CDGS40	127	0.685	$3.58^{+21.56}_{-1.75}$	4.31 ± 15.85	0.55 ± 2.04	84.13 ± 429.50	0.103 ± 0.037	0.345 ± 0.084	1.05 ± 0.47
CDGS41	2725	0.507	$2.16^{+1.11}_{-0.35}$	16.00 ± 18.03	2.12 ± 2.38	153.01 ± 134.27	0.046 ± 0.009	0.104 ± 0.072	0.84 ± 0.19
CDGS42	330	0.450	$1.67^{+1.65}_{-0.93}$	6.57 ± 49.42	0.87 ± 6.55	77.21 ± 164.94	0.119 ± 0.035	0.228 ± 0.059	1.60 ± 0.59
CDGS43	1478	0.791	$4.92^{+0.48}_{-0.40}$	3.90 ± 0.78	0.52 ± 0.10	95.14 ± 15.49	0.074 ± 0.008	0.397 ± 0.022	0.75 ± 0.10
CDGS44	2526	0.972	$7.37^{+1.78}_{-1.46}$	11.80 ± 4.08	1.58 ± 0.55	253.74 ± 83.36	0.035 ± 0.005	0.194 ± 0.010	0.59 ± 0.08
CDGS45	1334	0.777	$4.98^{+0.86}_{-0.47}$	5.76 ± 2.14	0.79 ± 0.29	124.31 ± 36.34	0.063 ± 0.008	0.292 ± 0.020	0.80 ± 0.13
CDGS46	1033	0.695	$4.13^{+0.86}_{-0.74}$	4.06 ± 1.33	0.56 ± 0.18	87.89 ± 25.12	0.099 ± 0.012	0.341 ± 0.025	0.80 ± 0.14

CDGS47	1262	0.757	$5.00^{+1.56}_{-1.68}$	16.36 ± 4.52	2.25 ± 0.62	249.86 ± 93.94	0.028 ± 0.006	0.122 ± 0.013	0.53 ± 0.13
CDGS48	1496	0.610	$3.31^{+1.19}_{-0.75}$	16.40 ± 12.87	2.25 ± 1.77	195.69 ± 121.22	0.080 ± 0.089	0.110 ± 0.034	0.95 ± 0.16
CDGS49	542	0.550	$2.53^{+0.88}_{-0.60}$	1.71 ± 2.29	0.24 ± 0.32	37.34 ± 32.01	0.160 ± 0.026	0.292 ± 0.051	1.53 ± 0.29
CDGS50	1531	1.063	$9.31^{+7.81}_{-4.54}$	8.68 ± 4.91	1.22 ± 0.69	237.14 ± 171.73	0.057 ± 0.007	0.512 ± 0.033	0.73 ± 0.08
CDGS51	3730	0.882	$6.68^{+1.00}_{-0.75}$	3.02 ± 0.48	0.43 ± 0.07	96.74 ± 16.53	0.097 ± 0.006	0.432 ± 0.014	0.97 ± 0.07
CDGS52	321	0.627	$3.34^{+1.69}_{-0.80}$	3.18 ± 3.09	0.46 ± 0.45	65.97 ± 52.96	0.126 ± 0.027	0.224 ± 0.038	1.49 ± 0.49
CDGS53	340	0.566	$2.85^{+1.14}_{-0.75}$	5.66 ± 45.89	0.84 ± 6.80	88.40 ± 163.53	0.120 ± 0.027	0.346 ± 0.083	0.78 ± 0.22
CDGS54	594	0.666	$4.36^{+2.27}_{-2.15}$	3.87 ± 4.79	0.60 ± 0.75	87.90 ± 84.47	0.093 ± 0.015	0.252 ± 0.028	1.07 ± 0.20
CDGS55	620	0.679	$5.44^{+8.15}_{-2.48}$	1.70 ± 10.42	0.28 ± 1.69	58.40 ± 216.32	0.242 ± 0.063	1.061 ± 0.367	1.03 ± 0.13
CDGS56	1781	0.980	$10.43^{+5.87}_{-3.32}$	3.41 ± 1.78	0.57 ± 0.30	136.92 ± 80.37	0.105 ± 0.009	0.406 ± 0.021	1.21 ± 0.12
CDGS57	1200	0.722	$5.98^{+2.13}_{-1.03}$	0.58 ± 0.86	0.10 ± 0.15	30.05 ± 27.71	0.139 ± 0.013	0.352 ± 0.022	1.39 ± 0.18
CDGS58	385	0.577	$4.75^{+1.82}_{-1.69}$	7.43 ± 8.63	1.33 ± 1.54	143.06 ± 102.50	0.098 ± 0.019	0.300 ± 0.042	0.83 ± 0.23
CDGS59	313	0.444	$2.57^{+0.37}_{-0.33}$	0.40 ± 8.35	0.07 ± 1.50	14.18 ± 57.47	0.073 ± 0.018	0.156 ± 0.029	1.88 ± 0.61
CDGS60	757	0.664	$6.07^{+2.87}_{-1.27}$	4.38 ± 2.59	0.86 ± 0.51	116.94 ± 67.07	0.090 ± 0.014	0.268 ± 0.026	0.98 ± 0.21
CDGS61	351	0.621	$6.50^{+4.10}_{-3.05}$	7.61 ± 23.68	1.51 ± 4.70	176.47 ± 251.38	0.109 ± 0.021	0.288 ± 0.045	1.00 ± 0.28
CDGS62	124	0.331	$1.81^{+0.68}_{-0.59}$	$3.64 \pm ***$	$0.73 \pm ***$	$53.11 \pm ***$	0.118 ± 0.044	0.147 ± 0.049	0.74 ± 0.55

3.3.4 Quantifying cool core status

In order to study the evolution of cooling in cluster cores, we need to choose an indicator of cool core strength. Ideally, this indicator should be able to distinguish CC and NCC systems in a way which is minimally affected by variations in redshift, temperature and data quality. As discussed earlier, several CC estimators have been used in the literature: some are based on the central temperature drop (Maughan et al. 2012), some quantify the central surface brightness excess (Maughan et al. 2012; Alshino et al. 2010; Santos et al. 2008), whilst others are based on physical characteristics like central cooling time or entropy (Peres et al. 1998; Bauer et al. 2005; Mittal et al. 2009).

Parameters that define the CC strength based on the amplitude of the central temperature drop observed in the temperature profile of the system are not accessible to us here because of the high quality data required to construct temperature profiles. As many of our systems lie not far above our 100 count lower limit, even calculating the ratio of central to outer temperature is not feasible. Central cooling leads to increased gas density, resulting in a sharp central cusp in surface brightness. This has been used to define a number of different CC diagnostics. These approaches have the advantage that they require only imaging data and can therefore be applied over a wide range in data quality. When defining these parameters, generally a size for the CC is assumed in order to separate the emission coming from the core from the larger scale emission. It is not *a priori* clear what scale should be chosen to separate core from cluster emission. Maughan et al. (2012) use a fraction of R_{500}, whilst Santos et al. (2008) argue that cluster cores cannot be expected to evolve in a self-similar fashion and so use a fixed metric radius of 40 kpc.

Given the wide mass and redshift ranges spanned by our sample, the choice of core radius has a significant impact, and is therefore a disadvantage for these methods. We therefore prefer to base the bulk of our analysis on more physically motivated CC indicators. However, in Chapter 3.4.2, we calculate some these cuspiness indicators for our sample, and compare the results with those from our preferred methods.

Central cooling time and entropy are gas properties which are well-established to differ between CC and NCC clusters. Both are determined primarily by gas density and temperature, though cooling time is also affected by metallicity, which we take to be 0.3 solar. As a result, the two properties are closely related. Cooling time ($t_{\rm cool}$) is more directly related to the cooling status of the system, so we use this for preference. As discussed in Chapter 3.3.2 above, our 'central' cooling time is actually calculated at a radius $0.01R_{500}$.

It will be helpful for some of our analysis to adopt a threshold value for $t_{\rm cool}$ to mark the transition between CC and NCC systems. Previous studies in which central cooling time is used as a CC diagnostic have used a variety of cooling time thresholds, ranging from 0.8 Gyr up to the age of the Universe (Peres et al. 1998; Bauer et al. 2005; Mittal et al. 2009). To help motivate our own choice, we note that some studies of the distribution of central entropy in groups and clusters have shown the existence of *bimodality* (Cavagnolo et al. 2009; Sanderson et al. 2009; Mahdavi et al. 2013). Moreover, Cavagnolo et al. (2008) show that systems with a central entropy lower than 30 keV cm^2 show evidence for gas cooling at the cluster centre, in the form of optical emission lines.

Although both the Cavagnolo and Mahdavi studies show the existence of bimodality in the entropy distribution, the break between the two peaks occurs at 30-50 keV cm^2 for Cavagnolo et al. (2009) but 70 keV cm^2 for Mahdavi et al. (2013). However, the difference between these two values can be explained by the difference in the radius at which the entropy has been calculated. This is effectively the centre in the former case, but is 20 kpc for the latter.

Since our measurement is closer to the first of these, we adopt a cooling time threshold corresponding to a central entropy of 40 keV cm^2, which lies within the 30-50 keV cm^2 interval from Cavagnolo et al. (2009). The tight correlation between our cooling time and entropy values is shown in Figure 3.3. Since entropy scales as $T/n_e^{2/3}$, whilst cooling time scales (in the bremsstrahlung regime) as $T^{1/2}/n_e \propto K^{3/2}/T$, we see that there is some offset in the Figure between groups and clusters, such that the gas in clusters has a rather shorter cooling time at given entropy. Averaging over our sample, we adopt 1.5 Gyr as a sensible cooling time threshold.

An important issue, highlighted in the recent study by McDonald et al. (2013), is the distinction between the rate of current cooling and the amount of gas which has been able to cool. $t_{\rm cool}$ is a measure of the former, but for a cluster at high redshift less time has been available for cooling to take effect. Since both current cooling and the accumulated effects of cooling are of interest to us, we construct a further cool core indicator, $t_{\rm cool}/t_{\rm Uni}$, in which cooling time is divided by the age of the Universe ($t_{\rm Uni}$) in our adopted cosmology, at the redshift of the cluster. This represents the fraction of gas which could have cooled in the lifetime of the cluster, in the absence of AGN feedback. In practice, the impact of AGN feedback is believed to suppress gas cooling by an order of magnitude (McNamara & Nulsen 2012), but cannot prevent it altogether. In these circumstances, the integrated fraction of a cluster's gas which could have cooled over its history should still scale roughly with $t_{\rm cool}/t_{\rm Uni}$, though the impact of cyclic AGN activity on the cooling time in the core will introduce considerable scatter.

We calculate the threshold value for this parameter, separating CC from NCC systems, by dividing the threshold used for $t_{\rm cool}$ (1.5 Gyr) by the age of the Universe at the median redshift of systems from our sample (8.7 Gyr). This gives a threshold value for $t_{\rm cool}/t_{\rm Uni}$ of 0.17, which will be used below.

3.4 Results

3.4.1 Cool core evolution

The evolution of CC strength, as quantified by $t_{\rm cool}$ and $t_{\rm cool}/t_{\rm Uni}$, as well as entropy, all evaluated at radius $0.01\rm R_{500}$, is shown in Figure 3.4. For each parameter, we plot the results obtained when using the entire sample (left panel), a subsample which contains only clusters ($T \geq 3$ keV, middle panel) and one which contains only groups (right panel). This temperature cut allows us to compare the behaviour of evolutionary trends in the two mass regimes.

In each panel, black points represent the data, whilst the contoured colour scale traces the smoothed density of points. The black dotted line shows the threshold adopted for separating CC from NCC systems (0.17 for $t_{\rm cool}/t_{\rm Uni}$, 1.5 Gyr for cooling time and 40 keV cm^2 for entropy). In each case, CC systems lie below the line.

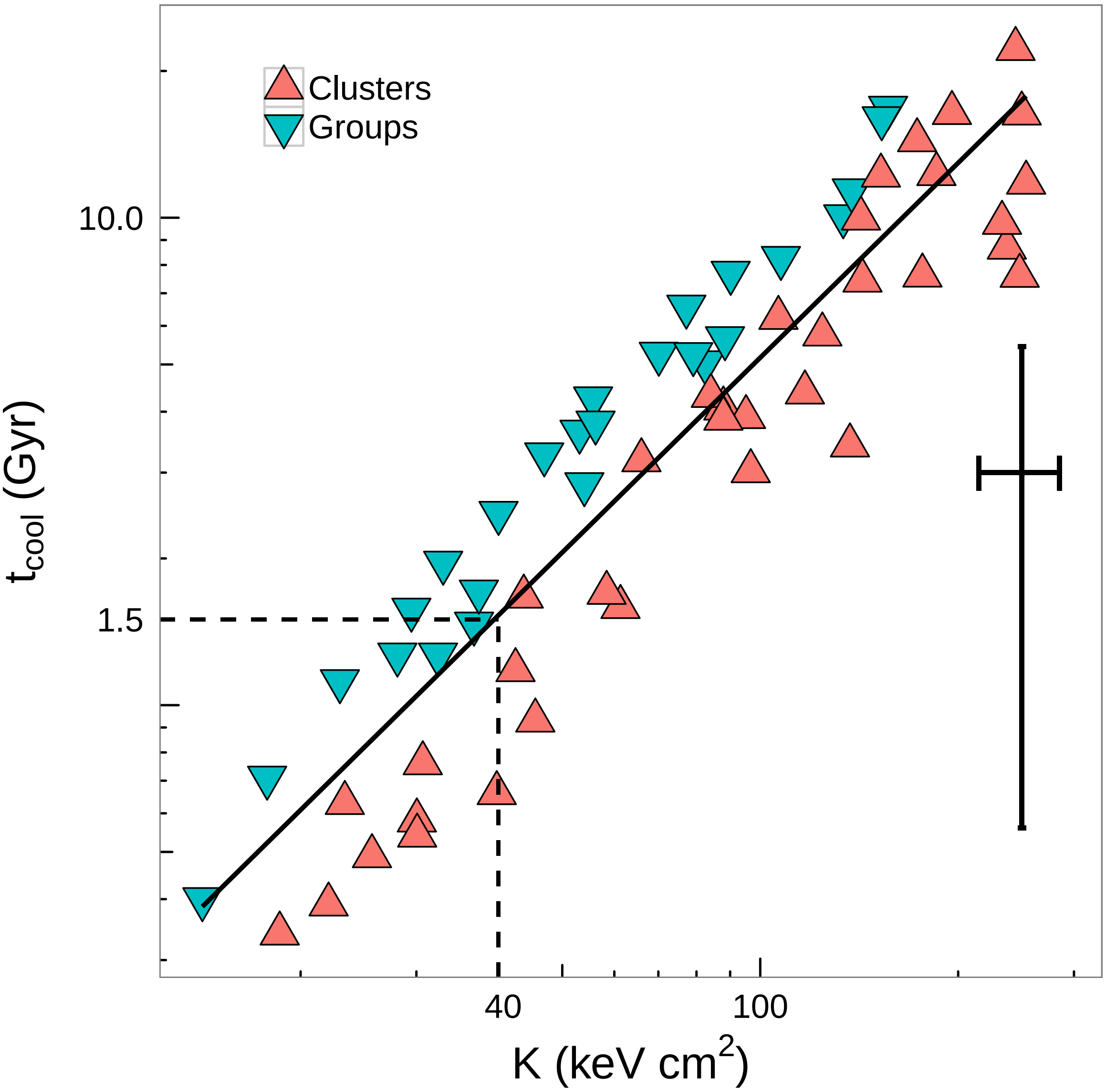

Figure 3.3: Relation between cooling time and entropy, both calculated at 0.01R$_{500}$, for our sample. Black solid line represents the best fit for all systems in the sample. Dashed lines mark the thresholds for K and $t_{\rm cool}$ used to separate CC from NCC systems. The error bars on the black point represent the median error for $t_{\rm cool}$ and K. These are 1σ errors.

A broadly similar pattern is seen in all three rows. Some bimodality is apparent in the distribution for all three parameters. This bimodality is more pronounced in the cluster sub-population, whilst in groups the pattern is quite similar, but the CC and NCC peaks move closer together and merge into a single elongated distribution.

Examining density plots such as Figure 3.4 is not a reliable way of establishing evolutionary trends. For example, the shape of the density contours can be substantially modified by transformations of the axes (plotting the cool core indicators in unlogged form, for example). We have therefore tested for correlations of our CC indicators with redshift by calculating the Spearman rank correlation coefficient. The results are shown in the first three rows of Table 3.3. Values for our X-ray selected sample occupy the left hand side of the Table. Corresponding values for our 'extended sample' will be discussed later, in Chapter 3.5.3.

Table 3.3: Statistical tests for redshift evolution of various cool core estimators. The correlation is quantified by Spearman's rank correlation coefficient which is given with associated p-value for each cool core parameter stated in the first column. Left hand side part of the table shows correlation test for X-ray selected sample presented in Table 3.2, while the right hand side shows correlation for the extended sample which will be described in Chapter 3.5.3. For each sample, correlation is tested for the entire sample, clusters and groups. The first three rows present the correlation for cooling time normalized by the age of the cluster, cooling time and entropy, while last three rows present correlation for three cool core cuspiness parameters which are described in Chapter 3.4.2.

	X-ray selected sample						Extended sample					
Parameter	All sample		Clusters		Groups		All sample		Clusters		Groups	
	Coeff	P-val	Coeff	P-val	Coeff	P-val	Coeff	P-val	Coeff	P-val	Coeff	P-val
$\mathbf{t}_{\rm cool}/\mathbf{t}_{\rm Uni}$	0.26	0.04	0.27	0.12	0.28	0.17	0.29	0.006	0.29	0.03	0.35	0.06
$\mathbf{t}_{\rm cool}$	0.07	0.58	0.12	0.49	0.14	0.49	0.11	0.35	0.14	0.30	0.19	0.32
K	0.26	0.04	0.22	0.20	0.17	0.41	0.29	0.006	0.24	0.07	0.22	0.25
$\mathbf{c}_{\rm SB}$	-0.17	0.19	-0.09	0.59	-0.31	0.12	-0.24	0.03	-0.18	0.18	-0.38	0.04

F_{core}	0.04	0.74	-0.07	0.70	-0.15	0.45	-0.06	0.57	-0.16	0.24	-0.26	0.17
f_c	-0.35	0.005	-0.35	0.03	-0.33	0.10	-0.34	0.001	-0.29	0.03	-0.36	0.05

The Table gives the values of the correlation coefficient for a trend in each CC indicator with redshift. Being a rank correlation coefficient, this is independent of any monotonic transformation of either axis. For each coefficient, the chance probability (2-tailed) of obtaining a value deviating from zero by this value or more is also quoted.

As can be seen from the Coeff and P-val columns corresponding to the X-ray selected sample (left part of Table 3.3), a significant trend ($p = 0.04$) is apparent in $t_{\rm cool}/t_{\rm Uni}$ (and to a lesser extent in entropy) for both the full (cluster + group) sample, and for clusters alone. The group subsample shows a correlation coefficient of similar size, but this is less significant, given the smaller number of systems involved. However, the $t_{\rm cool}$ indicator shows *no* significant trend with redshift.

As a further test, we examine the distribution of our two main CC indicators across the sample at low and high redshift, and apply a Kolmogorov-Smirnov (K-S) test to see whether they differ. We choose a redshift cut at 0.5 to separate the low and high redshift samples for this test, motivated by previous results in the literature which report a change in the properties of CCs at redshifts greater than 0.5 (Vikhlinin et al. 2007). However we have tested various redshift thresholds and find similar results for any cut between 0.5 and 0.65. For $t_{\rm cool}/t_{\rm Uni}$ we find a highly significant difference ($p = 0.009$) between the distributions at high and low redshift. As shown in Figure 3.5, our low redshift systems are more strongly concentrated towards low values of $t_{\rm cool}/t_{\rm Uni}$, confirming the redshift trend indicated by the Spearman rank analysis. Performing a similar analysis for $t_{\rm cool}$ we find a much weaker difference between the high and low redshift distributions, though it can still be significant, depending on the value of the redshift cut. We will return to this with our larger 'extended sample' in Chapter 3.5.3 below.

Returning to the interpretation of our two main CC indicators as representing *current* cooling ($t_{\rm cool}$) and *accumulated* cooling ($t_{\rm cool}/t_{\rm Uni}$) in the core, our conclusion at this stage seems to be that the latter is evolving, whilst the former is not. However, before we can draw such a conclusion, we need to examine the possibility that the trends we see could be driven primarily by a changing composition in cluster richness with redshift, rather than evolution in properties for clusters at a given richness. Despite the rather similar behaviour in clusters and groups seen in Figure 3.3, it is well known that groups have gas properties which differ systematically from richer clusters – with flatter surface brightness profiles (Ponman et al. 1999) and more compact central cooling regions (Rasmussen & Ponman 2007).

In Figure 3.6 we examine the distribution in system temperature with redshift within our sample. As expected, the galaxy groups ($T < 3$ keV), which are less luminous X-ray sources, are concentrated towards lower redshifts. However, interestingly this effect is largely confined to $z < 0.35$, and above this redshift, the mean temperature of our sample is essentially constant, at around 4.5 keV. We have already seen that our conclusions about the trend in $t_{\rm cool}/t_{\rm Uni}$ and the lack of evolution in $t_{\rm cool}$ apply even if we exclude groups from our analysis. If we instead retain the full temperature range, but exclude all systems with $z < 0.35$, a positive correlation (coefficient=0.21) remains, but its significance is reduced, due to the smaller sample and reduced redshift baseline. We conclude that our results are *not* being driven by redshift-dependent temperature biases in the sample.

3.4.2 Cuspiness cool core indicators

As we discussed earlier, most previous studies of cool core evolution have been based on an analysis of central surface brightness excess. We now apply some of these estimators to our own sample, for comparison with our above findings based on cooling time, and with results of earlier studies.

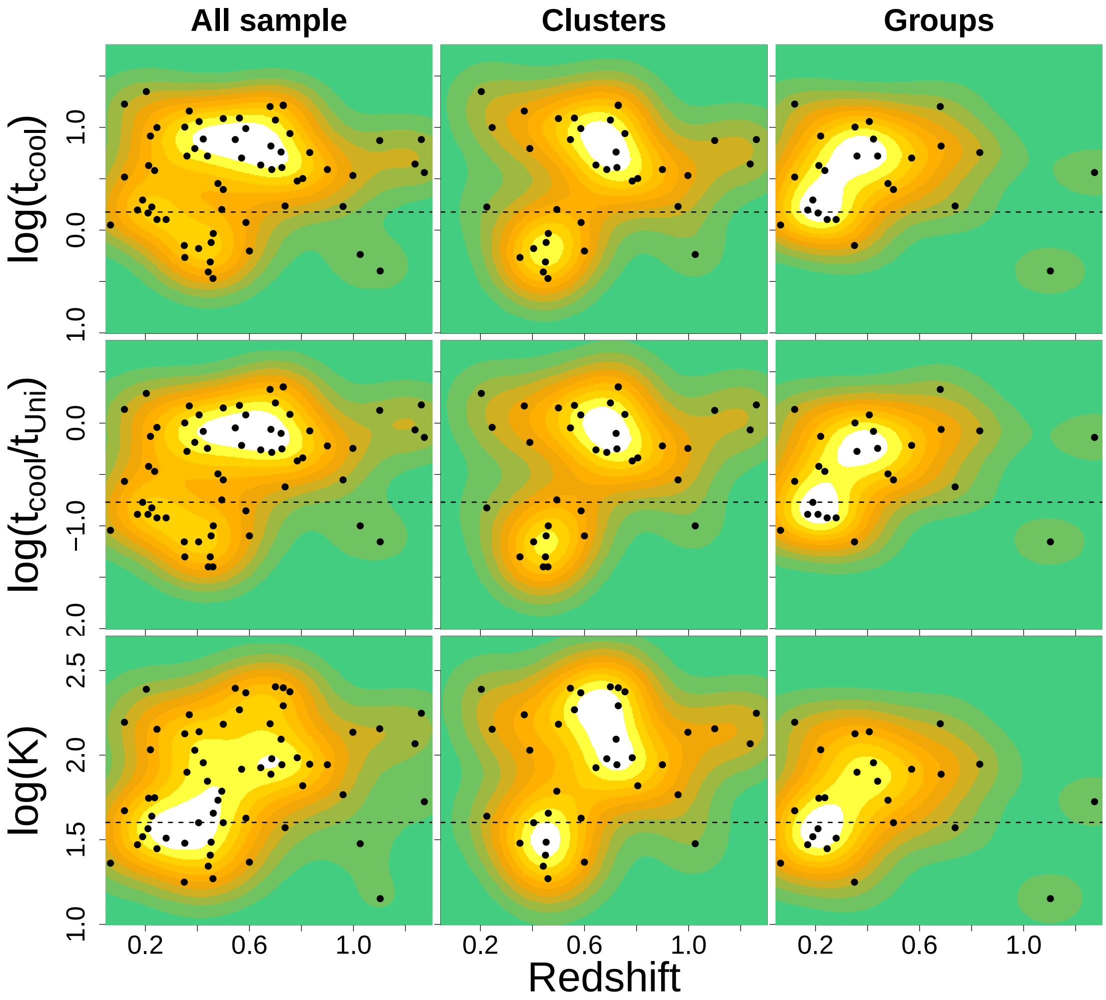

Figure 3.4: Distribution of different CC estimators with redshift: cooling time (top row), cooling time divided by the age of the Universe (middle row) and entropy (bottom row). For each parameter the distribution for all sample, clusters and groups is showed in the left, middle and right panel. Data points are showed as black dots and the contours represent number density contours. The dotted line represents the threshold between CCs and NCCs

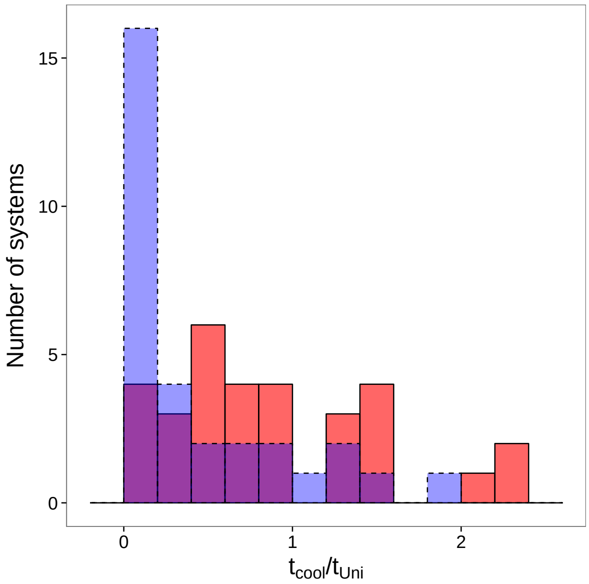

Figure 3.5: Distribution of $t_{\rm cool}/t_{\rm Uni}$ for the low (blue, dashed line) and high (red, solid line) redshift systems. The redshift threshold used to divide between these two subsamples is 0.5.

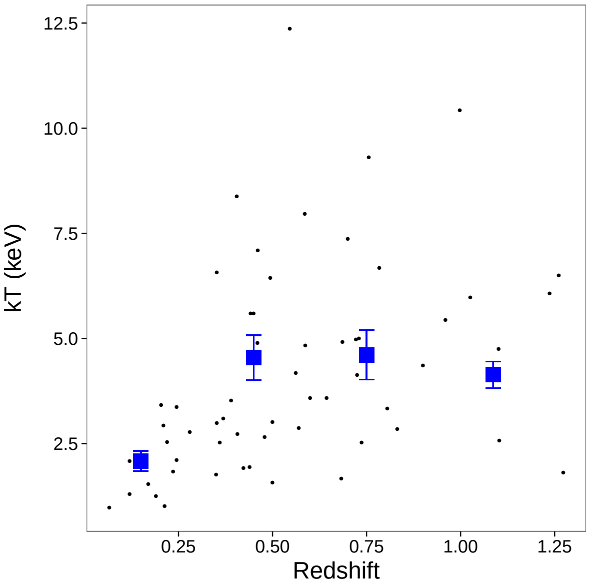

Figure 3.6: Relation between temperature and redshift for all systems in our sample. Black points marks individual systems while blue squares represent the mean temperature in four different redshift bins: 0-0.3, 0.3-0.6, 0.6-0.9, 0.9-1.27

We use three CC estimators defined in the literature: surface brightness concentration(c_{SB}; Santos et al. (2008)), the core flux ratio (F_{core}; Maughan et al. (2012)) and the central excess factor(f_{c}; Alshino et al. (2010)), for which we employ the same symbols as the original authors.

The c_{SB} parameter is defined as the ratio between the flux measured within circular apertures with radii of 40 kpc and 400 kpc, centred on the peak of the cluster X-ray emission. These radii were found by Santos et al. (2010) to optimize the separation between CC and NCC in a sample of simulated low redshift clusters. They motivated the use of a fixed physical radius rather than a fraction of the scale radius, R_{500}, by the fact that cool cores are the result of non-gravitational processes and therefore their sizes do not scale self-similarly. In their study, Santos et al. (2010) used c_{SB} to divide the sample into strong (SCC), weak (WCC) and non cool core (NCC) classes, with $c_{\mathrm{SB}} > 0.155$, $0.075 \leq c_{\mathrm{SB}} \leq 0.155$, and $c_{\mathrm{SB}} < 0.075$, respectively.

Similar to the c_{SB} parameter is the F_{core} parameter, which is defined also as a flux ratio, but with aperture radii defined as fractions of R_{500} instead of fixed physical sizes. Following Maughan et al. (2012), F_{core} is taken to be the ratio of flux within $0.15R_{500}$ to that within R_{500}. We add that while the definition of this parameter is similar to the one used by Maughan et al. (2012), the way in which we calculate the fluxes is based only upon imaging data, whilst Maughan et al. (2012) calculate the unabsorbed flux from spectra extracted within each aperture. If the core flux is greater than half of the flux within R_{500} (i.e. $F_{\mathrm{core}} > 0.5$), the system is characterized as a CC.

While c_{SB} and F_{core} are simple parameters which do not require any modelling of the data, the f_{c} parameter of Alshino et al. (2010) quantifies the strength of a CC using the central excess in surface brightness profile above a fitted beta model with a fixed core radius of $0.105R_{500}$. This core radius was chosen by Alshino et al. (2010) to correspond to the observed size of cores seen in the group-scale emission of well-resolved low redshift groups of galaxies by Helsdon & Ponman (2000). A CC is deemed to be present if the ratio (f_{c}) of the observed flux within $0.05R_{500}$ to the corresponding flux derived from the fitted beta model (with core radius of $0.105R_{500}$) is greater than unity.

All three of these CC indicators have been found by their proponents to show evolutionary trends, so we investigate their relationship with our $t_{\rm cool}$ indicator. Figure 3.7 shows in each panel the correlation between $t_{\rm cool}$ and the three surface brightness based CC estimators. Different symbol styles and colours differentiate groups and clusters, and the presence of a central black point denotes systems characterized as CC according to the y-axis parameter. (For $c_{\rm SB}$ we use the SCC criterion.) We have marked on the x-axis the value $t_{\rm cool}$=1.5 which is our adopted CC threshold.

Note that, in contrast to our calculation of $t_{\rm cool}$ and $t_{\rm cool}/t_{\rm Uni}$, no correction for any central AGN has been applied when calculating the surface brightness cuspiness indicators. Hence clusters with a bright central AGN will be biased towards showing CC properties. As we discuss later in Chapter 3.5.1, the indications are that AGN contamination is not a major problem in our sample.

Firstly, ignoring the distinction between groups and clusters, it can be seen that the best correlation with $t_{\rm cool}$ is found for $c_{\rm SB}$. We have calculated the Spearman coefficient for all parameters and find the highest coefficient for $c_{\rm SB}$ (-0.82), closely followed by $f_{\rm c}$ (-0.77), while the lowest correlation is found for the $F_{\rm core}$ parameter (Spearman coefficient of -0.60).

The correlation between $c_{\rm SB}$ and $t_{\rm cool}$ is much stronger than that between $F_{\rm core}$ and $t_{\rm cool}$, although both parameters are defined as the flux ratio between the core and the bulk of the system, the only difference being in the sizes adopted for the inner and outer regions. Before drawing any conclusions about this discrepancy, we remind the reader that each CC indicator has been optimized to be applied to samples dominated by either clusters ($c_{\rm SB}$ and $F_{\rm core}$) or groups ($f_{\rm c}$), while our sample includes both types of system. Therefore we compare the performance of each parameter on the system class for which it has been designed.

Applying $c_{\rm SB}$ and $F_{\rm core}$ to just our cluster subsample, we see that both parameters give similar

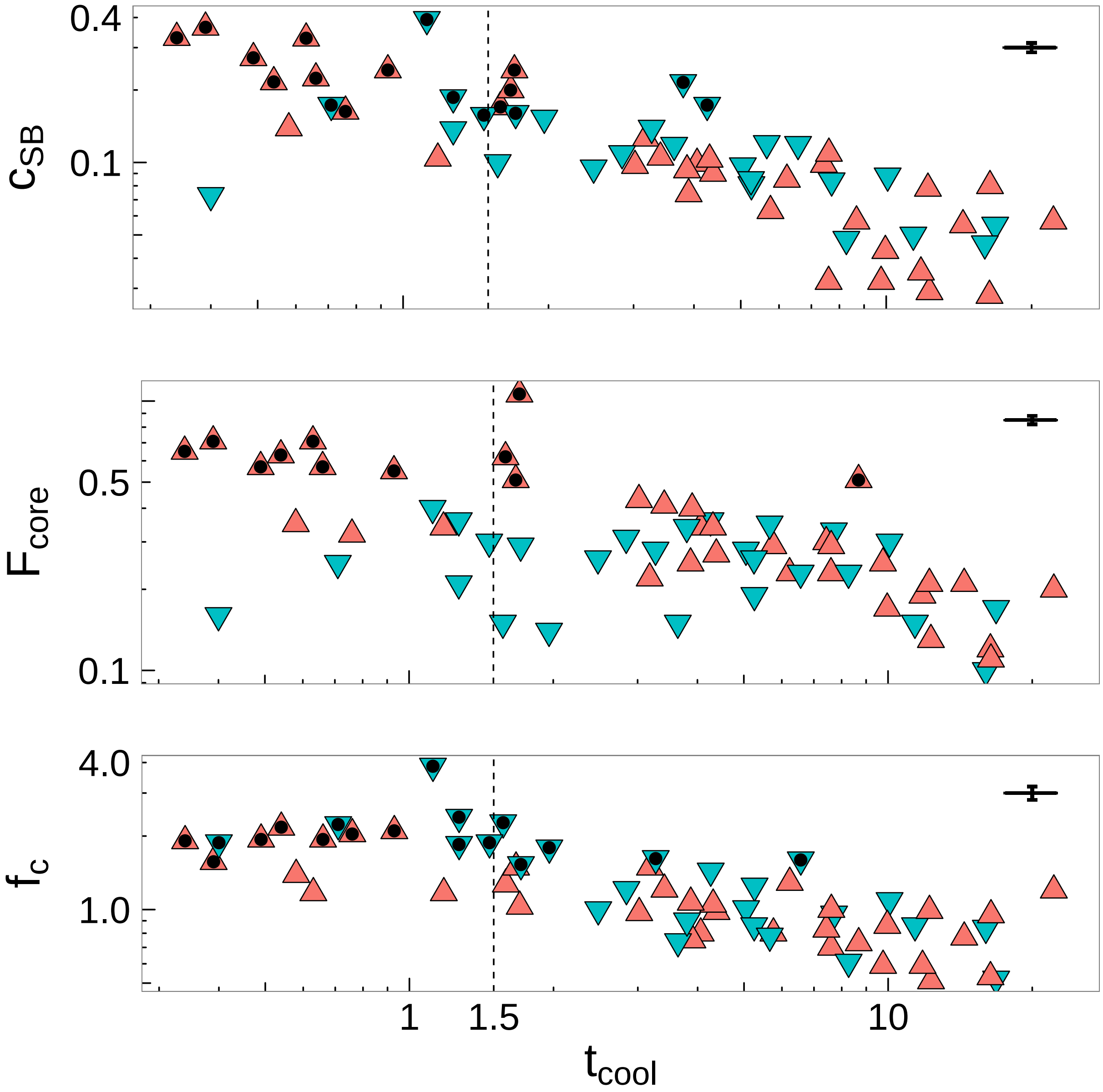

Figure 3.7: Correlation between t_{cool} and three cool core estimators based on cuspiness in surface brightness: c_{SB}, $F_{\mathrm{core}}$and f_{c}. In each panel, the symbol style and colour differentiates between groups (triangle point-down) and clusters (triangle point-up). Symbols which include a filled black circle are classified as CCs according to the surface brightness parameter represented on the y-axis. The dashed vertical line marks the threshold between CC and NCC for t_{cool}.

strong correlations: -0.85 (F_{core}) and -0.89 (c_{SB}). However, for the group subsample, there is a large discrepancy in the correlation coefficients: -0.64 for c_{SB} and -0.17 for F_{core}. The poor correlation seen for F_{core} in the case of groups can be explained by the large size of the radius chosen to characterize the core region ($0.15R_{500}$). For clusters, this is approximately the size of the cool core, when it is present, whilst in groups cores are smaller, extending to a radius of typically only $0.1R_{500}$ (Rasmussen & Ponman 2007).

Comparing the symbols marked by black circles in Figure 3.7 with the position of the vertical dashed line, we can examine the fraction numbers of CC systems amongst groups and clusters identified by each method. The c_{SB} indicator shows excellent agreement with t_{cool} when applied to clusters, whilst for groups it identifies a similar total number of CC systems, but not necessarily the same ones. For F_{core}, the clusters characterized as CC are again similar to those identified by t_{cool}, but not a single group is classified as a CC. f_{c} identifies fewer CC clusters than t_{cool}, but includes some groups with rather long cooling times as being CC systems.

In Figure 3.8 we plot the distribution of the surface brightness based CC estimators against redshift, in a similar fashion to Figure 3.4. Note that for these three estimators *high* values correspond to strong cool cores, in contrast to our three previous estimators. We have therefore flipped the y axis scales so that core dominance still increases downward on each plot. For the c_{SB} plot, the two horizontal lines correspond to the two thresholds used by Santos et al. (2008), dividing clusters into SCC (bottom), WCC (middle) and NCC (top) classes.

The distributions for all three indicators show similarities with our earlier cooling time and entropy based parameters. In particular, all show some signs of bimodality, at least for clusters. In the case of c_{SB}, there is the wide variety in the CC strength at low redshifts, while for redshifts greater than 0.6 the NCC and SCC classes largely disappear, leaving only WCC systems. F_{core} shows a similar pattern of narrowing towards intermediate core strength at $z > 0.7$, whilst f_{c} shows less symmetrical behaviour.

Results from Spearman rank tests for correlation with redshift are shown in the bottom three rows of Table 3.3, and confirm the visual impression from Figure 3.8. For the X-ray sample (left hand side of Table 3.3) only $f_{\rm c}$ shows a significant evolutionary trend. This correlation (negative, due to the reversed sense of the indicator compared to the physically based indicators shown in the first three rows of the Table) is apparent for clusters and groups individually, as well as for the combined sample.

3.4.3 Systems with photometric redshift

The majority of the sample used in this study (presented in Table 3.1 and Table 3.2) consists of groups and clusters, detected as extended sources in X-ray images, whose nature is confirmed through spectroscopic redshifts of galaxy members. However, for 23% (14 out of 62) of the sample no spectroscopic redshift was available in the literature, and the redshift used in our analysis is photometric.

While the accuracy of cluster photometric redshifts is typically at a level of $\sim 0.02 - 0.05$ out to redshift of 1 (Bahcall et al. 2003; Koester et al. 2007; Pelló et al. 2009; Takey et al. 2013), which is perfectly adequate for our purposes, occasional 'catastrophic errors' in photometric redshifts can be up to an order of magnitude higher (Mullis et al. 2003; Koester et al. 2007; Pelló et al. 2009). Moreover, in the absence of spectroscopic confirmation that associated galaxies are really clustered in redshift, the identification of a cluster must be regarded as provisional.

We have therefore examined the effects of excluding the systems with photometric redshifts from our analysis. This produces no significant difference in our results. The nature of the trends seen do not change, but some become rather stronger. The most noticeable differences are found for

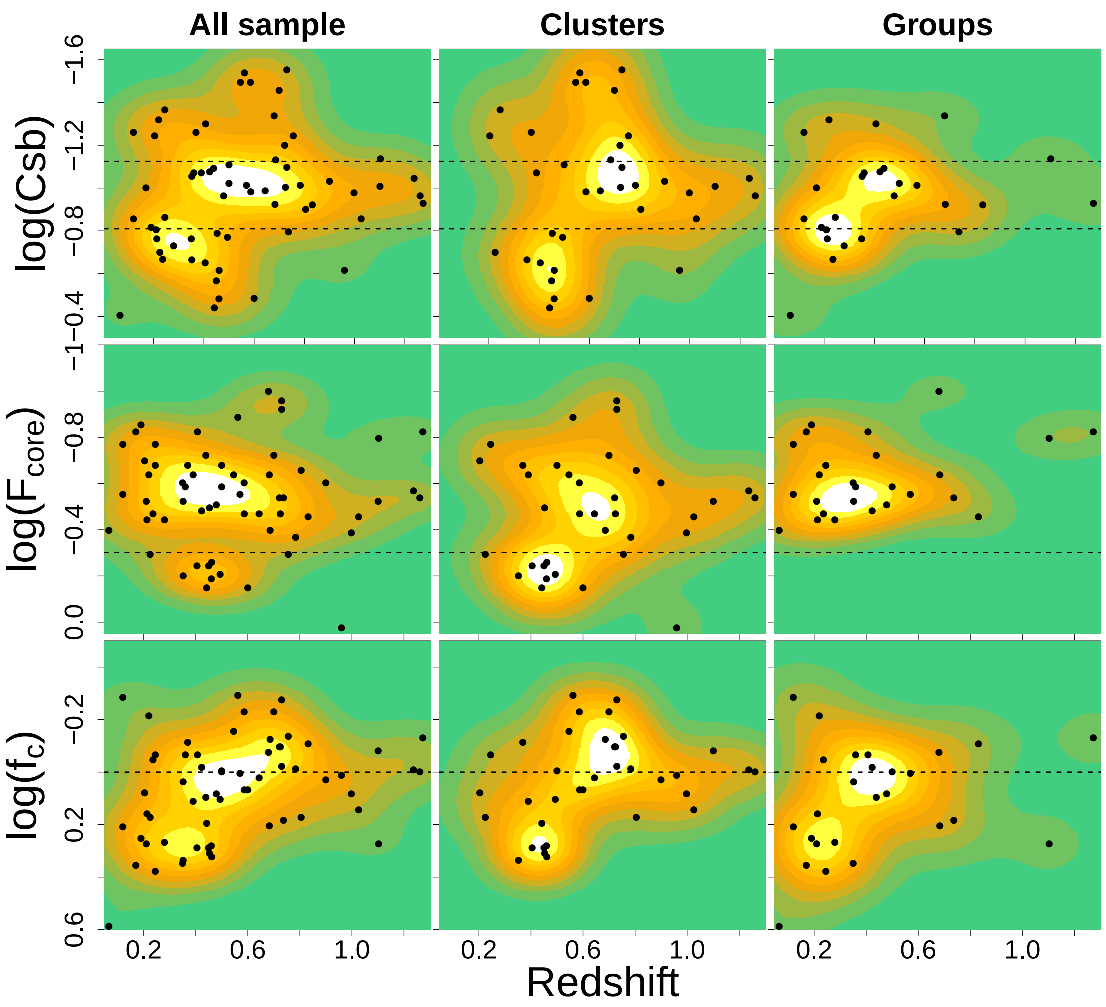

Figure 3.8: Redshift distribution for three different cool core estimators defined in the literature based on the surface brightness excess: $c_{\rm SB}$, $F_{\rm core}$ and $f_{\rm c}$. As in Figure 3.4, left column of panels corresponds to all sample, middle panel to clusters and right one to groups. In each plot, the black horizontal line divides the sample into different classes according to their cool core strength. For $c_{\rm SB}$, the two lines at $c_{\rm SB}$=0.075 and $c_{\rm SB}$=0.155 divides sample into: NCCs, WCCs, and SCCs, while a value for $F_{\rm core}$=0.5 and $f_{\rm c}$=1 divides clusters into CCs and NCCs. For comparison with Figure 3.4 we have used reversed axes for CC parameters so that CC systems lie at the bottom of each plot, as in Figure 3.4.

the evolutionary trends in the cluster subsample for $t_{\rm cool}/t_{\rm Uni}$ (Spearman's rank coefficient of 0.40; p-val=0.02), $t_{\rm cool}$(coefficient=0.25; p-val=0.16) and K(coefficient=0.34; p-val=0.06), which can be compared with the values in Table 3.3. In addition, the trends seen in $c_{\rm SB}$for the full sample (coefficient=-0.25; p-val=0.07) and the group subsample (coefficient=-0.44; p-val=0.06) become more significant.

3.5 Selection biases and AGN contamination

Before drawing conclusions about the evolution of CCs in groups and clusters of galaxies we must consider first whether any differences seen between the core properties of high and low redshift systems might simply result of the way in which our sample has been selected.

Our X-ray selected sample, constructed from extended sources detected in *Chandra* archival observations which meet the criteria mentioned in Chapter 3.1, contains two classes of systems: (i) groups and clusters which represent the target of the *Chandra* observation, and (ii) serendipitously detected sources. Figure 3.9 shows the $t_{\rm cool}$ distribution plot for the full X-ray sample, marking targetted and serendipitous sources with open and filled symbols respectively. It can be seen that targetted sources account for the majority of the sample at $z > 0.7$.

The inclusion of deliberately targetted sources in our sample might introduce bias in favour of systems with a particular morphology or special properties, since these systems may have been observed because of these characteristics. While this kind of bias, known as *archival bias* affects only the non-serendipitous sources, a bias to which both types of systems are subject is *detection bias*. This is due to the effect of source properties on the efficiency with which they can be detected in an X-ray image. We now examine both these sources of bias in turn.

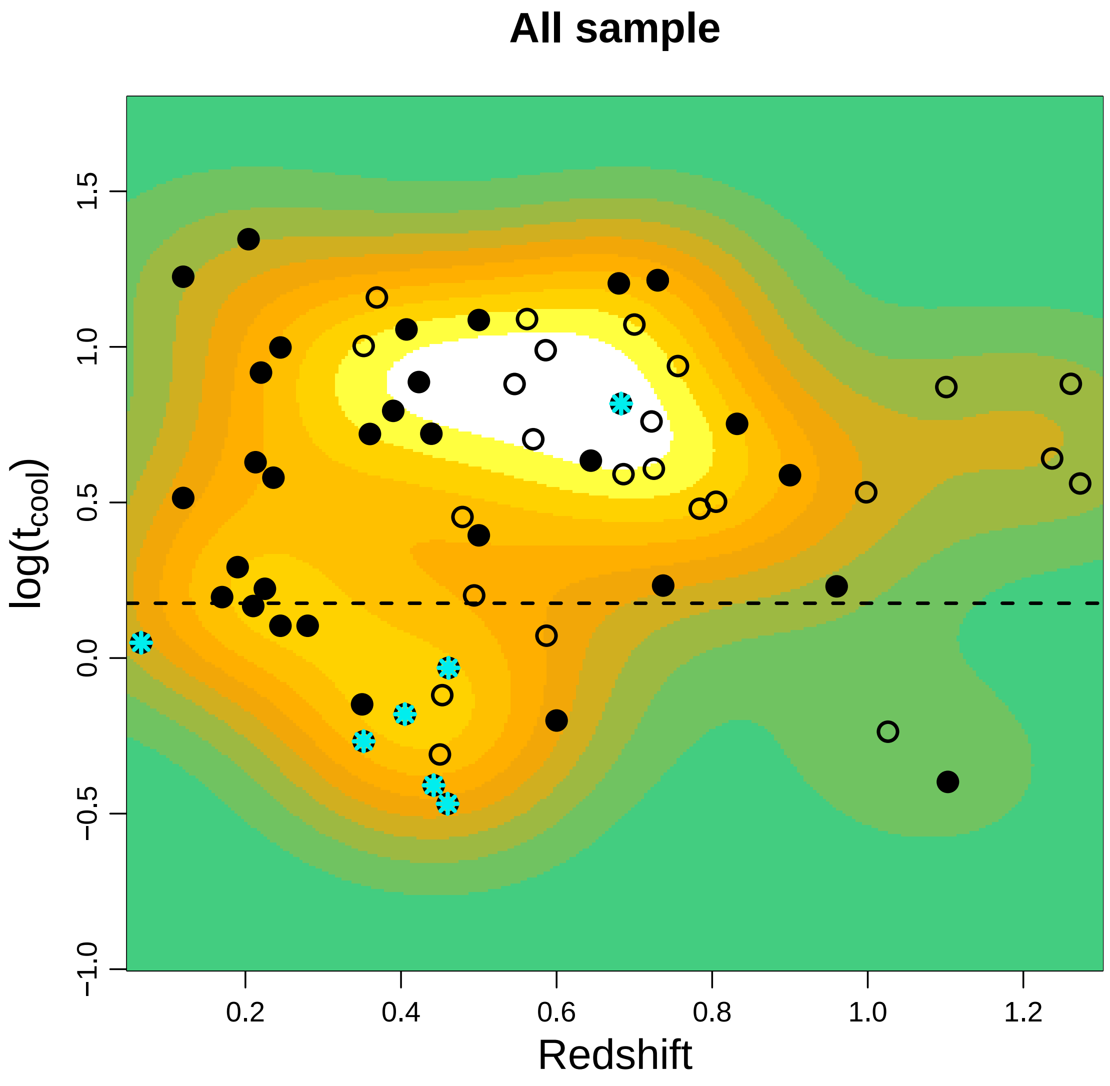

Figure 3.9: Same notations as in Figure 3.4 but with different symbols representing serendipitous systems (filled circles) and target systems (open circles). Systems marked with a cyan asterisk are those which are contaminated by a central AGN that has been masked during our data analysis.

3.5.1 Detection biases

When constructing an X-ray selected sample of clusters, the probability that a system with a given flux and size will be included in it depends on the source detection efficiency and the ability to characterize the detected system as extended when compared to the telescope's point spread function.

As detection probability is a function of both the flux and spatial distribution of the X-ray emission, a different detection efficiency may be expected for sources with different intrinsic properties such as core size (Eckert et al. 2011), substructure, and the presence of intracluster point sources (Vikhlinin et al. 1998; Burenin et al. 2007). For a given source flux, the detection probability may be increased by concentrating more of the flux in the core, until the concentration becomes so great that the cluster is rejected as appearing point-like.

Such an effect could, for example, account for the narrowing in core strength seen with the c_{SB} indicator at high redshift, if our detection method preferentially excludes systems with very large and very small core radii.

One way to check this hypothesis is by answering the following question: supposing that strong CC and NCC systems are common at high redshift, would we be able to detect such clusters with a flux value corresponding to our threshold limit of 100 soft band counts?

To answer this question we applied our detection algorithm to simulated observations of a high redshift CC and NCC cluster respectively. Observations were generated using the *Chandra* simulation software (MARX), which requires as input information about the system's spectral properties and its spatial distribution, in the form of a spectrum and values for beta model parameters, respectively. We base the properties on an observed high redshift cluster, but perturb its surface brightness distribution to generate an extreme CC and NCC system. Our template system is the cluster from our sample (Table 3.1) detected in CLJ1415.1+3612 field (CDGS57). This is a ~ 6 keV system at redshift 1.03. This provides the template for our input spectrum to MARX. For the spatial properties, we use the beta and normalization derived from our fit to the surface brightness profile of the CLJ1415.1+3612 cluster, but we perturb the core radius – to $0.007R_{500}$ to represent a SCC and $0.3R_{500}$ for a NCC profile, where R_{500} is the overdensity radius of our template system. These two values for core radius represent the median values for the size of core radii as a fraction of R_{500} for the low redshift ($z < 0.3$) CC ($t_{\rm cool}< 1.5$ Gyr) and strongly NCC (for which we adopt $t_{\rm cool}> 7$ Gyr) systems in our sample. Having chosen the spectral and spatial parameters, we varied the exposure time of our simulations to obtain 100 soft band counts, which represents our threshold limit for source selection.

So far, these simulated observations do not include any contribution from the background, which will degrade the source detection probability. To account for this, we added our simulated images to the observed image of our template cluster. Having the background level and spectral properties of a real detected system, we can now test if detection would still be possible in the case of CC and NCC cases. When we applied our detection and extension test procedure, we were able to reliably detect as extended sources both the CC system and the NCC one. This indicates that at our 100 count limit, the sample is not significantly affected by biases in detection efficiency due to the size of the core. Had we included much fainter sources in our sample, this would undoubtedly not have been the case.

Another potential source of detection bias is the presence of intracluster point sources, especially central AGN which have a double influence on the detection efficiency. In the first case, point sources embedded in the intracluster medium can cause a positive bias, increasing the detection efficiency due to the central flux excess they add to the surface brightness distribution. On the other hand, there can be a negative bias if a bright AGN at the centre of a cluster dominates the cluster emission and leads to a misclassification of the cluster as a point source. Burenin et al. (2007)

showed that the detection efficiency of a cluster varies in the presence of a central AGN according to the luminosity ratio between the AGN and the intracluster medium. The detection efficiency is raised if an AGN with a luminosity much less than that of the cluster is present. However, if the luminosity of the AGN dominates the cluster emission, the detection efficiency drops dramatically.

Our procedure for identifying central AGN was described in Chapter 3.3.1, and 7 cases fell into our AGN ‘class 1’, in which we were able to remove the central point source and analyse the cluster containing it. These systems are flagged with asterisks in Figure 3.9. A strong connection between the presence of a central AGN and CC status is apparent – most systems with a central point source are CCs. (Stott et al. 2012) showed that radio loud brightest clusters galaxies are more likely to be found in more massive systems and at the centre of CCs. Also, based on the observed correlation between the strength of CC and the radio power of the central AGN (Mittal et al. 2009), we might expect that, at least for clusters, high redshift systems dominated by strong AGN will be SCCs. Is it possible that this has introduced a bias against their inclusion in our sample?

The literature is limited in the number of X-ray studies of high redshift clusters with dominant central AGN. Two which have been studied are PKS1229-021 (Russell et al. 2012) and 3C186 (Siemiginowska et al. 2010). Both lie at $z > 1$ and have been reported to contain a strong CC. Since these two systems were observed with ACIS-S, they were not included in our sample, which concentrated on ACIS-I observations. We have analysed the *Chandra* data for these sources and checked into which of the previously mentioned AGN classes they would fall, had they been part of our sample. They would fall into our first AGN class – sources with clear signs of extension in which the central AGN does not dominate the total flux. We conclude from this that, at least for massive systems detected in observations with exposures of at least 70 ks like ours, we are not strongly biased against CCs. This may not be the case for less massive systems.

To further examine the impact of central AGN on our results, we show in Figure 3.10 the X-ray luminosity of the cluster and AGN emission in sources which appeared from our analysis to contain both point-like and extended components, and are confirmed from the literature to involve both an AGN and a cluster.

Points marked in red correspond to the AGN (asterisk symbols) and cluster (filled circles) contributions to the 7 systems in which we were able to remove the AGN component and still perform a useful analysis on the remaining cluster emission. The green points correspond to clusters which were excluded from our sample, since the remaining cluster component after removal of the central point source did not leave enough signal/noise for a reliable analysis.

Finally, we also mark (blue labelled symbols) the location of PKS1229-021 and 3C186. The luminosities here have been estimated by fitting a point source plus beta-model distribution to the X-ray surface brightness distribution. For the green points, where the cluster contribution is weak, the cluster luminosities should be regarded as rough estimates.

Most of the systems (red points) in which we have been able to successfully remove AGN contamination contain AGN which are less luminous than the cluster gas. The only exception to this is the lowest redshift system, which is a nearby galaxy group ($T \approx 1$ keV) with a correspondingly large X-ray extent. The clusters in which we were unable to perform a useful analysis after removing the central AGN (green points) have AGN which are brighter than the cluster, apart from the two systems at $z = 0.8$-1.0. These two are both observed at large off-axis angles, where the instrument point spread function is broader, and the central AGN contaminates a region about $20''$ in diameter.

In general, our results suggest that the problem of AGN contamination is a modest one in our sample. At low redshift ($z < 0.5$), we find that about 19% of our detected clusters contain central X-ray AGN, and in most of these the AGN contributes less than 10% of the cluster luminosity. With the exception of PKS1229-021 and 3C186, which were not part of our sample and were specially added to examine the case of powerful central AGN at high redshift, there is little sign

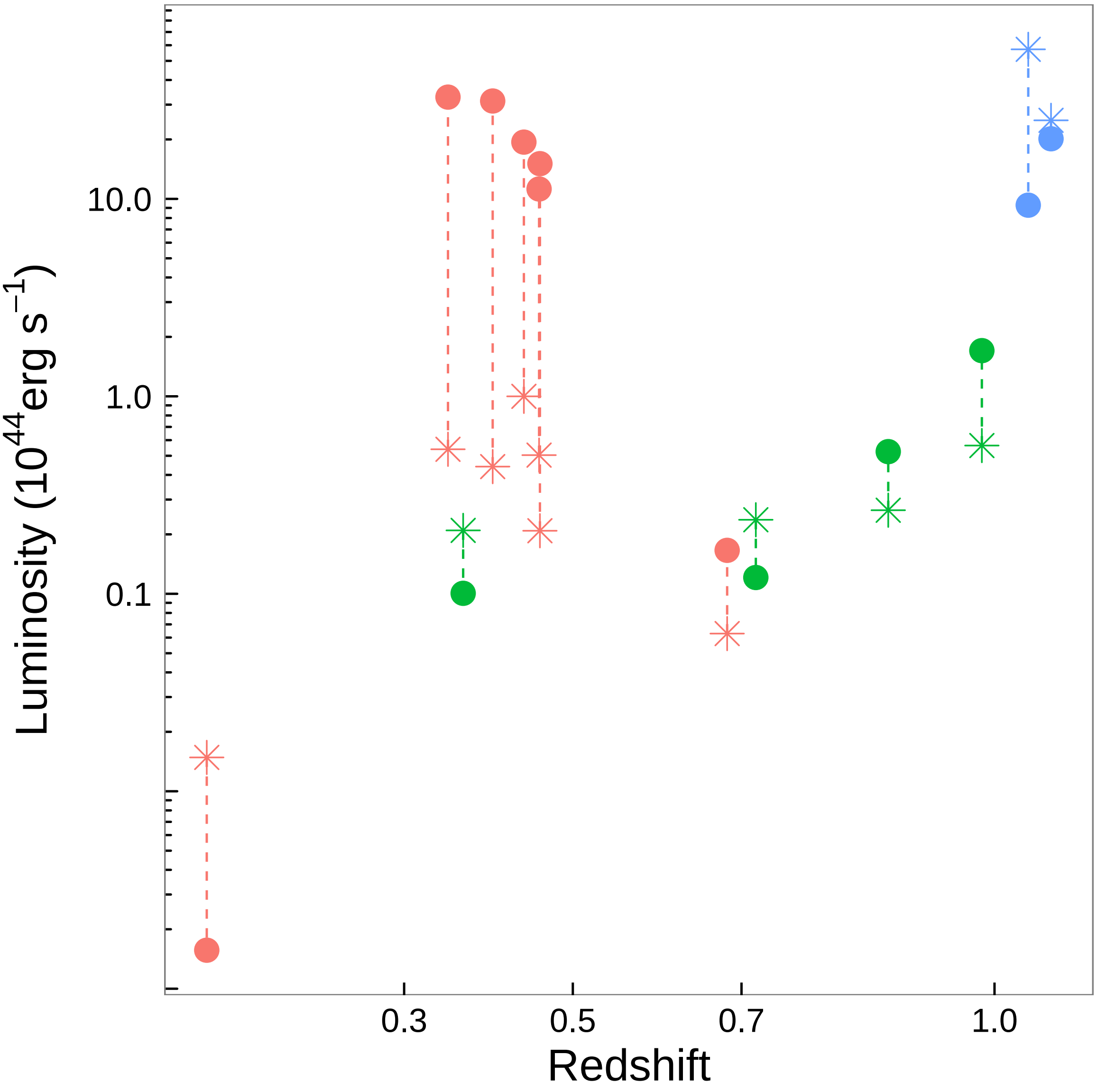

Figure 3.10: X-ray luminosity (0.5-7.0 keV) of the cluster (filled circles) and central point source (asterisks) as a function of redshift for: (a) sources in our sample from which a central point source that has been removed during the analysis (red); (b) extended sources detected in our fields and which have not been included into our sample because their X-ray flux is dominated by the central point source – for these sources evidence for the existence of a cluster has been found in the literature (green); (c) the PKS1229-021 and 3C186 systems (blue).

in Figure 3.10 that the luminosity of central AGN is increasing at redshifts above 0.3, in which case only systems with cluster luminosities $L_X \lesssim 10^{44}$ erg s^{-1} are likely to be lost from our sample due to AGN contamination. The limited impact of AGN is confirmed by the results of Santos and McDonald (private communication) who found the impact of central X-ray point sources in their cluster samples to be modest.

3.5.2 Archival biases

The inclusion of targetted systems introduces biases which depend upon the motivation of the observers who proposed these targets. It is very difficult to decide how serious such biases might be, or in which direction they might act, except that one would expect *exceptional* objects to be especially popular targets. The obvious way to avoid archival bias is by limiting the sample to serendipitous sources, though the avoidance of targetted clusters will introduce a certain bias in itself. Although we might like to include in our study only serendipitously detected systems, the lack of high redshift serendipitous sources motivates us to include targetted systems in order to improve the statistics available for evolutionary studies. It is clear from Figure 3.9 that including only serendipitous sources, it will be difficult to draw conclusions about CC evolution.

We note from Figure 3.9 that most targetted sources at $z > 0.7$ are WCC systems. This suggests that if an archival bias exists, it is towards systems with weak cool cores. This seems rather unlikely, since observers tend to target interesting clusters, which would be expected to favour dynamical disturbance (hence probably NCC) or strong AGN activity (strong CC).

3.5.3 Non X-ray selected clusters

The discussion above suggests that detection bias is unlikely to be a serious problem for our survey, in which we require a minimum of 100 X-ray counts from each accepted source. AGN contamination does not generally lead to the exclusion of luminous X-ray clusters from our sample, but might affect systems with $L_X \lesssim 10^{44}$ erg s^{-1}. The influence of archival bias, especially at high redshift, is difficult to assess due to the low number of high redshift systems and the shortage of serendipitous ones. If we look at the provenance of our high redshift systems we find that from 11 sources detected at a redshift greater than 0.8, only four are serendipitous systems. The other 7 systems represent the target of *Chandra* follow-up observation of systems detected in earlier surveys at a variety of wavelengths: near-infrared (1 system), Sunyaev-Zeldovich (SZ; 1 system), and two different *ROSAT* surveys (WARPS; 1 system and RDCS; 4 systems). Since the majority of high redshift sources come from *ROSAT* surveys, especially RDCS, we would expect any bias in the RDCS sample to be reflected in our sample. RDCS uses a wavelet-based source detection algorithm which is not expected to be substantially biased by the presence of a CC (Rosati et al. 1995). However, it is worth noting that the spatial resolution of *ROSAT* is an order of magnitude poorer than that of *Chandra*.

In case there is some bias in X-ray properties arising from any of the above factors, it is helpful to examine clusters selected in other ways. To do this, and to improve our statistics at high redshift, we added to our sample 24 systems with redshifts greater than 0.7, and with at least 100 counts in the soft band, which result from *Chandra* follow-up of groups and clusters selected from optical and SZ surveys. These systems were not included in our initial sample for one of three reasons: (a) they were observed for less than 70 ks, which represents the lower limit adopted for our survey, (b) they were not available in the archive at the time our sample was selected, or (c) they were observed with the ACIS-S configuration, rather than ACIS-I.

The South Pole Telescope (SPT) sample

The South Pole Telescope survey (Carlstrom et al. 2011) is a 2500 deg^2 survey that uses the distortion in the cosmic microwave background (CMB) due to inverse Compton scattering of CMB photons by electrons in the intracluster medium (Sunyaev Zeldovich effect) to detect galaxy clusters. From analysis of the first 720 deg^2 224 galaxy cluster candidates have been found (Reichardt et al. 2013). A significant number of SPT detected clusters (52) have follow-up observations in the *Chandra* archive, and from these we have selected 17 clusters with redshifts greater than 0.7 and at least 100 soft band *Chandra* counts. Our SPT sample is presented in Table 3.4a. Detection of clusters using the SZ effect is not expected to be significantly biased by the dynamical state of the cluster or the presence of cool cores (Motl et al. 2005).

The Red-Sequence Cluster Survey (RCS) sample

The red-sequence method (Gladders & Yee 2000) is a detection technique that exploits the observed tight correlation between the colour and magnitude of the early-type galaxies in a cluster. The RCS is a large optical imaging survey which uses the red sequence method to detect clusters of galaxies out to redshift of 1. It includes RCS1 (Gladders et al. 2007) which covers an area of about 100 deg^2 and contains a sample of 429 cluster candidates, and RCS2 which predicts the detection of 30000 clusters from an area about 10 times larger (Gilbank et al. 2011). From these surveys, 21 clusters have been followed-up by *Chandra*, from which we select only the 7 clusters at redshift greater than 0.7 and with at least 100 X-ray counts detected in ACIS-I observations. Since these clusters are optically selected, they are free from any direct bias arising from their X-ray properties, including the presence of AGN. Unlike SZ-detected clusters, which are invariably massive systems, the RCS sample includes several high redshift groups.

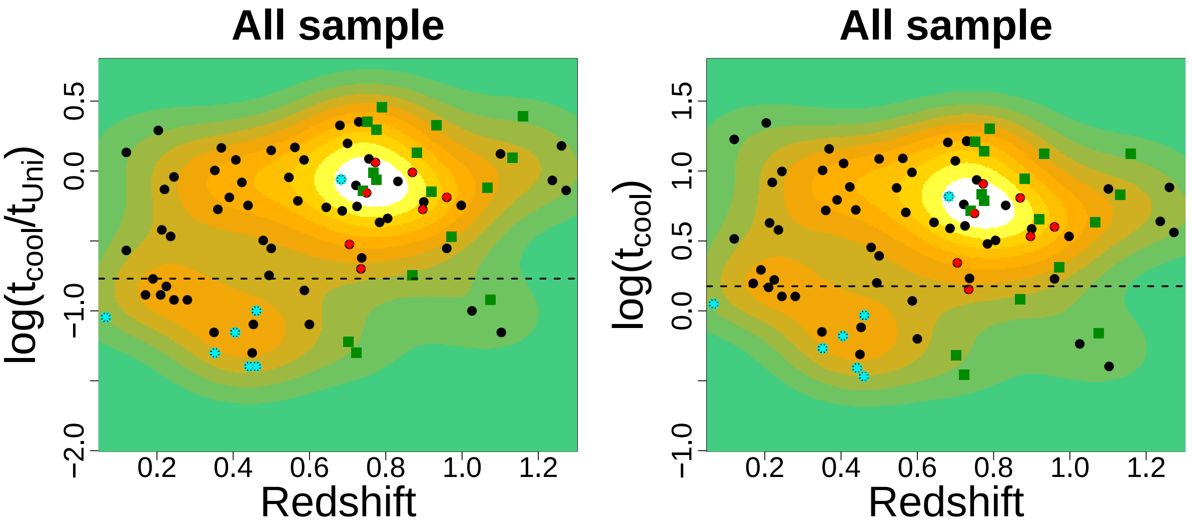

Figure 3.11: Evolution of $t_{\rm cool}$and $t_{\rm cool}/t_{\rm Uni}$for our extended sample, which includes the original X-ray selected sample to which we add 7 red-sequence selected systems (RCS sample) marked with red diamond symbols and 17 SZ selected systems (SPT sample) marked with green square symbols. AGN contaminated systems are marked with a cyan asterisk symbol. All other notations are the same as in Figure 3.4.

Results from the extended sample

The addition of 24 non-X-ray selected clusters doubles the number of high redshift systems in our survey and creates what we refer to below as our *extended sample*.

Figure 3.11 shows the core evolution for our extended sample using our two primary CC indicators: $t_{\rm cool}$ and $t_{\rm cool}/t_{\rm Uni}$. SPT clusters are shown in green, RCS clusters in red, and systems from which central AGN have been removed are flagged with asterisks. Examining the distribution of both $t_{\rm cool}$ and $t_{\rm cool}/t_{\rm Uni}$ in the extended sample, there is an indication of some broadening of the high redshift distribution, especially towards NCC systems. The spread in the NCC distributions at high redshift is introduced by the existence of SPT clusters with very long cooling times. This suggests that the shortage of such systems at high redshift in our X-ray sample may be a selection effect. Possibly NCC systems are underrepresented in the *ROSAT* surveys on which most of our targetted high redshift observations were based. It has already been noted in the context from Planck results (Planck Collaboration et al. 2011) that SZ-selected clusters include a high proportion of morphologically disturbed systems compared to X-ray selected samples.

With the addition of 24 high redshift clusters and the moderation of any archival biases in our X-ray selected sample, the extended sample forms a stronger basis for applying statistical tests for cool core evolution. The Spearman rank tests for all six CC indicators are given in the right hand half of Table 3.3. These results confirm and strengthen the conclusions from the X-ray sample discussed in Chapters 3.4.1 and 3.4.2. Using the full group+cluster sample, we see a highly significant ($p = 0.006$) correlation with redshift in $t_{\mathrm{cool}}/t_{\mathrm{Uni}}$, but little trend in t_{cool}. These results also apply to the group and cluster subsamples separately. In terms of other indicators, as for the X-ray sample, we see evolutionary trends in K and f_{c}, but now also in c_{SB}. All these trends imply stronger cool cores at low redshift.

For our two main CC indicators, t_{cool} and $t_{\mathrm{cool}}/t_{\mathrm{Uni}}$, we conduct two further simple statistical tests which involve cutting the extended sample into high and low redshift halves. The choice of the cut redshift is arbitrary, and the results scatter with this choice, so we present them for a series of cuts between $z = 0.5$ and $z = 0.7$. For each split sample we calculate (a) the mean and standard deviation for both CC indicators, and (b) a K-S test for consistency between the distribution seen in the high and low redshift samples. Table 3.5 shows the results. These broadly confirm the results of the Spearman rank test; $t_{\mathrm{cool}}/t_{\mathrm{Uni}}$ is clearly evolving, wherever the cut is placed, whilst differences in t_{cool} between the low and high redshift subsamples are much weaker, though the cooling time does show a significant tendency to be somewhat shorter at low redshift.

Table 3.4: Non X-ray selected samples: 1) Clusters detected by the SZ effect using the South Pole Telescope and 2) Optically selected clusters detected based on the Red Sequence technique.

SPT sample

Field name	Ra (deg)	Dec) (deg)	Redshift	Counts	R_{500} (Mpc)	kT (keV)	$t_{\rm cool}$ (Gyr)	$t_{\rm cool}/t_{\rm Uni}$	K (keV cm^2)
SPT-CLJ0001-5748	0.2500	-57.8093	0.702	1226	0.981	$8.01^{+3.61}_{-1.69}$	0.48 ± 0.40	0.06 ± 0.05	31.42 ± 20.16
SPT-CLJ2043-5035	310.8242	-50.5922	0.723	3957	0.797	$5.26^{+0.27}_{-0.23}$	0.35 ± 0.11	0.05 ± 0.02	20.02 ± 4.25
SPT-CLJ0324-6236	51.0483	-62.5994	0.74	1249	0.888	$6.55^{+1.45}_{-1.23}$	5.21 ± 1.08	0.72 ± 0.15	137.44 ± 34.24
SPT-CLJ0014-4952	3.6921	-49.8756	0.752	1600	0.951	$7.56^{+1.80}_{-1.17}$	16.17 ± 6.09	2.26 ± 0.85	318.22 ± 108.60
SPT-CLJ0528-5300	82.0216	-52.9971	0.768	1203	0.777	$5.14^{+1.09}_{-2.01}$	6.83 ± 2.44	0.97 ± 0.34	142.10 ± 59.54
SPT-CLJ0000-5010	359.9323	-50.1725	0.775	1447	0.925	$7.98^{+2.00}_{-2.17}$	13.86 ± 3.80	1.97 ± 0.54	296.50 ± 90.42
SPT-CLJ2337-5942	354.3574	-59.7074	0.775	1205	0.986	$8.26^{+3.77}_{-1.74}$	6.13 ± 2.61	0.87 ± 0.37	175.76 ± 86.11
SPT-CLJ0449-4901	72.2773	-49.0270	0.790	966	1.261	$13.66^{+0.00}_{-5.25}$	20.00 ± 10.30	2.87 ± 1.48	504.29 ± 245.82
SPT-CLJ0102-4915	15.7424	-49.2742	0.870	48627	1.178	$12.78^{+0.32}_{-0.34}$	1.21 ± 0.74	0.18 ± 0.11	75.59 ± 27.75
SPT-CLJ0534-5005	83.4071	-50.0965	0.881	342	0.702	$2.88^{+0.76}_{-1.22}$	8.80 ± 79.28	1.35 ± 12.18	119.35 ± 201.55
SPT-CLJ2034-5936	308.5370	-59.6051	0.92	647	0.801	$6.48^{+1.24}_{-0.76}$	4.51 ± 1.23	0.71 ± 0.19	124.16 ± 33.51
SPT-CLJ2146-4632	326.6450	-46.5495	0.933	1078	0.701	$5.34^{+1.34}_{-1.06}$	13.30 ± 6.53	2.12 ± 1.04	226.65 ± 93.38
SPT-CLJ0615-5746	93.9662	-57.7800	0.972	16236	1.143	$13.29^{+1.58}_{-0.94}$	2.05 ± 0.94	0.34 ± 0.15	110.20 ± 33.73
SPT-CLJ0547-5345	86.6556	-53.7606	1.066	1376	0.735	$7.12^{+5.05}_{-2.08}$	4.32 ± 2.38	0.76 ± 0.42	127.83 ± 86.22
SPT-CLJ2343-5411	355.6920	-54.1850	1.075	1426	0.599	$4.63^{+0.56}_{-1.13}$	0.69 ± 0.58	0.12 ± 0.10	28.78 ± 16.77
SPT-CLJ0446-5849	71.5210	-58.8308	1.16	281	1.001	$10.85^{+5.72}_{-5.72}$	13.26 ± 9.10	2.46 ± 1.69	347.84 ± 227.38
SPT-CLJ2106-5845	316.5226	-58.7424	1.132	886	0.888	$9.86^{+4.22}_{-2.14}$	6.79 ± 2.89	1.24 ± 0.53	210.16 ± 99.20

RCS sample

Field name	Ra (deg)	Dec) (deg)	Redshift	Counts	R_{500} (Mpc)	kT (keV)	$t_{\rm cool}$ (Gyr)	$t_{\rm cool}/t_{\rm Uni}$	K (keV cm^2)
RCS2327-0204	351.8647	-02.0776	0.705	5144	1.199	$10.71^{+1.84}_{-1.85}$	2.21 ± 1.07	0.30 ± 0.14	103.03 ± 35.03
RCS1107-0523	166.8504	-05.3890	0.735	896	0.694	$3.97^{+1.09}_{-1.08}$	1.42 ± 1.13	0.20 ± 0.16	42.64 ± 22.39
RCS1325+2858	201.6322	+29.0586	0.75	110	0.393	$1.43^{+3.33}_{-0.83}$	4.99 ± 10.05	0.70 ± 1.40	62.26 ± 130.37
RCS0224-0002	36.1430	-00.0406	0.773	758	0.614	$3.39^{+1.96}_{-0.76}$	8.07 ± 4.38	1.15 ± 0.62	123.70 ± 73.43
RCS1620+2929	245.0430	+29.4898	0.870	181	0.630	$2.81^{+1.21}_{-1.21}$	6.41 ± 3.10	0.98 ± 0.47	95.34 ± 46.60
RCS2319+0038	349.9718	+00.6370	0.897	1247	0.680	$4.99^{+0.60}_{-0.63}$	3.41 ± 1.31	0.53 ± 0.20	87.70 ± 24.13
RCS0439-2905	69.9075	-29.0800	0.960	183	0.423	$1.94^{+3.36}_{-0.38}$	3.99 ± 3.46	0.65 ± 0.56	58.08 ± 72.00

Table 3.5: Comparison between the distribution of two cool core parameters ($t_{\mathrm{cool}}$and $t_{\mathrm{cool}}/t_{\mathrm{Uni}}$) at low and high redshift. Five threshold between 0.5 and 0.7 are chosen for redshift to divide the sample into low and high redshift subsamples. For each parameter and each redshift threshold the mean value of the parameter for the low and high redshift subsample is given together with the standard error on the mean. Also the p-value for a Kolmogorov-Smirnov test for similarity in the distribution for the low and high redshift subsamples is given.

	$\mathbf{t}_{\mathrm{cool}}$			$\mathbf{t}_{\mathrm{cool}}/\mathbf{t}_{\mathrm{Uni}}$		
	Mean		K-S	Mean		K-S
Redshift	low	high	p-val	low	high	p-val
0.5	4.79 ± 0.98	6.29 ± 0.67	0.03	0.46 ± 0.09	0.92 ± 0.09	0.005
0.55	5.02 ± 0.93	6.23 ± 0.69	0.08	0.49 ± 0.09	0.92 ± 0.10	0.008
0.6	5.24 ± 0.86	6.16 ± 0.73	0.13	0.53 ± 0.08	0.92 ± 0.11	0.020
0.65	5.10 ± 0.83	6.32 ± 0.75	0.08	0.52 ± 0.08	0.95 ± 0.11	0.016
0.7	5.36 ± 0.81	6.14 ± 0.77	0.19	0.56 ± 0.08	0.94 ± 0.11	0.070

3.6 Discussion

We conclude from the evidence presented above that most, but not all, of the cool core indicators we have employed show evidence, confirmed by a number of statistical tests, for evolution in the properties of cluster cores. Concentrating on our two primary indicators, which are based on cooling time, we see significant evolution in $t_{\rm cool}/t_{\rm Uni}$ evaluated at $r = 0.01{\rm R}_{500}$, but at most a weak trend in the value of $t_{\rm cool}$ evaluated at this radius. This behaviour is apparent for both our X-ray and extended cluster samples, and it applies for clusters and groups separately and combined. (See, for example, Table 3.3.)

There is no evidence here for a difference between the behaviour of groups and clusters, such as was suggested by Alshino et al. (2010). These authors found, using *XMM-Newton* data for a sample of groups and clusters detected in the *XMM*-LSS X-ray survey, that the cores in groups were actually *more* cuspy at high redshift, in contrast to the situation in clusters. Using the same indicator as Alshino et al., the central excess ($f_{\rm c}$) above a standard beta-model fit, we find evolution towards *less* prominent cores at high redshift in both groups and clusters, as can be seen in Figure 3.8 and Table 3.3. The reason for this disagreement is unclear. The most relevant differences between the two studies seems to be the angular resolution of the X-ray data and the degree of uniformity of the survey.

Chandra has a much sharper point spread function than *XMM*, and so our surface brightness profiles are subject to less instrumental blurring. Although the PSF effects are modelled out during the profile fitting in both studies, the work of Alshino et al. will be much more vulnerable to any shortcomings in this process, since the impact of blurring is greater for high redshift clusters.

The second relevant difference between our survey and the *XMM*-LSS survey on which the results of Alshino et al. (2010) are based, is that *XMM*-LSS is a more uniform survey, with contiguous *XMM-Newton* exposures typically 10 ksec in duration, whilst CDGS is based on *Chandra* exposures of widely varying depth (exposure times ranging up to 4 Msec). This means that high redshift groups, having low source flux, will be amongst the lowest significance sources in *XMM*-LSS, but not necessarily in CDGS, especially since we have imposed a minimum count threshold of 100 counts on all our sources. A consequence is that the high redshift groups in the Alshino et al. survey will be subject to strong selection effects, which may result in more centrally peaked systems being preferentially detected. In contrast, the simulations reported above in Chapter 3.5.1 establish that no such significant bias should be present in our study. This seems to us to be the most likely explanation for the contrary behaviour of high redshift groups in the two studies.

In any case, we conclude that the combination of superior resolution and the avoidance of systems close to the detection threshold, means that the results from the present study regarding CC evolution in groups should be more reliable than those reported by Alshino et al. (2010).

We have considered the impact of systematic biases on our results, and conclude that both detection bias and the effects of AGN contamination appear to be modest. Archival bias, arising from the fact that many of our X-ray selected clusters (especially those at high redshift) were deliberately targetted for *Chandra* observations, is of greater concern. We addressed this by adding a further 24 clusters at $z > 0.7$ selected from SZ and optical surveys. These show a somewhat wider range in core properties than our high redshift X-ray sample, however the main thrust of our conclusions on core evolution are unchanged by the addition of these clusters to the sample.

Following the initial indications reported by Vikhlinin et al. (2007), subsequent studies of the cuspiness of the profiles of X-ray selected samples dominated by clusters ($T > 3$ keV) by Santos et al. (2008, 2010) and Maughan et al. (2012) have found a reduction in the fraction of clusters hosting strong central surface brightness cusps at high ($z > 0.5$) redshift. Our results are consistent with the existence of such a trend, which we have shown extends also to galaxy groups.

Using cool core indicators based on cooling time, a more nuanced picture emerges, which can be usefully compared with the study of McDonald et al. (2013, 2014). This examined the X-ray properties of a sample of 80 SZ-detected (hence rather rich) clusters and, like the present study, explored a variety of different CC indicators. The use of a SZ-selected sample reduces direct selection bias arising from the X-ray properties of the clusters. Indirect biases are still possible – for example, dense core gas does enhance the SZ signal, and radio-bright AGN may also increase the probability of cluster detection. McDonald et al. (2013) conclude that both are minor effects.

McDonald et al. (2013) also find no evolutionary trend in cooling time calculated within the core (in their case at a radius of $0.012\mathrm{R}_{500}$). They do not compute $t_{\mathrm{cool}}/t_{\mathrm{Uni}}$, but they do calculate c_{SB} and also find that this evolves towards increasing cuspiness, as do two other indicators: the logarithmic density slope at $0.04\mathrm{R}_{500}$, and the mass cooling rate integrated within a cooling radius, which itself depends upon the age of the Universe at the redshift of the cluster. These results are highly consistent with our own and suggests that these trends are rather robust against the method of cluster selection (X-ray vs SZ) and the mass range considered (our sample extends to considerably lower masses).

What do these results imply about the evolution of cluster cores? In the first place, it is clear that these cores do not follow the self-similar evolution seen in the outer regions of clusters. Here the gas density at a given scaled radius (e.g. R_{500}) scales with the critical density of the Universe, and hence as $E(z)^2$, whilst from the virial theorem the characteristic temperature is related to cluster mass via $T \propto (ME(z))^{2/3}$. If the core gas followed the same scaling laws, then the cooling time at a given scaled radius would (in the approximation that thermal bremsstrahlung dominates) scale as

$$t_{cool} \propto \frac{n_e T}{n_e^2 \Lambda(T)} \propto \frac{T^{1/2}}{n_e} \propto T^{1/2} E(z)^{-2}, \tag{3.6}$$

where the cooling function, $\Lambda(T)$, scales as $T^{1/2}$ for bremsstrahlung emission. This implies that cooling times should be significantly *shorter* at high redshift, which is clearly inconsistent with our observations.

Voit (2011) has proposed an interesting model for the thermal state of cluster cores whereby there exists a critical line in the radius-entropy plane, $K(r) \approx 5r_{\mathrm{kpc}}^{2/3}$, along which conductive heat transfer can balance radiative cooling. Above this line, cooling is subdominant, and the gas entropy drops inwards according to the $K \propto r^{1.1}$ relation predicted by simple models of gas accretion and shock heating. However, once this steeper radial trend intersects the conductive balance line the gas cools and ultimately becomes thermally unstable, and its entropy profile within this radius is determined by feedback processes, probably associated with a central AGN, which prevent catastrophic cooling.

The radial entropy profiles reported in a sample of low redshift groups and clusters by Panagoulia et al. (2014) seems to accord remarkably well with this model (though these authors seem not to have noticed this), and suggest that the entropy follows the conductive equilibrium line inwards in cool core systems, once the steeper outer entropy profile hits the critical equilibrium line. This might be explained if AGN feedback were able to prevent the entropy from falling much below the conductive balance value.

What evolutionary behaviour in cores would be predicted by such a model? The conductive balance $K(r)$ line is independent of redshift, but the radius at which we measure entropy ($0.01\mathrm{R}_{500}$) will evolve – for temperature T, R_{500} scales as $T^{1/2}E(z)^{-1}$, so the entropy at $0.01\mathrm{R}_{500}$ will scale as $T^{1/3}E(z)^{-2/3}$, and hence for a given temperature should be *lower* at high redshift (though not as much lower as for self-similar evolution). In practice (see Table 3.3) we see the reverse – somewhat higher entropies at high redshift. This suggests that the conductive equilibrium model in its simplest form cannot account for the evolutionary trend we observe.

A more recent development of the model by Voit et al. (2014) demonstrates that low redshift cool core clusters have cooling time profiles (which closely follow from entropy profiles – see

Figure 3.3) that are bracketed by the conductive balance locus (at high t_{cool}) and a lower t_{cool} limit set by the point at which thermal instability causes gas to generate cool clouds which can precipitate onto a central galaxy, causing AGN feedback which heats and mixes the core gas, limiting further cooling. This lower ‘precipitation line’ corresponds to the locus along which the cooling time is approximately 10 times the free fall time, which in turn is set by the gravitational potential. This will not evolve strongly with redshift, which might again lead to an expectation that $t_{\mathrm{cool}}(0.01\mathrm{R}_{500})$ would be smaller at high redshift, due to the smaller value of R_{500} (at a given system temperature). However, the model predicts that cooling time profiles will be distributed between the conductive balance and precipitation lines in a way which depends on details of the AGN feedback process, such as the duty cycle. This leaves open the possibility that the average cooling time over a sample of CC systems might evolve very little. Detailed entropy profiles for a sample of high redshift CC systems are required to explore the viability of the model. This may have to await the next generation of X-ray observatories.

In terms of our two main CC indicators, the fact that $t_{\mathrm{cool}}/t_{\mathrm{Uni}}$ is decreasing with time follows directly from the fact that t_{cool} is *not* evolving, since the age of the Universe (obviously) increases with time. The reason that t_{cool} does not evolve to any great extent must be connected to the processes which break self-similarity in cluster cores: cooling, conductive heat transfer and the feedback processes which prevent runaway cooling. It is well known that cooling in cluster cores is suppressed well below the naive rate derived from the observed X-ray luminosity. Nonetheless, some cooling does take place and, for example, star formation in central galaxies within cool cores implies that gas can cool at a rate 1-10% of the uncontrolled value, most likely due to countervailing AGN heating (O’Dea et al. 2008). If some of this gas is able to accumulate within the cluster core, outside $0.01\mathrm{R}_{500}$, it might explain why cuspiness indicators like c_{SB} evolve with time, in addition to quantities like $t_{\mathrm{cool}}/t_{\mathrm{Uni}}$. This is essentially the explanation proposed by McDonald et al. (2013) to account for their results, and in McDonald et al. (2014) they show that pressure tends to rise over time within CC clusters, which they take to be a result of a build-up of gas.

We can assess the evidence for such a rise in gas density in the outer core in our clusters by examining the evolution of gas density in CC systems at a range of different radii. For this purpose, we restrict ourselves to clusters. Groups have lower gas densities than clusters over most of their radial range as a result of the action of feedback processes (Ponman et al. 1999), and since groups are concentrated at low redshift this difference will swamp any evolutionary trends if they are included. We are interested only in CC systems here, so we include only systems which have $t_{\rm cool}(0.01\mathrm{R}_{500}) < 1.5$ Gyr. Figure 3.12 shows that the mean gas density for this subsample, derived from our analytical deprojection analysis, as a function of redshift for several different overdensity radii. This confirms that density increases more strongly with time immediately outside $0.01\mathrm{R}_{500}$. At larger radii ($> 0.1\mathrm{R}_{500}$) this evolution reverses as it tends towards self-similar behaviour.

3.7 Conclusion

We have presented in this chapter a study of the evolution of cluster cores, based on a sample of 62 X-ray selected systems with temperatures between 1-12 keV and redshifts up to 1.3. We have investigated the existence of evolutionary trends in the entire sample, as well as in the subsamples of 26 groups ($T < 3$ keV) and 36 clusters ($T \geq 3$ keV) separately. Our main results can be summarised as follows:

- Six different parameters have been used to quantify the strength of cool cores, and different evolutionary trends are found for CC strength, depending on the CC estimator used. This behaviour is found for the entire sample and the subsamples of clusters and groups separately.
- For the entire sample of 62 systems, we find a decrease in the fraction of CC with redshift using the $t_{\rm cool}/t_{\rm Uni}$, K and $f_{\rm c}$ indicators, a weak evolution for $c_{\rm SB}$, and no significant evolution

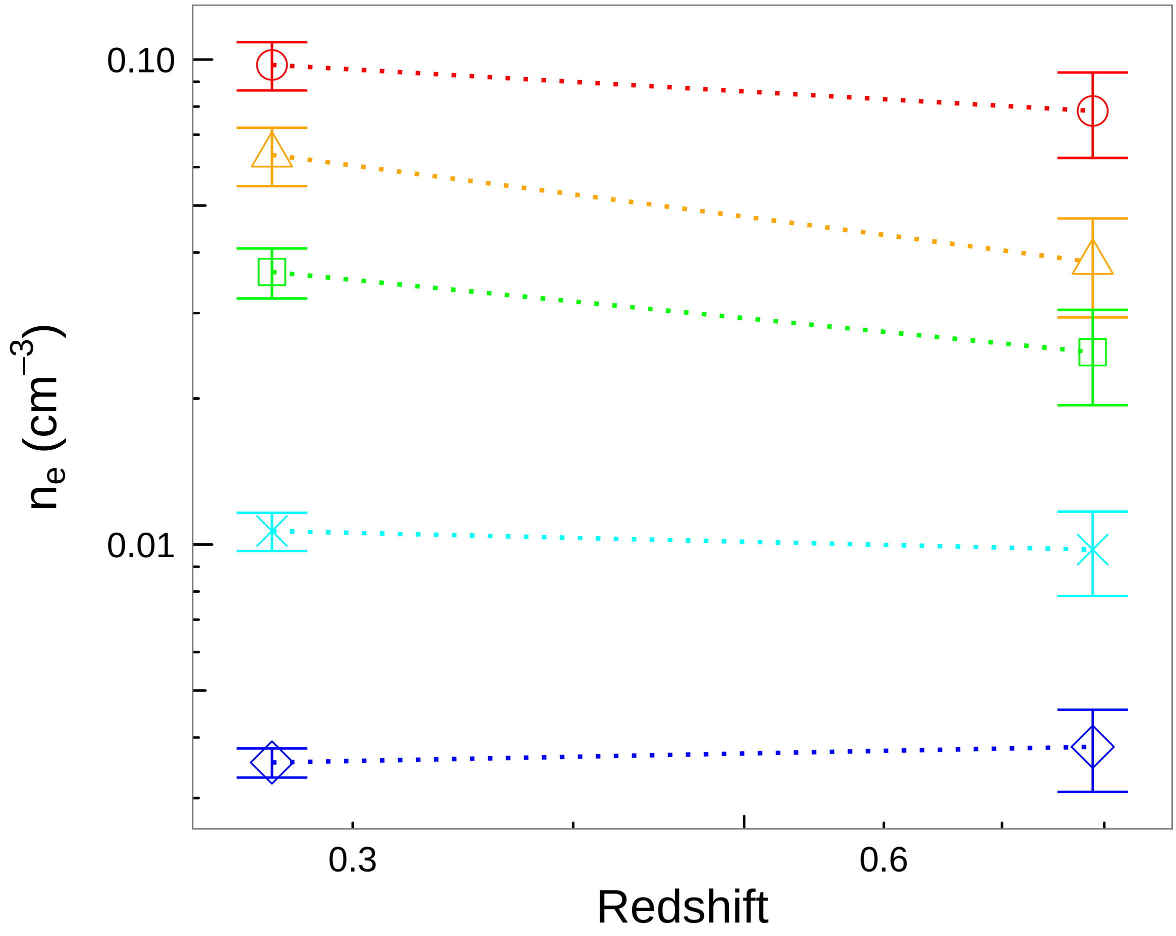

Figure 3.12: Evolution of mean density for cool core systems within the extended sample, calculated in two redshift bins for six different radii: 0.01R$_{500}$(circle), 0.02R$_{500}$(triangle), 0.04R$_{500}$(square), 0.1R$_{500}$(cross) and 0.2R$_{500}$(diamond). Each point in the plot represents the mean density of the sample, with associated standard error.

for $t_{\rm cool}$ and $F_{\rm core}$.

- Groups and clusters show similar trends irrespective of the parameter used to characterize CCs, although the statistical significance of the trends found for groups is lower than that for clusters. These trends are similar to those seen for the entire sample.
- In particular, a clear reduction in the fraction of cool cores at high redshift is found for both groups and clusters when the $f_{\rm c}$ indicator is used. This is inconsistent with the opposite trends for groups and clusters reported by Alshino et al. (2010) using this estimator.
- The impact on our results of a variety of different biases was investigated. Bias due to the impact of core properties on the ability to detect an extended X-ray source in our *Chandra* data appears to be modest, as do biases arising from the presence of a central AGN. The impact of archival bias, arising from the agenda of observers who targetted the non-serendipitous systems which dominate our sample at high redshift, is potentially more serious. Its impact was tested by adding 24 non-X-ray selected systems at $z > 0.7$ to generate an extended sample. In general, the effect of adding these systems is to strengthen the trends seen when using only the X-ray selected sample. The most noticeable difference is for $c_{\rm SB}$, which shows a more pronounced evolutionary trend in the extended sample. Removal from our sample of systems with photometric, rather than spectroscopic, redshifts also leave our findings substantially unchanged.
- A reasonable interpretation of our results is that, in both groups and clusters, the cooling time of gas in the inner core is held at an approximately constant value by AGN feedback. However, cooling gas accumulates in the outer core, driving an increase in the cuspiness of CC systems with time. We find evidence for this behaviour in the evolution of gas density as a function of radius, within CC systems.

Chapter 4

Conclusions and future work

The work presented in this Thesis is dedicated to the study of groups of galaxies using observations taken with *Chandra* X-ray telescope. X-ray images reveal the presence of one of the group's main component: the intragroup medium (IGM), a hot plasma which suffers various changes during the group's lifetime due to gravitational as well as non-gravitational processes. Because of the groups' shallower potential well compared to clusters, the impact of non-gravitational processes such as AGN and supernovae feedback on the IGM is higher for groups than clusters. This is one of the reasons for which groups represent an important astrophysical source.

The study of the properties of groups and especially the evolution of these properties requires a large sample, which covers a wide redshift interval. The *Chandra* deep group survey (CDGS) is a survey dedicated to the search for groups of galaxies in deep observations available from the *Chandra* data archive. This survey is presented in detail in Chapter 2. The strategy adopted for this survey is motivated by the scientific question which will be addressed with the sample constructed from the survey. Since the sample is dedicated to the study of groups, at low as well as high redshifts, spacial resolution is required to be able to resolve their cores at high redshifts. Therefore, *Chandra* telescope, which has the highest resolution compared to other X-ray telescopes, is used for the survey. Because detection of high redshift groups rely on long exposure times, only longest observations from *Chandra* archive are used for the search of groups. Finally, to construct a sample as large as possible, all observations available in the *Chandra* archive are used in the survey. The detection of all X-ray sources is done using a Voronoi Tesselation and Percolation algorithm which was proven to be efficient in detecting irregular, faint and/or extended sources, features which are common for groups in X-ray images. From all detected sources, potential groups are selected by comparing their spatial distribution to the distribution of point-like sources approximated with the telescope's point spread function.

In addition to the fact that groups have a low surface brightness, they are not always having a regular spatial distribution or their surface brightness might be contaminated by other point-like sources. This means that whether a group is detected or not depends on the efficiency of source detection algorithm. It has been showed in Chapter 2 that there is no perfect source detection algorithm and each of them has its own drawback. The tendency of a detection algorithm to select sources with a particular morphology is reflected in the property of the final sample, and can possible lead towards a bias in sample's properties.

Another bias which might appear during sample selection is in the process of characterizing a detected X-ray source as extended or not. In most cases, a group is selected based on its property to have an extended spatial structure when compared to the the telescope's PSF, which is a good approximation for a point-like source. However, in some cases, the presence of a central AGN or a bright compact core might lead to misclassification of the source as a point-like and therefore introduce a bias in the selected sample.

Since for CDGS there is a low count limit of 100 counts for a source to be included in the source catalogue, a bias introduced during source detection is thought to be minimal. The bias due to the presence of a compact core is tested using simulated images of a source with different sizes for the core and was found that this type of bias has a modes impact on source selection.

An important aspect for any X-ray group survey is obtaining optical confirmation for detected group candidates. The classification of an X-ray source as extended does not guarantee its group nature since there are other extended X-ray astrophysical sources. Therefore, optical confirmation of a galaxy overdensity is required to firmly characterize the X-ray source as a group. CDGS is a survey for which an optical follow-up is not yet available. However, a significant fraction of sources have been found in the literature to be confirmed groups/clusters.

The number of group candidates detected over an area of 9.6 deg^2 covered by CDGS is 162. Out of these, only 62 are confirmed groups and clusters with redshifts available from literature. The redshift distribution of these sources shows that the majority of sources detected are at medium redshifts of about 0.5 and the highest redshift is 1.27. The temperature distribution of these sources shows that almost half (42%) of the systems are groups (kT$<$ 3 keV), with the peak in the distribution at about 3 keV.

Compared to other *Chandra* archival surveys available in the literature (ChaMP - covers 13 deg^2 and Boschin (2002) - covers 5.5 deg^2), CDGS is a medium size survey. However, compared to large surveys from *XMM* and *ROSAT*, CDGS is significantly smaller. For example, the XCS survey, which is an *XMM* archival survey is about 40 times larger than CDGS and the compiled catalog contains 3675 cluster candidates with more than 50 counts. The lower effective area and lower field of view of *Chandra* telescope compared to *XMM* is the main cause of this significant difference between the archival samples constructed with *XMM* and that from CDGS. However, *Chandra*'s high spatial resolution allows a very detailed study of groups at low as well as high redshifts. With an angular resolution of $\sim$0.5 arcseconds, which corresponds to 4 kpc at a redshift of 1, *Chandra* can resolve a central compact core, contaminating point-like sources even at intermediate to high redshifts.

Another important aspect of this Thesis is the study of the evolution of X-ray properties of the IGM, study which is performed using a subsample of groups and clusters from CDGS for which a redshift is available from literature. The scientific question addressed with this subsample is how the thermal properties of central gas in groups evolve with redshift and whether this evolution is different in low mass systems compared to that for clusters. While there are literature studies of the evolution of CCs in clusters, which mostly agree that the number of CC is decreasing with increasing redshift, there is only one study of the evolution of CCs in groups. This CC study for groups show that groups and clusters have opposite evolutionary trends. The investigation of the evolution of CCs in groups and a comparison to that in clusters is presented in Chapter 3. A CC is established in a group or cluster when the gas temperature and density are such that it can efficiently lose energy through radiation. Therefore, observationally, a CC is characterized by a drop in gas' central temperature and an increase in its surface brightness. A unique definition, however, of what a CC is, is not available and in the literature there are various parameters used to quantify the strength of the CC based on the expected observed properties. In Chapter 3 six parameters are used to quantify the cooling state of a system and study its evolution: central cooling time ($t_{\rm cool}$), central entropy (K), central cooling time normalized by the age of the Universe ($t_{\rm cool}/t_{\rm Uni}$), ratio of the flux within central 40 kpc to that within 400 kpc ($c_{\rm SB}$), ratio of the flux within $0.15{\rm R}_{500}$ to that within ${\rm R}_{500}$ ($F_{\rm core}$) and the central flux excess above a beta model with a fixed core radius corresponding to the observed size of CCs in low redshift groups ($f_{\rm c}$). The main result found by studying the evolution of CCs using these six parameters is that groups and clusters have a similar evolutionary trend, irrespective of the CC estimator. However, another interesting result found is that the evolutionary trend is depended on the parameter used to quantify the CC. For example, the fraction of CCs in groups and clusters is decreasing with redshift if the $t_{\rm cool}/t_{\rm Uni}$, K and $f_{\rm c}$ parameters are used, there is a weak evolution for $c_{\rm SB}$ and no significant evolution for

t_{cool} and F_{core}. An improvement of this work compared to other literature studies of this kind is a careful investigation of the possible impact of different selection biases on the observed results. It was found that the bias due to the impact of core properties or the presence of a central AGN on the ability to characterize a source as extended is modest.

One way in which this work can be improved is by increasing the number of high redshift serendipitous sources. This would be possible with deep X-ray survey, covering a wide area. At present, there is no other X-ray telescope with an angular resolution comparable to *Chandra*'s. As regards future missions, eROSITA is the only approved mission which will perform an all-sky survey allowing the detection of a large number of clusters out to redshifts greater than 1. Although the number of clusters will be significantly increased, the resolution of eROSITA it is lower than that of *Chandra* and the study of cores in high redshift systems will be hindered by the poorer resolution. Other planned future missions are SMART-X (Square Meter Arcsecond Resolution X-ray Telescope) which would have *Chandra*'s angular resolution and more effective area.

With respect to future work, there are several possible studies which can arise from the work presented in this thesis. Most important would be the optical follow-up of possible groups and clusters detected in the survey to confirm their nature. Therefore, this larger sample constructed from CDGS can be used to answer other scientific questions such as: what is the correlation between different X-ray properties? is it an evolution in the observed correlation? In addition to this, important knowledge about these systems can be obtained by studying multiwavelength properties of groups and clusters. The extension of the survey to other wavelengths such as optical, radio or infrared can be used to study AGN feedback and its redshift dependence in low and high mass systems or the impact of gas within groups and clusters to the properties of the brightest galaxy within the system.

BIBLIOGRAPHY

Agnes P. et al., 2014, ArXiv e-prints

Akerib D. S. et al., 2004, Physical Review Letters, 93, 211301

Akerib D. S. et al., 2013, Nuclear Instruments and Methods in Physics Research A, 704, 111

Alam U., Lukić Z., Bhattacharya S., 2011, ApJ, 727, 87

Alcock C. et al., 2000, ApJ, 542, 281

Allen S. W., Rapetti D. A., Schmidt R. W., Ebeling H., Morris R. G., Fabian A. C., 2008, MNRAS, 383, 879

Alshino A., Ponman T., Pacaud F., Pierre M., 2010, MNRAS, 407, 2543

Aprile E. et al., 2005, New Astron. Rev., 49, 289

Asplund M., Lambert D. L., Nissen P. E., Primas F., Smith V. V., 2006, ApJ, 644, 229

Babul A., Balogh M. L., Lewis G. F., Poole G. B., 2002, MNRAS, 330, 329

Bahcall N. A. et al., 2003, ApJ, 148, 243

Bania T. M., Rood R. T., Balser D. S., 2002, Nature, 415, 54

Barkhouse W. A. et al., 2006, ApJ, 645, 955

Bauer F. E. et al., 2002, AJ, 123, 1163

Bauer F. E., Fabian A. C., Sanders J. S., Allen S. W., Johnstone R. M., 2005, MNRAS, 359, 1481

Benson A. J., Bower R. G., Frenk C. S., Lacey C. G., Baugh C. M., Cole S., 2003, ApJ, 599, 38

Birnboim Y., Dekel A., 2003, MNRAS, 345, 349

Bîrzan L., Rafferty D. A., McNamara B. R., Wise M. W., Nulsen P. E. J., 2004, ApJ, 607, 800

Blake C. et al., 2011, MNRAS, 418, 1707

Blanton E. L., Randall S. W., Clarke T. E., Sarazin C. L., McNamara B. R., Douglass E. M., McDonald M., 2011, ApJ, 737, 99

Bleem L. E. et al., 2015, Astrophysical Journal, Supplement, 216, 27

Boehringer H., Voges W., Fabian A. C., Edge A. C., Neumann D. M., 1993, MNRAS, 264, L25

Böhringer H., Chon G., Collins C. A., 2014a, ArXiv e-prints

Böhringer H., Chon G., Collins C. A., Guzzo L., Nowak N., Bobrovskyi S., 2014b, ArXiv e-prints

Böhringer H. et al., 2002, ApJ, 566, 93

Böhringer H. et al., 2001, A&A, 369, 826

Bonamente M., Landry D., Maughan B., Giles P., Joy M., Nevalainen J., 2012, MNRAS, 177

Borgani S., Governato F., Wadsley J., Menci N., Tozzi P., Quinn T., Stadel J., Lake G., 2002, MNRAS, 336, 409

Boschin W., 2002, A&A, 396, 397

Bower R. G., Benson A. J., Lacey C. G., Baugh C. M., Cole S., Frenk C. S., 2001, MNRAS, 325, 497

Bower R. G., Benson A. J., Malbon R., Helly J. C., Frenk C. S., Baugh C. M., Cole S., Lacey C. G., 2006, MNRAS, 370, 645

Bower R. G., McCarthy I. G., Benson A. J., 2008, MNRAS, 390, 1399

Bradač M., Allen S. W., Treu T., Ebeling H., Massey R., Morris R. G., von der Linden A., Applegate D., 2008, ApJ, 687, 959

Branchesi M., Gioia I. M., Fanti C., Fanti R., 2007, A&A, 472, 739

Brandt W. N., Alexander D. M., Bauer F. E., Hornschemeier A. E., 2002, Royal Society of London Philosophical Transactions Series A, 360, 2057

Brighenti F., Mathews W. G., 2001, ApJ, 553, 103

Bryan G. L., 2000, Astrophysical Journal, Letters, 544, L1

Bryan G. L., Norman M. L., 1998, ApJ, 495, 80

Burenin R. A., Vikhlinin A., Hornstrup A., Ebeling H., Quintana H., Mescheryakov A., 2007, ApJS, 172, 561

Burns J. O., Hallman E. J., Gantner B., Motl P. M., Norman M. L., 2008, ApJ, 675, 1125

Cao X. et al., 2014, Science China Physics, Mechanics, and Astronomy, 57, 1476

Carlstrom J. E. et al., 2011, PASP, 123, 568

Cash W., 1979, ApJ, 228, 939

Castellano M. et al., 2011, A&A, 530, A27

Cavagnolo K. W., Donahue M., Voit G. M., Sun M., 2008, ApJ, 682, 821

Cavagnolo K. W., Donahue M., Voit G. M., Sun M., 2009, ApJS, 182, 12

Cavaliere A., Fusco-Femiano R., 1976, A&A, 49, 137

Chen L.-W., Fabian A. C., Gendreau K. C., 1997, MNRAS, 285, 449

Chen Y., Reiprich T. H., Böhringer H., Ikebe Y., Zhang Y.-Y., 2007, A&A, 466, 805

Chiappetti L. et al., 2013, MNRAS, 429, 1652

Coc A., Vangioni E., 2010, Journal of Physics Conference Series, 202, 012001

Cole S. et al., 2005, MNRAS, 362, 505

Collaboration P. et al., 2013a

Collaboration P. et al., 2013b

Couch W. J., Ellis R. S., MacLaren I., Malin D. F., 1991, MNRAS, 249, 606

Croston J. H., Hardcastle M. J., Birkinshaw M., 2005, MNRAS, 357, 279

Croston J. H. et al., 2008, A&A, 487, 431

Croton D. J. et al., 2006, MNRAS, 365, 11

Dalton G. B., Maddox S. J., Sutherland W. J., Efstathiou G., 1997, MNRAS, 289, 263

Davis M., Efstathiou G., Frenk C. S., White S. D. M., 1985, ApJ, 292, 371

De Grandi S. et al., 1999, Astrophysical Journal, Letters, 513, L17

De Luca A., Molendi S., 2004, A&A, 419, 837

De Lucia G., Blaizot J., 2007, MNRAS, 375, 2

Dickey J. M., Lockman F. J., 1990, ARA&A, 28, 215

Diemand J., Zemp M., Moore B., Stadel J., Carollo C. M., 2005, MNRAS, 364, 665

Dodelson S., Knox L., 2000, Physical Review Letters, 84, 3523

Donahue M., Voit G. M., Scharf C. A., Gioia I. M., Mullis C. R., Hughes J. P., Stocke J. T., 1999, ApJ, 527, 525

Dong R., Rasmussen J., Mulchaey J. S., 2010, ApJ, 712, 883

Dressler A., Gunn J. E., 1992, Astrophysical Journal, Supplement, 78, 1

Dubinski J., Carlberg R. G., 1991, ApJ, 378, 496

Dutton A. A., Macciò A. V., 2014, MNRAS, 441, 3359

Ebeling H., Barrett E., Donovan D., Ma C.-J., Edge A. C., van Speybroeck L., 2007, Astrophysical Journal, Letters, 661, L33

Ebeling H., Edge A. C., Allen S. W., Crawford C. S., Fabian A. C., Huchra J. P., 2000, MNRAS, 318, 333

Ebeling H., Edge A. C., Bohringer H., Allen S. W., Crawford C. S., Fabian A. C., Voges W., Huchra J. P., 1998, MNRAS, 301, 881

Ebeling H., Edge A. C., Mantz A., Barrett E., Henry J. P., Ma C. J., van Speybroeck L., 2010, MNRAS, 407, 83

Ebeling H., Wiedenmann G., 1993, Phys. Rev. E., 47, 704

Eckert D., Molendi S., Paltani S., 2011, A&A, 526, A79

Eckmiller H. J., Hudson D. S., Reiprich T. H., 2011, A&A, 535, A105

Edge A. C., Stewart G. C., Fabian A. C., 1992, MNRAS, 258, 177

Edge A. C., Stewart G. C., Fabian A. C., Arnaud K. A., 1990, MNRAS, 245, 559

Efstathiou G., 2000, MNRAS, 317, 697

Efstathiou G., Frenk C. S., White S. D. M., Davis M., 1988, MNRAS, 235, 715

Eisenstein D. J. et al., 2005, ApJ, 633, 560

Eke V. R., Cole S., Frenk C. S., 1996, MNRAS, 282, 263

Ellis S. C., Jones L. R., 2002, MNRAS, 330, 631

Elvis M. et al., 2009, Astrophysical Journal, Supplement, 184, 158

Elvis M. et al., 2012, ApJ, 759, 6

Erfanianfar G. et al., 2013

Ettori S., Tozzi P., Borgani S., Rosati P., 2004, A&A, 417, 13

Evrard A. E., 1990, ApJ, 363, 349

Fabian A. C. et al., 2000, MNRAS, 318, L65

Fassbender R. et al., 2011, New Journal of Physics, 13, 125014

Feruglio C. et al., 2008, A&A, 488, 417

Fields B. D., 2011, Annual Review of Nuclear and Particle Science, 61, 47

Finlator K., Davé R., Papovich C., Hernquist L., 2006, ApJ, 639, 672

Finoguenov A. et al., 2009, ApJ, 704, 564

Finoguenov A. et al., 2007, Astrophysical Journal, Supplement, 172, 182

Finoguenov A., Reiprich T. H., Böhringer H., 2001, A&A, 368, 749

Freeman P. E., Kashyap V., Rosner R., Lamb D. Q., 2002, ApJS, 138, 185

Fukugita M., Kawasaki M., 2006, ApJ, 646, 691

Fumagalli M., O'Meara J. M., Prochaska J. X., 2011, Science, 334, 1245

Gastaldello F., Buote D. A., Humphrey P. J., Zappacosta L., Bullock J. S., Brighenti F., Mathews W. G., 2007, ApJ, 669, 158

Gastaldello F., Buote D. A., Temi P., Brighenti F., Mathews W. G., Ettori S., 2009, ApJ, 693, 43

Gehrels N., 1986, ApJ, 303, 336

Geller M. J., Huchra J. P., 1983, Astrophysical Journal, Supplement, 52, 61

Ghigna S., Moore B., Governato F., Lake G., Quinn T., Stadel J., 2000, ApJ, 544, 616

Giacconi R. et al., 2002, Astrophysical Journal, Supplement, 139, 369

Gilbank D. G., Gladders M. D., Yee H. K. C., Hsieh B. C., 2011, AJ, 141, 94

Gilli R., Comsatri A., Hasinger G., 2007, Astronomy and Astrophysics, 463, 79

Gioia I. M., Henry J. P., Maccacaro T., Morris S. L., Stocke J. T., Wolter A., 1990a, Astrophysical Journal, Letters, 356, L35

Gioia I. M., Maccacaro T., Schild R. E., Wolter A., Stocke J. T., Morris S. L., Henry J. P., 1990b, Astrophysical Journal, Supplement, 72, 567

Gitti M., Nulsen P. E. J., David L. P., McNamara B. R., Wise M. W., 2011, ApJ, 732, 13

Gitti M., O'Sullivan E., Giacintucci S., David L. P., Vrtilek J., Raychaudhury S., Nulsen P. E. J., 2010, ApJ, 714, 758

Gladders M. D., Yee H. K. C., 2000, AJ, 120, 2148

Gladders M. D., Yee H. K. C., Majumdar S., Barrientos L. F., Hoekstra H., Hall P. B., Infante L., 2007, ApJ, 655, 128

Gonzalez A. H., Tran K.-V. H., Conbere M. N., Zaritsky D., 2005, Astrophysical Journal, Letters, 624, L73

Grego L., Carlstrom J. E., Reese E. D., Holder G. P., Holzapfel W. L., Joy M. K., Mohr J. J., Patel S., 2001, ApJ, 552, 2

Hao J. et al., 2010, Astrophysical Journal, Supplement, 191, 254

Häring N., Rix H.-W., 2004, Astrophysical Journal, Letters, 604, L89

Hasselfield M. et al., 2013, Journal of Cosmology and Astroparticle Physics, 7, 8

Helsdon S. F., Ponman T. J., 2000, MNRAS, 315, 356

Henley D. B., Shelton R. L., Kwak K., Joung M. R., Mac Low M.-M., 2010, ApJ, 723, 935

Henning J. W., Gantner B., Burns J. O., Hallman E. J., 2009, ApJ, 697, 1597

Hernquist L., 1990, ApJ, 356, 359

Hickox R. C., Markevitch M., 2006, ApJ, 645, 95

Hilton M. et al., 2012, MNRAS, 424, 2086

Hinshaw G. et al., 2013, Astrophysical Journal, Supplement, 208, 19

Hlavacek-Larrondo J., Fabian A. C., Edge A. C., Ebeling H., Sanders J. S., Hogan M. T., Taylor G. B., 2012, MNRAS, 421, 1360

Holden B. P. et al., 2001, AJ, 122, 629

Holden B. P., Stanford S. A., Squires G. K., Rosati P., Tozzi P., Eisenhardt P., Spinrad H., 2002, AJ, 124, 33

Horner D. J., 2001, PhD thesis, University of Maryland

Horner D. J., Perlman E. S., Ebeling H., Jones L. R., Scharf C. A., Wegner G., Malkan M., Maughan B., 2008, Astrophysical Journal, Supplement, 176, 374

Hsieh B. C., Yee H. K. C., Lin H., Gladders M. D., 2005, Astrophysical Journal, Supplement, 158, 161

Huang X. et al., 2009, Astrophysical Journal, Letters, 707, L12

Huchra J. P., Geller M. J., 1982, ApJ, 257, 423

Hudson D. S., Mittal R., Reiprich T. H., Nulsen P. E. J., Andernach H., Sarazin C. L., 2010, A&A, 513, A37

Humphrey P. J., Liu W., Buote D. A., 2009, ApJ, 693, 822

Izotov Y. I., Thuan T. X., 2010, Astrophysical Journal, Letters, 710, L67

Jaacks J., Choi J.-H., Nagamine K., Thompson R., Varghese S., 2012, MNRAS, 420, 1606

Jaffe A. H. et al., 2001, Physical Review Letters, 86, 3475

Jeltema T. E. et al., 2009, MNRAS, 399, 715

Jetha N. N., Ponman T. J., Hardcastle M. J., Croston J. H., 2007, MNRAS, 376, 193

Jing Y. P., Suto Y., 2000, Astrophysical Journal, Letters, 529, L69

Jones L. R., McHardy I., Newsam A., Mason K., 2002, MNRAS, 334, 219

Kauffmann G., Colberg J. M., Diaferio A., White S. D. M., 1999, MNRAS, 303, 188

Kay S. T., da Silva A. C., Aghanim N., Blanchard A., Liddle A. R., Puget J.-L., Sadat R., Thomas P. A., 2007, MNRAS, 377, 317

Kazin E. A. et al., 2014, MNRAS, 441, 3524

Keshet U., Waxman E., Loeb A., Springel V., Hernquist L., 2003, ApJ, 585, 128

Kim D.-W. et al., 2004, Astrophysical Journal, Supplement, 150, 19

Kirkman D., Tytler D., Suzuki N., O'Meara J. M., Lubin D., 2003, Astrophysical Journal, Supplement, 149, 1

Kleinmann S. G., Hamilton D., Keel W. C., Wynn-Williams C. G., Eales S. A., Becklin E. E., Kuntz K. D., 1988, ApJ, 328, 161

Knight P. A., Ponman T. J., 1997, MNRAS, 289, 955

Knobel C. et al., 2012, ApJ, 753, 121

Kocsis B., Haiman Z., Frei Z., 2005, ApJ, 623, 632

Koens L. A., Maughan B. J., Jones L. R., Ebeling H., Horner D. J., Perlman E. S., Phillipps S., Scharf C. A., 2013, MNRAS, 435, 3231

Koester B. P. et al., 2007, ApJ, 660, 239

Kotov O., Vikhlinin A., 2006, ApJ, 641, 752

Kuntz K. D., Snowden S., 2008, A&A, 478, 575

Laird E. S. et al., 2009, Astrophysical Journal, Supplement, 180, 102

Lehmer B. D. et al., 2005, Astrophysical Journal, Supplement, 161, 21

Lidman C. E., Peterson B. A., 1996, AJ, 112, 2454

Lloyd-Davies E. J. et al., 2011, MNRAS, 418, 14

Lumb D. H. et al., 2004, A&A, 420, 853

Lumb D. H., Warwick R. S., Page M., De Luca A., 2002, A&A, 389, 93

Ma C.-J., McNamara B. R., Nulsen P. E. J., 2013, ApJ, 763, 63

Magorrian J. et al., 1998, AJ, 115, 2285

Mahdavi A., Hoekstra H., Babul A., Bildfell C., Jeltema T., Henry J. P., 2013, ApJ, 767, 116

Manners J. C. et al., 2003, MNRAS, 343, 293

Marconi A., Hunt L. K., 2003, Astrophysical Journal, Letters, 589, L21

Markevitch M., 1998, ApJ, 504, 27

Markevitch M., 2002, ArXiv Astrophysics e-prints

Markevitch M. et al., 2003, ApJ, 583, 70

Maughan B. J., Giles P. A., Randall S. W., Jones C., Forman W. R., 2012, MNRAS, 2419

McCarthy I. G., Babul A., Balogh M. L., 2002, ApJ, 573, 515

McCarthy I. G., Babul A., Bower R. G., Balogh M. L., 2008, MNRAS, 386, 1309

McCarthy I. G., Balogh M. L., Babul A., Poole G. B., Horner D. J., 2004, ApJ, 613, 811

McCarthy I. G., Schaye J., Bower R. G., Ponman T. J., Booth C. M., Dalla Vecchia C., Springel V., 2011, MNRAS, 412, 1965

McDonald M. et al., 2014, ArXiv e-prints

McDonald M. et al., 2013, ApJ, 774, 23

McNamara B. R., Nulsen P. E. J., 2007, ARA&A, 45, 117

McNamara B. R., Nulsen P. E. J., 2012, New Journal of Physics, 14, 055023

McNamara B. R. et al., 2000, ApJ, 534, L135

Mehrtens N. et al., 2012, MNRAS, 423, 1024

Menci N., Cavaliere A., 2000, MNRAS, 311, 50

Merloni A. et al., 2010, ApJ, 708, 137

Merloni A. et al., 2012, ArXiv e-prints

Mittal R., Hicks A., Reiprich T. H., Jaritz V., 2011, A&A, 532, A133

Mittal R., Hudson D. S., Reiprich T. H., Clarke T., 2009, A&A, 501, 835

Miyazaki S., Hamana T., Ellis R. S., Kashikawa N., Massey R. J., Taylor J., Refregier A., 2007, ApJ, 669, 714

Mohr J. J., Mathiesen B., Evrard A. E., 1999, ApJ, 517, 627

Moore B., Quinn T., Governato F., Stadel J., Lake G., 1999, MNRAS, 310, 1147

Morita U., Ishisaki Y., Yamasaki N. Y., Ota N., Kawano N., Fukazawa Y., Ohashi T., 2006, PASJ, 58, 719

Motl P. M., Hallman E. J., Burns J. O., Norman M. L., 2005, ApJ, 623, L63

Muanwong O., Kay S. T., Thomas P. A., 2006, ApJ, 649, 640

Mulchaey J. S., 2000, ARA&A, 38, 289

Mullis C. R. et al., 2003, ApJ, 594, 154

Mullis C. R. et al., 2004, ApJ, 607, 175

Mushotzky R. F., Loewenstein M., 1997, ApJ, 481, L63

Navarro J. F., Frenk C. S., White S. D. M., 1995, MNRAS, 275, 720

Navarro J. F., Frenk C. S., White S. D. M., 1997, ApJ, 490, 493

Netterfield C. B. et al., 2002, ApJ, 571, 604

Neumann D. M., Arnaud M., 1999, A&A, 348, 711

Night C., Nagamine K., Springel V., Hernquist L., 2006, MNRAS, 366, 705

O'Dea C. P. et al., 2008, ApJ, 681, 1035

Oh S. P., Benson A. J., 2003, MNRAS, 342, 664

O'Hara T. B., Mohr J. J., Bialek J. J., Evrard A. E., 2006, ApJ, 639, 64

O'Meara J. M., Burles S., Prochaska J. X., Prochter G. E., Bernstein R. A., Burgess K. M., 2006, Astrophysical Journal, Letters, 649, L61

Osmond J. P. F., Ponman T. J., 2004, MNRAS, 350, 1511

O'Sullivan E., Giacintucci S., David L. P., Gitti M., Vrtilek J. M., Raychaudhury S., Ponman T. J., 2011a, ApJ, 735, 11

O'Sullivan E., Giacintucci S., David L. P., Gitti M., Vrtilek J. M., Raychaudhury S., Ponman T. J., 2011b, ApJ, 735, 11

Pacaud F. et al., 2007, MNRAS, 382, 1289

Pacaud F. et al., 2006, MNRAS, 372, 578

Paczynski B., 1986, ApJ, 304, 1

Panagoulia E. K., Fabian A. C., Sanders J. S., 2014, MNRAS, 438, 2341

PandaX Collaboration et al., 2014, ArXiv e-prints

Pascut A., Ponman T. J., 2015, MNRAS, 447, 3723

Peimbert M., Luridiana V., Peimbert A., 2007, ApJ, 666, 636

Pelló R. et al., 2009, A&A, 508, 1173

Peres C. B., Fabian A. C., Edge A. C., Allen S. W., Johnstone R. M., White D. A., 1998, MNRAS, 298, 416

Perlman E. S., Horner D. J., Jones L. R., Scharf C. A., Ebeling H., Wegner G., Malkan M., 2002, Astrophysical Journal, Supplement, 140, 265

Perlmutter S. et al., 1999, ApJ, 517, 565

Pettini M., Zych B. J., Murphy M. T., Lewis A., Steidel C. C., 2008, MNRAS, 391, 1499

Pierre M. et al., 2007, MNRAS, 382, 279

Pierre M., Pacaud F., Juin J. B., Melin J. B., Valageas P., Clerc N., Corasaniti P. S., 2011, MNRAS, 414, 1732

Pierre M. et al., 2004, Journal of Cosmology and Astroparticle Physics, 9, 11

Planck Collaboration et al., 2014, A&A, 571, A29

Planck Collaboration et al., 2011, A&A, 536, A8

Ponman T. J., Cannon D. B., Navarro J. F., 1999, Nature, 397, 135

Ponman T. J., Sanderson A. J. R., Finoguenov A., 2003, MNRAS, 343, 331

Poole G. B., Fardal M. A., Babul A., McCarthy I. G., Quinn T., Wadsley J., 2006, MNRAS, 373, 881

Pratt G. W., Arnaud M., 2003, A&A, 408, 1

Pratt G. W., Croston J. H., Arnaud M., Böhringer H., 2009, A&A, 498, 361

Puccetti S. et al., 2009, Astrophysical Journal, Supplement, 185, 586

Rafferty D. A., McNamara B. R., Nulsen P. E. J., Wise M. W., 2006, ApJ, 652, 216

Ramella M., Geller M. J., Pisani A., da Costa L. N., 2002, AJ, 123, 2976

Randall S. W., Jones C., Markevitch M., Blanton E. L., Nulsen P. E. J., Forman W. R., 2009, ApJ, 700, 1404

Rasmussen J., Ponman T. J., 2007, MNRAS, 380, 1554

Rasmussen J., Ponman T. J., 2009, MNRAS, 399, 239

Reed D. S., Bower R., Frenk C. S., Jenkins A., Theuns T., 2007, MNRAS, 374, 2

Reichardt C. L. et al., 2013, ApJ, 763, 127

Reichert A., Böhringer H., Fassbender R., Mühlegger M., 2011, A&A, 535, A4

Riess A. G. et al., 1998, AJ, 116, 1009

Romer A. K. et al., 2000, ApJS, 126, 209

Romer A. K., Viana P. T. P., Liddle A. R., Mann R. G., 2001, ApJ, 547, 594

Rosati P., Della Ceca R., Burg R., Norman C., Giacconi R., 1995, ApJ, 445, L11

Rosati P. et al., 2000, The Messenger, 99, 26

Rosati P., Stanford S. A., Eisenhardt P. R., Elston R., Spinrad H., Stern D., Dey A., 1999, AJ, 118, 76

Rosati P. et al., 2004, AJ, 127, 230

Rossetti M., Molendi S., 2010, A&A, 510, A83

Roulet E., Mollerach S., 1997, Physics Reports, 279, 67

Rumbaugh N., Kocevski D. D., Gal R. R., Lemaux B. C., Lubin L. M., Fassnacht C. D., Squires G. K., 2013, ApJ, 763, 124

Russell H. R., Fabian A. C., Taylor G. B., Sanders J. S., Blundell K. M., Crawford C. S., Johnstone R. M., Belsole E., 2012, MNRAS, 422, 590

Russell H. R., McNamara B. R., Edge A. C., Hogan M. T., Main R. A., Vantyghem A. N., 2013, MNRAS, 432, 530

Ryan, Jr. R. E. et al., 2007, ApJ, 668, 839

Ryan S. G., Beers T. C., Olive K. A., Fields B. D., Norris J. E., 2000, Astrophysical Journal, Letters, 530, L57

Sahlén M. et al., 2009, MNRAS, 397, 577

Samuele R., McNamara B. R., Vikhlinin A., Mullis C. R., 2011, ApJ, 731, 31

Sanderson A. J. R., O'Sullivan E., Ponman T. J., 2009, MNRAS, 395, 764

Sanderson A. J. R., Ponman T. J., O'Sullivan E., 2006, MNRAS, 372, 1496

Santos J. S., Rosati P., Tozzi P., Böhringer H., Ettori S., Bignamini A., 2008, A&A, 483, 35

Santos J. S., Tozzi P., Rosati P., Böhringer H., 2010, A&A, 521, A64

Santos J. S., Tozzi P., Rosati P., Nonino M., Giovannini G., 2012, A&A, 539, A105

Sarazin C. L., 1988, X-ray emission from clusters of galaxies. Cambridge University Press

Sbordone L. et al., 2010, A&A, 522, A26

Scannapieco E., Oh S. P., 2004, ApJ, 608, 62

Scharf C. A., Jones L. R., Ebeling H., Perlman E., Malkan M., Wegner G., 1997, ApJ, 477, 79

Schechter P., 1976, ApJ, 203, 297

Schmidt R. W., Allen S. W., 2007, MNRAS, 379, 209

Semler D. R. et al., 2012

Serlemitsos P. J. et al., 2007, PASJ, 59, 9

Shan H. et al., 2012, ApJ, 748, 56

Short C. J., Thomas P. A., Young O. E., 2012, ArXiv e-prints

Siemiginowska A., Burke D. J., Aldcroft T. L., Worrall D. M., Allen S., Bechtold J., Clarke T., Cheung C. C., 2010, ApJ, 722, 102

Silk J., Mamon G. A., 2012, Research in Astronomy and Astrophysics, 12, 917

Slack N. W., Ponman T. J., 2014, MNRAS, 439, 102

Snowden S. L., Egger R., Finkbeiner D. P., Freyberg M. J., Plucinsky P. P., 1998, ApJ, 493, 715

Snowden S. L., Mushotzky R. F., Kuntz K. D., Davis D. S., 2008, A&A, 478, 615

Somerville R. S., Hopkins P. F., Cox T. J., Robertson B. E., Hernquist L., 2008, MNRAS, 391, 481

Song J. et al., 2012, ArXiv e-prints

Spite F., Spite M., 1982, A&A, 115, 357

Springel V., Di Matteo T., Hernquist L., 2005, MNRAS, 361, 776

Stanford S. A., Elston R., Eisenhardt P. R., Spinrad H., Stern D., Dey A., 1997, AJ, 114, 2232

Steigman G., 2001, ArXiv Astrophysics e-prints

Stern D., Jimenez R., Verde L., Stanford S. A., Kamionkowski M., 2010, Astrophysical Journal, Supplement, 188, 280

Stott J. P. et al., 2012, MNRAS, 422, 2213

Struble M. F., Rood H. J., 1987, Astrophysical Journal, Supplement, 63, 543

Sun M., Jones C., Forman W., Vikhlinin A., Donahue M., Voit M., 2007, ApJ, 657, 197

Sun M., Voit G. M., Donahue M., Jones C., Forman W., Vikhlinin A., 2009, ApJ, 693, 1142

Sutherland R. S., Dopita M. A., 1993, Astrophysical Journal, Supplement, 88, 253

Szokoly G. P. et al., 2004, ApJS, 155, 271

Takey A., Schwope A., Lamer G., 2013, A&A, 558, A75

Tanaka M. et al., 2008, A&A, 489, 571

Tinker J., Kravtsov A. V., Klypin A., Abazajian K., Warren M., Yepes G., Gottlöber S., Holz D. E., 2008, ApJ, 688, 709

Tisserand P. et al., 2007, A&A, 469, 387

Tozzi P., Norman C., 2001, ApJ, 546, 63

Tran K.-V. H., Saintonge A., Moustakas J., Bai L., Gonzalez A. H., Holden B. P., Zaritsky D., Kautsch S. J., 2009, ApJ, 705, 809

Tran K.-V. H., van Dokkum P., Illingworth G. D., Kelson D., Gonzalez A., Franx M., 2005, ApJ, 619, 134

van Engelen A. et al., 2012, ApJ, 756, 142

Viana P. T. P. et al., 2013, Astronomische Nachrichten, 334, 462

Vikhlinin A., Burenin R., Forman W. R., Jones C., Hornstrup A., Murray S. S., Quintana H., 2007, in Heating versus Cooling in Galaxies and Clusters of Galaxies, Böhringer H., Pratt G. W., Finoguenov A., Schuecker P., eds., p. 48

Vikhlinin A., Kravtsov A., Forman W., Jones C., Markevitch M., Murray S. S., Van Speybroeck L., 2006, ApJ, 640, 691

Vikhlinin A., Markevitch M., Forman W., Jones C., 2001, ApJ, 555, L87

Vikhlinin A., Markevitch M., Murray S. S., Jones C., Forman W., Van Speybroeck L., 2005, ApJ, 628, 655

Vikhlinin A., McNamara B. R., Forman W., Jones C., Quintana H., Hornstrup A., 1998, ApJ, 502, 558

Vikhlinin A., van Speybroeck L., Markevitch M., Forman W. R., Grego L., 2002, ApJ, 578, L107

Voges W., 1993, Advances in Space Research, 13, 391

Voges W. et al., 1999, A&A, 349, 389

Voit G. M., 2005, Reviews of Modern Physics, 77, 207

Voit G. M., 2011, ApJ, 740, 28

Voit G. M., Balogh M. L., Bower R. G., Lacey C. G., Bryan G. L., 2003, ApJ, 593, 272

Voit G. M., Donahue M., Bryan G. L., McDonald M., 2014, ArXiv e-prints

Voit G. M., Ponman T. J., 2003, Astrophysical Journal, Letters, 594, L75

Wang Y., Xu H.-G., Gu J.-H., Gu L.-Y., Wang J.-Y., Zhang Z.-L., 2010, Research in Astronomy and Astrophysics, 10, 1013

Wen Z. L., Han J. L., 2011, ApJ, 734, 68

Wen Z. L., Han J. L., Liu F. S., 2012, Astrophysical Journal, Supplement, 199, 34

White S. D. M., Rees M. J., 1978, MNRAS, 183, 341

Willis J. P. et al., 2013, MNRAS, 430, 134

Wittman D., Dell'Antonio I. P., Hughes J. P., Margoniner V. E., Tyson J. A., Cohen J. G., Norman D., 2006, ApJ, 643, 128

Wittman D. M. et al., 2002, in Society of Photo-Optical Instrumentation Engineers (SPIE) Conference Series, Vol. 4836, Survey and Other Telescope Technologies and Discoveries, Tyson J. A., Wolff S., eds., pp. 73–82

Wu X.-P., Xue Y.-J., Fang L.-Z., 1999, ApJ, 524, 22

Wyrzykowski Ł. et al., 2010, MNRAS, 407, 189

Wyrzykowski Ł. et al., 2009, MNRAS, 397, 1228

Wyrzykowski L. et al., 2011, MNRAS, 416, 2949

Xue Y.-J., Wu X.-P., 2003, ApJ, 584, 34

Yang Y., Mushotzky R. F., Steffen A. T., Barger A. J., Cowie L. L., 2004, AJ, 128, 1501

Zhao H., 1996, MNRAS, 278, 488

Appendix A

X-ray images

X-ray images of all group candidates detected in the Chandra Deep Group Survey. Each panel represents the soft, exposure corrected image of the source detected as extended in the survey.

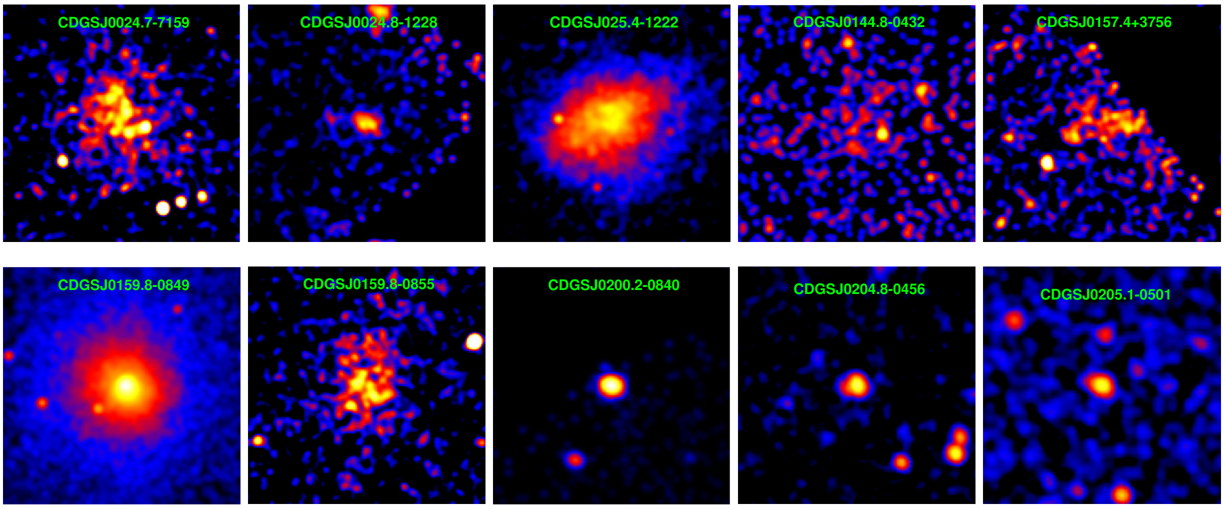

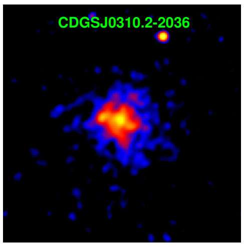
CDGSJ0310.2-2036

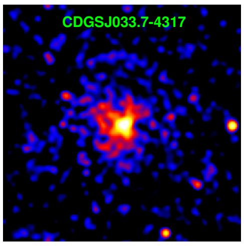
CDGSJ033.7-4317

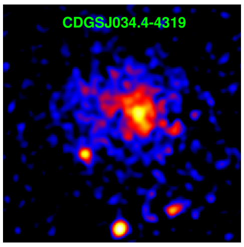
CDGSJ034.4-4319

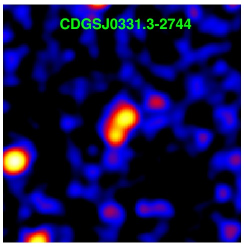
CDGSJ0331.3-2744

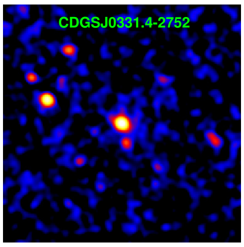
CDGSJ0331.4-2752

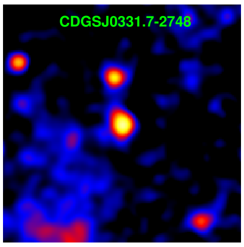
CDGSJ0331.7-2748

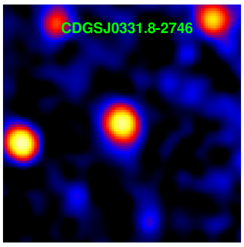
CDGSJ0331.8-2746

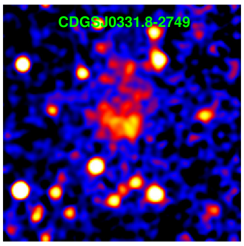
CDGSJ0331.8-2749

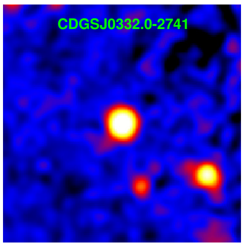
CDGSJ0332.0-2741

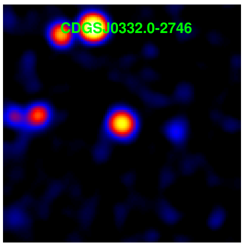
CDGSJ0332.0-2746

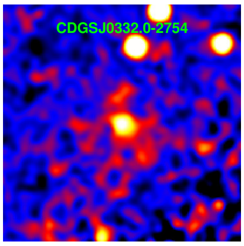
CDGSJ0332.0-2754

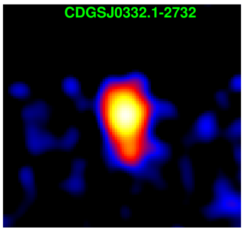
CDGSJ0332.1-2732

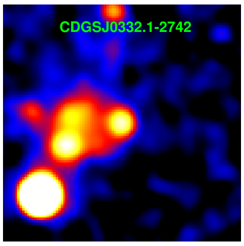
CDGSJ0332.1-2742

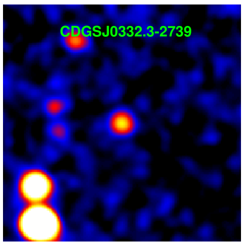
CDGSJ0332.3-2739

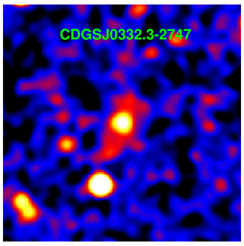
CDGSJ0332.3-2747

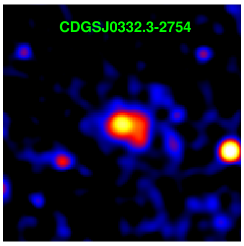
CDGSJ0332.3-2754

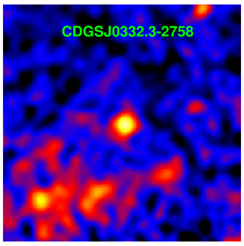
CDGSJ0332.3-2758

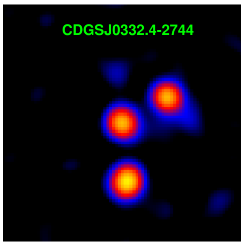
CDGSJ0332.4-2744

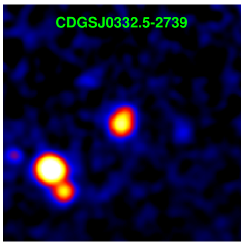
CDGSJ0332.5-2739

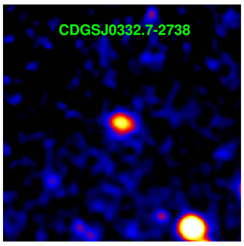
CDGSJ0332.7-2738

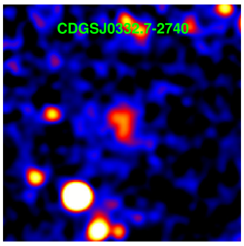
CDGSJ0332.7-2740

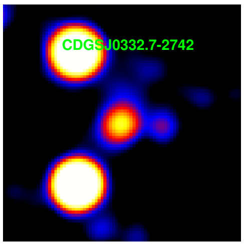
CDGSJ0332.7-2742

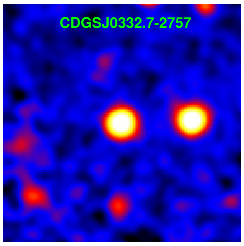
CDGSJ0332.7-2757

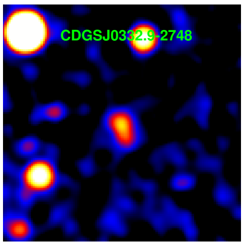
CDGSJ0332.9-2748

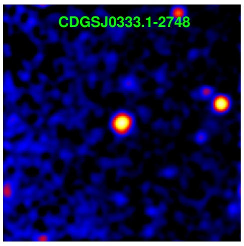
CDGSJ0333.1-2748

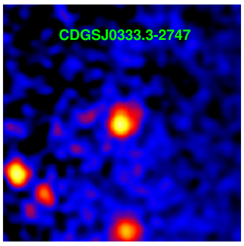
CDGSJ0333.3-2747

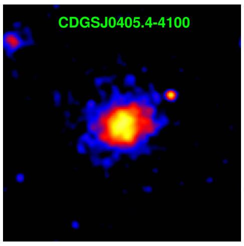
CDGSJ0405.4-4100

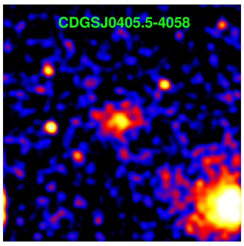
CDGSJ0405.5-4058

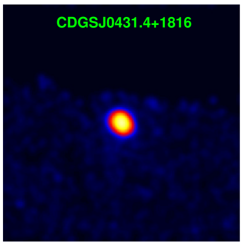
CDGSJ0431.4+1816

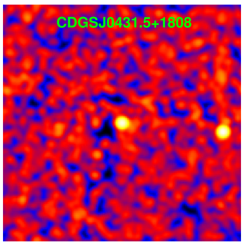
CDGSJ0431.5+1808

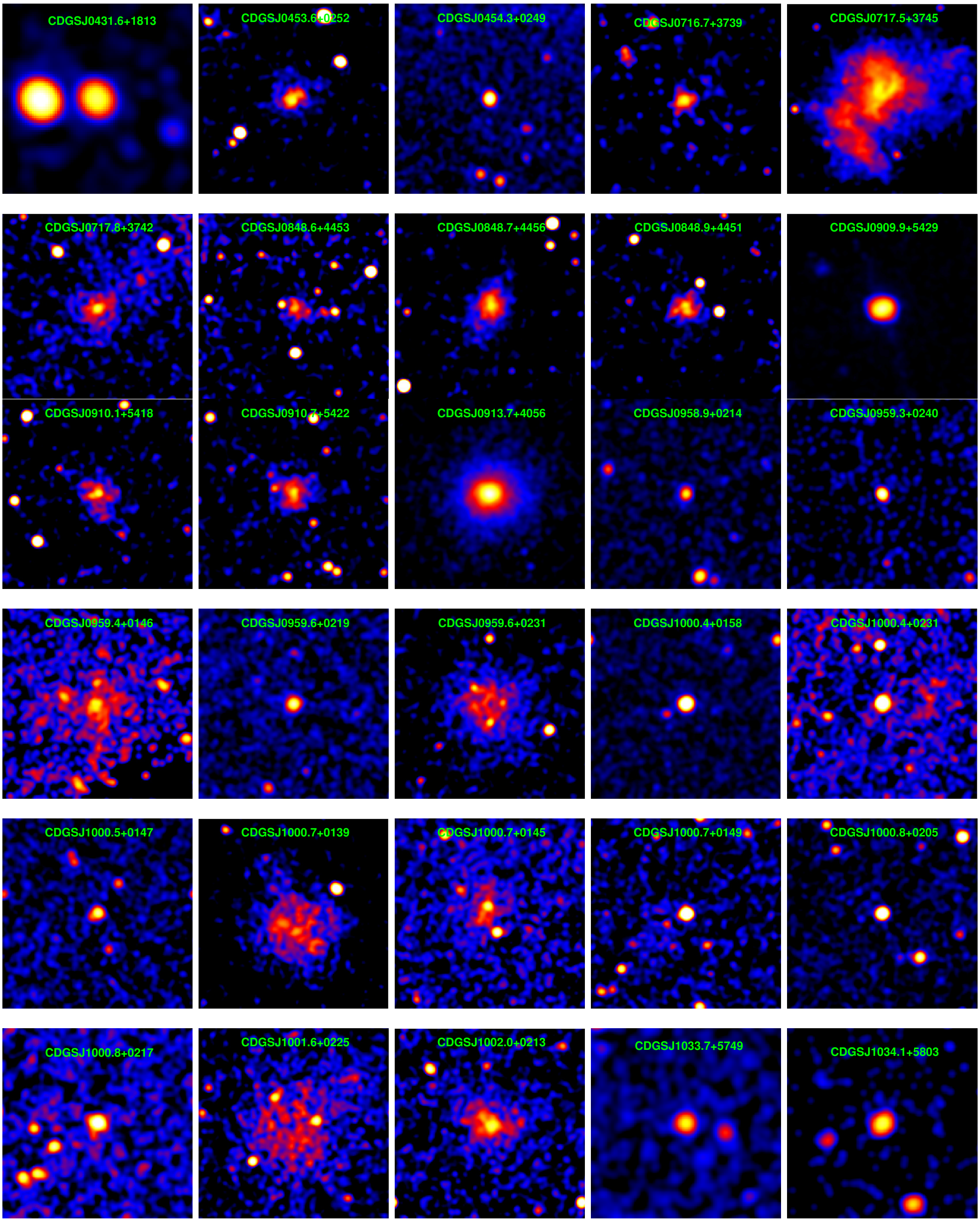
CDGSJ0431.6+1813
CDGSJ0453.6+0252
CDGSJ0454.3+0249
CDGSJ0716.7+3739
CDGSJ0717.5+3745
CDGSJ0717.8+3742
CDGSJ0848.6+4453
CDGSJ0848.7+4456
CDGSJ0848.9+4451
CDGSJ0909.9+5429
CDGSJ0910.1+5418
CDGSJ0910.7+5422
CDGSJ0913.7+4056
CDGSJ0958.9+0214
CDGSJ0959.3+0240
CDGSJ0959.4+0146
CDGSJ0959.6+0219
CDGSJ0959.6+0231
CDGSJ1000.4+0158
CDGSJ1000.4+0231
CDGSJ1000.5+0147
CDGSJ1000.7+0139
CDGSJ1000.7+0145
CDGSJ1000.7+0149
CDGSJ1000.8+0205
CDGSJ1000.8+0217
CDGSJ1001.6+0225
CDGSJ1002.0+0213
CDGSJ1033.7+5749
CDGSJ1034.1+5803

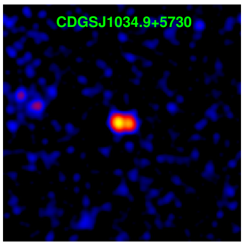
CDGSJ1034.9+5730

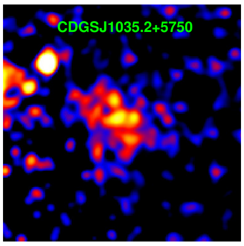
CDGSJ1035.2+5750

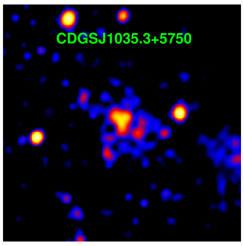
CDGSJ1035.3+5750

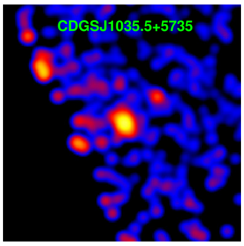
CDGSJ1035.5+5735

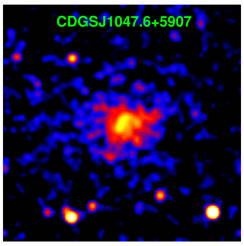
CDGSJ1047.6+5907

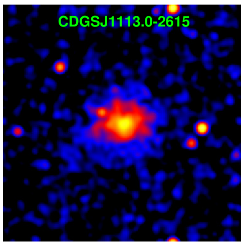
CDGSJ1113.0-2615

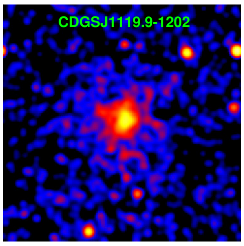
CDGSJ1119.9-1202

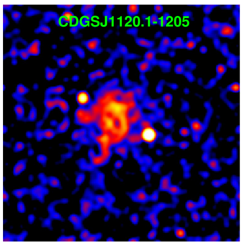
CDGSJ1120.1-1205

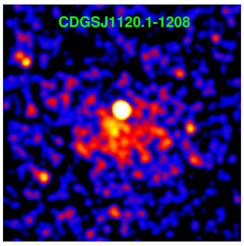
CDGSJ1120.1-1208

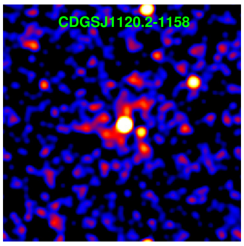
CDGSJ1120.2-1158

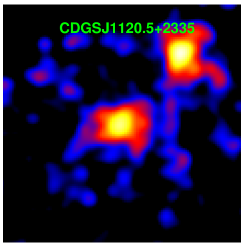
CDGSJ1120.5+2335

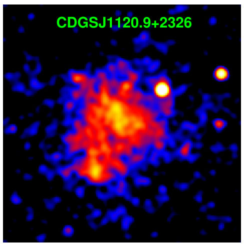
CDGSJ1120.9+2326

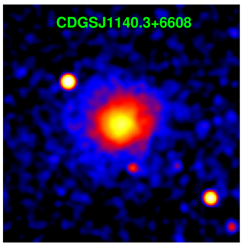
CDGSJ1140.3+6608

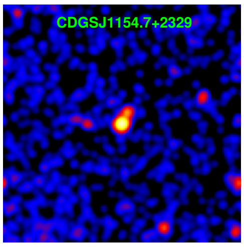
CDGSJ1154.7+2329

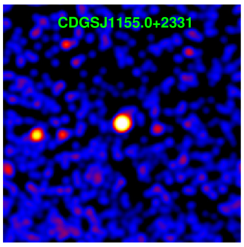
CDGSJ1155.0+2331

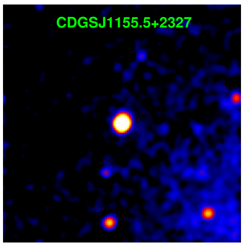
CDGSJ1155.5+2327

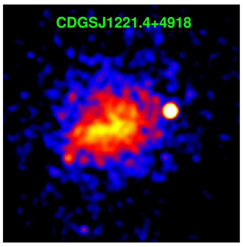
CDGSJ1221.4+4918

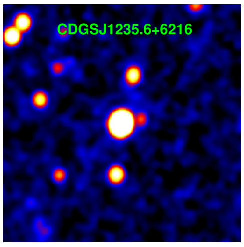
CDGSJ1235.6+6216

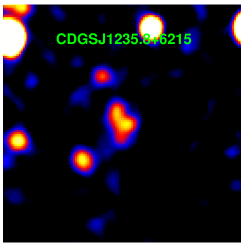
CDGSJ1235.8+6215

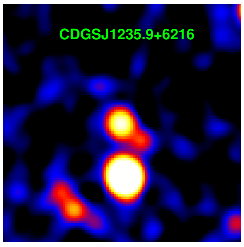
CDGSJ1235.9+6216

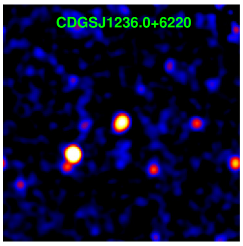
CDGSJ1236.0+6220

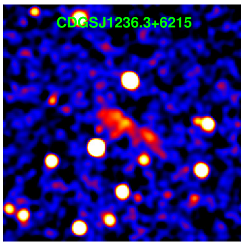
CDGSJ1236.3+6215

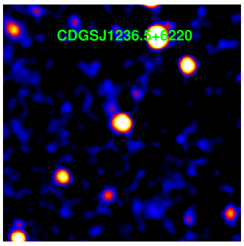
CDGSJ1236.5+6220

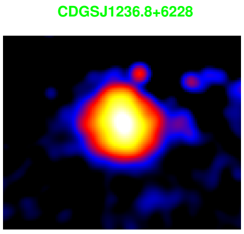
CDGSJ1236.8+6228

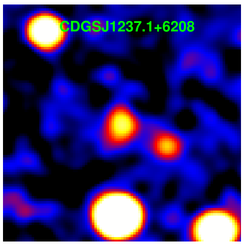
CDGSJ1237.1+6208

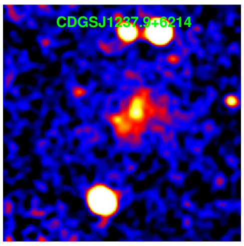
CDGSJ1237.9+6214

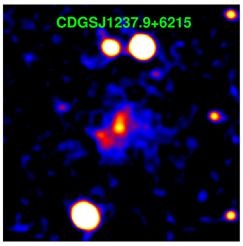
CDGSJ1237.9+6215

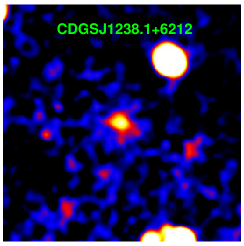
CDGSJ1238.1+6212

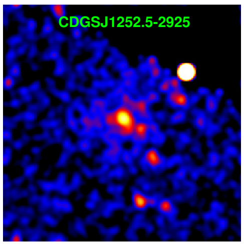
CDGSJ1252.5-2925

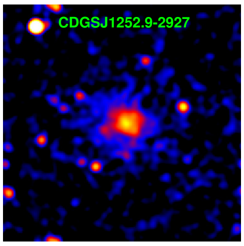
CDGSJ1252.9-2927

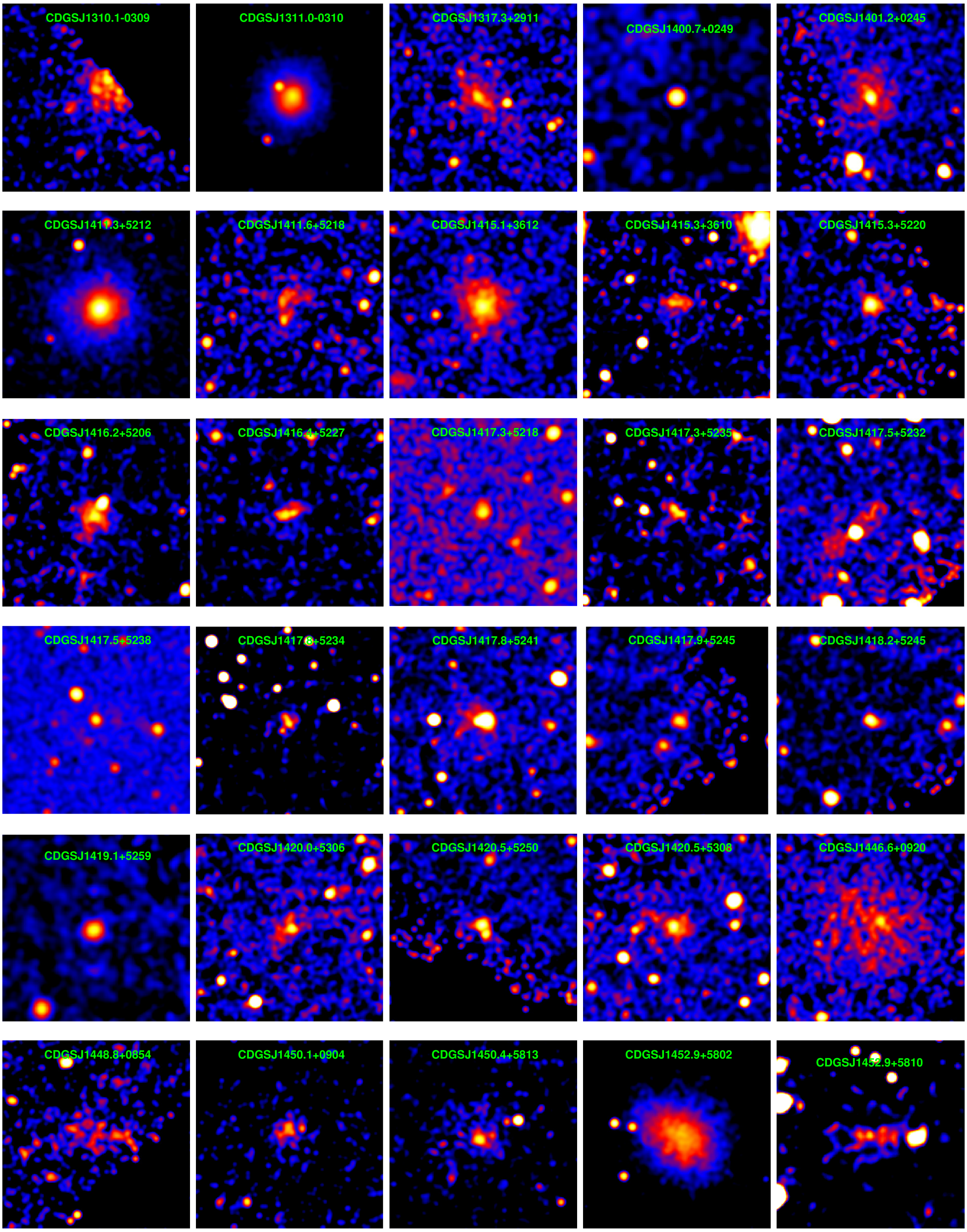
CDGSJ1310.1-0309
CDGSJ1311.0-0310
CDGSJ1317.3+2911
CDGSJ1400.7+0249
CDGSJ1401.2+0245
CDGSJ1411.3+5212
CDGSJ1411.6+5218
CDGSJ1415.1+3612
CDGSJ1415.3+3610
CDGSJ1415.3+5220
CDGSJ1416.2+5206
CDGSJ1416.4+5227
CDGSJ1417.3+5218
CDGSJ1417.3+5235
CDGSJ1417.5+5232
CDGSJ1417.5+5238
CDGSJ1417.8+5234
CDGSJ1417.8+5241
CDGSJ1417.9+5245
CDGSJ1418.2+5245
CDGSJ1419.1+5259
CDGSJ1420.0+5306
CDGSJ1420.5+5250
CDGSJ1420.5+5308
CDGSJ1446.6+0920
CDGSJ1448.8+0854
CDGSJ1450.1+0904
CDGSJ1450.4+5813
CDGSJ1452.9+5802
CDGSJ1452.9+5810

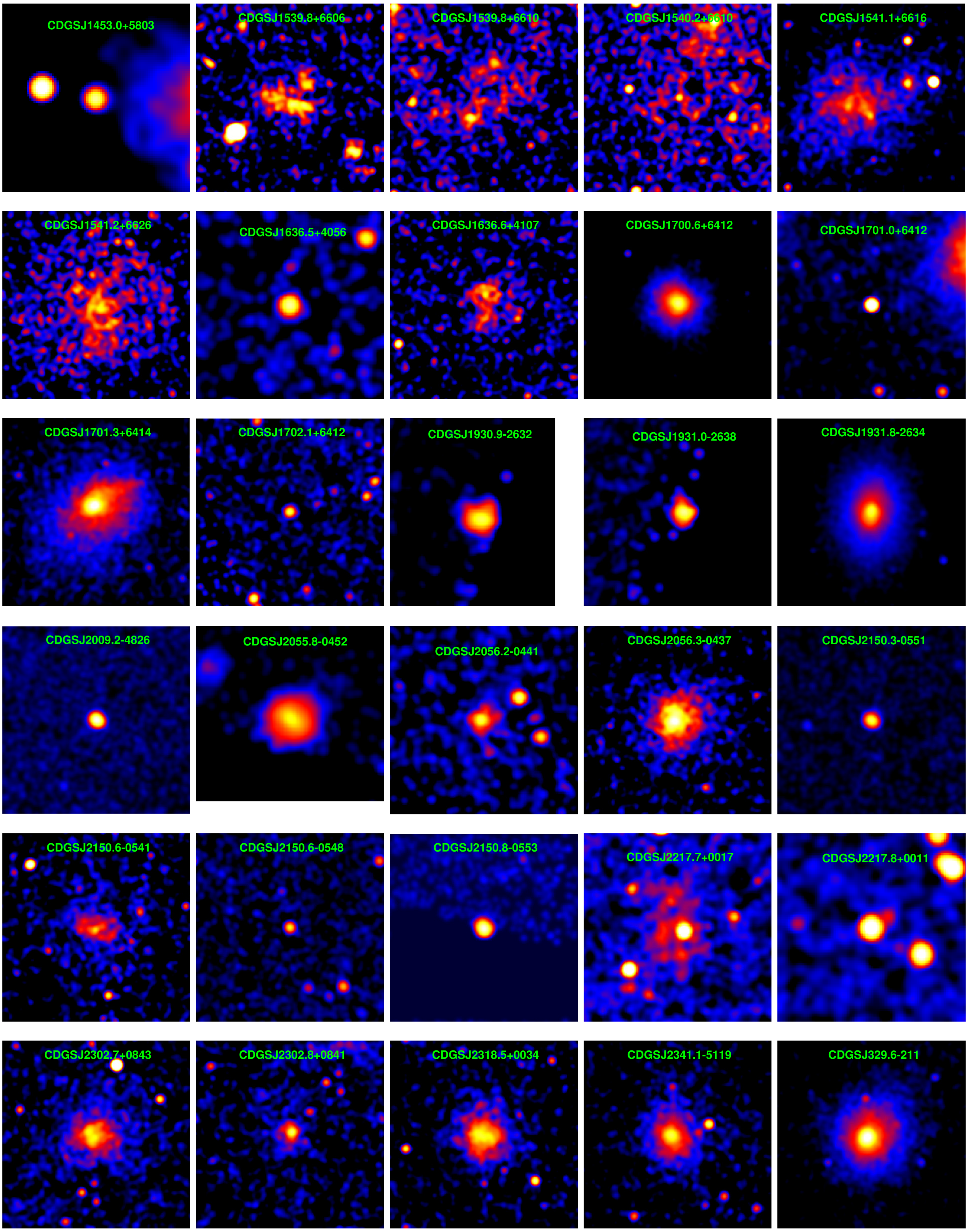
CDGSJ1453.0+5803
CDGSJ1539.8+6606
CDGSJ1539.8+6610
CDGSJ1540.2+6610
CDGSJ1541.1+6616
CDGSJ1541.2+6626
CDGSJ1636.5+4056
CDGSJ1636.6+4107
CDGSJ1700.6+6412
CDGSJ1701.0+6412
CDGSJ1701.3+6414
CDGSJ1702.1+6412
CDGSJ1930.9-2632
CDGSJ1931.0-2638
CDGSJ1931.8-2634
CDGSJ2009.2-4826
CDGSJ2055.8-0452
CDGSJ2056.2-0441
CDGSJ2056.3-0437
CDGSJ2150.3-0551
CDGSJ2150.6-0541
CDGSJ2150.6-0548
CDGSJ2150.8-0553
CDGSJ2217.7+0017
CDGSJ2217.8+0011
CDGSJ2302.7+0843
CDGSJ2302.8+0841
CDGSJ2318.5+0034
CDGSJ2341.1-5119
CDGSJ329.6-211

Appendix B

Analytical deprojection of a beta model

To derive the analytical form of the deprojected beta model, we start from the distribution of gas emissivity, given by:

$$j(r) = j_0(r^2/r_c^2)^{-\eta}, \tag{B.1}$$

where j_0 is the amplitude of the emissivity, r_c is the core radius and η is the slope of the distribution. The projection of this emissivity along the line of sight gives the observed surface brightness profile. Therefore, the surface brightness at a distance ω from the cluster centre is (see also Figure B.1):

$$S(\omega) = 2\int_0^\infty \mathrm{j(r)}\,\mathrm{d}z \tag{B.2}$$

Replacing Equation B.1 in Equation B.2, we obtain:

$$S(\omega) = 2j_0\int_0^\infty (\mathrm{r}^2/\mathrm{r}_\mathrm{c}^2)^{-\eta}\,\mathrm{d}z \tag{B.3}$$

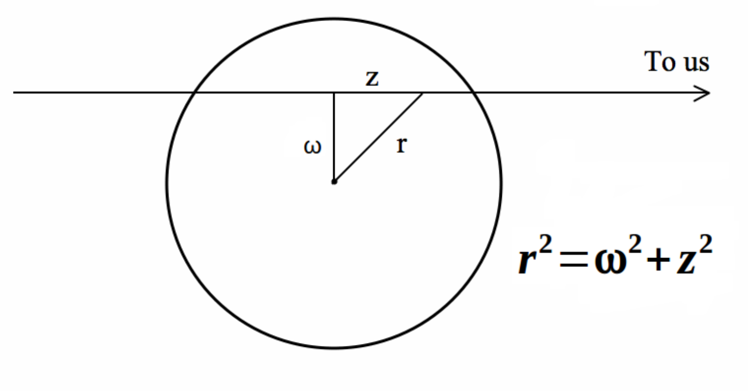

Figure B.1: Geometrical representation of a cluster used to calculate the emissivity integral along the line of sight through the cluster.

$$S(\omega) = 2j_0 \int_0^{\infty} \left(1 + \frac{\omega^2 + \mathrm{z}^2}{\mathrm{r}_\mathrm{c}^2}\right)^{-\eta} \mathrm{d}z \tag{B.4}$$

$$S(\omega) = 2j_0 \left(\frac{\omega^2 + r_c^2}{r_c^2}\right)^{-\eta} \int_0^{\infty} \left(1 + \frac{\mathrm{z}^2}{\omega^2 + \mathrm{r}_\mathrm{c}^2}\right)^{-\eta} \mathrm{d}z \tag{B.5}$$

Using the substitution $\tan\alpha = z^2/(r_c^2 + \omega^2)$, where z is the line-of-sight direction along which one is integrating, then

$$S(\omega) = 2j_0 \left[\int_0^{\pi/2} (1 + \tan^2\alpha)^{-\eta}\, \mathrm{d}\alpha\right] (\omega^2 + r_c^2)^{1/2} \sec^2\alpha \left(\frac{\omega^2 + r_c^2}{r_c^2}\right)^{-\eta} \tag{B.6}$$

Using $\tan^2\alpha = \sec^2\alpha - 1$

$$S(\omega) = 2j_0(\omega^2 + r_c^2)^{1/2} \int_0^{\pi/2} (\sec^2\alpha)^{-\eta} \sec^2\alpha\, \mathrm{d}\alpha \tag{B.7}$$

$$S(\omega) = 2j_0(\omega^2 + r_c^2)^{1/2} \left(\frac{\omega^2 + r_c^2}{r_c^2}\right)^{-\eta} \int_0^{\pi/2} \cos^{2\eta}\alpha \frac{1}{(\cos^2\alpha)}\, \mathrm{d}\alpha \tag{B.8}$$

$$S(\omega) = 2 j_0 r_c^{2\eta} (\omega^2 + r_c^2)^{-\eta+1/2} \int_0^{\pi/2} (\cos\alpha)^{2(\eta-1)}\, \mathrm{d}\alpha \tag{B.9}$$

For a surface brightness of the form:

$$S(\omega) = S_0 \left[1 + \left(\frac{\omega}{r_c} \right)^2 \right]^{-3\beta+0.5} \tag{B.10}$$

Comparing Equation B.10 with Equation B.9 we obtain: $\eta = 3\beta$ and

$$S_0\, (r_c^2)^{3\beta-0.5} = 2 j_0 r_c^{2\eta} \int_0^{\pi/2} (\cos\alpha)^{2(\eta-1)}\, \mathrm{d}\alpha \tag{B.11}$$

Therefore

$$j_0 = \frac{S_0}{2 r_c \int_0^{\pi/2} (\cos\alpha)^{2(\eta-1)}\, \mathrm{d}\alpha} \tag{B.12}$$

Finally, we obtain the emissivity 3D distribution as a function of parameters obtained by fitting the 2D surface brightness profile with a single beta model:

$$j(r) = \frac{S_0}{2 r_c \int_0^{\pi/2} (\cos\alpha)^{2(\eta-1)}\, \mathrm{d}\alpha} \left[1 + \left(\frac{r}{r_c} \right)^2 \right]^{-3\beta} \tag{B.13}$$